MRI and histological analysis of brain metastasis and the effect of systemic inflammation

Alastair Hamilton



New College
University of Oxford

Hilary Term 2013

for Janet and Rollin,

Table of Contents

Acknowledgments **7**

Abstract **8**

Abbreviations **9**

Introduction **12**
1.1 Neoplasia **13**
1.2 Metastasis **15**
1.3 Metastasis to the brain **17**
1.4 Immune cell entry into the CNS **21**
1.5 Metastatic cell entry into the brain **25**
1.6 The BBB in diagnosis and treatment of brain metastasis **34**
1.7 Magnetic Resonance Imaging **35**
1.8 Molecular MRI in neurological disease **38**
1.9 Aims of this thesis **41**

Materials and Methods **43**
2.1 Experimental schedules **43**
2.2 Materials **45**
2.2.1 Chemicals and reagents 45
2.2.2 Injectable agents 46
2.2.3 Antibodies 46
2.2.4 Cells 47
2.2.5 Cell culture tools and reagents 47
2.2.6 Animals and materials 48
2.2.7 Immunohistochemistry and immunofluorescence materials 48
2.2.8 Cytokine measurement kits 49
2.2.9 Adenoviral preparation 49
2.2.10 Instrumentation 50
2.2.11 Software 51
2.3 Methods **52**
2.3.1 Cell culture 52
2.3.2 Adenoviral preparation 53
2.3.3 Preparation of injectable agents 60
2.3.4 Animal work 61
2.3.5 Magnetic Resonance Imaging (MRI) 65
2.3.6 Immunohistochemistry 66
2.3.7 Immunocytochemistry 69
2.3.8 MRI analysis 69
2.3.9 Immunohistochemical analysis 70

2.3.10 Statistical analysis 71

Chapter 3 73

MRI detection of VCAM-1 upregulation at sites of brain metastasis 73

3.1 Introduction 73

3.1.1 VCAM-1 upregulation in brain metastases 73
3.1.2 VCAM-MPIO proof of principle 74
3.1.3 VCAM-MPIO in brain metastases 75
3.1.4 Outstanding questions 76

3.2 Methods 77

3.2.1 Animal model 78
3.2.2 MRI 78
3.2.3 Immunohistochemistry / immunofluorescence 78
3.2.4 Analysis tools 79
3.2.5 Statistics 80

3.3 Results 80

3.3.1 Colocalisation 80
3.3.2 Analysis automation 84
3.3.3 Filtering procedures 109

3.4 Discussion 118

3.4.1 Colocalisation 118
3.4.2 Analysis automation 119
3.4.3 Image filtering 121
3.4.4 Concluding remarks 122

Chapter 4 124

Development of 4T1-GFP metastases in the brain 124

4.1 Introduction 124

4.1.1 Tumour development 125
4.1.2 Vascular labelling 126
4.1.3 Outstanding questions 128

4.2 Methods 129

4.2.1 Animal model 129
4.2.2 MRI 129
4.2.3 Immunohistochemistry / immunofluorescence 130
4.2.4 Immunocytochemistry 130
4.2.5 Analysis tools 130
4.2.6 Statistics 131

4.3 Results 131

4.3.1 Correlation between metastatic loci and hypointensities in the brain 132
4.3.2 Relative abundance of tumours across brain regions 135
4.3.3 Characterisation of tumour morphology 137
4.3.4 Comparison of morphology between brain regions 141
4.3.5 Development of metastases on arterioles and venules 149

4.4 Discussion 153

4.4.1 Spatial distributions of metastases and hypointensities 153
4.4.2 Development of metastases in the brain 154
4.4.3 Vascular localisation of brain metastases 157
4.4.4 Future work 158
4.4.5 Concluding remarks 159

Chapter 5 160

Effects of systemic and local inflammation on the neurovasculature and the development of brain metastases 160

5.1 Introduction 160

5.1.1 Inflammatory stimulus 160
5.1.2 Outstanding questions 164
5.2 Methods 165
5.2.1 Adenoviruses 165
5.2.2 Animal models 165
5.2.3 MRI 167
5.2.4 Immunohistochemistry / Immunofluorescence 167
5.2.5 Analysis tools 167
5.2.6 Statistics 168
5.3 Results 168
5.3.1 Adenovirus effects on systemic inflammation 168
5.3.2 Adenovirus effects on cerebral VCAM-1 expression 174
5.3.3 MRI of adenovirus-injected animals 176
5.3.4 Adenovirus effects on tumour development 178
5.3.5 MRI of adenovirus and tumour injected animals 190
5.3.6 Effects of central inflammation on tumour development 197
5.3.7 Effects of central inflammation on VCAM-MPIO hypointensities in the brain 199
5.4 Discussion 203
5.4.1 Systemic inflammatory effects of adenoviruses 203
5.4.2 Neuroinflammatory effects of adenoviruses 207
5.4.3 Effects of a systemic inflammatory challenge on tumour development 208
5.4.4 MRI analysis of virus and tumour-burdened animals 210
5.4.5 Future work: systemic inflammation 211
5.4.6 Pilot study on local neuroinflammation 218
5.4.7 Concluding remarks 219

Discussion 221
6.1 VCAM-1 expression at the site of metastasis is associated with MRI hypointensities 223
6.1.1 Identification of hypointensities 223
6.1.2 Co-localisation of tumours and hypointensities 225
6.2 Tumour development in different anatomical brain regions 226
6.3 Adenovirus-mediated inflammation 228
6.4 VCAM-1 expression as a possible effector and consequence of brain metastasis 230
6.5 Effects of inflammation on tumour morphology 233
6.6 Effects of localised neuroinflammation on tumour development 234
6.7 Wider implications of the work 234

References 237

Appendix 1 261

Appendix 2 263
MATLAB scripts for automated hypointensity analysis 263
MATLAB scripts for GE3D filtering 270
MATLAB script for metastasis analysis 275

Appendix 3 279

Acknowledgments

None of this work would have been possible without the help, guidance and assistance of many others working in the field and beyond. Firstly, I would like to thank the Systems Biology Doctoral Training Centre and the University of Oxford for giving me the opportunity to study for a DPhil, and New College for looking after me so well over the best part of a decade. Nor would this work have been possible without the financial support of the EPSRC and Cancer Research UK.

I am indebted to my supervisors, Nicola Sibson and Daniel Anthony, whose wealth of scientific knowledge and experience has directed, supported and guided me over the last few years, and to the students and post-docs working in both laboratories, in particular John Connell, Alexandre Khrapitchev, James Larkin, Emma O'Brien, Manuel Sarmiento-Soto and Sébastien Serres.

I would also like to thank the wider community working in the Oncology Department, whose input, personal as well as professional, has been indispensible. There are too many to name them all here, but particular mention must go to Danny Allen, Lukxmi Balathasan, John Beech, Magdalena Flieger, Alex Gordon-Weeks, Kamila Hussien, Sean Smart, Thomas Tapmeier, Alison Tedcastle and Karla Watson.

I also owe a huge debt of thanks to Kerstin Weller, who has taken care of me so well over the last few months and has coped so well with the vagaries of my mood in the run up to submitting and defending this thesis. Vielen herzlichen Dank!

Finally, I would like to thank my brothers, Richard and Gordon, and my parents, Janet and Rollin, whose enthusiasm for science first prompted my curiosity in biology, and whose continued support has encouraged me to pursue my interests in the subject.

Abstract

Background
Brain metastasis is a leading cause of cancer mortality and affects 20-40% of all cancer patients. The BBB is responsible for isolation and protection of the brain parenchyma from many diagnostic and therapeutic agents. New molecular agents that target tumour-associated VCAM-1 expression on the brain endothelium show improvements in the early diagnosis of brain metastasis. The vascular endothelium of the CNS plays an important role in the maintenance of the brain microenvironment and possibly aids the extravasation of tumour cells via expression of CAMs.

Aims
Using the breast carcinoma-derived 4T1 cell line, syngeneic to BALB/c mice, this work aimed (i) to determine the level of colocalisation between VCAM-1 expression at sites of brain metastasis and the presence of VCAM-MPIO-induced hypointensities in MR datasets; (ii) to describe the normal developmental characteristics of the intracardial BALB/c-4T1 brain metastatic model in the absence of overt inflammation; (iii) to test the effects of an adenovirus-induced systemic inflammatory challenge on metastatic uptake and development in the brain.

Results
The level of correspondence of VCAM-MPIO-derived hypointensities with VCAM-1 expression at the tumour site was found to be dependent on the size of metastasis. An improved method for detection of VCAM-MPIO hypointensities using an automated method has been presented. Tumours were found to develop preferentially on venous rather than arteriolar blood vessels, and showed greater and lesser abundance in different anatomical brain regions. Adenovirus injection was found to cause an upregulation of a range of peripheral pro-inflammatory cytokines, and expression of VCAM-1 on cerebral vasculature, preferentially on arteriolar blood vessels. Both pre- and post-treatment with adenovirus caused a two-fold reduction in tumour numbers and altered developmental characteristics of established tumours, although no significant differences were observed in VCAM-MPIO hypointensities in MR datasets.

Conclusions
The development of molecular MRI approaches to target VCAM-1 expression at the site of brain metastases has improved the sensitivity of tumour detection. 4T1-GFP metastasis to the brain is specific both to anatomical sites and to regions of the vascular bed, suggesting differences in vascular morphology and/or signalling dynamics in these locations. The changes in tumour number and morphology as a result of systemic inflammation suggest an anti-tumour effect of adenoviral treatment and, given the role of the systemic immune system and its importance in the development of immunotherapies, possible future directions for research.

Abbreviations

αSMA = alpha Smooth Muscle Actin
ACTH = Adrenocorticotropic Hormone
Ad = Adenovirus
ADH = Antidiuretic hormone
AME = Absorptive-Mediated Endocytosis
ANOVA = Analysis of Variance
A-P = Alkaline Phosphatase
AP = Anterior Posterior
APC = Antigen-Presenting Cell
ATCC = American Type Culture Collection
BBB = Blood-Brain Barrier
BOLD = Blood Oxygenation Level Dependent
CD = Cluster of Differentiation
CNS = Central Nervous System
CT = Computed Tomography
CTL = Cytotoxic T Lymphocyte
DAB = 3,3'-diaminobenzidine
DAPI = 4',6-diamidino-2-phenylindole
DMEM = Dulbecco's Modified Eagle Medium
DNA = deoxyribonucleic acid
DPX = Distyrene and Plasticisers in Xylene
ds = double stranded
DTH = Delayed-Type Hypersensitivity
DTI = Diffusion Tensor Imaging
DTPA = Diethylene Triamine Pentaacetic Acid
EAE = Experimental Autoimmune Encephalomyelitis
EC = Endothelial Cell
EDTA = Ethylenediaminetetraacetic Acid
(E)GFP = (Enhanced) Green Fluorescent Protein
EMEM = Eagles' Minimum Essential Medium
EMT = Epithelial-Mesenchymal Transition
Eph = Ephrin
eph = ephrin
ET = Endothelin
FasL = Fas Ligand
FBS = Foetal Bovine Serum
FID = Free Induction Decay
fMRI = Functional MRI
FSEMS = Fast Spin Echo Multi Slice
GEMS = Gradient Echo Multi Slice
GE3D = 3-Dimensional Gradient Echo

Gd = Gadolinium
h = hour
HBMEC = Human Brain Microvascular Endothelial Cell
HEK = Human Embryonic Kidney
HEPES = 4-(2-hydroxyethyl)-1-piperazineethanesulfonic Acid
HEV = High Endothelial Venule
HUVEC = Human Umbilical Vein Endothelial Cell
i.c. = intra-cardial
i.s. = intra-striatal
i.p. = intra-peritoneal
i.v. = intra-venous
ICAM-1 = Intercellular Adhesion Molecule 1
IFN(-γ) = Interferon (Gamma)
Ig = Immunoglobulin
IL(-1β) = Interleukin(-1 beta)
IL-1ra = Interleukin-1 receptor antagonist
IMS = Industrial Methylated Spirits
I-Tac = Interferon-Inducible T-Cell Alpha Chemoattractant
kb = kilobases
KC = Keratinocyte Chemoattractant
LFA-1 = Lymphocyte Function-Associated Antigen 1
LOD = Limit Of Detection
LPS = Lipopolysaccharide
MΦ = Macrophage
Mac-1 = Macrophage-1 Antigen
MANOVA = Multivariate Analysis of Variance
MC = Mast Cell
MCP-1 = Monocyte Chemotactic Protein 1
MHC = Major Histocompatibility Complex
MIG = Monokine Induced by Interferon Gamma
min = minute
MMP = Matrix Metalloproteinase
MPIO = Micro-Particle(s) of Iron Oxide
MR(I) = Magnetic Resonance (Imaging)
MTT = 3-(4,5-Dimethylthiazol-2-yl)-2,5-diphenyltetrazolium bromide
MWCO = Molecular Weight Cut Off
NIfTI = Neuroimaging Informatics Technology Initiative
NK = Natural Killer (cell)
NMR = Nuclear Magnetic Resonance
NO = Nitric Oxide
NRP = Neuropilin
P = Platelet
PBS = Phosphate Buffered Saline
PC = Pericyte
PET = Positron Emission Tomography
PFA = Paraformaldehyde
pfu = plaque-forming units
Pgp = P-glycoprotein
PI-3K = Phosphoinositide 3-kinase/protein kinase
PLP = Paraformaldehyde lysine periodate
PMN = Polymorphonuclear Leukocyte

Poly I:C = polyinosinic:polycytidylic acid
r.t. = Room Temperature
RF = Radio Frequency
RME = Receptor-Mediated Endocytosis
ROI = Region Of Interest
ROS = Reactive Oxygen Species
RRI = Radiobiology Research Institute
s.d. = standard deviation
SDF-1α = Stromal Cell-Derived Factor 1α
sec = second
SNR = Signal-to-Noise Ratio
SPIO = Superparamagnetic Particle(s) of Iron Oxide
.tiff = Tagged Image File Format
T = Tesla
$TCID_{50}$ = 50% Tissue Culture Infective Dose
TE = Echo Time
TE = Tris-EDTA
TGF-β = Transforming Growth Factor beta
TJ = Tight Junction
TMB = Tris-NaCl Blocking Buffer
TNF-α = Tumour Necrosis Factor alpha
TR = Repetition Time
TSA = Tyramide Signal Amplification
USPIO = Ultra-Small Paramagnetic Particle(s) of Iron Oxide
VCAM-1 = Vascular Cell Adhesion Molecule-1
VEGF(R) = Vascular Endothelial Growth Factor (Recptor)
VLA-4 = Very Late Antigen 4
VOI = Voxel Of interest
WBRT = Whole Brain Radiotherapy
w.t. = wild-type

Introduction

Cancer is a disease that has been recorded throughout millennia of human history. Although the disease was first named by Hippocrates, who likened the subcutaneous tumours he observed to the shape of a crab, evidence of tumours in human populations dates back to the early Egyptians and the Edwin Smith Papyrus of 1500 BC. However, it was not until the dramatic increases in life expectancy over the last century that cancer became the disease of significant mortality that it is today. It was President Richard Nixon's National Cancer Act of 1971, popularly known as 'The War on Cancer', that set the scene for large increases in funding for its "prevention, diagnosis and treatment". Despite this, cancer incidence and mortality has continued to increase, partly as a result of our increasingly ageing population, and is one of the leading killers in the world today, accounting for approximately 13% of all deaths worldwide (Ferlay et al., 2010).

Cancer is a genetic disease that results in the unchecked proliferation of cells within tissues of the body. It occurs as a result of altered intra-cellular replication machinery, either via an inherited genotype, exposure to mutagenic or carcinogenic agents, or via replication errors during successive rounds of DNA polymerisation upon cell division. DNA replication is extremely faithful with errors occurring in eukaryotic cells at the rate of approximately one base pair in 10^7 - 10^8 (Boyer et al., 1993). However, mutations in regions of DNA such as oncogenes and tumour suppressor genes, whose function is to maintain genomic stability, can cause the cells that contain these mutations to increase the rate at which they acquire

further mutations, a condition known as a mutator phenotype (Loeb, 2001). Over the course of a lifetime, as more rounds of DNA replication take place, the likelihood of a harmful mutation increases, and consequently, an increase in the probability of damage to replication machinery, resulting in the development of neoplasms. Cancer is, therefore, a malady for which the risk increases with age (Cancer Incidence by Age: Cancer Research UK).

Recent epidemiological studies suggest that more than one in three in the UK population will develop cancer at some point over their lifetime (Sasieni et al., 2011). However, cancer can occur at any stage of life. Specifically, patterns of incidence differ between cancer types, with prostate cancers occurring in the male population almost exclusively over 50 years of age and a large peak in the incidence of breast cancer in females aged 25-49. By contrast leukaemia and Hodgkin's lymphoma are cancers of childhood and early adulthood, rarely occurring after the age of 25 (Cancer Incidence by Age: Cancer Research UK).

Neoplasms can occur in any tissue in the body, although are more frequent where there are rapidly replicating cell populations, most notably in endothelial and epithelial tissues. Cancers affecting these tissue types are named carcinomas, and account for 80% of cancer mortality in the Western world (Weinberg 2006). Cancers derived from a greater variety of slower-growing tissues, the sarcomas, leukaemias, neuro-ectodermal tumours and melanomas account for the remaining 20% of cancer mortality.

1.1 Neoplasia

Many of the steps in the formation and development of cancers are now well established, including many of the specific mutations that can trigger sustained proliferation in cell populations leading to neoplastic growth. Hanahan and Weinberg have set out the most important features of cancer growth in their recent update to their seminal review (Hanahan

and Weinberg, 2011), with a list of ten attributes that cells need to acquire in order to develop a cancerous phenotype. I will describe all of them briefly and concentrate on the three that are most important in the context of this thesis: the abilities to metastasize, to avoid immune destruction and to promote inflammation.

Most fundamentally, neoplastic growth is the result of continued proliferative signalling within a cell. Deregulation of the genetic control of cell proliferation pathways allows cells to continue dividing and to form a clonal mass. This process is often the result of mutations in oncogenes or tumour suppressor genes. Oncogenes commonly code for members of cell proliferation signalling pathways such as receptor proteins, G proteins, tyrosine kinases, serine-threonine kinases and transcription factors, proteins that exert a level of control over a wide range of intracellular and extracellular signalling pathways (Hanahan and Weinberg, 2011). Loss- or gain-of-function mutations in these genes can lead to alterations in gene expression patterns and responses to growth factors, aberrant signalling pathways and changes in cellular phenotype. This is the case for *Src*, the classic proto-oncogene that codes for a non-receptor tyrosine kinase, which was first identified in the Rous sarcoma virus (RSV) as *v-src*, and later in the chicken genome as *c-src*. Infection of normal chicken cells by RSV leads to transformation of those cells into tumour cells and formation of a sarcoma (Stehelin et al., 1976). In contrast, tumour suppressor genes often play important roles in the maintenance of cellular homeostasis and progression through the cell cycle. Mutations in these genes can therefore lead to a rapid development of neoplastic growth (Hanahan and Weinberg, 2011). The archetypal tumour suppressor gene *Rb* normally regulates progression through the cell cycle between G1 and S phase via control of E2F transcription factors (Wu et al., 1995; Das et al., 2005), and was the gene identified as mutated in familial and sporadic retinoblastoma (Knudson, 1971).

Mutations in oncogenes and tumour suppressor genes often increase the probability of further mutation. Mutations in genes controlling telomerase activity prevent the cell from entering a senescence or crisis phase after multiple rounds of cell division (Collado and Serrano, 2010), leading to a feature of cancer cell lines known as immortalization. Similarly, mutations in genes that control cellular metabolism allow tumour cells to shift their metabolic activity and continue to divide. This feature of tumour growth is demonstrated by the Warburg effect, the dramatic increase in glycolysis in aerobic environments (Warburg, 1956). Finally, as the tumour continues to expand, it requires a greater supply of oxygen and metabolites. Changes in regulation and expression of genes, frequently in the vascular endothelial growth factor receptor (VEGFR) and Neuropilin (NRP) signalling pathways (Koch and Claesson-Welsh, 2012), allow the formation of new blood vessels at the tumour site, a process known as angiogenesis (Gomes et al., 2013).

1.2 Metastasis

One further important feature of tumour growth and development, and perhaps the most feared, is the ability to metastasise. Metastasis is the spread of cells that slough off a primary tumour and travel through the bloodstream or the lymphatic vessels to new sites in the body where they are able to arrest and continue to proliferate, forming secondary tumours frequently at sites distant to the primary tumour. The spread of tumours through the lymphatic system is normally more anatomically localized than that through the bloodstream (Wong and Hynes, 2006), with tumours spreading to sequential draining lymph nodes away from the tumour site. By comparison, tumour cells released into the bloodstream are capable of accessing all organs in the body and, as long as these cells are capable of surviving, arresting and proliferating at the distant site, will be competent to form new tumours at these locations (Luzzi et al., 1998; Chambers et al., 2002; Fidler, 2003).

Survival in the bloodstream is dependent on several derived features of these cells. Competent metastatic cells must be able to detach from a basement membrane and survive unattached in the bloodstream. Normally, detachment from an extracellular matrix leads to anoikis, a specific type of apoptotic cell death, and a process that is aberrant in metastatic cells. A set of genetic changes known as the epithelial-mesenchymal transition (EMT) that occurs often via the deregulation of the TGF-β pathway (Bierie and Moses, 2006; Massagué, 2008; Ikushima and Miyazono, 2010), is necessary in order for carcinoma cells to become metastatic, and includes the acquisition of anoikis resistance (Jia et al., 2012; Frisch et al., 2013). The EMT is, therefore, one of the primary drivers in enabling primary neoplastic cells to metastasise.

The second part of the metastatic cascade is the ability of circulating tumour cells to extravasate at sites anatomically distant to the primary tumour. Very much less is known about this process compared to the primary steps in the formation of competent metastatic cells. However, clinical data have demonstrated that metastatic dissemination is organ specific (Paget, 1889). For example, colon carcinoma frequently metastasises to the lung and the liver, but almost never to other parts of the intestine, the kidneys or the muscle (Chambers et al., 2002). Similarly, brain metastases are most frequently derived from breast, lung and melanoma primaries (Fidler et al., 2002). Several theories have been put forward to explain the specificity of metastasis to secondary sites, including paracrine signalling via tumour cell surface protein and carbohydrate moieties (Turner, 1982; Reading and Hutchins, 1985; Raz and Lotan, 1987) and adhesion molecules on the vascular endothelium (Nicolson, 1988a, 1988b).

The spread of metastatic cells around the body is significant not least for its effect on cancer survival. Metastatic deaths account for over 90% of cancer mortality (Gupta and Massagué,

2006), in part due to our increasing ability to treat primary tumours successfully. By far the most frequent sites of metastasis are the local and regional lymph nodes, accounting for over 30% of all metastasis from the primary tumour. Before the advent of modern cancer treatment regimes the most common sites of metastatic spread through the bloodstream were the lung and the liver, both highly vascularized organs, each of which account for a further 10% of total metastatic spread (Disibio and French, 2008). The brain was apparently a much less frequent site of metastasis with approximately 1% of metastasis occurring here (Disibio and French, 2008). More recently, however, metastatic spread to the brain has become more common, possibly as a result of the improved treatment of primary tumours and longer life expectancies (Nussbaum et al., 1996). Critically, metastatic spread to the brain is often lethal owing to the potential paraneoplastic endocrine and physiological effects of brain metastases and the difficulties associated with diagnosing metastatic lesions, planning surgery or administering drugs to treat them, as discussed below. A variety of features of the brain, both anatomical and physiological, make this a unique organ in which to study metastasis.

1.3 Metastasis to the brain

Metastatic dissemination to the brain is of particular clinical and research importance. Brain metastases outnumber primary brain tumours by ten to one (Nussbaum et al., 1996), and it is now estimated that between 20% and 40% of cancer patients will develop brain metastases (Nussbaum et al., 1996). These patients have a dismal prognosis, with a median survival time of 3-6 months (Lagerwaard et al., 1999). Treatment regimes usually comprise surgical removal of metastatic lesions when numbers are low (≤ 3) and/or whole-brain radiotherapy (WBRT), but with median survival times of 9-12 months these treatments confer only a minimal benefit in overall survival (Tsao et al., 2012b). Any increase in brain

volume is limited by the dura and the skull, so tumour growth can cause an increased intracranial pressure, which in turn can lead to reduced cerebral blood flow (Kety et al., 1948). Thus, depending on their intracranial location, tumours in the brain may induce a wide variety of neurological symptoms, most frequently headaches, and often impairment of sensory and motor functions and cognitive impairment (Gavrilovic and Posner, 2005; Tsao et al., 2012a). Paraneoplastic endocrine effects are also common, as is often the case in pituitary adenomas via the ectopic production of antidiuretic hormone (ADH) or adrenocorticotropic hormone (ACTH) (Suojun et al., 2012). Thus, brain metastases can exhibit profound pathological effects early in their development, presumably a factor that is responsible for short survival times in patients.

Brain metastases are extremely hard to diagnose early (Weil et al., 2005) and, consequently, difficult to treat effectively (Fokas et al., 2013). Blood vessels of the central nervous system (CNS) have a specialized vessel wall, termed the blood-brain barrier (BBB). Like blood vessels elsewhere in the body, the lumen is surrounded by a layer of endothelial cells, which in the brain express tight junction proteins (Reese and Karnovsky, 1967; Brightman and Reese, 1969; Nagy et al., 1984), preventing the paracellular transport of solutes from blood plasma into the tissue fluid of the brain[1]. Transcellular transport is tightly regulated by brain endothelial cells, allowing a relatively small selection of molecules to pass into the brain. Small and/or lipophilic substances such as water and dissolved blood gases are free to diffuse across endothelial cell membranes (Pardridge, 1998). Facilitated diffusion via glucose transporter-1 (GLUT-1) allows passage of glucose into the brain (Dick and Harik, 1986). Macromolecular transport occurs either via receptor-mediated endocytosis (RME) or absorptive-mediated endocytosis (AME). The highly specific RME is responsible for the

[1] Tight junctions can also be found between endothelial cells in the testis, the epididymis (Mital et al., 2011) and the eye (Streilein, 2003).

transport of proteins such as insulin (Duffy and Pardridge, 1987), transferrin (Fishman et al., 1987) and insulin-like growth factors (Duffy et al., 1988). AME appears to be less specific than RME and allows transport of cationic peptides such as histone (Pardridge et al., 1989) and cationized albumin (Pardridge et al., 1990). Nevertheless, the list of molecules that are able to cross the BBB is relatively short, and many pharmaceutical agents used in the treatment of cancer in other organs are prevented from accessing the brain parenchyma by the protective actions of the BBB (Rajadhyaksha et al., 2011). Transcranial (Pathirana et al., 2009), focused ultrasound (Husseini and Pitt, 2009) and nasal (Landis et al., 2012) CNS drug delivery systems are currently the focus of much research, as are attempts to harness the RME and AME pathways (Pardridge, 2005; Barbu et al., 2009). In addition the lipidisation of hydrophilic molecules, the use solute carriers for drug co-transport (Anderson and Thwaites, 2010), magnetic nanoparticles and targeting peptides with high membrane penetration (Thomsen et al., 2012) are further avenues of research interest.

These properties of the BBB have led to the brain being called an immune-privileged organ. In reality the brain should instead be thought of as an immune-specialized organ (Cossetti et al., 2012). The BBB acts primarily to control the movement of metabolites from the blood to the tissue fluid of the brain, and to prevent the colonization of the brain parenchyma by infectious agents. Very few pathogens and parasites are able to infect the brain parenchyma and those that are able to do so, such as the rabies virus, have developed highly specialized entry mechanisms (Niu et al., 2011). Immune policing of the BBB must play a role in the ability of pathogens to cross, as patients with retroviral illness such as HIV infection exhibit altered permeability of the BBB (Afonso et al., 2008) and a greater incidence of brain pathogenesis (Itzhaki et al., 2004; Scully et al., 2008; Kamerkar and Davis, 2012).

Approaches to delivering diagnostic or pharmaceutical agents across the BBB either require selective permeabilisation of the BBB at sites of pathology or contrast agents of the correct size and lipophilicity to cross the BBB, and with the correct biological specificity to yield information relating to local pathology. So far efforts to harness the AME and RME pathways to allow transit of contrast agents into the brain parenchyma have not yielded much success (Pardridge, 2005; Barbu et al., 2009). However, a variety of methods have been developed to transiently permeabilise the BBB. These include the injection of mannitol (Ikeda et al., 2002; Wadghiri et al., 2003; Wang et al., 2007), and putrescine (Poduslo and Curran, 1996a, 1996b; Wengenack et al., 2000), both of which lead to a global increase in the permeability of the BBB. Tests in rabbits have also shown the possibility of delivering transcranial focused ultrasound, guided by MR, to cause a transient permeabilisation of the BBB at a single site (Huang et al., 2012) and recent work in our group has explored the possibility of permeabilisation at the site of brain metastasis using bolus systemic injection of cytokines (Connell et al., in review).

Nonetheless, circulating immune system cells are able to cross the BBB and enter the perivascular space and the brain parenchyma, although the ability to do so may be more tightly regulated by endothelial cells in the brain than in other organs of the body (Ransohoff and Engelhardt, 2012). Such cells are thought to cross into the brain parenchyma by one of three routes (Ransohoff et al., 2003). Firstly, T cell populations have been shown to cross from the blood to the cerebrospinal fluid across the choroid plexus via a P-selectin-dependent pathway (Carrithers et al., 2002), that appears to favour CD4+ T cells, possibly via upregulation of VLA-4 (Svenningsson et al., 1993) or CXCR3 (Kivisäkk et al., 2002). Secondly, lymphocyte recruitment from the blood to the subarachnoid space (Hickey and Kimura, 1988) also appeared to be dependent on P-selectin and α4 integrin expression (Kerfoot and Kubes, 2002). Finally, activated T cell blasts have been observed to cross from the blood to

the perivascular space (Wekerle and Fierz, 1985; Hickey and Kimura, 1988), a route that was shown to be upregulated in response to systemic exposure to LPS or TNF-α (Piccio et al., 2002), and also dependent on P-selectin and P-selectin glycoprotein ligand 1 (PSGL1) (Kerfoot and Kubes, 2002).

The metastatic tumours discussed in this thesis are all associated with cerebral blood vessels; although occasional leptomeningeal tumours were observed they were not counted in the analyses presented in this thesis. Therefore, I will concentrate on the blood-perivascular space route of metastatic and immune cell entry into the CNS.

1.4 Immune cell entry into the CNS

Increasing evidence over the past decade has suggested that invading cells of the immune system are a common feature of neoplasms (De Palma et al., 2007; Johansson et al., 2008; Murdoch et al., 2008; Nelson, 2008; Bindea et al., 2010; Coffelt et al., 2010; DeNardo et al., 2010; Egeblad et al., 2010; Ferrone and Dranoff, 2010; Pagès et al., 2010). Although these cells were initially thought to have an exclusively tumour-preventing role, promoting apoptosis in tumour cell populations (Burnet, 1957), evidence has linked tumour-associated immune system cells with a wide range of tumour-promoting activities, such as the expression of growth factors (DeNardo et al., 2009), the stimulation of angiogenesis (De Palma et al., 2007) and remodelling of the extracellular matrix (Lu et al., 2012). Cells of the innate immune system also produce reactive oxygen species (ROS) and nitric oxide (NO) during phagocytosis (Babior, 2000), as do infiltrating peripheral mononuclear cells in multiple sclerosis lesions (Vladimirova et al., 1999; Lu et al., 2000). ROS are also released in response to activation by TNF (Kohchi et al., 2009). However, an unfortunate side effect of ROS production is an increase in the rate of mutation in tumour cells that are resistant to

pro-apoptotic signals (Grivennikov et al., 2010). Thus, despite the ostensible benefits of systemic immune cells in the destruction of target cancer cells, the role of inflammation at the tumour site may in fact be of benefit to tumour survival (Dvorak, 1986), and pro-tumorigenic effects of elevated ROS levels have also been suggested in relation to the development of brain metastases (Salganik et al., 2000; Albright et al., 2004).

Over the last couple of decades, it has also become clear that a level of cross talk exists between resident CNS inflammatory cells and the systemic immune system (Matyszak and Perry, 1995; Cunningham et al., 2005; McColl et al., 2007; Pott Godoy et al., 2008; Serres et al., 2009; Couch et al., 2011). The inflammatory cells of the brain comprise perivascular macrophages, a small population of perivascular mast cells, parenchymal macrophages, microglia and astrocytes (Figure 1.1, step 1). Under normal physiological conditions the entry of immune cells to metastatic sites in the CNS is closely regulated. By contrast, during pathological conditions immune cell entry into the CNS is increased (Prendergast and Anderton, 2009). Little is known about the mechanisms by which circulating leukocytes are able to cross the endothelial cell layer in cerebral blood vessels in resting state conditions for immune surveillance. Much of the work to elucidate these mechanisms has been based on the inflammatory pathology of the CNS (Lossinsky and Shivers, 2004). Neutrophils and mononuclear cells appear to migrate paracellularly, and it has been demonstrated that neutrophil-induced BBB breakdown can be induced in juvenile rats by loss of occludin and zonula occludens-1 (ZO-1), following intrastriatal injection of IL-1β (Bolton et al., 1998), allowing migration of immune cells between the vessel lumen and the brain parenchyma. Lymphocytes and leukemic cells, on the other hand, appear to migrate transcellularly across the endothelial cell layer (Lossinsky and Shivers, 2004), possibly through pores in the endothelium. This mechanism may account for the majority of transendothelial migration by both lymphocytes and circulating metastatic cells (Lossinsky and Shivers, 2004). Despite

these insights, our understanding of the precise mechanisms involved remains incomplete, although some common signalling factors appear to be involved in cell adhesion and extravasation. Neutrophils are some of the first to respond to local inflammation both in the CNS and in other organs. Remodelling of the luminal surfaces of endothelial cells in post-capillary venules results in extensive microvilli with high expression levels of selectins and other adhesion molecules, such as VCAM-1, ICAM-1 and PECAM-1 (Harlan and Liu, 1992) (Figure 1.1, step 4). The characteristic rolling behaviour of neutrophils is induced by endothelial selectin expression, followed by slow rolling via the cell surface ligands LFA-1 and Mac-1, and finally firm adhesion via endothelial ICAM-1. A similar mechanism is also used by lymphocytes and monocytes, which for the most part use the VLA-4/VCAM-1 ligand-receptor complex to adhere to endothelial cells in the brain vasculature (Lossinsky and Shivers, 2004). Up-regulation of adhesion molecules by endothelial cells occurs in response to metastasis in many organs including the lung (Ludwig et al., 2004; Läubli and Borsig, 2010) and the liver (Brodt et al., 1997; Khatib et al., 1999; Vidal-Vanaclocha et al., 2000). The suggestion that metastatic cells extravasate following many of the same mechanisms and signalling cues as circulating leukocytes confers particular importance to the potential role of these mechanisms at the earliest stages in the formation of metastatic colonies (Haddad et al., 2010). Work in our group has recently demonstrated the up-regulation of VCAM-1 on brain endothelium in response to brain metastases, and the utility of new molecular MRI contrast agents targeting VCAM-1 for the early detection of these tumours (Serres et al., 2012). These arguments suggest a pro-metastatic effect of increased adhesion molecule expression on brain endothelia, but it is important to establish whether this is a cause or a consequence of CNS metastasis. Prophylactic up-regulation of VCAM-1 may therefore increase the arrest and proliferation of metastatic cells in the CNS, as will be further discussed during this thesis.

Following the attachment of circulating immune system cells to the vessel wall, it has been reported that they are often activated by chemokines. This family of molecules serve a variety of different functions in normal physiological conditions and during inflammation. They are responsible for the regulation of cell migration during organ development and repair, and at sites of inflammation, both in the brain and elsewhere in the body. In the case of brain metastasis by breast tumour cells the CXCR4/CXCL12 axis seems to be particularly important, both for crossing the BBB and for downstream tumour angiogenesis (Lee et al., 2004; Hinton et al., 2008). However, it is important to note that expression of specific chemokines results in a differential recruitment of neutrophils at various sites within the brain and at various stages of neurodevelopment (Campbell et al., 2002). Furthermore, expression of different pro-inflammatory cytokines in the CNS results in differential recruitment of neutrophils and mononuclear cells to the inflammatory site (Blond et al., 2002). These findings suggest that crosstalk between pro-inflammatory cytokines is reduced in the brain compared to other organs and that specificity of cell recruitment is governed by local expression of specific pro-inflammatory agents.

Thus, metastatic cells that extravasate from the cerebral vasculature may experience immune surveillance from a variety of resident and non-resident cells. The perivascular space that surrounds blood vessels in the brain contains a population of pericytes that are responsible for the maintenance of the BBB (Liu et al., 2012), resident macrophages and a small population of mast cells, as well as CD95L 'death' signalling from astrocyte end-feet. Macrophages, neutrophils, natural killer (NK), NKT, CD4+, CD8+ and B cells are all capable of crossing the BBB into the perivascular space and later into the brain parenchyma, and demonstrate a range of pro- and anti-metastatic effects (Hamilton and Sibson, 2013; Figure 1.1, steps 2 & 4-9), although the mechanisms by which these cells are able to traverse the brain vascular endothelium are still poorly understood.

1.5 Metastatic cell entry into the brain

There is currently considerable interest in elucidating the mechanisms by which metastasizing tumour cells are able to arrest in the brain capillaries, extravasate into the perivascular space and continue to proliferate. Some of the work investigating the extravasation of metastatic cells from capillaries has involved *in vitro* assays with human brain microvascular endothelial cells (HBMEC) as the model system (Lee et al., 2003, 2004). More recent *in vitro* models of the human BBB have been developed, but have not yet been tested against *in vivo* observations (Cucullo et al., 2013; Daniels et al., 2013; Lippmann et al., 2013). However, given the complexity of the BBB and the extra-luminal properties of blood vessels in the brain, it has traditionally been hard to recreate adequate features of the brain for real study into metastatic survival and proliferation (Reichel et al., 2003). Consequently, much of the *in vitro* work to date has used more typical cell lines such as human umbilical vein endothelial cells (HUVEC), and attempted to draw more general conclusions based on these findings. One pair of studies has demonstrated the difficulties in comparing *in vivo* and *in vitro* data for extravasation of metastatic cells across the BBB and HBMEC cells in culture, with poor correlation between the two models for five different breast cancer cell lines (Lorger and Felding-Habermann, 2010; Lorger et al., 2011). These results suggest that much work is still needed to improve *in vitro* assays to make them more relevant to studying the BBB.

In vivo observations made of metastatic cell extravasation into the brain suggest that the pathways by which tumour cells are able to enter the perivascular space may be under tighter regulation, or indeed be entirely different from those in other organs. Several studies suggest that tumour cells remain within the lumen of cerebral blood vessels for longer than elsewhere in the body. Viable cells were found between 3 and 5 days post intra-carotid injection in a variety of rodent *in vivo* models (Ballinger Jr. and Schimpff, 1979; Kawaguchi et

al., 1982; Paku et al., 2000; Lorger and Felding-Habermann, 2010). 3LL-HH Lewis lung carcinoma cells were directly compared at different sites of metastasis at several time points following injection, and were almost entirely absent from the vasculature of the liver, lungs, adrenals and kidneys just 24 hours post injection (Lorger and Felding-Habermann, 2010). The delay in extravasation to the brain may help explain the differences in metastatic development between days 5, 10 and 13 in the mouse 4T1-GFP breast carcinoma model (Serres et al., 2012).

Given the difficulty of developing adequate *in vitro* models and the scarcity of *in vivo* data, many of the hypotheses relating to mechanisms of metastatic extravasation in the brain have arisen from observations in other *in vitro* and *in vivo* disease models (Maru, 2007; Green et al., 2009; Haddad et al., 2010; Wirtz et al., 2011; Pytliak et al., 2012). Firstly, tumour cells may be able to employ similar mechanisms to those used by systemic immune cells, as discussed above, to adhere to proteins expressed by endothelial cells thus allowing them to cross the BBB into the perivascular space. Secondly, tumour cells may be able to adhere to systemic immune cells via receptor-ligand interactions and cross through the BBB with the 'hijacked' cell, a proposal that has long been mooted for non-brain tissues (Aichel, 1911; Munzarová and Kovarík, 1987). Thirdly, tumour cells, having been mechanically arrested in the blood vessels, may be able to modify the endothelial cell wall via expression of MMPs, allowing them to extravasate into the perivascular space (Kienast et al., 2010; Wirtz et al., 2011; Pytliak et al., 2012). This final mechanism shares many of the features of protease-assisted crossing shown by neutrophils (Gottesman, 1990).

Metastatic tumour cells show many similar patterns of behaviour to macrophages, some of the most versatile cells in the body, in their ability to alter their shape and extravasate to sites of local inflammation and, subsequently, to express cytokines and growth factors in

order to promote wound healing (Burke and Lewis, 2002). These similarities have not gone unnoticed, and gene expression data has suggested a link between macrophages and metastatic cells. For instance, VM-M2, VM-M3 and the RAW264.7 macrophage cell lines all express CD11b, Iba1, F4/80, CD68, CD45 and CXCR4 (Huysentruyt et al., 2008), and various other human tumour lines have been described as showing similar properties to macrophages (Ruff and Pert, 1984; Calvo et al., 1987; Munzarová and Zemanová, 1992; Munzarová et al., 1992). Thus, the concept that metastatic cells may use similar mechanisms compared to inflammatory cells to extravasate into the perivascular space is not without foundation. Given the specificity that cells from certain sites of primary tumour growth have for certain secondary sites, the basis for Paget's 1889 'seed and soil' hypothesis (Paget, 1889), which has since been studied with specific reference to brain metastases (Fidler, 2002; Carbonell et al., 2009), it seems likely that signalling processes between metastatic cells and the specific tissue vasculature play at least a partial role in the entry of metastatic cells into the brain. Various molecules including VCAM-1 (Vidal-Vanaclocha et al., 2000; Läubli and Borsig, 2010), E-selectin (Brodt et al., 1997; Khatib et al., 1999; Läubli and Borsig, 2010), P-selectin (Ludwig et al., 2004; Läubli and Borsig, 2010) and L-selectin (Läubli and Borsig, 2010) that control the passage of systemic immune cells have been found to be expressed in the lung and the liver and unpublished work from our group indicates similar expression in the brain. The expression of these markers may be a result of metastatic extravasation at these loci, and it remains to be seen whether they have a role in the mechanism of extravasation *per se*.

The second of the three hypotheses outlined above may be the most subtle. This mechanism proposes that the metastatic cells have the ability to 'hijack' circulating systemic immune cells by binding to them and relying on the leukocyte to extravasate from blood vessels rather than doing so themselves (Figure 1.1, step 2). Thus, it is the circulating leukocytes that

may be responding to up-regulation of adhesion molecules expressed on endothelial surfaces (Green et al., 2009), possibly as a result of tumour cell arrest and interaction with the endothelium. At the same time, systemic or localized neuroinflammation could substantially up-regulate brain endothelial adhesion molecule expression and, thus, amplify metastatic uptake to the brain either by this mechanism or by direct interaction of the metastatic cells with the brain endothelium, as will be discussed in this thesis. Subsequent extravasation of the inflammatory cells across the endothelium may facilitate simultaneous movement of the metastatic cells bound to them.

The antigenic similarities between metastatic cells and circulating macrophages may suggest another role of macrophages in promoting the metastatic niche: the fusion of macrophages with neoplastic cells has been suggested to cause a shift towards malignancy as a result of altered gene expression in the macrophage genome (Munzarová and Kovarík, 1987). First put forward by Otto Aichel in 1911 (Aichel, 1911), this theory is once again gaining ground (Chakraborty et al., 2001, 2003; Duelli and Lazebnik, 2003; Vignery, 2005). Circulating macrophages are capable of clonal expansion in response to M-CSF, and can then fuse to form tetraploid multinucleate giant cells. Fusion of cellular membranes between macrophages requires self-recognition, and it has been suggested that metastatic cells may be capable of the same fusion mechanism. The fusion of cells of the primary tumour to macrophages provides a useful non-mutational explanation for the development of metastatic traits in cells of the primary tumour. Furthermore, shifts in gene expression patterns in hybrid metastatic-macrophage cells may increase levels of pro-metastatic factors such as integrins (Pawelek and Chakraborty, 2008). To date limited examples of such fusion have been reported in human cancers (Bagnara, 1985; Andersen et al., 2007; Lazova et al., 2011). The second of these suggests for the first time that such a fusion event took place in the brain of a patient with metastatic melanoma following bone marrow transplant.

The third proposal, of physical damage to the BBB and subsequent tumour extravasation, has mixed support. Electron microscopy data from rodent models of brain metastasis suggest disruption of the brain endothelium, with clearly visible fenestrations and modifications to gap junctions, particularly around the middle of the metastatic lesion (Long, 1979). However, the presence of fenestrations has not been reported in cases of human brain metastasis. Fidler's experiments from 1988 showed that both metastatic cells and macrophages were able to extravasate into sites of experimentally-induced lesions in the brain across an intact BBB (Schackert et al., 1988). In accord with this, we have recently demonstrated in two separate mouse models of brain metastasis that the BBB remains intact throughout the early phase of tumour evolution in the brain (Serres et al., 2012). Similarly, a study of eight different human neoplasms injected into nude mice suggested that BBB compromise was a function of the location, the growth pattern and the size of metastases, with an upper limit of around 0.2 mm^3 (Zhang et al., 1992). This suggests that extravasating cells do not cause permanent damage to the BBB, and instead that any compromise of the BBB comes as a result of metastatic proliferation at a later stage. Interestingly, a more recent paper has suggested that extravasation of *HER-2/neu* positive breast carcinoma cells does not cause disruption of the BBB, whereas triple negative tumours and basal type tumours do cause disruption. These findings suggest a possible link between the aggressiveness of the tumour and subsequent damage to the BBB (Yonemori et al., 2010).

The endothelium of the brain may also be able to protect itself from the entry of metastatic cells via the expression of certain proteins such as the Fas ligand (FasL). FasL is expressed on endothelial cells of the brain, eye and testis (Osanai et al., 2002) and has been found to cause apoptosis of Fas-positive activated T cells, thus possibly reducing their extravasation

from blood vessels (Figure 1.1, step 6). Endothelial FasL has also been shown to cause apoptosis of Fas-positive tumour cells *in vitro* and its expression on the brain endothelium may prevent extravasation of Fas-positive metastatic cells also.

PLACEHOLDER FOR FIGURE 1.1

Figure 1.1 – A model for the recruitment of systemic immune cells to sites of metastasis in the brain

The major steps in the recruitment of systemic immune cells are outlined in this figure.

1. The area below the blood vessel (red) is a simplified model of the brain vasculature in its naïve state with resident pericytes (PC), mast cells (MC) and macrophages (MΦ) contained within the perivascular space, bounded on either side by endothelial cells (EC) and the astrocytic end-feet (light green) that make up the glia limitans. Tight junctions (TJ) between ECs maintain control over the movement of solutes between the blood and the tissue fluid. The glia limitans ensures a second barrier between the perivascular space and the brain parenchyma. For simplicity, laminin basement membranes are not shown.
2. At the earliest stages of metastatic development, tumour cells (dark green) may be able to enter the perivascular space by 'hijacking' circulating macrophages (purple) that maintain a population of resident perivascular macrophages (blue). Recruitment of macrophages is often mediated by expression of CSF-1 and MCP-1 on endothelial cells. (For simplicity, no distinction is made between transcellular and paracellular migration in this diagram.)
3. Independent extravasation may be the major mechanism by which tumour cells enter the perivascular space. This may be the result of tumour interactions with adhesion molecules expressed by endothelial cells, and may also require remodelling of the EC extra-cellular matrix by MMPs. These mechanisms may be hindered by endothelial factors such as Fas.
4. Further recruitment of systemic immune cells may occur as a result of the expression of inflammatory markers by endothelial cells. Many candidate molecules are shown in this diagram; many of their functions remain unclear. Neutrophils (PMN) are likely to be recruited first, as they make up such a large proportion of the circulating white cell population. Their extravasation is promoted by elevated local levels of IL-8. The dotted lines denote binding between endothelial ICAM-1 and Mac-1 / LFA-1.
5. Down-regulation of MHC molecules and binding of platelets (P) may allow tumour cells to escape much of the immune surveillance of circulating NK cells. Elevated platelet activity can also lead to increased ICAM-1 expression, possibly promoting further extravasation events by

tumour cells and circulating systemic immune cells. NK cells are able to extravasate, although the mechanisms by which they do this are poorly understood.

6. Adaptive immune system CD4+ and CD8+ T cell populations extravasate, aided by prior exposure to tumour antigens (possibly via APCs in the clavicular lymph nodes), or pro-inflammatory cytokines. Fas expression on the brain endothelium may prevent extravasation of either cell type. Differences in the ability of each cell type to extravasate may give rise to altered CD4+/CD8+ ratios, and more or less aggressive tumour phenotypes accordingly.
7. B cell extravasation is likely to occur last, possibly shortly prior to angiogenesis or BBB compromise. VEGF expression may facilitate TJ disruption, allowing B cells to gain entry into the perivascular space.
8. Continued development of the metastatic tumour in the perivascular space leads to eventual disruption of the glia limitans, allowing the tumour to spread into the brain parenchyma (neuropil). This occurs either by the mechanical forces of the growing tumour or following chronic inflammation at the tumour site, leading to the withdrawal of astrocyte foot-processes.
9. The insert describes some of the known methods by which cells of the systemic immune system may promote or antagonise metastatic growth in the brain. In all cases, pointed arrows denote molecular up-regulation, pathway activation or pro-cellular signals; flat arrows denote molecular down-regulation, pathway repression or cell death signalling.

Sources:

(Seki et al., 2002; Baba et al., 2008; Rochman et al., 2009)

1.6 The BBB in diagnosis and treatment of brain metastasis

As previously discussed, the specificity of molecular transport across the BBB imposed by brain endothelial cells (Rajadhyaksha et al., 2011), and the presence of efflux transporters such as P-glycoprotein (Pgp) that can actively transport a range of lipophilic drugs back into circulation (Löscher and Potschka, 2005), limits potential for the diagnosis and treatment of brain metastasis. Metastatic cells that have crossed from the bloodstream into the perivascular space are isolated from most circulating metabolites, including the diagnostic contrast agents that are employed in an attempt to detect them. Current clinical diagnosis requires a disrupted BBB to allow passage out of the bloodstream of diagnostic compounds that can be detected by tomographic imaging methods. Gadolinium-based compounds such as gadolinium-DTPA (Gadodiamide, Omniscan) serve as magnetic resonance contrast agents that reveal sites of brain pathology (see Section 1.8). MRI has become the imaging modality of choice for brain metastasis, with greater sensitivity over both computed tomography (CT) and PET/CT (Hochstenbag et al., 2000; Suzuki et al., 2004; Krüger et al., 2011). However, disruption of the BBB is a relatively late stage event in the neuroinflammatory pathway (Grossman et al., 1988) and therefore even MRI is unable to provide diagnosis until brain metastases have developed to a size of *ca.* 0.5 cm or more in diameter (Serres et al., 2012). At this point patient prognosis is dismal, with a median survival time of 3-6 months (Lagerwaard et al., 1999).

There are two realistic solutions to the problem of drug delivery across an intact BBB. Firstly, we wish to develop diagnostic agents that are able to cross the BBB and inform us about local CNS pathology. As already discussed, this is not a trivial problem, and one which is currently receiving much research attention (Pardridge, 2005; Barbu et al., 2009). The other solution is to develop diagnostic agents that do not need to cross the BBB, but are instead able to inform us about local brain pathology from the lumen of blood vessels in the CNS.

This second approach has seen much progress over recent years with the development of various nanotechnologies and now, molecularly-targeted MRI contrast agents.

1.7 Magnetic Resonance Imaging

The beginnings of magnetic resonance imaging (MRI) date back to the early 1970s with the work of Paul Lauterbur (Lauterbur, 1973) and Peter Mansfield (Garroway et al., 1974), which earned them the 2003 Nobel Prize in Physiology or Medicine. It has since become the imaging modality of choice in neuroimaging for both scientific and clinical studies (Modo and Bulte, 2011; Barajas and Cha, 2012). MRI draws its history from nuclear magnetic resonance (NMR), a technique developed in the 1930s by Rabi (Rabi et al., 1938) and later by Bloch (Bloch and Rabi, 1945) and Purcell (Purcell et al., 1946). The principle behind both techniques is the magnetic moment found within specific MR active nuclei. The movement of any charged particle creates a magnetic field. In the case of ^{1}H, the most commonly studied MR active nucleus, the single proton is the charged particle and its spin induces a magnetic field known as the magnetic moment of the nucleus. Many other MR active nuclei have been studied, most notably ^{13}C and ^{31}P. The unifying feature of all MR active nuclei is their intrinsic magnetic moment, caused by a non-zero net spin. Thus, all nuclei with an odd number of protons and/or neutrons are MR active.

Placing a large number of these nuclei inside a constant, homogeneous magnetic field causes the magnetic moments of each nucleus to align in the direction of the applied magnetic field. Their alignment can be perturbed by applying an electromagnetic pulse, normally at a radio frequency (RF), the energy from which imparts resonance to the nuclei and causes them to precess away from the applied magnetic field. In order to induce resonance the nuclei must be given an RF pulse at the correct frequency for the specific nucleus and magnetic field strength used, as determined by the Larmor equation,

$$\omega_0 = B_0 \times \lambda \,,$$

where ω_0 is the precessional frequency, B_0 is the applied magnetic field strength and λ is the gyro-magnetic ratio of the nucleus. In short, this equation states that the frequency required to cause resonance in a population of MR active nuclei is proportional to the strength of the magnet into which the nuclei are placed. The constant of proportionality is given by λ, the frequency of a specific MR nucleus in a 1 Tesla magnetic field, which can be calculated from the magnetic moment of the nucleus and its proton mass. The gyro-magnetic ratio of ^{1}H is 42.57 MHz/T. Thus, at an applied field strength of 7 T, the precessional frequency is 298 MHz.

On application of an RF pulse the magnetic moments of the MR active nuclei move away from the direction of the longitudinal magnetic field and a proportion of the magnetic moment can be described to be in the transverse plane. The proportion of this shift is determined by the 'flip angle', which is dependent on the amplitude and the duration of the RF pulse; a perfect 90° pulse would put all of the magnetic moment into the transverse plane. Magnetisation in the transverse plane allows us to measure the MR signal.

When the RF pulse is removed, the nuclei, over time, lose the energy given to them, a process known as relaxation. Relaxation takes two forms: the recovery of magnetization in the longitudinal plane (T1 recovery) and the decay of in-phase spins (T2 decay). The two processes are independent of one another and can be measured by the induction of currents in the receiver coils surrounding the sample. The reduction in signal in the coils is known as the free induction decay (FID). T1 and T2 relaxation times differ between various tissues, and this can be used as a means to distinguish between them. For instance fatty

tissues have a much shorter T1 recovery time and T2 decay time than more aqueous tissues. Rather than giving a single RF pulse, and then allowing the magnetic moments to fully re-align with the applied magnetic field, multiple RF pulses are normally applied in sequence, and the time between each is termed the repetition time (TR). At a specific echo time (TE) after the start of the RF pulse measurement of the signal in the receiver coils is made. By manipulating the TR and TE of the sequence it is possible to weight the sequence more or less to T1 and/or T2 effects. By weighting the contrast on the image towards T1 or T2 relaxation, images can be acquired that reveal different properties of the tissues of interest. For example, T1 weighted images show a bright fat signal and a low water signal, whereas T2 weighted images show a bright water signal and a low fat signal. Thus, in the brain we are able to distinguish white matter from grey matter based on the water to fat content using T1 or T2 weighting. As well as using T1- or T2-weighting to provide information about different structures in the body, we are also able to use contrast agents to reveal further differences not otherwise visible by conventional MRI. Paramagnetic T1 agents with positive magnetic susceptibilities such as gadolinium cause a preferential reduction in T1 relaxation and cause a bright signal when using a T1-weighted scan. Superparamagnetic T2* agents such as iron oxide reduce T2* relaxation times and cause a decrease in signal in T2*-weighted scans.

When the RF pulse is removed one final type of decay comes into play – T2* decay. This decay consists of T2 decay, together with dephasing of the magnetic moment as a result of inhomogeneities in the magnetic field. The precessional frequencies will increase in nuclei that experience a higher magnetic field strength, while they will decrease in areas of lower magnetic field strength. Consequent dephasing can cause a rapid loss in the coherent transverse magnetization, reducing the signal in T1 or T2 weighted images. The pulse sequence is often modified to compensate for this by giving a second 180 degree pulse, flipping the magnetization and refocusing the signal (Hahn, 1950; Carr and Purcell, 1954).

MR sequences that contain these refocusing RF pulses are known as spin echo sequences. However, investigating the T2* properties of a tissue can be revealing because of the nature of the local heterogeneity of the magnetic field. The haem prosthetic group in haemoglobin for example is made up of an iron ion in the middle of a porphyrin ring, that when oxygenated is diamagnetic and when deoxygenated is paramagnetic. Imaging of blood using T2* weighting allows us to compare oxygenated and de-oxygenated blood based on their different magnetic properties and is the basis of the blood oxygenation level dependent (BOLD) signal used in functional MRI (fMRI) studies. Furthermore, contrast agents such as iron oxide particles cause local changes in the magnetic field strength and create a T2* effect that can be observed. Rather than using a spin echo sequence to refocus the signal a gradient echo sequence is used. Following application of an RF pulse, a proportion of the net magnetization is flipped into the transverse plane. T1, T2 and T2* relaxations start to occur as soon as the RF pulse is removed. Rather than rephasing magnetic moments using a 180-degree RF pulse the gradient echo sequence uses opposing magnetic gradients to refocus dephasing magnetic moments. The advantage of a gradient echo sequence over a spin echo sequence is that a shorter time is taken to rephase the magnetic moments and, therefore, a reduction in the overall scan time. Importantly, however, gradient echo sequences do not take into account the effects of inhomogeneities in the magnetic field, so T2* decay can be measured (Westbrook et al., 2005).

1.8 Molecular MRI in neurological disease

A wide variety of superparamagnetic iron oxide-based agents have been developed for molecular MRI. Most of these agents consist of a crystalline core made of magnetite (Fe_3O_4) or maghemite (Fe_2O_3) that is surrounded by a low molecular weight carbohydrate (e.g. dextran) or polymer coat. They are defined based on their size as ultra-small

superparamagnetic particles of iron oxide (USPIO), ranging from *ca.* 20-60 nm in diameter, superparamagnetic particles of iron oxide (SPIO), ranging from *ca.* 50-1000 nm, and microparticles of iron oxide (MPIO) which are of diameter *ca.* ≥ 0.9 μm (Thorek and Tsourkas, 2008; McAteer and Choudhury, 2009). These particles have been used in the imaging of a range of neuropathologies including multiple sclerosis (Serres et al., 2009), cerebral malaria (Von Zur Muhlen et al., 2008), brain ischemia (Fréchou et al., 2013), glioma (Chien et al., 2011; Chaumeil et al., 2012; Mamani et al., 2012), Alzheimer's disease (Beckmann et al., 2011) and tumour angiogenesis (Gambarota et al., 2008; Beaumont et al., 2009; McAteer and Choudhury, 2009; Anthony et al., 2011).

USPIO have become popular for imaging changes in cerebral perfusion, but have several drawbacks when used as molecular MRI agents: firstly, their long half-life in circulation can lead to an unwanted level of background contrast effect making identification of specific binding difficult; secondly, they can be non-specifically phagocytosed by endothelial cells, thus reducing their efficacy as molecular markers. Conversely, phagocytosis of USPIO by circulating macrophages can provide information about their infiltration into the CNS in instances of neuroinflammation in EAE (Dousset et al., 1999a, 1999b; Rausch et al., 2003; Deloire et al., 2004; Floris et al., 2004; Serres et al., 2009), cerebral ischemia (Rausch et al., 2001, 2002; Schroeter et al., 2004; Kleinschnitz et al., 2005) and primary brain tumours (Zimmer et al., 1995). USPIO have also been used in the visualisation of experimental brain metastases (Leenders et al., 2003), but it remains unclear whether the signal is associated with macrophage infiltration to the site of metastasis or whether it remains restricted within blood vessels.

The contrast agent used throughout the experiments in this thesis is a micron-sized particle of iron oxide, the surface of which is bound by antibodies to VCAM-1. As an iron oxide

particle, it is superparamagnetic and acts as a preferential T2 contrast agent. However, it can also be used as a T2* contrast agent by creating local magnetic inhomogeneities thus increasing the speed of T2* decay. A T2*-weighted image of the brain that has a focal increased concentration of iron oxide particles will have a faster T2* decay and there will be less signal acquired at TE than in the surrounding tissues.

MPIO are potent molecular MRI contrast agents whose T2* effect extends to approximately 50 times the diameter of the particle (Shapiro et al., 2006), owing to their high iron content (Sibson et al., 2011). A large effect size means that doses of MPIO need not be as high as those of USPIO and, because MPIO are less susceptible to uptake by endothelial cells than USPIO, they are more useful for investigating the expression of proteins or carbohydrate moieties on the luminal surface of endothelial cells in the CNS (Briley-Saebo et al., 2006). Biodegradability of MPIO is the largest current problem facing their clinical use in humans, so much work has recently focussed on in developing particles with biodegradable coats (Hemmingsson et al., 1987; Chen et al., 2005; Hamoudeh and Fessi, 2006; Zhu et al., 2006).

Current research in our lab has been focused on the development of MPIO conjugated to antibodies to VCAM-1. VCAM-1 (also known as CD106) is the receptor for the α4β1 integrin (VLA-4), both of which are important in the recruitment of circulating leukocytes (Elices et al., 1990; Griffin et al., 2012; see Section 1.4), in a wide range of neuropathologies (Yednock et al., 1992; Cannella and Raine, 1995; Piraino et al., 2002; Polman et al., 2006). Endothelial cells do not constitutively express VCAM-1; it is instead up-regulated as a result of endothelial activation (Carlos et al., 1990). VCAM-1 has previously been shown to be upregulated in the early stages of liver and lung metastasis (Khatib et al., 1999; Vidal-Vanaclocha et al., 2000; Ludwig et al., 2004; Läubli and Borsig, 2010; Ferjancic et al., 2013), and has recently been shown to be upregulated in the early stages of brain metastasis

(Carbonell et al., 2009; Serres et al., 2012). Interestingly, macrophages and T cells also express VLA-4 (Rosner et al., 2001). Owing to VCAM-1 expression on the luminal surfaces of cerebral endothelial cells, diagnostic and therapeutic agents targeted to this molecule are not required to cross the intact BBB. Work in our group has used 1 μm diameter Dynal Dynabeads bound with VCAM-1 antibodies as a molecular MRI contrast agent (McAteer et al., 2007), which have proved effective in determining the locations of multiple sclerosis lesions (Serres et al., 2009) as well as early-stage brain metastasis (Serres et al., 2012). Thus, VCAM-1 could serve as a useful biomarker for early stage neuropathologies, including brain metastasis. This approach, using endothelial activation by the presence of metastatic lesions beyond the BBB, is the one that I have taken throughout this thesis using antibody-tagged microparticles of iron oxide, specific to VCAM-1, to report on local brain pathology as a result of endothelial up-regulation of VCAM-1 expression (Serres et al., 2012).

1.9 Aims of this thesis

On the basis of this previous work I sought to test the following hypotheses:

1 That VCAM-1 expression on endothelial cells at the site of cerebral metastasis and VCAM-MPIO-derived signal in MR images colocalise with each other (Chapter 3).

2 That the signal generated by VCAM-MPIO binding in the brain can be reliably and reproducibly extracted using an automated computational approach (Chapter 3).

3 That spatial and temporal image filtering can improve MR image quality and improve the detection of VCAM-MPIO-derived signal (Chapter 3).

4 That normal development patterns of 4T1-GFP metastasis are site-specific within the brain, and specific to venous regions of the vascular bed (Chapter 4).

5 That an adenovirus-induced systemic inflammatory response causes both an increase in peripheral cytokine concentrations and neurovascular expression of VCAM-1 on brain endothelium, which can be detected using MRI (Chapter 5).

6 That the number and morphological characteristics of brain metastases are affected as a result of a systemic inflammatory response (Chapter 5).

7 That differences in tumour burden as a result of a systemic inflammatory response result in detectable changes in VCAM-MPIO-derived signal (Chapter 5).

8 That cytokine-induced central inflammation increases the number of metastases that develop in the injected (ipsilateral) hemisphere compared to the uninjected (contralateral) hemisphere (Chapter 5).

Materials and Methods

2.1 Experimental schedules

Three broad experimental designs for *in vivo* work were used over the course of the thesis. These are outlined in Figures 2.1, 2.2 and 2.3 below. The initial setup of the metastatic model (Chapters 3 & 4) is the most straightforward, with injection of 4T1-GFP cells into the left ventricle of the heart of 7-10 week-old female BALB/c mice, which were then allowed to develop for 10 days prior to imaging (Figure 2.1). Although other time-points were used in Serres et al. (2012), all experiments performed for this thesis were at a time-point 10 days following initial injection of tumour cells.

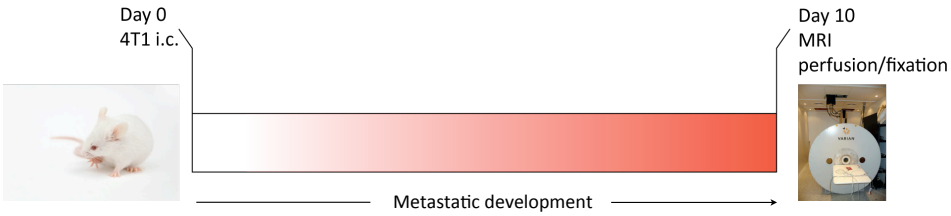


Figure 2.1 – Intracardiac injection of 10^5 4T1-GFP cells was followed by ten days to allow metastases to develop before the animals were imaged and killed by perfusion/fixation.

A systemic inflammatory response was initiated by intravenous injection of 8×10^6 plaque-forming units (pfu) of adenovirus (Chapter 5) either 1 day prior to, or 5 days following tumour cell injection. In the former scenario, tumour cells were injected into an animal in which a systemic inflammatory response had already been initiated; in the latter tumour

cells were injected into a naïve animal and allowed to develop for 5 days prior to initiation of a systemic inflammatory response (Figure 2.2). Animals were imaged and perfused/fixed 10 days after injection of 4T1-GFP cells.

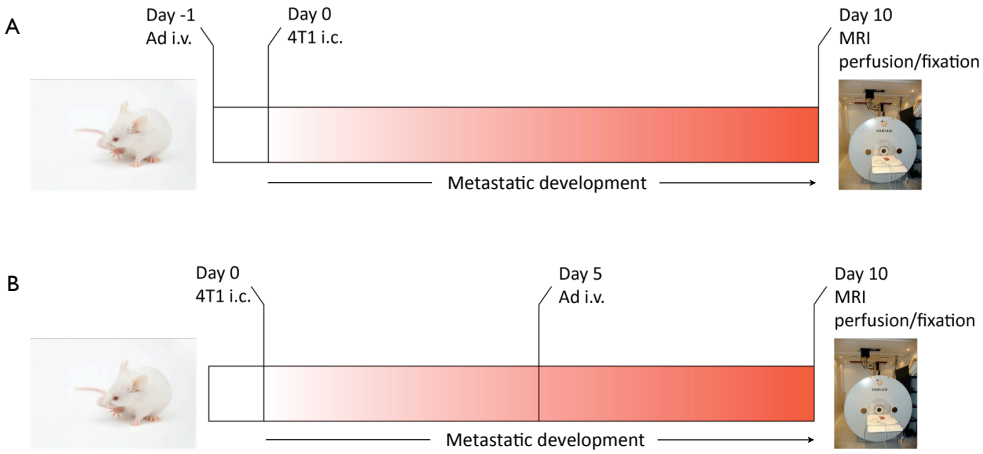


Figure 2.2 – Experimental schedule for induction of a systemic inflammatory response. (A) Injection of adenovirus 1 day prior to tumour cell injection and (B) 5 days following tumour cell injection. Tumours were allowed to develop for 10 days post intracardiac injection, at which point the animals were imaged and perfused/fixed.

A localized neuroinflammatory response was initiated via injection of a pro-inflammatory cytokine into the left striatum (Chapter 5) 4 h before injection of tumour cells. The cytokines used were rmTNF-α and rmIL-1β, with sterile saline to act as a control (Figure 2.3). Animals were imaged and perfused/fixed 10 days after injection of 4T1-GFP cells.

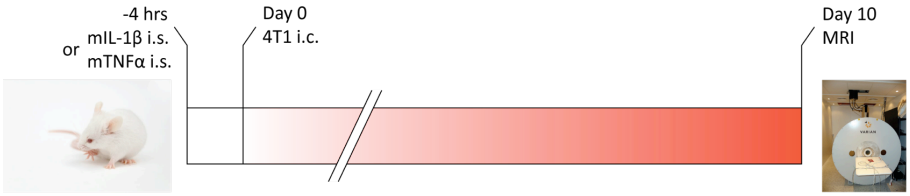


Figure 2.3 – Experimental schedule for induction of a localised neuroinflammatory response. Injection of pro-inflammatory cytokines IL-1β or TNF-α, or sterile saline control, 4 h prior to tumour cell injection. Tumours were allowed to develop for 10 days post intracardiac injection, at which point the animals were imaged and killed by perfusion/fixation.

2.2 Materials

2.2.1 Chemicals and reagents

Sodium dihydrogen orthophosphate dihydrate (S/3760/53), di-sodium hydrogen orthophosphate (Sorrenson's salt) (S/4440/60), sucrose (S/8600/60), tris(hydroxymethyl)aminomethane hydrochloride (BPE153-1), sodium chloride (BP358-212), magnesium chloride (M/0600/53) and Triton X-100 (BP151-500) were obtained from Fisher Scientific (Loughborough, UK). Paraformaldehyde (PFA) (15,812-7), L-lysine monohydrochloride (L5626), zinc chloride (208086), (-)-tetramisole hydrochloride (L9756), ethylenediaminetetraacetic acid (EDTA) (E5134) and glutaraldehyde (G5882) were obtained from Sigma-Aldrich (Gillingham, UK). Sodium metaperiodate (27986.235) was obtained from VWR (Lutterworth, UK). Phosphate buffered saline (PBS) (Dulbecco A) tablets (BR0014G) were obtained from Oxoid (Basingstoke, UK).

2.2.2 Injectable agents

Injectable saline (S8776) was obtained from Sigma-Aldrich. VCAM-MPIO were obtained from Dr Martina McAteer at the Wellcome Trust Centre for Human Genetics, Roosevelt Drive, Oxford. Gadolinium-DTPA (diethylenetriaminepentacetate) (Omniscan®) (J-100) was obtained from GE Healthcare (Chalfont St Giles, UK). Euthatal pentobarbital solution was obtained from Merial (Marlow, UK).

2.2.3 Antibodies

Chicken polyclonal antibodies to GFP (ab13970), rabbit polyclonal antibodies to αSMA (ab5694) and rabbit polyclonal antibodies to laminin 1+2 (ab7463) were obtained from Abcam (Cambridge, UK). Rat monoclonal antibodies to mouse VCAM-1 (CBL1300) were obtained from Millipore (Billerica, MA, USA). Goat polyclonal antibodies to mouse EphB4 (AF446) were obtained from R&D Systems (Abingdon, UK). Rat monoclonal antibodies to mouse CD11b (MCA74G) were obtained from AbDserotec (Kidlington, UK). Mouse monoclonal antibodies to mouse NK1.1 (NB100-77528) were obtained from Novus Biologicals (Cambridge, UK). Rat anti-mouse antibodies to VCAM-1 (1510-01) for VCAM-MPIO preparation were obtained from Cambridge Bioscience (Cambridge, UK).

Rabbit polyclonal biotinylated secondary antibodies to chicken IgY (ab6752) were obtained from Abcam. Rabbit anti-rat (BA-4001), goat anti-rabbit (BA-1000), horse anti-mouse (BA-2001) and horse anti-goat (BA-9500) biotinylated IgG secondary antibodies were obtained from Vector Laboratories (Burlingame, CA, USA).

2.2.4 Cells

4T1 murine mammary carcinoma cells (CRL-2539) (Dexter et al., 1978; Aslakson and Miller, 1992; Pulaski and Ostrand-Rosenberg, 2001) were originally obtained from ATCC (Teddington, UK) and had previously been transfected with a plasmid promoting the expression of EGFP (Cormack et al., 1996). HEK-293 cells (CRL-1573) were obtained from ATCC.

2.2.5 Cell culture tools and reagents

All cell culture was performed in a BioMAT^2 class II microbiological safety cabinet (Medical Air Technology, Manchester, UK) and cells were incubated in HeraCell 150 cabinets (Thermo Electron Corporation, Hemel Hempstead, UK).

Dulbecco's modified Eagle medium (DMEM) high glucose (4.5 g/L) (E15-810), trypsin-EDTA (L11-004), penicillin-(10,000 U/mL) streptomycin (10 mg/mL) solution (P11-010) and L-glutamine (M11-004) were obtained from PAA (Yeovil, UK). Eagles' minimum essential medium (EMEM) (M4655) was obtained from Sigma-Aldrich (Poole, UK). Cellstar T-175 flasks (658 175), 48-well plates (677 180) and rubber cell scrapers (541 070) were obtained from Greiner Bio-One (Stonehouse, UK). HYPERflask® Cell Culture Vessels (hyperflasks) (10031) and 6-well (3506) and 96-well (3595) plates were obtained from Corning (Tewksbury, MA, USA). Foetal bovine serum (FBS) (FB-1000) was obtained from BioSera (Ringmer, UK).

Concentrations of living cells were calculated using a NucleoCassette (941-0002) and NucleoCounter (Chemometec, Lillerød, Denmark).

2.2.6 Animals and materials

Female BALB/c mice, aged between 6 and 10 weeks were purchased from Charles River (Margate, UK) and housed in isolated negative-pressure cages (Tecniplast, Buguggiate, Italy) in the animal facility at the Radiobiology Research Institute (RRI). A controlled environment was maintained at 19-21 °C, 50 ± 15% humidity with a 12 h light-dark routine. Food and water were provided *ad libitum*. To minimize potential stress animals were acclimatized to their new environment for a minimum of three days prior to performing any experiments.

All animal anaesthesia was induced and maintained using an isoflurane vaporiser (340471) (Harvard Apparatus, Edenbridge, UK). Isoflurance (IsoFlo) was obtained from Abbott Laboratories (Abbott Park, IL, USA). Intracardiac injections were performed with ultrasound guidance using a Vevo 770 ultrasound machine (VisualSonics, Toronto, Canada) with a 707-B probe. Intrastriatal injections were performed using a stereotaxic frame (Kopf, Tujunga, CA, USA) and a dissecting microscope (Wild Heerbrugg, Gais, Switzerland) using murine TNF-α (315-01A) and murine IL-1β (211-11B) obtained from Peprotech (London, UK). Perfusions were performed using a perfusion pump (505L, Watson Marlow, Falmouth, UK). Heparin sodium (25,000 I.U./mL) was obtained from Wockhardt (Wrexham, UK). Polyvinyl alcohol lubricating eye drops (Liquifilm® Tears) were obtained from Allergan (Marlow, UK). Vicryl sutures were obtained from Ethicon (Norderstedt, Germany). Homeothermic monitoring equipment for MRI was obtained from Harvard Apparatus. Data was fed to a monitor via a MP150 data acquisition system (Biopac Systems, Goleta CA, USA).

2.2.7 Immunohistochemistry and immunofluorescence materials

All immunohistochemistry and immunofluorescence was performed using Shandon Sequenza® slide clips and trays (Thermo Scientific). Image-iT® FX signal enhancer (I36933), ELF® 97 phosphatase substrate (E-6588) and streptavidin-Cy3 (43-4315) were obtained from

Invitrogen (Paisley, UK). Vectashield mounting medium with (H-1200) and without (H-1000) 4',6-diamidino-2-phenylindole (DAPI), Vectorstain Elite ABC amplification (PK-6100) and streptavidin- and biotin-blocking (SP-2002) kits were obtained from Vector Laboratories. Tyramide signal amplification (TSA) amplification reagents (Tris-NaCl blocking buffer (TNB), amplification diluent, streptavidin-HRP and BiotinylTyramide reagent) (NEL749B001KT) were obtained from Perkin-Elmer (Waltham, MA, USA). 3,3'-diaminobenzidine (DAB) (112090050) and cresyl violet acetate (229630250) were obtained from Acros Organics (Geel, Belgium). Ethanol (E/0650DF/17), acetic acid (A/0400/PB17) and xylene (X/0200/17) were obtained from Fisher Scientific. Polink-2 Plus AP detection kits for rabbit (D70-18) and rat (D67-18) primary antibodies were obtained from Golden Bridge International (Mukilteo, WA, USA).

2.2.8 Cytokine measurement kits

An initial, semi-quantitative measurement of cytokine concentrations in mouse serum was made using the Mouse Cytokine Array Panel A (ARY006) from R&D Systems. Further studies were made using a fully quantitative, custom-made Quantibody® cytokine assay purchased from Raybiotech (Norcross, GA, USA) spotted with antibodies reacting to murine TNF-α, Granzyme B, IFN-γ, IL-4, I-Tac, KC, MCP-1, MIG and SDF-1α; human IL-1β. Streptavidin, Alexa Fluor® 700 conjugate (S-21383) was obtained from Invitrogen.

2.2.9 Adenoviral preparation

Ultra-centrifuge tubes (344060) were obtained from Beckman-Coulter (Brea, CA, USA).

Agarose (A9539), 3-(4,5-Dimethylthiazol-2-yl)-2,5-diphenyltetrazolium bromide (MTT) (M-2128) and caesium chloride (C4036) were obtained from Sigma-Aldrich. 4-(2-hydroxyethyl)-1-piperazineethanesulfonic acid (HEPES) (BP310-1), tris(hydroxymethyl)aminomethane (T/P630/60), glycerol (G/0650/17) and *n*-butanol (B/4850/17) were obtained from Fisher

Scientific. EDTA (27285) and calcium chloride (12074) were obtained from Riedel-de Haën (Seelze, Germany). Magnesium chloride (26123) was obtained from BDH (Poole, UK). Benzonase nuclease (99% purity, 25 U/mL) (70664-3) was obtained from Novagen (Madison, WI, USA). Quant-iT™ PicoGreen® dsDNA kit (dsDNA reagent, TE buffer, lambda DNA standard) (P11496) was obtained from Invitrogen. 10,000 molecular weight cut-off (MWCO), 3-12 mL (66810) and 20,000 MWCO 0.5-3 mL (66003) dialysis cassettes were obtained from Thermo Scientific. Black well microplates (3915) were obtained from Greiner Bio-One.

2.2.10 Instrumentation

MR data were acquired using a 7.0 T magnet with a Varian Inova spectrometer (Varian, Yarnton, UK) at the RRI and a quadrature birdcage coil (2.6 cm internal diameter; RAPID MR International, Columbus, OH, USA).

Light microscopy was performed using a Nikon Eclipse E800 light microscope (Nikon, Kingston upon Thames, UK). Slides were digitally scanned using an Aperio ScanScope CS (Aperio, Vista, CA, USA). Fluorescence microscopy was performed using a DM IRBE Leica epifluorescent microscope (Leica Microsystems, Milton Keynes, UK) with a mounted digital camera (C4742-95, Hamamatsu, Japan) and Simple PCI software v6.5.2.0 (Sewickley, PA, USA). Confocal microscopy was performed using an LSM-710 Zeiss confocal microscope (Carl Zeiss Microimaging, Jena, Germany) and Zen 2009 software (Carl Zeiss, Cambridge, UK).

R&D cytokine assay panels were scanned using a LI-COR Odyssey (LI-COR Biosciences, Lincoln, NE, USA). 4T1-GFP cells were imaged using an InCell Analyzer 1000 (GE Healthcare). A Wallac Victor^2 1420 multilabel counter (Perkin-Elmer) was used for measuring absorbance for the PicoGreen assay.

Heraeus biofuge pico and 400R centrifuges were used for normal bench centrifugation, and a Jouan CR4i centrifuge was used for tissue culture centrifugation (Thermo Scientific). A Beckman L8-70M ultracentrifuge and SW-40 Ti swing out rotor arm were used for ultracentrifugation during adenoviral purification (Beckman-Coulter). An Orion 5 star pH meter (Thermo Scientific) was used for measuring the pH of solutions. dH_2O for normal laboratory use was obtained by reverse osmosis; ddH_2O for adenoviral work was obtained using an Elga Purelab (DV35) (Elga Process Water, Marlow, UK) at resistivity of ≥ 18.2 MΩ/cm. Sterilization of surgical tools and solutions took place at 121 °C for 20 min.

Tissue sections were mounted in Tissue Tek® OCT™ compound (Sakura, Alphen aan den Rijn, The Netherlands) and cut onto SuperFrost Plus positively coated slides (J1800AMNZ, Thermo Scientific), using a Leica CM1900 cryostat (Leica Microsystems).

2.2.11 Software

MRI acquisition and data analysis were performed using VNMRJ v3.1 revision A (Agilent, Wokingham, UK). Brain segmentation and hypointensity visualisation were performed using ITK-SNAP v2.4.0 (Yushkevich et al., 2006; http://www.itksnap.org). Analysis of cerebral hypointensities, colocalisation of blood vessel markers, calculation of metastatic burden and statistical analysis were all performed using MATLAB v7.11.0.584 (2010b) (Mathworks, Cambridge, UK) with the Image Processing v7.1 and Statistics v7.4 Toolboxes installed. The 'Tools for NIfTI and ANALYZE image' files were downloaded from the MATLAB Central File Exchange (http://www.mathworks.co.uk/matlabcentral/fileexchange/8797-tools-for-nifti-and-analyze-image). Data were further manipulated and analysed using Microsoft® Excel for Mac 2011 v14.3.1 (Microsoft Corporation, Redmond, WA, USA).

Digital slide images were analysed using the ImageScope Viewer v11.1.2.760 (Aperio). Light microscopy and fluorescence images were viewed and analysed using ImageJ v1.43u (http://rsb.info.nih.gov/ij). ImageJ was also used for quick visualisation of MRI volumes with the 'NIfTI Input/Output' plugin (http://rsbweb.nih.gov/ij/plugins/nifti.html). Confocal images were viewed and analysed using Zen 2009 (Zeiss).

Graphs were prepared using Plot v0.997 (http://plot.micw.eu). Thesis text and graphics were prepared using Microsoft® Word for Mac 2011 v14.3.1 (Microsoft Corporation), Keynote '09 v5.3 (Apple, Cupertino, CA, USA), MATLAB (Mathworks) and Adobe Illustrator CS4 v14.0.0 (Adobe Systems, San Jose, CA, USA).

2.3 Methods

2.3.1 Cell culture

4T1-GFP cells were cultured in sterile uncoated polystyrene flasks in a 37 °C incubator with a 5% CO_2, 95% air, water-saturated atmosphere. Growth medium was DMEM containing 4.5 g/L (25 mmol/L) glucose and supplemented with 2 mM L-glutamine and 10% v/v FBS. Cells were grown for 3-5 days until *ca.* 80-90% confluent. For harvesting, the medium was aspirated from the flasks, the cells were washed with PBS at 37 °C and incubated in 3 mL 1 × trypsin-EDTA solution at 37 °C for 5-10 min to detach the cells from the flask. Cells were confirmed detached by microscopic observation. Trypsin was neutralised with 3 mL growth medium and the cells were sedimented by centrifugation (250 ×g, 4 °C, 5 min). The supernatant was aspirated and the cell pellet was resuspended in 1-2 mL sterile PBS. The cell suspension was kept on ice, and the concentration of living cells was measured. Cells were

diluted in sterile PBS to give a final concentration of 1×10^6 cells/mL. All injections were performed within 2 h of dilution, to minimise cell death.

2.3.2 Adenoviral preparation

The viruses used in these experiments were all replication-deficient Ad5 adenoviruses, lacking the E1 and E3 early stage replication genes. However, they can be successfully replicated by infection into transformed human embryonic kidney (HEK)-293 cells (Graham et al., 1977), which contain adenovirus type 5 DNA from the left 11% of the Ad5 genome, including the E1 gene necessary for viral replication (Louis et al., 1997). By deleting the E1 and E3 genes, inserts of up to 7.8 kb can be inserted into the Ad5 genome (Bett et al., 1994). The control virus (Ad70-3) used in these experiments has a deletion in E1 and a deletion/substitution in E3, with an overall deletion length of 3.2 kb compared to the Ad5 w.t. genome (Bett et al., 1994). A second virus (Ad-hIL1β) had been transfected with human IL-1β cDNA in the E1 region of the genome (Kolb et al., 2001). A third virus (Ad-mTNFα) had been transfected with mutant murine TNF-α cDNA in the E1 regions of the genome, encoding a bioactive form of the protein that remains membrane-bound rather than being secreted (Marr et al., 1997).

All seed virus was obtained from existing stocks in the Department of Pharmacology. The synthesis and use of these viruses has previously been described (Bett et al., 1994; Richards et al., 1995; Marr et al., 1997; Kolb et al., 2001; Margetts et al., 2002).

2.3.2.1 Adenoviral culture

HEK-293 cells were cultured in hyperflasks in a 37 °C incubator with a 5% CO_2, 95% air water-saturated atmosphere (all further HEK-293 incubations occurred under the same conditions

unless explicitly stated). The growth medium was EMEM supplemented with 10% v/v FBS and 2 mM L-glutamine. Cells were grown until *ca.* 70-80% confluent. To infect the cells, the growth medium was poured off and replaced by infection medium (EMEM supplemented with 2% v/v FBS and 2 mM L-glutamine), seeded with virus at a concentration of approximately 100 virus particles per cell. The cells were returned to the incubator and were monitored over the following days to look for signs of cell lysis, indicating adenoviral infection. As a result of cell lysis, confluence decreases and the viral titre within the flask increases, leading to further rounds of infection and cell lysis. Between 48 h and 7 days after viral inoculation (depending on the initial viral titre and the infectivity of the virus) the cells take on the appearance of bunches of grapes, at which point the viral concentration within the flask is at its highest. At this point the infection medium was poured off and 100 mL sterile PBS was added. Cells were physically dislodged by hitting the side of the flask, and the cell suspension was poured out. Cells were sedimented by centrifugation (250 × g, 5 min, 4 °C), and the resulting pellet was re-suspended in 14 mL PBS, snap frozen in liquid nitrogen and stored at -80 °C prior to purification.

2.3.2.2 Adenoviral purification

Cells were thawed in a water bath at 37 °C, and underwent two further liquid nitrogen freeze-thaw cycles in order to lyse the highest practical fraction of cells. The cell fragments were clarified by centrifugation (700 x g, 10 min, 4 °C). The sedimented material was discarded and the supernatant was transferred to a fresh tube and incubated with 1/100 volume of *n*-butanol on ice. After 60 min, the suspension was clarified by centrifugation (1100 x g, 10 min, 4 °C) and the supernatant was transferred to a fresh tube. A caesium chloride gradient was prepared in an ultra-centrifuge tube as follows: 3 ml CsCl ρ = 1.32 (2.795 M CsCl, 50 mM Tris, pH 7.9) underlaid with 2 ml CsCl ρ = 1.45 (4.242 M CsCl, 50 mM Tris, pH 7.9) and overlaid with 2 ml 40 % v/v glycerol in 10 mM tris-HCl, 1 mM EDTA, pH 7.9.

All solutions were filter sterilised through 0.22 µm pore size filters prior to use. The viral supernatant was overlaid on the top of the caesium chloride gradient, and any remaining space in the ultracentrifuge tube was filled with sterile PBS (Figure 2.4). The tubes were then allowed to come to density equilibrium by ultracentrifugation (25,000 rpm (min 46607 × g, max 110962 × g, mean 78749 × g); acceleration, 5; deceleration, 0; ≥ 2 h; 4 °C; in a vacuum).

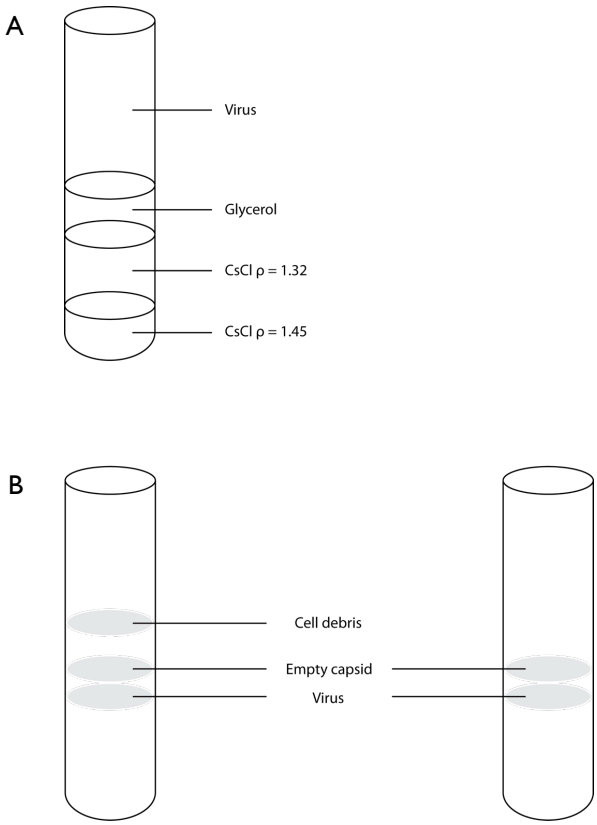


Figure 2.4 – Spin columns pre- and post-centrifugation. (A) The setup of the spin column prior to centrifugation. It is possible to see the boundaries between the different layers during column preparation. (B) The spin column as it looks following the first (left) and second (right) rounds of centrifugation. The bands appear as thin milky-white layers within the spin column. No cell debris should be visible following the second round of centrifugation.

Post-centrifugation the spin column was punctured below the viral band using a green needle (21G × 1½") and a 2 mL syringe. The viral band was removed and collected in a fresh

tube. Viral bands from all similar tubes were pooled and transferred to a 10,000 MWCO, 3-15 mL dialysis cassette and dialysed overnight in Dialysis Buffer 1 (50 mM HEPES, 1 × PBS, 2 mM $MgCl_2$, 0.4 mM $CaCl_2$, 10 % v/v glycerol, pH 7.8) to remove excess caesium chloride. Dialysis buffer was changed after 1 h and 2 h.

Following the first round of purification, the virus was removed from the dialysis cassette and incubated with 6 µL/mL benzonase endonuclease for 30 min at r.t. in order to remove polynucleotides that may otherwise adhere to the virus. A second caesium chloride gradient, identical to the first, was prepared and the partially purified virus was added and further purified by centrifugation as described above. After centrifugation, purified virus was collected and dialysed in a 10,000 MWCO 0.5-3 mL dialysis cassette overnight in Dialysis Buffer 2 (same constituents and pH as Dialysis Buffer 1, but with a 1 mM concentration of $MgCl_2$). The second dialysis buffer was changed after 1 h and 2 h. The virus was then removed from the cassette and stored in 10 µL aliquots at -80 °C.

2.3.2.3 Adenoviral quantification

Virus quantification was performed for each preparation using three different methods, the Pico Green assay, the 50% tissue culture infective dose ($TCID_{50}$) and the plaque assay.

PicoGreen assay

The PicoGreen assay (http://probes.invitrogen.com/media/pis/mp07581.pdf) allows precise spectroscopic quantification of the quantity of dsDNA in a sample of lysed virus against a dsDNA standard of known concentration. The results of the assay give a value for the number of virus particles that are present per mL of sample, although does not give any information about the infectivity of the virus in question.

Lambda DNA was dissolved in Tris-EDTA (TE) buffer (10 mM Tris-HCl, 1 mM EDTA, pH 7.5) to prepare standard concentration solutions at 0.5, 0.25, 0.125, 0.0625, 0.03 and 0 ng/µL. Unknown concentration viral samples were diluted with 19 volumes of TE supplemented with 0.05% w/v SDS then heated at 65 °C for 15 min in a water bath. From this, two different dilution preparations were made, one at 1:9 and one at 9:1 DNA:TE. Standards and unknown samples (100 µL) were pipetted in duplicate into wells of a black 96-well plate. 100 µL PicoGreen® dsDNA reagent was added to each well at a 1:40 dilution and the plate analysed using a Victor Plate Reader with a excitation/emission wavelengths of 485nm /515nm. A linear standard curve was constructed and the viral titre in virus particles /mL was deduced using the following equation:

$$Viral\ titre\ (virus\ particles/mL) = Extrapolated\ concentration \times Dilution\ factor \times Particle\ number\ factor$$

$$Particle\ number\ factor = 2.7{\times}10^{10}$$

$TCID_{50}$ assay

The $TCID_{50}$ assay (http://www.virapur.com/protocols/TCID50%20Protocol.pdf), unlike the PicoGreen® assay, determines the quantity of infectious virus within a sample. This assay can be used with any virus that has a cytopathic effect in tissue culture. For replication-deficient adenoviruses, $TCID_{50}$ titres can be determined by viral inoculation into a tissue culture of HEK-293 cells at varying dilutions. The $TCID_{50}$ is defined as the amount of virus required to cause a cytopathic effect in 50% of the cells in an inoculated cell culture.

HEK-293 cells were seeded in a 48-well plate at a density of 4 x 10^4 cells/well. Growth

medium was DMEM supplemented with 7.5% v/v FBS, 4mM L-glutamine, and 1% penicillin-streptomycin solution (final concentrations 100 U/mL penicillin and 100 µg/mL streptomycin). One day after seeding, seven serial tenfold viral dilutions were made in sterile PBS to give effective dilutions from 10^{-2} to 10^{-8}. Growth medium was aspirated and replaced with 0.1 mL fresh growth medium and 0.1 mL of the appropriate viral dilution was added in quadruplicate. Four wells on each plate were left uninfected. Cells were incubated for 2 h to allow the virus to adsorb, and 0.5 mL of infection medium (DMEM supplemented with 2% v/v FBS, 4 mM L-glutamine, 1% penicillin-streptomycin solution) was added to each well. Cells were further incubated for a period of 6 days, and examined microscopically each day to determine the number of infected and uninfected wells. The $TCID_{50}$ titre was calculated using a Microsoft® Excel® spreadsheet downloaded from the Yale School of Medicine website (www.med.yale.edu/micropath/pdf/Infectivity%20calculator.xls) using the formulae

$$I = \left\{ \frac{(\%\ wells\ infected\ at\ dilution >\ 50\%) - 50\%}{(\%\ wells\ infected\ at\ dilution > 50\%) - (\%\ of\ wells\ infected\ at\ dilution < 50\%)} \right\}$$

and

$$50\%\ endpoint\ titre = 10^{(\log total\ dilution > 50\%) - (Ilogh)}$$

where I is the interpolated value of the 50% endpoint and h is the dilution factor.

Plaque assay

The plaque assay is the traditional method of determining the viral concentration within a sample (http://www.virapur.com/protocols/Virus%20Plaque%20Assay%20Protocol.pdf). This assay determines the number of plaque forming units (pfu)/ mL and, like the $TCID_{50}$, it gives a value to the infectivity of the viral sample by observing the cytopathic effect of the

virus on the cell culture. Specifically, a confluent layer of cells is infected with the virus at varying dilutions in a semi-solid infection medium containing agar. Cytopathic plaques are formed as a result of the viral infection of a group of cells, surrounded by uninfected cells. It is an assumption of the assay that each plaque formed is the result of a single virus particle.

HEK-293 cells were seeded in a 6-well plate at a density of 1 x 10^6 cells/well. Growth medium was DMEM supplemented with 10 % v/v FBS, 4 mM L-glutamine. At *ca.* 90% confluency, four serial hundred-fold viral dilutions were made in sterile PBS to give effective dilutions of 10^{-2}, 10^{-4}, 10^{-6} and 10^{-8}. Growth medium was aspirated and replaced with 0.1 mL fresh growth medium and 100 µL of the appropriate viral dilution. The monolayers were incubated for 6 h with occasional gentle shaking to allow the virus to adsorb. An agar overlay was prepared by autoclaving a 4% agarose solution at 121 °C for 20 min, and incubated in a 65 °C water bath. Growth medium was gently aspirated out of the wells and 2 mL placing medium (DMEM supplemented with 2% v/v FBS, 4 mM L-glutamine, 0.4% agarose) at 37 °C was added. Plates were left at r.t. for 15 min to allow the agarose overlay to solidify, and incubated at 37 °C with an 8.5% CO_2, 91.5% air water-saturated atmosphere for 6 days. In order to aid plaque visualisation, plates were stained with 5 mg/mL MTT for 3 h at 37 °C, after which the plaques appeared as clear areas on a blue/black monolayer. The plaques were counted and converted to a pfu/mL value using the following equation:

$$Viral\ titre\ (plaque\ forming\ units/mL) = Number\ of\ plaques \times Dilution\ factor \times (1000/Volume\ (\mu l)\ of\ initial\ viral\ inoculum)$$

The results of the adenoviral quantification are shown in Table 2.1.

Quantification technique	Virus		
	AdIL-1β	AdTNF-α	Ad70-3
Pico Green assay (vp/mL)	1.95×10^{11}	6.19×10^{10}	1.06×10^{12}
$TCID_{50}$ (viral titre/mL)	3.16×10^{8}	3.16×10^{7}	$> 3.16 \times 10^{9}$
Plaque assay (pfu/mL)	6×10^{9}	5×10^{9}	1.2×10^{10}

Table 2.1 – Quantification of viral stocks. Animals were injected with 8×10^{6} pfu of virus.

2.3.3 Preparation of injectable agents

VCAM-MPIO

Synthesis of VCAM-MPIO was carried out by Martina McAteer (Wellcome Trust for Human Genetics, Roosevelt Drive, Oxford) as previously described (McAteer et al., 2007; Sibson et al., 2011). In brief, 5 mg of MyOne™ tosylactivated MPIO, containing 5×10^{9} MPIO, were washed in 0.1 M sodium borate buffer, pH 9.5, and then conjugated to 200 µL rat anti-mouse VCAM-1 antibody (1510-01) in 1 M ammonium sulphate (40 µg antibody per microgram of MPIO) for 20 h at 37 °C. The antibody solution was removed and replaced with blocking buffer and incubated overnight at 37 °C to block any unbound tosyl sites. The beads were washed and then stored on a rolling shaker at 4 °C prior to use.

2.3.4 Animal work

All animal work was performed in accordance with Home Office regulations under Project License 30/2620 and Personal License 30/8896.

2.3.4.1 Preparation of reagents

Phosphate buffer was prepared by dissolving 20 mM sodium dihydrogen orthophosphate dihydrate and 76 mM Sorrenson's salt in dH_2O. PLP_{light} was prepared by dissolving 75mM L-lysine monohydrochloride, 10 mM Sorrenson's salt, 2% w/v PFA, 10 mM sodium metaperiodate, 0.1% v/v gluteraldehyde of 25% glutaraldehyde solution in water, all in phosphate buffer; pH 7.2.

2.3.4.2 Intracardiac injection

Intracardiac injections were performed under isoflurane anaesthesia. Body temperature was maintained at 37 °C using a heated plate, and heart rate monitored to assess the depth of anaesthesia. Once fully anaesthetized, as determined by loss of pedal reflex, hair was removed by clipping from the area above the right-hand side of the ribcage. The animal was immobilized and the left ventricle of the heart was located using the ultrasound probe. Cells were triturated and 1×10^5 cells were injected in 100 µL PBS using a grey (27G × ¾") needle. A successful injection was determined by the presence of 'blushing' on the ultrasound image at the point at which cells were injected, and also by the return of blood back up the needle during or after the injection. Poorly injected animals were killed by a Schedule 1 technique to prevent any potential compromise in the reliability of the data. Animals were recovered

from anaesthesia in a heated recovery chamber and weighed. Their weights and overall health were monitored for the duration of the experiment (see Appendix 1 for the criteria by which the animals were scored).

2.3.4.3 Intravenous injections

All intravenous injections were performed on awake animals. When awake, animals' tails were immobilised by use of an injection box. In all cases, tails were swabbed using 70% v/v industrial methylated spirits (IMS) in water and warmed using a heat lamp for *ca.* 10-15 sec to promote peripheral circulation prior to injection. Care was taken not to overheat or burn the tails during this process. Injections were aborted if the procedure took more than two attempts on each side of the tail, to prevent blockage of the vein and subsequent tissue necrosis.

For procedures where remote injection of substances was required (e.g. gadolinium contrast agent during MRI), a 30G tail cannula with calibrated tubing of length approximately 1 m was inserted into the lateral tail vein under isoflurane anaesthesia as described above and secured with surgical tape.

2.3.4.4 Intrastriatal injections

Intrastriatal injections were performed under isoflurane anaesthesia. Once fully anaesthetized, as determined by loss of pedal reflex, a small patch of hair was clipped off the top of the head. Newly anaesthetised animals were placed on a stereotaxic frame, using ear bars to keep the head stable throughout surgery. The scalp was swabbed with 70% v/v IMS in water prior to making an incision above the left striatum. Bregma was identified by applying mild pressure to the skull and a burr hole was made using a dental drill 0.5 mm

anterior, and 2.0 mm lateral to bregma. 0.5 µL of cytokine (mIL-1β at 0.02 µg/µL; mTNF-α at 1.5 µg/µL) or saline control was injected over the course of five minutes through a glass microcapillary at a depth of 2.5 mm from the dorsal surface of the brain. At the end of injection the microcapillary was slowly removed to prevent unwanted spread of the cytokine up the microcapillary track. Following the injection, the scalp was sutured and the animal was recovered.

2.3.4.5 Animal preparation for MRI

Animals were intravenously injected with 4 mg Fe/kg VCAM-MPIO in sterile saline, with a total volume of 116 µL 1 h prior to the start of gradient echo (GE3D) acquisition. Animals were monitored for any adverse effects prior to the start of imaging. Approximately 20-30 min prior to imaging animals were anaesthetised and a cannula placed in the tail vein (as previously described). Lubricating eye drops were administered and the animal was placed in a cradle housed in the RF coil. The head was immobilised using a tooth bar and a screw-adjusted clamp. Body temperature was monitored using a rectal probe and maintained using a heating blanket and homeothermic monitor. Breathing was monitored using a pressure pad placed next to the chest. Vital signs were monitored throughout imaging. Isoflurane concentrations were adjusted to maintain a breathing rate of approximately 40 breaths per minute (*ca.* 1.6-1.75% in 50:50 N_2:O_2). Animals were recovered at the end of imaging.

2.3.4.6 Blood collection from animals

Blood collection from animals was performed in a non-recovery procedure similar to intracardiac injections, as described previously. Briefly, animals were anaesthetised and ultrasound guidance used to place a needle in the left ventricle of the heart. A 5 mL syringe was used to generate adequate negative pressure for maximal blood collection

(approximately 1 mL). To ensure non-recovery the isoflurane concentration was increased to 5% towards the end of blood collection. If required, the animals were rapidly perfused/fixed post-blood collection to allow organ collection, as described below.

2.3.4.7 Animal killing by perfusion/fixation

Animals were injected intraperitoneally (i.p.) with 13 mg pentobarbital. Following the loss of pedal reflex, animals were dissected to reveal the heart, and were transcardially perfused at a rate of approximately 40 mL/min with cold heparinised saline to clear vessels of blood, and then with PLP_{light}. Following complete fixation, as indicated by the stiffness of the hindlimbs and liver, relevant organs were dissected out and post-fixed in PLP_{light} for 4-6 h at 4 °C before being transferred to a 30% w/v sucrose solution at 4 °C for 1-2 days for cryoprotection.

2.3.4.8 Adenoviral time-course

Animals were injected intravenously with 8×10^6 pfu adenovirus in 100 µL sterile saline. Blood from animals was collected at 1, 4, 12 and 24 h, 3, 5, 8, 11 and 14 days post-viral injection, and organs harvested immediately after. Blood was collected in silicone-coated clot-activating tubes and left to stand (30 min, r.t.). The blood clot was separated by centrifugation (1700 × g, 10 min, r.t.), the serum collected in 100 µL aliquots and stored at -80 °C.

Cytokine quantification using the R&D Systems kit was performed with a few alterations to the manufacturer's protocol. In brief, the array membranes were blocked in 2 mL of Array Buffer 6 for 1 h at r.t. on a rocking platform. Samples were prepared by mixing 0.5 mL Array Buffer 4, 0.4 mL Array Buffer 6 and 15 µL reconstituted Detection Antibody Cocktail with 600 µL of each sample (sera from multiple animals in the same treatment group were pooled)

and incubating at r.t. for 1 h. Array Buffer 6 was aspirated off the array membranes and replaced with the prepared samples and incubated overnight at 4 °C on a rocking platform. Membranes were washed for 3 × 10 min in 1 × Wash Buffer, and were incubated with streptavidin-AlexaFluor 700 at a dilution of 1:7500 in Array Buffer 6 for 30 min in the dark at r.t. on a rocking platform. Membranes were washed for 3 × 10 min and imaged using the LI-COR Odyssey. Files were analysed using a MATLAB script developed by Dr Danny Allen (RRI) (http://www.mathworks.co.uk/matlabcentral/fileexchange/35128-protein-array-tool).

Cytokine quantification using the Raybiotech kit was performed as per the manufacturer's instructions. In brief, seven serial two-fold dilutions of the Cytokine Standard Mix and a negative control were prepared. Slides were blocked with 100 µL Sample Diluent for 30 min at r.t. and incubated with 100 µL standard cytokines or serum samples (pooled samples with the exception of naïve sera, which were prepared individually) overnight at 4 °C. Slides were washed, incubated with 80 µL reconstituted detection antibody cocktail for 2 h at r.t., washed and incubated with 80 µL streptavidin-Cy3 for 1 h at r.t. in the dark. Slides were washed and dried by centrifugation (190 × g, 3 min). Slides were kept at 4 °C in the dark and sent to Raybiotech for imaging and analysis.

2.3.5 Magnetic Resonance Imaging (MRI)

A scout image was acquired to position the centre of the brain in the centre of the magnet and to enable positioning of volumes and slices for further imaging protocols. A manual shim was completed prior to the start of imaging.

2.3.5.1 3D Gradient Echo (GE3D)

T_2*-weighted GE3D datasets were acquired with the following parameters: flip angle, 27°; repetition time, 65 ms; echo time, 7.5 ms; field of view, 11.2 mm × 22.5 mm × 22.5 mm; matrix size, 96 × 192 × 256; two averages; total acquisition time, *ca*. 40 min. The mid-point of acquisition was 1.5 ± 0.1 h after VCAM-MPIO injection. The data were reconstructed off-line, giving a final isotropic resolution of 88 µm.

2.3.5.2 Fast spin echo multi-slice (FSEMS)

T2-weighted images were acquired with the following parameters: TR = 3500 ms; effective TE = 61.92 ms; two averages; field of view, 25 × 25 mm; matrix size, 256 × 256; 35 × 0.5 mm coronal slices; total acquisition time, *ca.* 8 min. The data were used to aid co-localization of T2*-weighted slices and data acquired from histology.

2.3.5.3 Gradient echo multi-slice (GEMS)

T1-weighted images were acquired with the following parameters: TR = 500 ms; TE = 20 ms; field of view, 25 × 25 mm; matrix size, 128 × 64; 11 × 1 mm coronal slices; acquisition time, *ca.* 4 min. T1-weighted datasets were acquired pre- and 5 min post-bolus injection of 30 µL (1.2 mL/kg) Gd-DTPA to identify BBB permeability.

2.3.6 Immunohistochemistry

2.3.6.1 Preparation of reagents and buffers

TNB was prepared using 0.5% w/v blocking reagent (supplied in the TSA kit) in 0.1 M Tris-HCl and 0.15 M NaCl, pH 7.5. TNB (Perkin Elmer) Aliquots (10 mL) were stored at -20 °C.

Pre-reaction buffer (30mM Tris-HCl, 100mM NaCl, 10 mM $MgCl_2$, 0.1mM $ZnCl_2$; pH 7.5) and reaction buffer (30mM Tris-HCl, 100mM NaCl, 10 mM $MgCl_2$, 0.1mM $ZnCl_2$; pH 7.8) were prepared for use on the same day. Stop buffer (50mM Tris-HCl, 100mM NaCl, 100mM EDTA, 1mM tetramisole, 0.05% v/v Triton X-100; pH 7.2) and wash buffer (30mM Tris-HCl, 100mM NaCl; pH 7.2) were stored for up to 6 weeks at r.t.

2.3.6.2 Tissue preparation

Following cryoprotection, tissue was frozen in Tissue Tek® and stored at -80 °C. Brains were sectioned into slices 10 µm thick and mounted onto positively-coated slides then dried at 37 ^{o}C for at least 18 h prior to immunohistochemistry.

2.3.6.3 DAB immunohistochemistry

To identify 4T1-GFP colonies in the brain, sections were rehydrated in PBS, endogenous peroxidase activity was quenched for 20 min with a 1:100 v/v solution of 30% (w/w) H_2O_2 in PBS, washed with PBS, blocked for 1 h in TNB and incubated with an chicken anti-GFP primary antibody at a 1:1000 dilution in TNB overnight at 4 °C. Sections were washed with PBS, incubated with a biotinylated rabbit anti-chicken IgY secondary antibody at a 1:1000 dilution in TNB for 1 h, washed with PBS and amplified with a Vectorstain Elite ABC kit (both reagents at 1:100 dilution in PBS). Slides were developed in 0.1M sodium phosphate buffer, pH 7.4 containing 2.3 mM 3,3'-diaminobenzidine (DAB) and 1.5×10^{-4} w/v H_2O_2 for 7-10 min, dipped briefly in acetic acid (13 µmol/L in dH_2O) counterstained with cresyl violet, rinsed in dH_2O, dehydrated by transfer through 70%, 95%, 100% and 100% v/v ethanol in water, transferred to xylene and cover-slipped with distyrene and plasticisers in xylene (DPX) mounting medium. All steps were carried out at room temperature unless otherwise specified.

2.3.6.4 Tyramide signal amplification (TSA) and alkaline phosphatase (A-P) immunofluorescence

Identification of VCAM-1, laminin, αSMA and EphB4 used TSA for single staining procedures and a combination of TSA and A-P amplification for co-localization studies.

TSA: sections were rehydrated in PBS, quenched for 20 min with a 1:100 v/v solution of 30% (w/w) H_2O_2 in PBS, washed with PBS, streptavidin- and biotin-blocked for 15 min each, blocked for 30 min in TNB, and incubated with the appropriate primary antibody, diluted in TNB at 4 °C overnight. Slides were washed and incubated with an appropriate secondary antibody at a dilution of 1:250 in TNB for 30 min, washed with PBS, incubated with streptavidin-HRP 1:200 in TNB for 30 min, washed with PBS, and incubated for 8 min in the dark with TSA-biotin diluted 1:100 in amplification diluent. Slides were washed and incubated with a streptavidin-Cy3 fluorophore at a dilution of 1:100 in TNB for 30 min.

A-P: Slides were incubated with an enhancer solution for 20 min and with a polymer-conjugated secondary antibody for 30 min, washed with PBS and washed with pre-reaction wash buffer. Slides were incubated with ELF97 phosphatase substrate at a dilution of 1:50 in reaction buffer for 20 min. The reaction was terminated by the addition of stop buffer. Slides were washed with wash buffer at 4 °C overnight and cover-slipped with Vectashield mounting medium. The ELF-97 signal appears yellow on the DAPI channel, so when double staining with ELF-97 was performed no DAPI was used to avoid masking the ELF-97 signal. For single fluorophore work using only TSA amplification, Vectashield containing DAPI was used.

2.3.7 Immunocytochemistry

4T1-GFP cells were cultured as previously described. When cell confluence was *ca.* 80%, cells were detached from the surface of the flask using a rubber cell scraper, sedimented by centrifugation (250 x g, 5 min, 21 °C) and re-suspended in 2 mL growth medium. The cell suspension was transferred to a 96-well plate (100 µL per well). Cells were allowed to attach for 24-48 h, after which the medium was aspirated, the cells were washed with PBS and fixed using 4% paraformaldehyde (PFA) for 10 minutes. Cells were washed in PBS and endogenous streptavidin and biotin was blocked for 15 min each, with PBS washes between each blocking step. Cells were blocked with TNB for 1 h before incubation with a primary antibody at a dilution of 1:250 in TNB overnight at 4 °C. Cells were washed with PBS, incubated with an appropriate biotinylated secondary antibody at a dilution of 1:250 in TNB for 1 h, washed with PBS, and incubated with a streptavidin-Cy3 fluorophore at a 1:100 dilution in PBS for 30 min. Cells were washed with PBS and stained with DAPI for 15 min prior to imaging.

2.3.8 MRI analysis

2.3.8.1 3D Gradient echo (GE3D) datasets

The methods developed for analysing these datasets are described in detail in Chapter 3. In brief, NIfTI files output from the scanner were obtained and brain volumes were selected from the raw data using the region-growing tool in ITK-SNAP (parameter settings: threshold direction, above; upper threshold, adjusted to suitable mid-brain intensity threshold, c. 350000; balloon force, -3.0; curvature force, 0.42). The raw data and the masked brain volume were loaded into MATLAB, normalized and analysed using the automated hypointensity detection software. The workflow for this software is as follows:

```
(1)   LoadBrainVolumes;
(2)   CreateMeanSdBrainVolume(5);
(3)   CreateBrainHypoMask_regionprops('meanfrac',0.65,20,3);
```

Alternatively, the brain could be analysed using the `automate_gui` command with variable values: radius = 5; margin 1 = 0; type = 'meanfrac'; value = 0.65; size threshold = 20; margin 2 = 3. The MATLAB code for these files can be found in Appendix 2.

2.3.9 Immunohistochemical analysis

Brain metastases were identified on digital slide images by the presence of GFP DAB staining, or by general morphology. Digital slide images were obtained from the Aperio ScanScope CS and were analysed by manually segmentation of tumours. Tumours were assigned an ID, and the area and perimeter or each tumour were measured for each section on which they appeared. The data were imported into MATLAB for analysis (Appendix 2). To determine overall tumour volume, the areas of all individual parts of the same tumour in a given section were summed and multiplied by 10 to give a volume in μm^3. Consecutive sections were intentionally omitted when cutting; volumes of 'missing' sections were estimated by linear interpolation. The total volume was calculated as the sum of all the tumour volumes on each section.

Tumour ranges were given as the z-distance (in the AP axis) over which the tumour was observed. The number of objects for each section was measured and the mean value was calculated. The sphericity of tumours was calculated as the ratio between the perimeter of a discrete tumour area and the circumference of a circle with the same area, averaged across all objects and sections.

2.3.10 Statistical analysis

For single comparisons between two groups of parametric data, a Student's t-test was performed to determine significance. For data that could be modeled to a Gaussian distribution, a 1-way or 2-way analysis of variance (ANOVA) with a suitable *post hoc* test was performed to test for differences between groups.

The majority of data describing features of metastatic lesions was not normally distributed, and instead was heavily skewed to the left. Attempts were made to transform the data to normalize it, using reciprocal, square root, logarithmic or Box Cox transformations (Figure 2.6), but in cases where these did not provide adequately Gaussian distributions for parametric analysis the Kruskal-Wallis non-parametric test was used instead with a suitable *post hoc* correction.

Tukey's honestly significant difference criterion was used as a suitable *post hoc* correction for multiple comparisons.

All data are presented as means ± standard deviations unless otherwise specified.

Statistical significance was assigned at $p < 0.05$ (*), $p < 0.01$ (**), $p < 0.001$ (***).

PLACEHOLDER FOR FIGURE 2.5 SHOWING TRANSFORMATIONS OF DATA

Chapter 3

MRI detection of VCAM-1 upregulation at sites of brain metastasis

3.1 Introduction

Contrast-enhanced MRI has been has become the imaging modality of choice for the clinical diagnosis of brain metastases (Modo and Bulte, 2011; Barajas and Cha, 2012). However, traditional gadolinium-based contrast agents rely on BBB disruption as a result of tumour proliferation before focal contrast can be detected (Percy et al., 2011). More recently iron oxide particles have been developed for pre-clinical and clinical MRI (Jefferson et al., 2012; Rosen et al., 2012; Cheng et al., 2013), which can be antibody-tagged to target them to specific protein and carbohydrate moieties in a range of pathologies, both inside and outside the CNS (Burrell et al., 2011, 2012). Work in our group has used MPIO for detection of VCAM-1 expression at inflammatory lesions in multiple sclerosis (Serres et al., 2009), and more recently in brain metastasis (Serres et al., 2012). This chapter aims to characterise the colocalisation of VCAM-MPIO-derived cerebral hypointensities with VCAM-1 upregulation at the site of metastasis, and the development of novel MRI analysis techniques.

3.1.1 VCAM-1 upregulation in brain metastases

The vascular endothelium in the brain, as in many other organs, plays an essential role in the maintenance of tissue homeostasis. It is responsive to changes in pathology, and can react

by upregulating the expression of protein markers on the luminal surface of endothelial cells. Certain proteins such as cellular adhesion molecules (CAMs) provide a tether to circulating leukocytes and facilitate their extravasation into the brain (Ley et al., 2007). VCAM-1 in particular has been implicated in a variety of animal and human neuropathologies (Yednock et al., 1992; Cannella and Raine, 1995; Piraino et al., 2002; Polman et al., 2006). Recent studies of brain metastases in mice and humans have demonstrated VCAM-1 upregulation and suggest that brain metastases cause activation of the local vascular endothelium (Küsters et al., 2002; Carbonell et al., 2009; Serres et al., 2012). Thus, it is possible that VCAM-1 plays a pivotal role in the early stages of brain metastasis seeding. Interestingly, data from lung and liver metastases suggest that upregulation of VCAM-1 on the vascular endothelium may in itself promote the arrest and extravasation of circulating metastatic cells (Khatib et al., 1999; Vidal-Vanaclocha et al., 2000; Ludwig et al., 2004; Läubli and Borsig, 2010).

3.1.2 VCAM-MPIO proof of principle

Structural changes in the brain can often be identified using MRI approaches, most notably using gadolinium as a contrast agent (see Introduction, Section 1.8). More recently, molecularly-targeted contrast agents, such as VCAM-MPIO, have been developed that allow us to observe cerebral lesions in rodents associated with experimental autoimmune encephalomyelitis (EAE) (Serres et al., 2011), the rodent model of human multiple sclerosis, stroke (Hoyte et al., 2010), epilepsy (Duffy et al., 2012) and brain metastasis (Serres et al., 2012). VCAM-1 expression occurs on the luminal surface of endothelial cells in a variety of neuropathologies (Yednock et al., 1992; Cannella and Raine, 1995; Piraino et al., 2002; Polman et al., 2006). Thus, VCAM-MPIO in circulation, which is not capable of crossing the BBB, is free to bind to VCAM-1 expressed by endothelial cells (McAteer et al., 2007). MRI signal resulting from VCAM-MPIO is, therefore, observed in association with blood vessels of

the brain, a feature that has to be extracted reliably and reproducibly from the data (Figure 3.1).

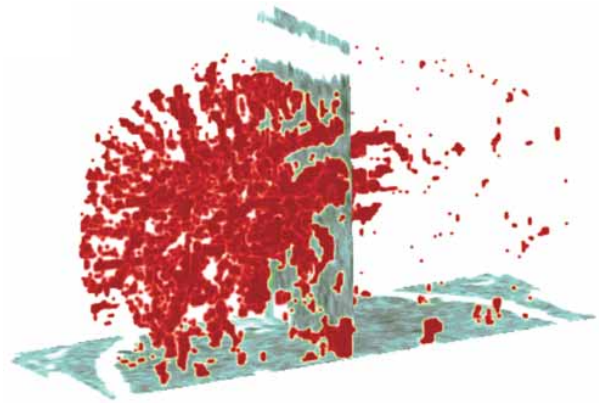


Figure 3.1 – Vascular localization of VCAM-1 signal is detected using VCAM-MPIO. Injection of IL-1β into the left hemisphere of the mouse brain leads to transient upregulation of VCAM-1 expression on cerebral blood vessels, here detected using VCAM-MPIO and reconstructed in 3D (red signal) (from McAteer et al., 2007).

3.1.3 VCAM-MPIO in brain metastases

The 4T1 mammary cell carcinoma line model of metastatic brain disease used in these studies (Materials & Methods, Section 2.2.4) results in dissemination of metastases to multiple sites throughout the brain, and recapitulates many aspects of clinical disease. Development of tumours is rapid using the 4T1 cell line and there is no need to seed a primary tumour. Instead, cells are allowed to enter the systemic circulation by direct injection into the left ventricle of the heart. After 10 days VCAM-1 is clearly visible on blood vessels at the tumour site (Serres et al., 2012), matching human post-mortem tissue (Küsters et al., 2002; Serres et al., 2012). These findings have led us to investigate the use of VCAM-MPIO as an early diagnostic biomarker for brain metastasis (Serres et al., 2012).

3.1.4 Outstanding questions

Several outstanding questions remain from the work described. Fundamental to this thesis is the degree of correspondence between hypointensities and metastases. How often does a hypointensity in the MRI data correspond to the presence of a metastatic lesion? Furthermore, does VCAM-1 upregulation at the site of metastasis necessarily correspond to its detection by VCAM-MPIO? In order to answer these questions, I have systematically looked at the colocalisation of MRI hypointensities, brain metastases and VCAM-1 expression at the tumour site and sought to determine the relationship between the three.

Limitations in the detection and analysis of hypointensities must also be overcome. Previous work in the laboratory using VCAM-MPIO assessed locations and volumes of hypointensities from MRI data using an approach that was open to operator subjectivity and hence potential inter-operator, and even intra-operator, differences. The approach taken was to convert MRI datasets to a stack of 256 .tiff (Tagged Image File Format) images, each of which was manually and independently masked and thresholded in Adobe Photoshop such that any voxels with an intensity of greater than approximately 3 standard deviations below the regional mean value were treated as hypointense. For this purpose each brain was split into *ca.* 3-4 regions. The threshold level had to be adjusted for the signal-to-noise ratio (SNR) in each brain and consistency of results was assessed by repeat analysis between multiple independent operators.

The above approach suffered two potential drawbacks: a systematic bias when accepting or rejecting marginal voxels as hypointense as well as a random bias by treating neighbouring slices in the same brain or equivalent slices in different brains in a slightly different manner to each other. This process also became laborious and time-consuming when analysing large data sets. One of the aims of this chapter was to develop a novel automated detection

technique for brain hypointensities that is operator-independent and reduces both the subjectivity of identifying hypointensities and the time taken to analyse MRI datasets.

This work presented in this chapter covers three topics:

1 The expression of VCAM-1 at the tumour site and its colocalisation with VCAM-MPIO-derived hypointensities in MRI datasets.

2 The development of an automated computational method for the reliable detection of hypointensities in the brain.

3 The use of filtering techniques to improve image quality and increase the potential correspondence between hypointensities and metastases.

I wish to acknowledge the help of Dr Sébastien Serres for teaching me many of the animal handling methods and MRI techniques used in this chapter, and Dr Danny Allen for his assistance developing the automated hypointensity detection method.

Some of this work has recently been published in Serres et al. (2012).

3.2 Methods

3.2.1 Animal model

Female BALB/c mice aged 7-10 weeks were intracardially injected with 1×10^5 4T1-GFP cells in 100 µL PBS, and were imaged 10 days later (Figure 3.2; Section 2.1). The animals were killed after imaging by perfusion/fixation with 0.9% heparinised saline and PLP_{light}, and the brain dissected out for immunohistochemical and immunofluorescent staining.

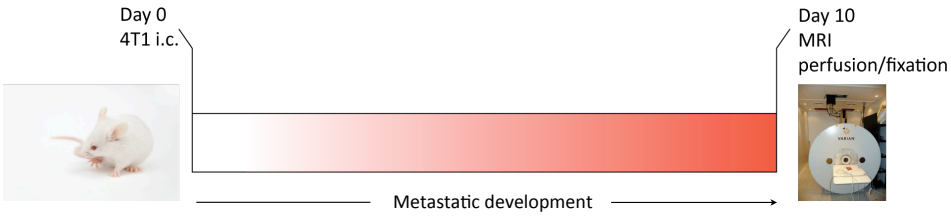


Figure 3.2 – Experimental schedule. Metastatic lesions were allowed to develop for 10 days following intracardiac injection before the animals were imaged and perfused/fixed.

3.2.2 MRI

Animals were injected with VCAM-MPIO (4 mg Fe/kg) (Section 2.3.5) in 100 µL sterile saline 1 h prior to imaging and the tail vein cannulated immediately prior to imaging. Animals were imaged at 7 T under isoflurane anaesthesia in 50:50 O_2:N_2. For detection of VCAM-MPIO, a T_2^*-weighted 3D gradient echo dataset was acquired. A T2-weighted dataset was acquired to aid colocalisation of metastatic lesions and hypointensities. Total imaging time was approximately 1-1.25 h per animal.

3.2.3 Immunohistochemistry / immunofluorescence

Brains were cryoprotected in 30% sucrose and rapidly frozen in Tissue Tek® before being cut on a cryostat. Sections were either DAB stained immunohistochemically for GFP to locate and characterize metastatic lesions in the brain, or stained immunofluorescently to

colocalise VCAM-1 expression with GFP expression on tumours, using TSA amplification (Section 2.3.6).

3.2.4 Analysis tools

GE3D datasets acquired from MRI were analysed using ITK-SNAP (Yushkevich et al., 2006) and MATLAB, as described in this chapter (Section 2.3.8). Briefly, NIfTI files were constructed from GE3D datasets and masked in ITK-SNAP to extract the brain volume. The NIfTI file and mask were analysed using MATLAB to determine the location of hypointensities in the brain based on statistical differences in voxel intensity between a central voxel and its local distribution. Analysis returned a total volume and number of hypointensities recorded, classified by size, and a new NIfTI file showing the locations of hypointensities that could be overlaid on top of the original brain volume in ITK-SNAP.

Immunohistochemical slides were photographed using an Aperio slide scanner, and the images viewed in Aperio ImageScope (Section 2.3.9). Metastatic lesions were identified by eye on the basis of GFP expression, or by morphology if GFP expression levels were low. Tumour characteristics (volume, range, number of objects, sphericity) were measured by hand.

Positively stained sections using immunofluorescence techniques were photographed using a digital camera mounted on a Leica epifluorescent microscope. VCAM-1 expression at the tumour site were determined to be present or absent after imaging all sequential sections of the same tumour.

3.2.5 Statistics

The statistics employed in the identification of hypointensities in GE3D datasets are described in detail over the course of this chapter. All other statistical analyses in this chapter were performed using MATLAB (Section 2.3.10).

3.3 Results

3.3.1 Colocalisation

3.3.1.1 MRI hypointensities and metastatic lesions in the brain

VCAM-MPIO have previously been used to detect brain lesions in the experimental autoimmune encephalomyelitis (EAE) mouse model of human multiple sclerosis (MS) (Serres et al., 2011) and more recently in a systematic analysis of metastatic brain tumours over a time course from 5 to 13 days post-induction (Serres et al., 2012). The total volume of hypointensity in the brain increased over this time-course against a control IgG-MPIO contrast agent (Serres et al., 2012). Certain hypointensities clearly colocalised with the sites of metastatic tumours in the brain (Figure 3.3). At the same time metastases were found to be associated with endothelial VCAM-1 expression.

However, certain difficulties are inherent in the correlation of MRI and histological data, owing to differences in spatial resolution between the two modalities. Thus, it was not immediately clear to what extent the presence of hypointensities in the MR images correlated with actual tumour presence. Conversely, whilst the majority of hypointensities in the MR images reflect true VCAM-1 expression and VCAM-MPIO binding there is also a low level of non-specific contrast either due to noise or to non-specific retention of the particles.

At the same time not all metastases may induce VCAM-1 expression. Therefore, one element of my work was to determine the percentage of tumours that were either VCAM-1 or MRI positive and to thus determine the false positive rate in the MRI data. Each of these could then be related to the size of the lesion and the presence or absence of VCAM-1 expression at the metastatic locus.

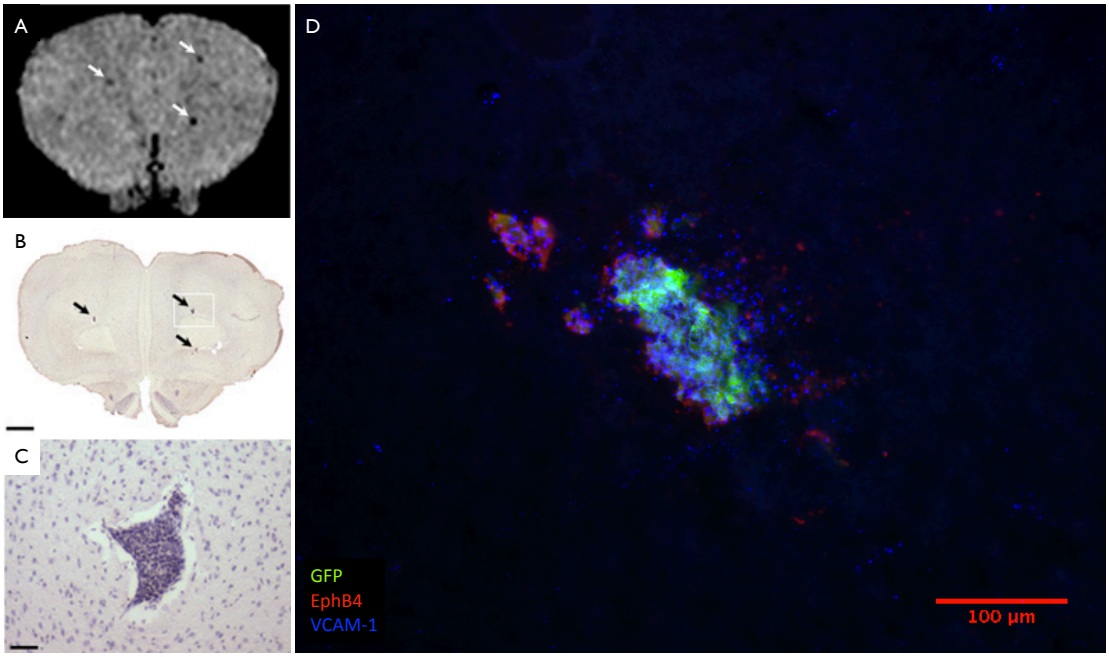


Figure 3.3 – Colocalisation of MRI hypointensities and metastatic lesions. (A) Hypointensities identified in a single slice from a 3D dataset. (B) Metastatic tumours corresponding to similar locations within the brain detected immunohistochemically (scale bar = 1000 µm). (C) One of the metastatic lesions (box in B) at increased magnification (scale bar = 100 µm). (D) VCAM-1 expression at the site of metastasis. Adapted from Serres et al., 2012.

For tumours above the mean volume of 0.0008 µL (*ca.* 760 cells, where the volume of one cell is approximated at 10 μm^3), approximately 68% were associated with VCAM-MPIO-

induced hypointensities in T2*-weighted MR images, which corresponds almost exactly with the 65% of tumours above the mean volume that are VCAM-1 positive (Figure 3.4A). Fewer tumours with volumes less than the mean were VCAM-1 positive or MRI positive, and a slightly poorer association was observed, with 36% of MRI positive tumours and 43% of VCAM-1 positive tumours. These tumours can be further subdivided into four groups depending on their colocalisation with VCAM-1 expression and association with MRI hypointensities (Figure 3.4B). Those that are VCAM-1 negative / MRI negative have the lowest mean (mean = 0.0004 μL), and a Kruskal-Wallis test with multiple comparisons showed that these tumours are significantly smaller than VCAM-1 positive / MRI negative tumours (mean = 0.0007 μL) and VCAM-1 positive / MRI positive tumours (mean = 0.0013μL) ($p = 0.0002$). VCAM-1 negative / MRI positive tumours had a mean volume of 0.0007 μL.

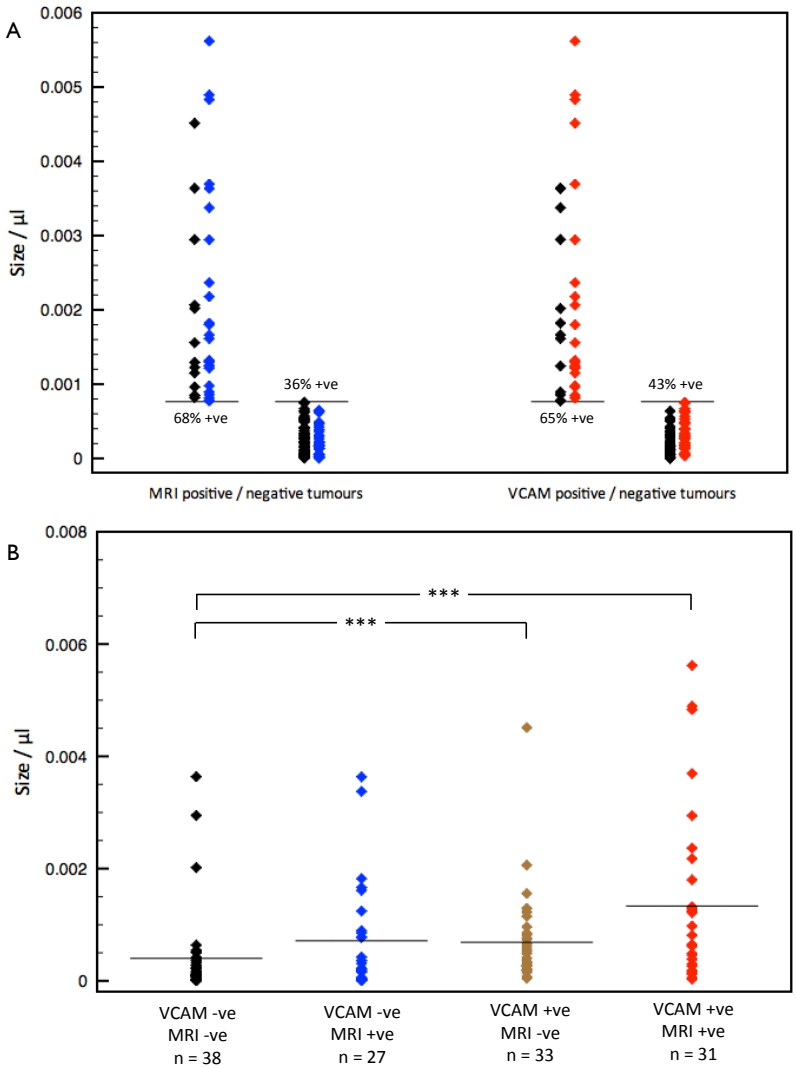


Figure 3.4 – IHC of VCAM-1 expression at the tumour site and manual colocalisation with MRI hypointensities. (A) A set of metastases taken from three different brains, showing the range of sizes and their colocalisation with MR hypointensities (left) and VCAM-1 expression (right) at the metastatic locus. The horizontal line represents the mean of the size distribution of metastases. Above the mean 68% of tumours are associated with MR hypointensities, which tallies closely with the number of tumours above the mean that are VCAM-1 positive (65%). Below the mean the correspondence of tumours and hypointensities is much lower (36%), a proportion that tallies roughly with the number that are VCAM-1 positive (43%). (B) Representation of the same set of metastases showing the distributions of tumours that are VCAM-1 negative / MRI negative (black), VCAM-1 negative / MRI positive (blue), VCAM-1 positive / MRI negative (brown) and VCAM-1 positive / MRI positive (red). Significant differences between groups are marked with asterisks.

3.3.2 Analysis automation

3.3.2.1 Description of the automated analysis

To address the issues inherent in the current analytical approach, I developed, with the help of Dr Danny Allen, a method to computationally distinguish between hypointense voxels and normal-intensity voxels in the brain. This approach uses global parameter values to compare individual voxels to their neighbours and determine whether they are hypointense based on statistical similarity or difference to their neighbourhood. Importantly, this approach does not identify hypointense voxels using global contrast levels within the brain, but rather by using local contrast levels. Contrast levels decrease from the anterior to the posterior of the brain as the position of the animal changes relative to the centre of the radio frequency (RF) coil (Figure 3.5C). As a result the posterior of the brain usually appears darker than the anterior, independent of VCAM-MPIO-induced signal. Thus, using global contrast levels (Figure 3.5A) to detect hypointensity across the brain volume returns a greater proportion of signal in the posterior regions than elsewhere (Figure 3.5B). The use of regional contrast values reduces the proportion of hypointense signal identified in the posterior regions of the brain (Figure 3.5D).

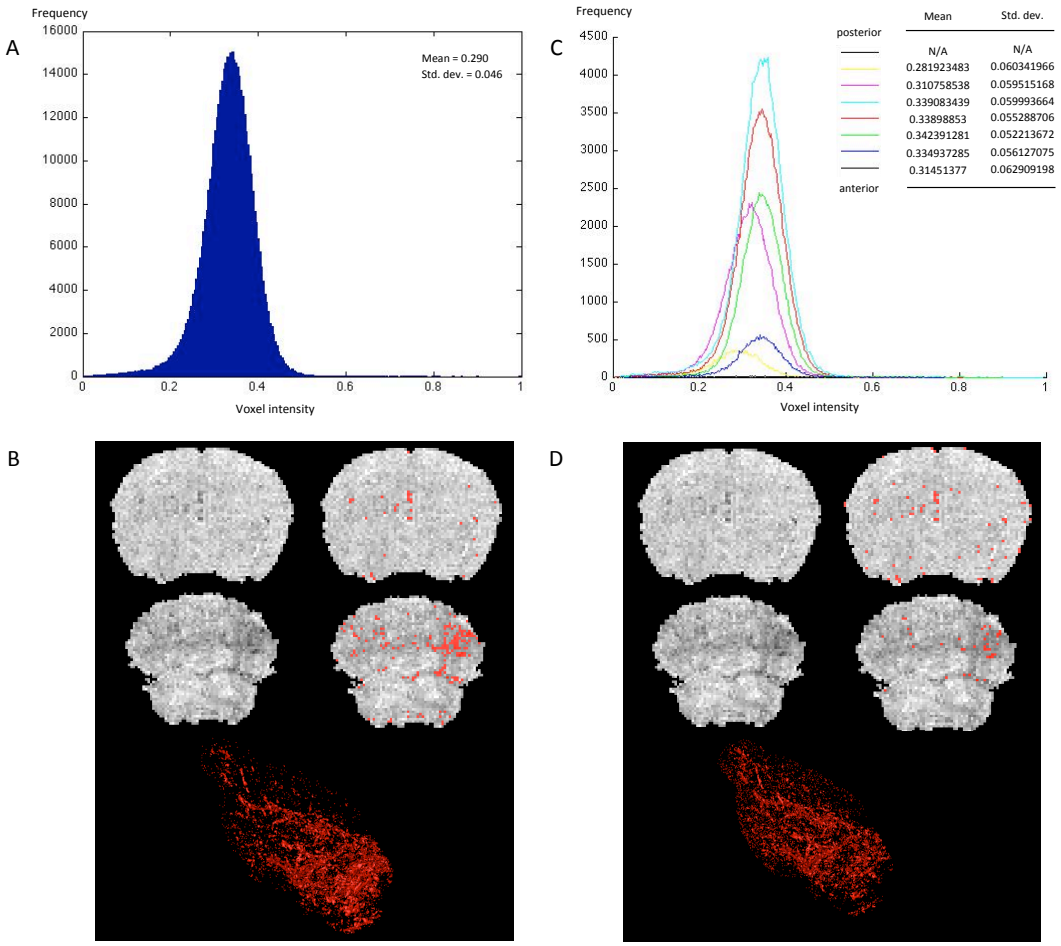


Figure 3.5 – Global and regional approaches to identifying hypointensities. (A) Global distribution of voxel intensities in the brain show a slight negative skew and a slight positive kurtosis (mean = 0.290; standard deviation = 0.046). (B) Thresholding the brain volume two standard deviations below the mean returns a set of hypointensities weighted towards the posterior of the brain as a result of contrast changes along the AP axis, independent of the signal derived from VCAM-MPIO binding. This extra signal hampers detection of 'true' VCAM-MPIO-derived signal. (C) Changes in contrast are caused by the position of the brain within the RF coil, with lower mean intensities towards the posterior of the brain. (D) Threholding at two standard deviations below the regional mean improves the identification of hypointense voxels at the posterior of the brain, but can lead to noisy signal in the mid-brain.

Rather than using global or regional contrast levels, I sought to use local voxel intensity distributions to define hypointense voxels. Local contrast levels were calculated using a sphere of voxels surrounding a central voxel of interest (VOI). For each VOI the mean and standard deviation were calculated for the intensities of all the voxels in the surrounding sphere, excluding the VOI. The VOI was then determined to be normal or hypointense based either on whether its value was above or below a specified fraction of the local mean or a specified number of standard deviations below the local mean. If the outcome of the test was positive then the voxel was scored as hypointense (given a value of 1), otherwise it was scored as normal (given a value of 0). Thus, the inequalities

$$v_{ind} = \begin{cases} 1, & v_i < \overline{v}/_x \\ 0, & v_i \geq \overline{v}/_x \end{cases}$$

or, exclusively

$$v_{ind} = \begin{cases} 1, & v_i < \overline{v} - y\sigma_v \\ 0, & v_i \geq \overline{v} - y\sigma_v \end{cases}$$

where v_{ind} is the value of the indexed VOI, v_i is the intensity of the VOI, $\overline{v}$ is the mean of the local voxel distribution, σ_v is the standard deviation of the local voxel distribution, x is the cut-off fraction of the mean and y is the cut-off number of standard deviations, describe the identification of hypointense voxels based on the statistical parameters of the local voxel distribution.

This process of calculating the local intensity distribution and testing the value of the VOI was repeated for each voxel within the brain. The scores for each voxel were stored as a separate variable, which could be overlaid onto the original brain image to visualize the locations of hypointense voxels within the brain. The MATLAB code can be found in Appendix 2.

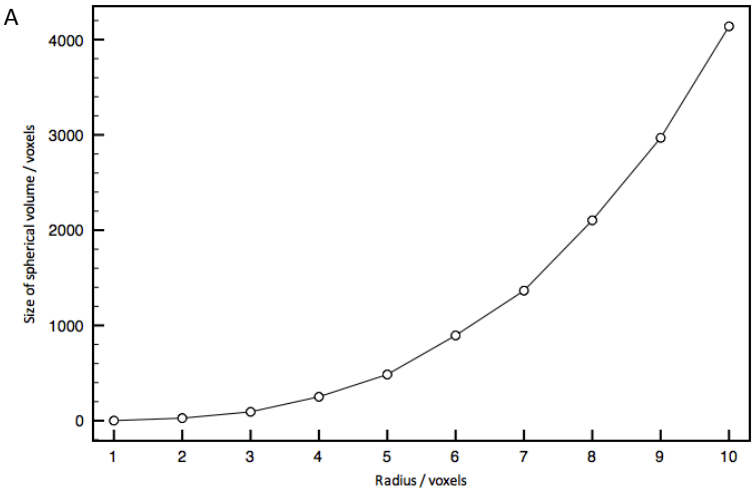
3.3.2.2 Testing variable values for automated hypointensity detection

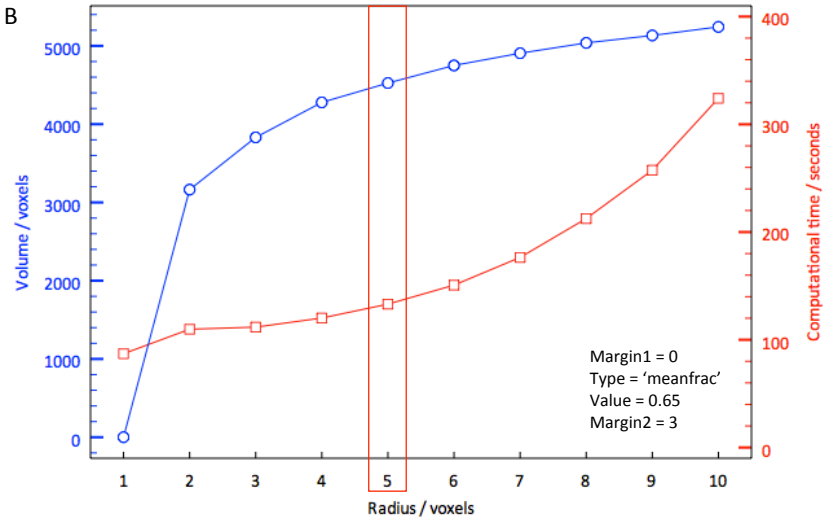
A number of variable values could be changed in order to provide an appropriate measurement of the number and volume of hypointense voxels within the brain. The effect of changing each of these variables is discussed below, and representative data for each are presented.

Radius

The radius determines the size of the local distribution that is calculated for each VOI. If the radius is small then only a small number of points are included in the local distribution (Figure 3.6A). As the value of the radius increases, the size of the local distribution increases by the cube of the radius (Figure 3.6A). This leads to an equivalent increase in computational time to calculate the local mean and standard deviation (Figure 3.6B). Increasing the radius increased the total volume of hypointensities measured in the brain towards an asymptote (Figure 3.6B). Two sample datasets (Figure 3.6C & D) demonstrate the effects of changing the radius on the volume of hypointensity detected.

Thus, small radius values do not allow reliable detection of all hypointense voxels in the brain, particularly if the hypointensity is very large. Conversely, increasing the radius of the analysed distribution will eventually yield distributions that describe regional brain intensities rather than local ones. Thus there is a trade-off between increasing the radius of the analysed distribution for each VOI and local specificity of the signal intensity. The benefits and drawbacks of different values of the radius are summarized in Table 3.1.


A
Size of spherical volume / voxels
Radius / voxels
0
1000
2000
3000
4000
1
2
3
4
5
6
7
8
9
10


B
Volume / voxels
Computational time / seconds
Radius / voxels
Margin1 = 0
Type = 'meanfrac'
Value = 0.65
Margin2 = 3

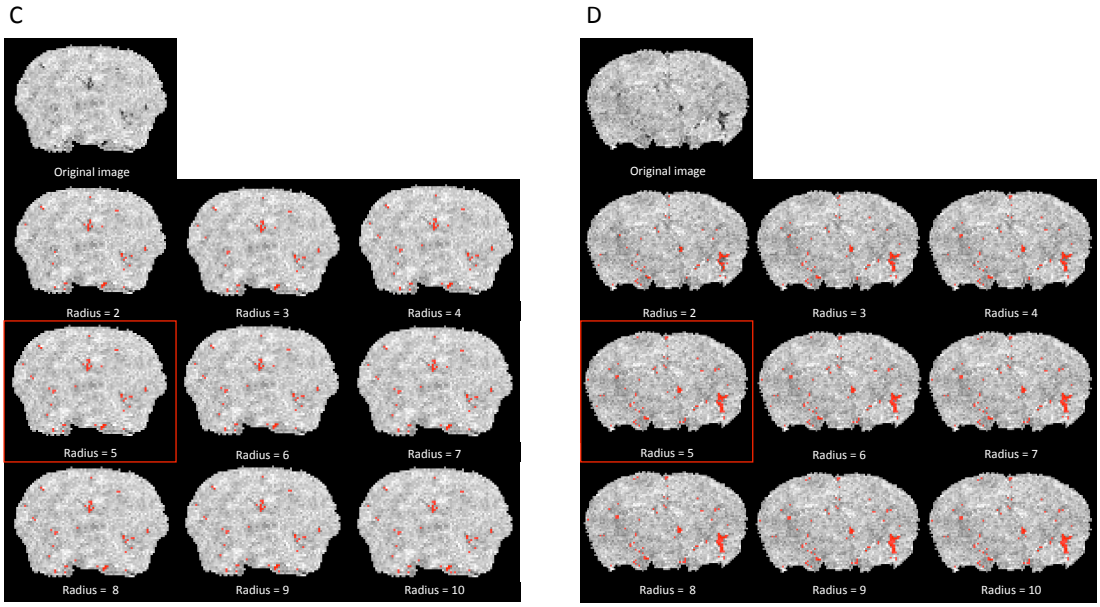

C
D
Original image
Radius = 2
Radius = 3
Radius = 4
Radius = 5
Radius = 6
Radius = 7
Radius = 8
Radius = 9
Radius = 10

Figure 3.6 – The effects of changing the radius on (A) the size of the local distribution and (B) the computational time and the volume of hypointensity measured. A distribution of radius 1 produces a non-existent distribution so the computational time presented for radius 1 represents the baseline time taken to read through all voxels in the brain volume. Equivalently, no hypointensities are identified for distributions of this radius. (C) A radius value of 5 gives coverage of all hypointensities in this slice through the brain, as well as the larger hypointensities as seen in (D).

	Pros	Cons
Small radius	Low computational time	May lose larger hypointensities
Large radius	Large distribution from which to calculate the test statistic	High computational time Loss of specific local contrast

Table 3.1 – Pros and cons of changing the radius size in the measurement of hypointensity of the brain.

Test method

As mentioned above, two different metrics were considered to test whether the VOI was hypointense or not: the fraction of the local mean or a number of standard deviations below the local mean. Assessment of the individual local distributions indicated that a subset of distributions were approximately normal, whilst other subsets were skewed either left or right and a small subset of distributions appeared to be bi-phasic (Figure 3.7C). For those local distributions that appear normal the standard deviation from the mean was found to yield a good method of identifying hypointense voxels. However, distributions that are skewed in either direction have a higher standard deviation than those that are normal. Thus, voxels that would appear hypointense by eye may not be identified as such by this

approach. The same effect also holds for biphasic distributions. In contrast, the mean of a skewed distribution will not shift as dramatically as the standard deviation and, thus, under these circumstances the mean fraction remains a more stable measure of hypointensity than the standard deviation. Large hypointensities will skew the local distribution to the left, owing to the presence of neighbouring hypointense voxels. This observation may explain why the standard deviation does not appear to detect larger hypointensities as reliably as the mean fraction (see Figure 3.8).

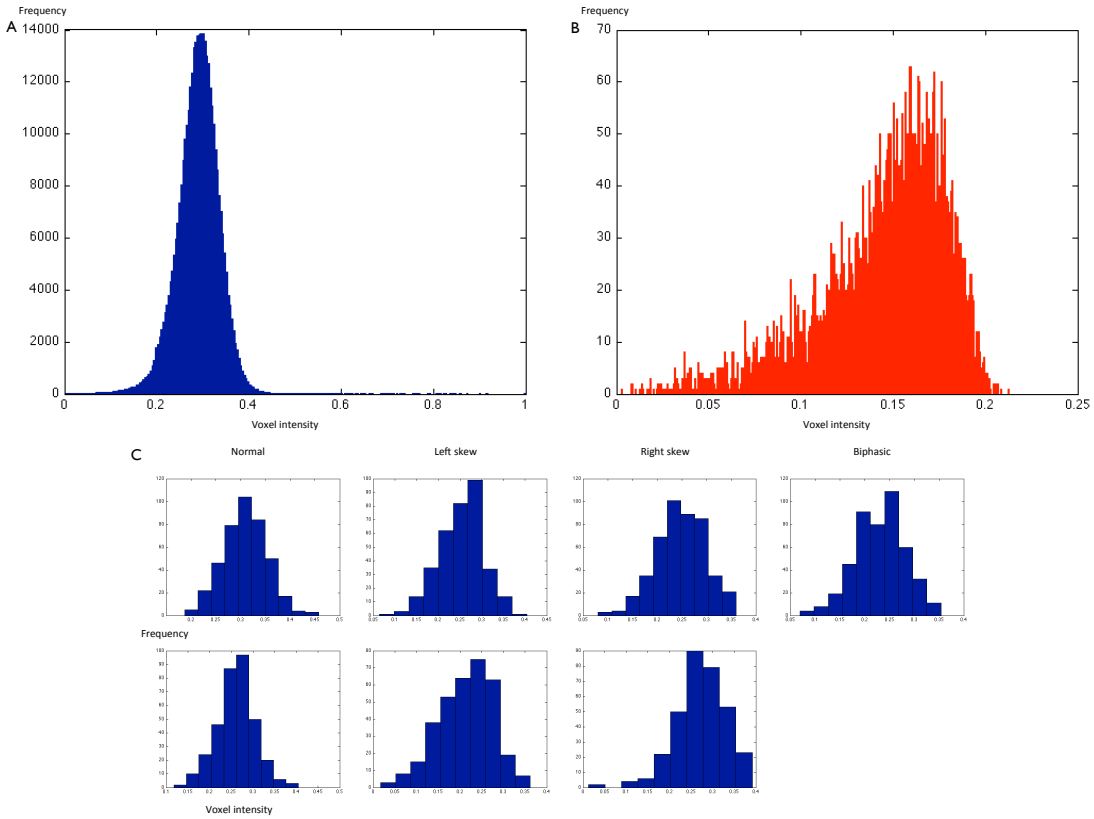


Figure 3.7 – Voxel intensity distributions for (A) the whole brain volume, (B) all hypointense voxels within the brain and (C) local distributions from which hypointense voxels are defined.

Value

Value refers to the value of the test statistic, i.e. the fraction of the mean or the number of standard deviations below the mean to use as our cut-off. At high values of the mean

fraction and low values of the standard deviation a large amount of signal is acquired from voxels that do not appear by eye to be hypointense. As the fraction of the mean is reduced or the value of the standard deviation is increased, fewer voxels are identified as hypointense. An optimum value can be found for each test by eye (Figure 3.8). A degree of subjectivity is inherent in choosing optimum values by eye, so these values have been further tested with mock hypointensities, as described later (Figures 3.11 & 3.12).

These data indicate that by using a fraction of the mean as the test method rather than a number of standard deviations below the mean, it is possible to distinguish larger hypointense regions of the brain that are otherwise not detected. A mean fraction value of 0.65 appears to yield a reasonable level of identification of hypointense voxels. Further evaluation of this value is discussed below in Sections 3.3.2.3 & 3.3.2.4.

[PLACEHOLDER FOR FIGURE 3.8]

[PLACEHOLDER FOR FIGURE 3.8 CAPTION]

Margin

Minor miss-segmentation errors result in a mask that is slightly larger than the brain volume and can lead to edge effects when defining hypointense voxels. These can appear as a rim around the edges of the brain. At these points, voxels that make up the dark boundary to the brain will be included in the analysis and create an edge around the brain volume that is recorded as hypointense. This effect can be remedied by applying a margin onto the brain volume, excluding voxels at the edge from the analysis. The results of applying a margin to the data are shown in Figure 3.9.

It was found that a margin of greater than or equal to half the radius of VOI distribution is required for an effect to be observed. At margins greater than half the radius of the VOI a step-wise reduction in the volume of hypointensity in the brain is calculated. However, as the margin is increased hypointensities from within the brain volume may begin to be eliminated, i.e. 'true' hypointensities. For this reason it was concluded that a margin of half the radius, or of half the radius, rounded up to the nearest integer, is optimal.

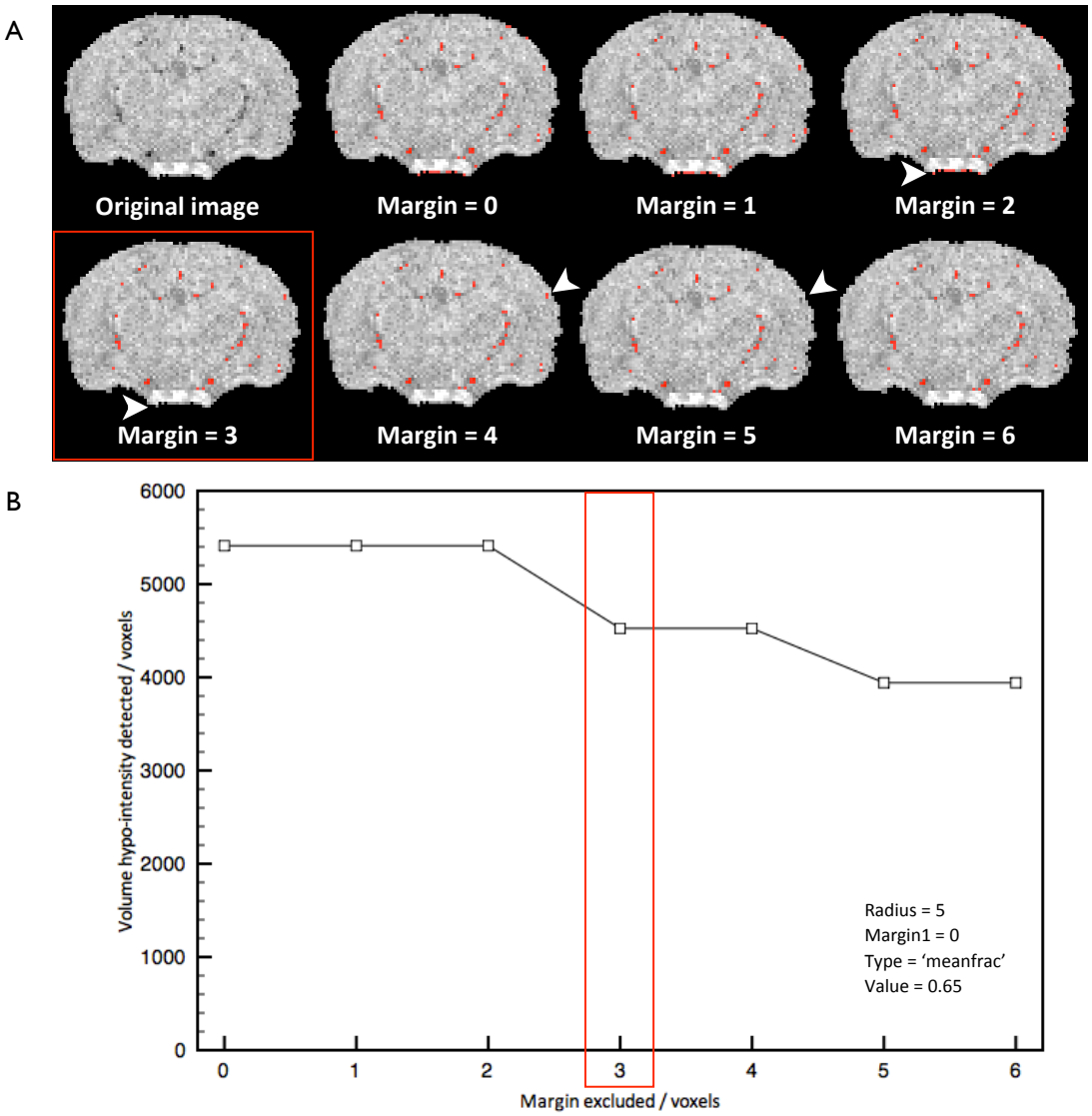


Figure 3.9 – The effect of a margin on removing false hypointensities at the edge of the brain volume. An edge effect is evident at the ventral surface of the brain slice (A) at margin values of 0, 1, & 2 (top row, white arrow), but is removed by a margin of 3 or greater. At increasing values of the margin further signal is lost, as highlighted by the loss of the hypointensity between margin values of 4 and 5 (bottom row, white arrows). (B) Loss of surface regions leads to a consequent reduction in the volume of hypointensity measured. Optimal values are highlighted in red.

Size threshold

Each variable described so far has been used to quantify hypointensity in the brain, but we may also wish to classify hypointense voxels in the brain based on size. Thus, singleton hypointense voxels were defined as 'small' and were recorded separately to any hypointensities of ≥ 2 voxels (≥ 0.0014 μL) in the brain. 'Small' hypointensities are likely to represent noise, in a similar manner to the background VCAM-MPIO signal observed in naïve animals. Thus, the volume of 'small' hypointensities was recorded, but was excluded from analysis. At the same time an upper size threshold of 20 voxels (0.0136 μL) was defined, above which hypointensities were considered 'large'; for the most part these 'large' hypointensities reflected ventricles and sinuses and were unrelated to tumour burden or contrast agent. These 'large' volumes are sizeable and the largest can measure up to nearly 500 voxels (*ca.* 0.3 μL) in size. However, it was also found that signal obtained from these structures may increase in the presence of pro-inflammatory agents (see Figure 5.20) and thus should not be disregarded entirely. Hypointensities of size $1 < x \leq 19$ voxels were classified as 'medium' hypointensities. In the metastatic model punctate hypointensities with the medium hypointensity range were dominant. The upper size cut-off is primarily aimed at distinguishing these hypointensities from the large hypointensities obtained from ventricles and sinuses of the brain (Figure 3.10). The size threshold was initially determined using a by eye approach, and is further tested using mock hypointensities later in this chapter (Figures 3.11 & 3.12). The optimum values for each variable can be found in Table 3.2.

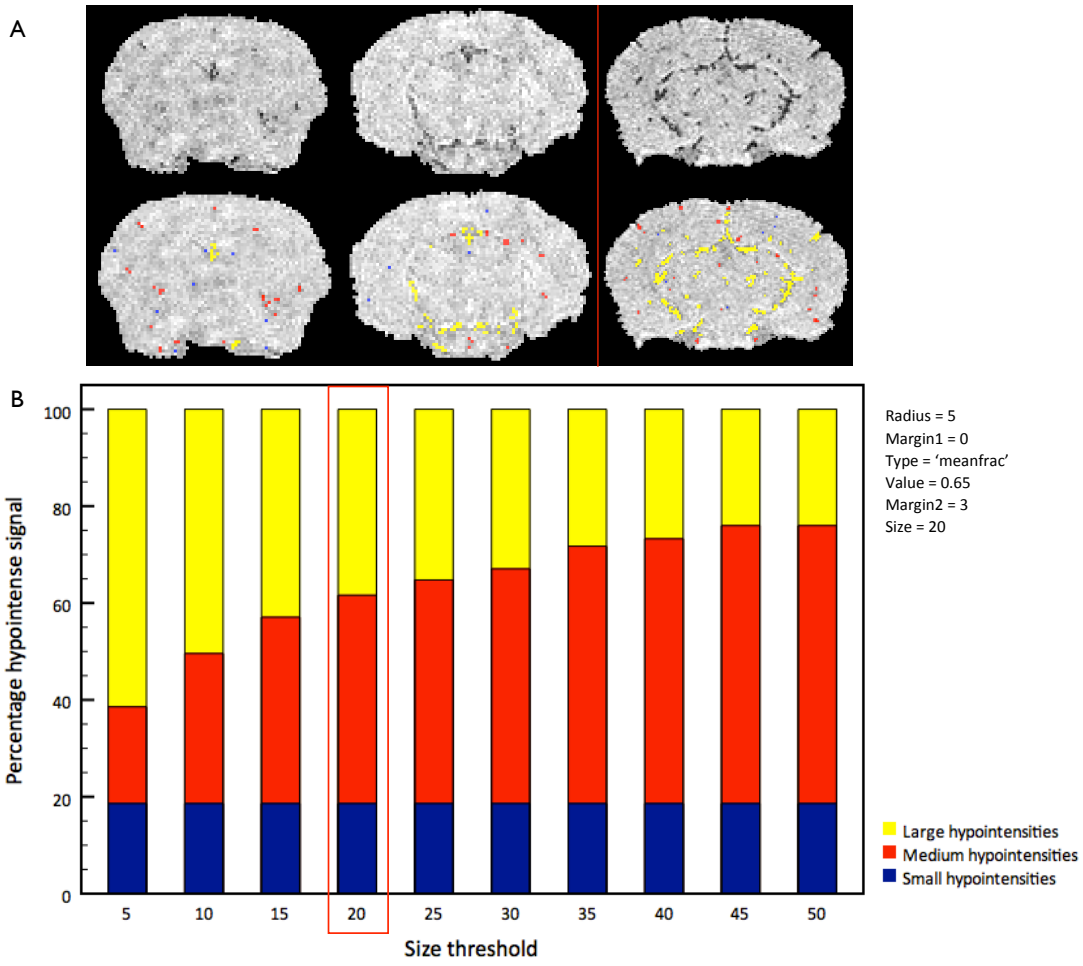


Figure 3.10 – Classification of hypointense regions by size into small (blue), medium (red) and large (yellow) hypointensities in 3 slices from a 3D dataset. (A) This classification enables differentiation between punctate hypointensities and signal derived from sinuses and ventricles, as shown in two different slices from the same brain volume (left and middle panels). Two brain volumes may also have markedly different large hypointense volumes, as shown by two slices from two brain volumes, at approximately equivalent anatomical locations (middle and right panels). These differences may arise from the pooling of de-oxygenated blood or large-scale inflammation, particularly of vessels in the choroid. (B) Small hypointensities are always defined as those of 1 voxel only and comprise approximately 20% of all hypointensities in a given brain. As the size threshold cut-off increases the proportion of medium to large hypointensities increases.

Variable	Working Value
Radius	5
Type	Fraction of the mean ('meanfrac')
Value	0.65
Margin	3
Size threshold	20

Table 3.2 – Working values for the identification of hypointense voxels in GE3D brain volumes.

3.3.2.3 Testing automated hypointensity detection using mock brain volumes

In order to test the automated approach for hypointensity detection a set of hypointensities were identified in a 'donor' brain using the automated method, each with known volume. These 'artificial' hypointensities were seeded into mock brains and the analysis was re-run to determine the volume of hypointense signal that was obtained from these mock brains. Mock brains were defined as cubes with a normal distribution of intensities and a range of global means and standard deviations. Acquired brain volumes were approximately 500,000 voxels in size. A cube with side length 79 ($\approx \sqrt[3]{500{,}000}$) was not large enough to contain some of the largest hypointensities, so mock brain volumes were specified as cubes with side lengths of 100 voxels to give a larger overall size (100^3 = 1,000,000). At low standard deviation values and high mean values the output from the unseeded mock brains was at or close to 0%, but as the mean decreased and the standard deviation increased the quantity of hypointense voxels identified by the automated method increased (Figure 3.11A & B). When artificial hypointensities were added the volume retrieved was almost exactly 100% of the volume added at low values of the standard deviation and higher values of the mean. Again, as the standard deviation increased and the mean decreased the retrieved signal returned to background levels (Figure 3.11C & D).

[PLACEHOLDER FOR FIGURE 3.11]

[PLACEHOLDER FOR FIGURE 3.11 CAPTION]

3.3.2.4 Testing automated hypointensity detection using real brain volumes

In order to test the automated analysis approach further, artificial hypointensities were seeded onto a naïve brain volume and the analysis re-run. In order to make the test as relevant as possible the naïve brain was seeded with medium sized hypointensities only, as the naïve brain already contains large hypointense signal from the sinuses and ventricles present in the brain. The volume of native hypointensities in the naïve brain, and mock hypointensities from the donor brain was known. The global mean and standard deviation of the signal intensity in donor brain was matched as closely as possible to that of the naïve brain in the first instance (donor brain: mean = 0.3000, standard deviation = 0.0478; recipient brain: mean = 0.3058, standard deviation = 0.0481). The analysis was run eight times to determine the average percentage of hypointensities returned as a proportion of the known total volume of hypointensities in the brain. An average of 98.3% of the total brain hypointensity was detected on each run (standard deviation = 0.49%, min = 97.49%, max = 98.88%) (Figure 3.12).

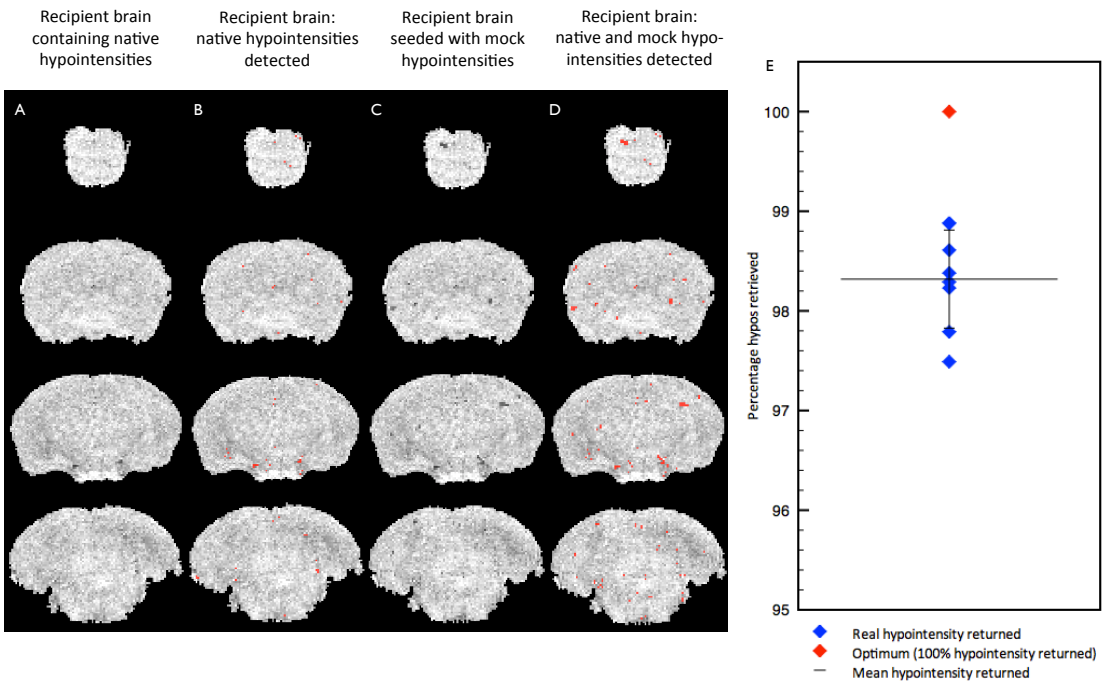
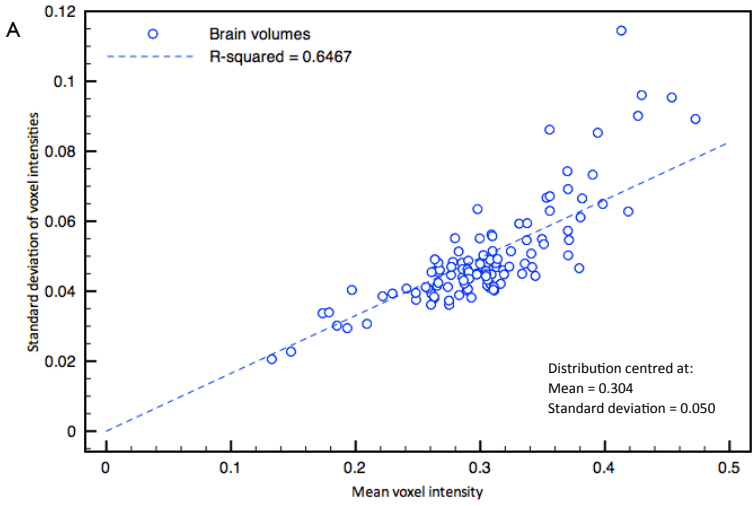


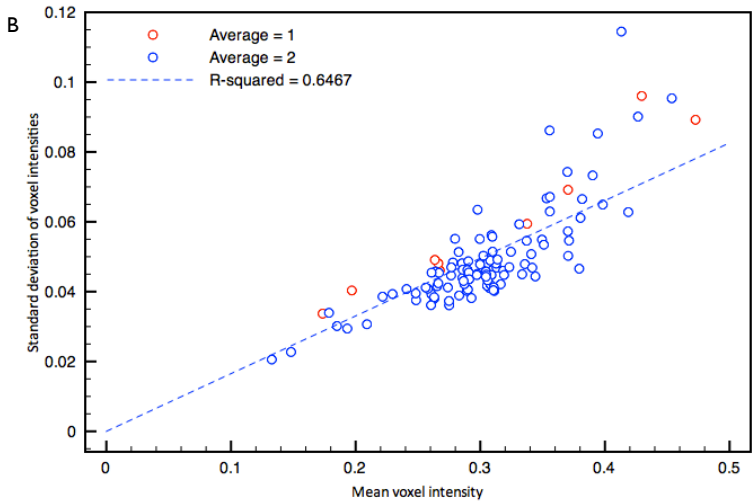
Figure 3.12 – Detection rates of artificial hypointense voxels seeded into naïve brains. Representative sections through (A) the naïve recipient brain containing native hypointensities without artificial hypointensities added, (B) the naïve recipient brain after hypointensities have been detected, (C) the naïve recipient brain with mock hypointensities added from the donor brain, (D) the naïve recipient brain after the native and mock hypointensities have been detected. (E) Graph showing the accuracy with which segmented hypointensities are retrieved from the recipient brain (mean = 98.3%, standard deviation = 0.49%, min = 97.49%, max = 98.88%).

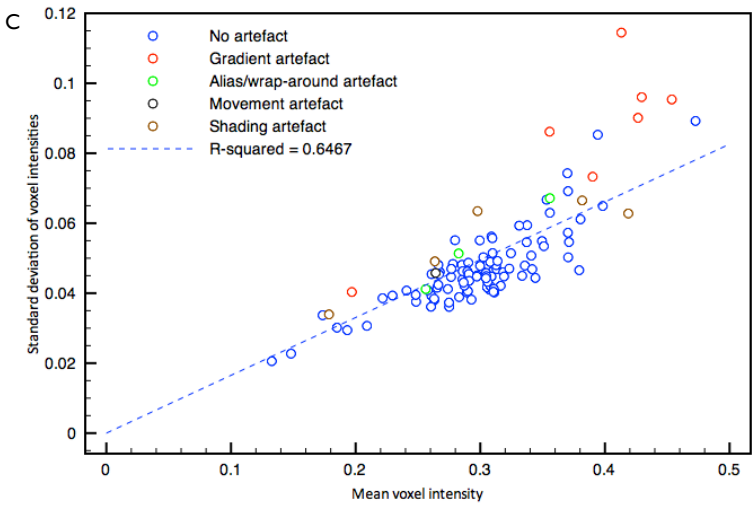
3.3.2.5 Effect of signal-to-noise ratio on analysis reliability

The mean and standard deviation of the global voxel intensities in the brain were calculated for a sample of 110 brains. These data show a cluster of means and standard deviations centred at 0.3038 and 0.0497 respectively, with an approximately linear positive correlation between the mean and the standard deviation. A departure from this linear relationship exists at values of the mean above *ca.* 0.4, with an uptick in the values of the standard deviation (Figure 3.13A). Brains that were imaged with a GE3D sequence of one average had

an elevated value of the standard deviation compared to those imaged with two averages (Figure 3.13B), possibly explaining the difference in the volume of hypointensity detected between the two groups (see Figure 3.19C). MRI artefacts were relatively common (14.5% of all brains in this sample) and increase the standard deviation of voxel intensities compared to their means (Figure 3.13C). Three of the most common artefacts are also shown in Figure 3.13D. One average scans and gradient artefacts account for six out of the seven brains in the uptick at high values of the mean voxel intensity.


A
Brain volumes
R-squared = 0.6467
Distribution centred at:
Mean = 0.304
Standard deviation = 0.050
Standard deviation of voxel intensities
Mean voxel intensity
0
0.02
0.04
0.06
0.08
0.1
0.12
0.1
0.2
0.3
0.4
0.5


B
Average = 1
Average = 2
R-squared = 0.6467
Standard deviation of voxel intensities
Mean voxel intensity
0
0.02
0.04
0.06
0.08
0.1
0.12
0.1
0.2
0.3
0.4
0.5


C
No artefact
Gradient artefact
Alias/wrap-around artefact
Movement artefact
Shading artefact
R-squared = 0.6467
Standard deviation of voxel intensities
Mean voxel intensity
0
0.02
0.04
0.06
0.08
0.1
0.12
0.1
0.2
0.3
0.4
0.5

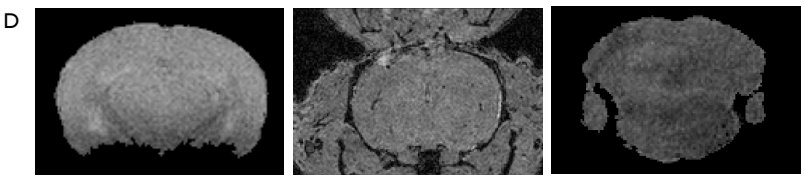

D

Figure 3.13 – Global intensity values for brain volumes. (A) A sample of 110 brains used throughout this thesis shows a distribution clustered around a mean of 0.304 and standard deviation of 0.050. (B) Imaging of brains using a one average scan (red circles) gives a dataset that has a similar spread of mean values, but a general increase in the standard deviation. (C) Artefacts in the brain image can also cause an increase in the standard deviation. (D) Three of the most common are shown on the right hand side: gradient (left panel), alias / wrap-around (middle) and shading (right).

3.3.2.7 Comparison to the operator-dependent approach

Comparing data from nine mouse brains that were independently analysed by the operator-dependent method and the automated method suggests that the two approaches are well aligned to one another (Pearson's $\rho = 0.6612$, $p = 0.0525$) (Figure 3.14). There does not appear to be a systematic positive or negative discrepancy between the two approaches and the ranked volumes of hypointensities recorded are fairly well maintained. These findings suggest that the automated method developed here is capable of achieving a similar quality of analysis to the operator-dependent method with several substantial advantages. These advantages are a decrease in the time taken to perform the analysis, and a reduction in the inter- and intra-operator bias. Brain volumes can also be re-analysed using different variable values to extract different features, making the automated method a more flexible approach.

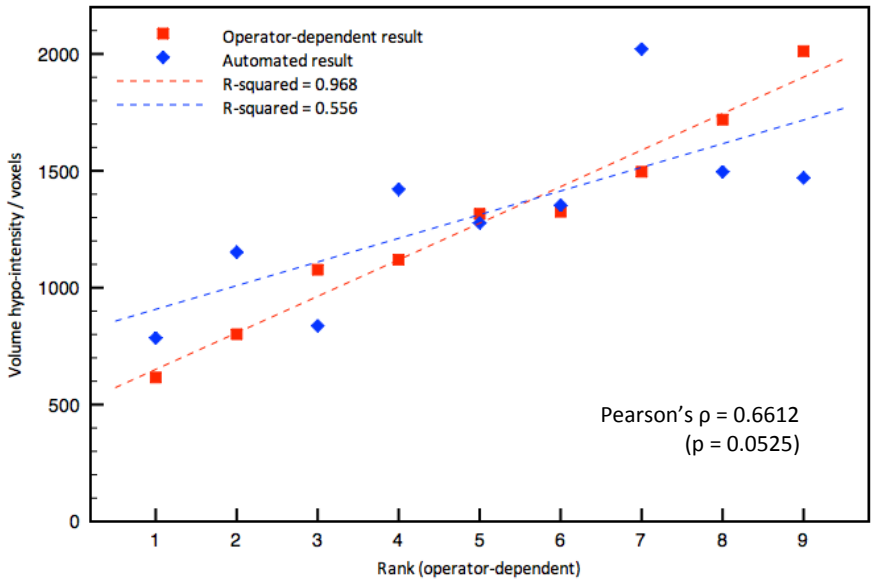


Figure 3.14 – Hypointensities detected by the automated approach as compared to the operator-dependent approach. Data are ranked according to the operator-dependent approach (red squares) and the equivalent automated results are shown (blue diamonds).

3.3.2.6 Analysis of a human brain

A human brain had previously been imaged using a Siemens 3 T clinical scanner using modified GE3D acquisition parameters (1.0 mm^3 voxels, TE = 17.5 ms (7.5 ms at 7 T), TR = 50 ms (65 ms at 7 T), flip angle = 27°, and bandwidth = 200 Hz/pixel, one average, scan time = 9.5 mins). The data from this brain were compared to those from the mouse brains to appreciate the differences in voxel intensity distribution and to determine the robustness of the automated approach. The global voxel intensity characteristics of the human brain differ from those of the mouse brains analysed. The global distribution is a slightly different shape to that of a mouse brain, with a mild negative skew (Figure 3.15A). The human brain has a slightly lower mean value than the majority of the mouse brains (0.185 as opposed to 0.304) and a slightly greater standard deviation (0.054 as opposed to 0.050) (Figure 3.15B).

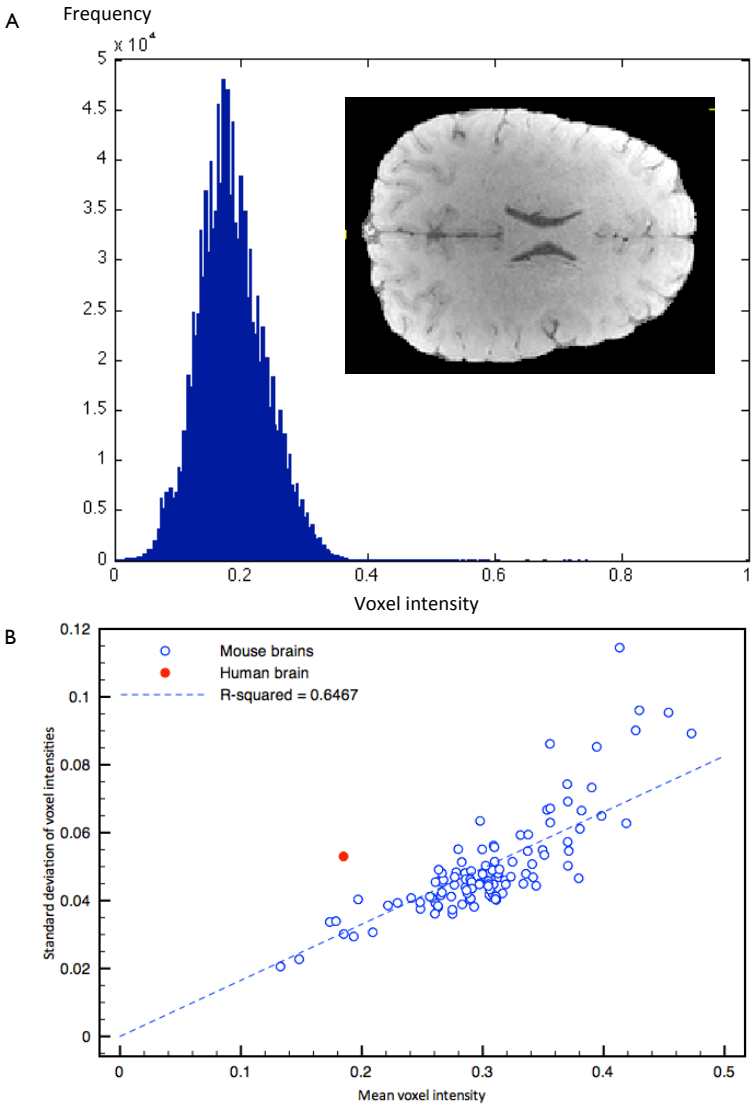


Figure 3.15 – Mean and standard deviation of a human GE3D scan. (A) Global distribution of voxel intensities in a human brain. The distribution is approximately normal, with a slight negative skew and positive kurtosis. A representative axial slice is shown (insert). (B) Distribution of mouse brain mean and standard deviation voxel intensity values (blue circles), showing the values of the human brain by comparison (mean: 0.185, standard deviation: 0.054).

The global intensity characteristics of the human brain appear close enough to those of the mouse brains that the same method was used to find hypointensities in a normal human

brain (Figure 3.16). This method returned a sizeable volume of large hypointensities associated with the ventricles and the sulci. The parameters for the analysis will likely require modification to account for the structural differences between the human and mouse brains.

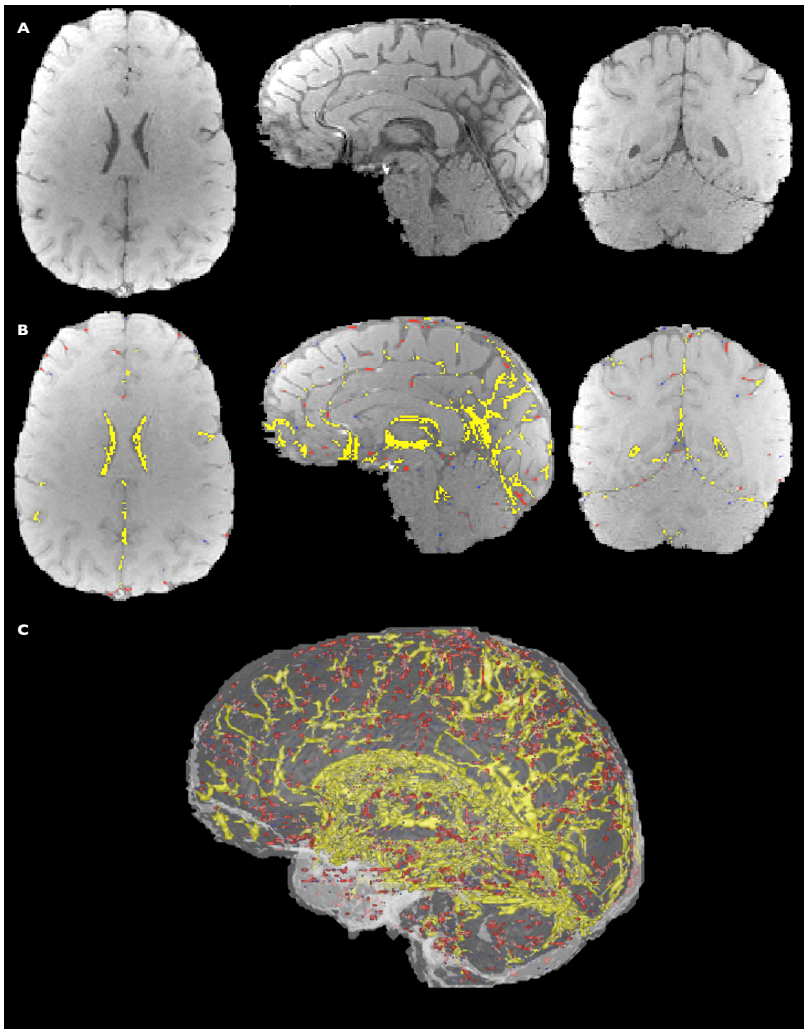


Figure 3.16 – Automatic hypointensity analysis of a human brain. (A) Representative axial, sagittal and coronal sections through a human brain. (B) The same images following hypointensity analysis using the same variable values as set out in Table 3.3. (C) 3D reconstruction.

3.3.3 Filtering procedures

One problem with the colocalisation data presented was the rate of false positives in the data, i.e. manually detected hypointensities in an MRI dataset that did not correlate with the locations of metastases (Figure 3.4B). In an attempt to reduce the number false positives in the MRI data certain mean and median filtering methods were used, as described below.

Mean filter

Hypointense voxels in the MRI brain volume may be caused by transient arrest of VCAM-MPIO in blood vessels not associated with metastatic lesions. Thus, a hypointensity detected during a single scan may either be derived from transient arrest or VCAM-MPIO binding to endothelial VCAM-1. Some animals underwent two 40 min GE3D scans (2 averages each scan). Other animals were scanned twice for 20 min (1 average each scan), and then for a further 40 min (2-average) scan (Figure 3.18). If we observe two instances of VCAM-MPIO binding at the same location in sequential MRI scans it is more likely that this represents valid binding of VCAM-MPIO to blood vessels at sites of endothelial VCAM-1 expression. Therefore, I tested the hypothesis that repeat scanning of the brain may enable identification of 'true' hypointensities compared to 'false' hypointensities that are only present in one of the two scans (Figures 3.18 and 3.19).

In order to compare hypointensities in sequential scans, a mean filter was passed over pairs of GE3D datasets (Figure 3.17 and Table 3.3) and the automated hypointensity analysis was run on both of the input datasets and the output dataset from the mean filter. The standard 2-average GE3D sequence takes two averages of the data, i.e. runs the same scan twice and sums the data. This sequence has a sufficient signal-to-noise ratio (SNR) to detect MPIO-derived hypointensities, as already demonstrated in this chapter, and repeat scanning using this sequence comes at the cost of doubling the acquisition time (Figure 3.17A). In order to

test the potential benefits of a mean filter without increasing the overall acquisition time, two 1-average GE3D sequences were also obtained, and the mean filter was passed over each of the input datasets. A further mean filter was passed over the outputs of a 1-average and a 2-average scan (Figure 3.17B).

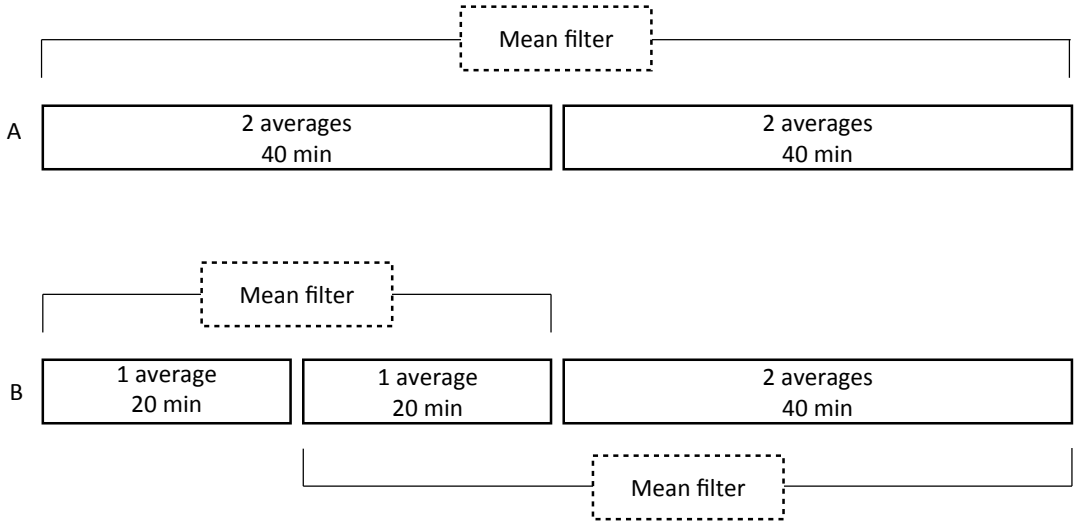


Figure 3.17 – Imaging and filtering protocols. (A) Animals were imaged with two 2-average scans. A mean filter was passed over the pair of scans (Figure 3.18). (B) Certain animals were imaged with two 1-average scans and a further 2-average scan. Mean filters were passed over the first and second pair of scans. A further mean filter was passed over all three scans (Figure 3.19).

Median filter

An alternative approach to improve detectability of the 'true' hypointensities and reduce false positives was to use a median filter, which smoothes the data and allows noise reduction in the image, such as noise associated with MR image acquisition. The filter can be passed over as large or as small a region as desired; the larger the region the greater the

level of smoothing of the original image. All median filters used in these analyses were 1-pixel 2-dimensional filters.

Datasets used	Total averages in datasets	Filter	Total averages in filters
1 avg.	1	NONE	0
2 avg.	2	NONE	0
1 avg.	1	Median	1
2 avg.	2	Median	1
1 avg. + 1 avg.	2	Mean	1
1 avg. + 2 avg.	3	Mean	1
2 avg. + 2 avg.	4	Mean	1
(1 avg. + 1 avg.) + 2avg.	4	Mean – Mean	2

Table 3.3 – The tested combinations of datasets for increasing the SNR in GE3D datasets. Singleton scans of either one or two averages were not filtered or smoothed using a median filter. Pairs of scans were treated using a mean filter as per Figure 3.17. Pairs of 1-average scans were followed by a 2-average scan; the mean filter from the first pair and the 2-average scan were also treated using a mean filter.

A specific hypointensity that exists in two sequential scans is said to be conserved (Figure 3.18A, columns 1 & 2), whereas a hypointensity that is present in one scan and absent in the next has not been conserved (columns 3 & 4). The effect of running a mean filter over two scans may be the maintenance or deletion of hypointensities. Conserved hypointensities are almost always maintained as a result of mean filtering (Figure 3.18B, columns 1 & 2), whereas non-conserved hypointensities may either be maintained (column 4) or deleted (column 3). The effect is an overall reduction in the total hypointense signal detected in the brain, especially the small hypointensities (Figure 3.18D). By comparison, the median filter is

much more deleterious of hypointensities, and conserved hypointensities can be deleted (Figure 3.18C, column 1), as well as non-conserved hypointensities (columns 3 & 4). The result is a large decrease in the hypointense signal obtained across all sizes of hypointensities (Figure 3.18D). These results were obtained from a single animal so it is not possible to draw definite conclusions from these data. However, it would appear that mean filtering of data is a sensible approach for deleting non-conserved hypointensities, which may potentially reduce the number of false positive hypointensities, while maintaining conserved hypointensities. By comparison, median filtering appears to be too deleterious of conserved hypointensities to be a useful approach for trying to eliminate false positive hypointensities.

Repeat scanning using 1-average scans followed by mean filtering is presented in Figure 3.19. In a similar fashion to the data presented in Figure 3.18, conserved hypointensities are maintained by mean filtering, while non-conserved hypointensities are either maintained or deleted. Greater hypointensity volumes were recorded in each of the 1-average scans compared to the 2-average scan (Figure 3.19C), which may reflect unsuitable parameter values for use with 1-average scans compared to 2-average scans. However, the effect of mean filtering over two 1-average scans results in a dataset that has lower recorded hypointensity levels than the 2-average scan, suggesting that this approach may be ideal for reducing the detection of false positive hypointensities, without increasing the overall scan time. Mean filtration over one 1-average and one 2-average scans has a high level of recorded hypointensity compared to the 2-average scan alone, and mean filtration over all three scans, although reducing the hypointensity volume recorded, requires a doubling in overall scan time. Although these results were obtained from a single animal, it would appear that repeat 1-average scanning followed by mean filtration is a sensible approach to

follow for reducing the volume of hypointensities detected, without any consequent increase in overall acquisition time.

[PLACEHOLDER FOR FIGURE 3.18]

PLACEHOLDER FOR 3.18 CAPTION

[PLACEHOLDER FOR FIGURE 3.19]

[PLACEHOLDER FOR 3.19 CAPTION]

3.4 Discussion

The work presented in this chapter sought to determine the level of colocalisation between MRI hypointensities, metastases and VCAM-1 expression, the development of a novel method for automated hypointensity detection and use of image filters to reduce the potential number of false positive hypointensities.

3.4.1 Colocalisation

The colocalisation studies detected VCAM-1 expression on tumour-associated vasculature in the majority of tumours above *ca.* 0.001 µL in volume, and the presence of VCAM-1 expression above this size was well correlated with tumour detection determined by VCAM-MPIO hypointensity (Figure 3.4). This represents a significant improvement in the detectability of tumours when compared to clinical techniques currently used in patients. Not only was there no gadolinium contrast visible in these brains, but the size of tumour detected is approximately four orders of magnitude smaller than the limit of detection in humans. Even taking into account the greater resolution available when scanning for 40 minutes at a 7 T field strength, the use of this targeted contrast agent improves the limit of detection approximately ten-fold (Serres et al., 2012).

One unanswered question arising from these data is the finding that there were hypointensities in the GE3D dataset that were not associated with VCAM-1 expression. There are several possible explanations for this disparity. Firstly, variable quality in antigenic presentation within tissue sections can lead to concomitant quality in immunohistochemical staining and may have prevented confirmation of VCAM-1 expression at the tumour site. Secondly, microscopy sections were also used for VCAM-1 staining every 30 µm, leaving a gap of 20 µm between each tissue section where VCAM-1 expression may have gone undetected. Thirdly, background signal in the MRI data, similar to that seen in naïve animals

injected with VCAM-MPIO, may have suggested colocalisation where none was in fact present. This possibility led to the use of image filters to attempt to remove some of the noise and improve the colocalisation of hypointensities and metastases (see Section 3.4.3).

3.4.2 Analysis automation

As imaging techniques have become more refined there has been an increasing need to define objects and features within images to facilitate diagnosis, surgical intervention and therapy monitoring (Kundel, 2006), to aid in identifying structural and functional impairment of tissues and organs, and to provide information relating to pathology. In image analysis terms the structures in question are often curvilinear, that is to say, made up from or bounded by a set of curved lines. A variety of structures within the body can be described as curvilinear. These include the bronchial tree, the biliary and pancreatic ducts and networks of blood vessels, all of which are structures often associated with pathology. Imaging these structures is crucial for diagnosis, treatment and surgical intervention (Kikinis et al., 1996; Chabrerie et al., 1997, 1998; Nakajima et al., 1997; Sato et al., 1998; Lin et al., 2009; Zudaire et al., 2011; Golby et al., 2011; Kim et al., 2011; Pathak et al., 2011; Zamani Boroujeni et al., 2012; Pu et al., 2012). As imaging techniques and standards have improved, reliable extraction of such structures has become ever more important. The improvements in 3D imaging modalities have driven progress in extraction of 3D curvilinear structures, one example of which is the vascular map generated by Pathak et al. (2011) with µMRI. This approach used a 'tubeness' filter that was generated from the eigenvalues of the Hessian matrix at each voxel, and allowed the authors to extract the sizes of vessels within the brain from their data. However, the diffusion tensor imaging (DTI) data used was obtained from an *ex vivo* sample perfused with Microfil®, at a resolution of *ca.* 30 µm. In contrast, in the *in vivo* model used for this study the obtainable resolution was lower, *ca.* 88 µm, and the data had a lower signal-to-noise ratio (SNR) than in those previous studies. Furthermore, not all

of the signal effects generated by MPIO in the brain are shaped like a tube; some of the hypointensities are punctate and, therefore, not necessarily retrievable by the technique of Pathak et al. (2011). Consequently, rather than emulating the method outlined above, I decided to approach the problem using a local statistical determinant of hypointense voxels instead.

Compared to the manual approach that had previously been used, the automated approach had several advantages as listed below:

1 Once a suitable set of variable values are chosen, the only manual step of the automated approach is the masking of the brain volume in ITK-SNAP. This increases the speed and reproducibility of the analysis and reduces inter- and intra-operator variability.

2 As long as the SNR is adequate, the automated approach is able to reliably detect hypointensities using one set of variable values for the whole brain volume. This reduces any systematic bias introduced in the operator-dependent approach.

3 The automated approach provides a flexible platform for analysing a range of image types and signal types and could alternatively be used to identify hyperintense regions of the brain or other organs if required.

4 The automated approach is able to make distinctions between hypointensities based on size, yielding a classification of different signals. This classification enables investigation of treatment effects on smaller punctate signals and larger ventricle- and sinus-associated signals.

There are several refinements that could be made to improve the performance of the automated approach. Firstly, the development of algorithms for automatic brain segmentation could potentially improve the speed of analysis, the quality and standardisation of the segmentation, and therefore the quality of the data output from the analysis. Secondly, an adaptive value for the test statistic could improve the detection of hypointensities in regions of the brain with different regional contrast levels. This second refinement will be discussed in more detail in light of results presented in the next chapter.

3.4.3 Image filtering

The image filters described in this chapter were quick and easy to implement and seemed to show some efficacy in reducing the quantity of noise in the MRI data, maintaining some hypointensities and deleting others. The initial premise for this work was that transient non-specific binding or arrest of MPIO in cerebral blood vessels could cause unwanted hypointensities that would contribute to the false positive rate. Identification of the same hypointensity in two consecutive scans would suggest that the signal was derived from specific binding of VCAM-MPIO at sites of VCAM-1 expression. Thus, the image analysis techniques developed were required to maintain the signal from conserved hypointensities while discriminating against non-conserved hypointensities.

The potential advantage of the spatial median filter was to reduce unwanted noise that may otherwise have been recorded as hypointense. However, even a low power 2D 1-pixel median filter appeared to smooth the data too heavily and deleted a large volume of hypointensity from the brain volumes, thus discarding what appeared to be 'real' signal. Therefore, this choice of image filtering was not pursued further. In contrast, temporal mean filtering improved the SNR of the data, maintaining conserved hypointensities and deleting some of the non-conserved hypointensities (Figure 3.18). Furthermore, running the mean

filter over two 1-average datasets appeared to improve the image quality without an increase in overall scan time (Figure 3.19), suggesting that this may be a preferred protocol for future imaging of MPIO-contrasted brains.

Although the data presented is promising, more work is required to verify that an improvement has been made in the ability to detect VCAM-1 expression at the site of metastasis using these filtered datasets.

3.4.4 Concluding remarks

In conclusion, I have shown that VCAM-MPIO-derived hypointensities in MRI datasets frequently colocalise with VCAM-1 expression at the sites of larger brain metastases in experimental animals. However, in some cases hypointensities do not correspond to sites of metastasis in the brain, likely reflecting transient non-specific binding or arrest of VCAM-MPIO in cerebral blood vessels. In order to address this issue I have presented two methods, one for the automated detection of hypointensities in brain volumes, and the other an image filtering technique to reduce the numbers of false positive hypointensities.

The automated method has proved to be a robust approach for reliably and reproducibly detecting hypointensities in T2*-weighted brain MRI datasets, using a statistical method based on local contrast levels. It is flexible and can easily be adapted for use with other datasets. Once a suitable set of variable values has been chosen, the automated method provides a standardised, unbiased analysis technique, making it a useful tool for a variety of MRI protocols. Image filtering techniques also appear to aid in the detection of 'real' hypointensities that are conserved between two sequential GE3D datasets. Furthermore, the improvement in image quality and potential reduction in false positive hypointensities as a result of temporal mean filtering come at no apparent cost to overall acquisition time.

Further work is warranted to validate the improvements offered by the automated method and image filtering that relate these techniques to the correspondence between hypointensities and VCAM-1 expression at the site of metastasis.

Chapter 4

Development of 4T1-GFP metastases in the brain

4.1 Introduction

In the previous chapter the intravascular contrast agent, VCAM-MPIO, was used to detect increased expression of VCAM-1 on brain endothelium at tumour sites and new methods were developed by which such co-localization could be improved using an automated approach for hypointensity detection, and image filtering. In this chapter I will describe the development, both spatial and morphological, of cerebral tumours ten days post-intracardial injection of 4T1-GFP cells.

The 4T1 cell line is derived from the spontaneously arising 410.4 mammary adenocarcinoma, first isolated in an MMTV+ BALB/c mouse (Dexter et al., 1978; Pulaski and Ostrand-Rosenberg, 2001), and was selected based on its resistance for its resistance to 6-thioguanine. The 4T1 model is highly tumorigenic and can spontaneously metastasize from a transplanted primary tumour in the breast fat pad, as well as by direct injection into the bloodstream (Lorger and Felding-Habermann, 2010; Serres et al., 2012; Balathasan et al., 2013). 4T1-GFP cells used in these studies had previously been stably transfected with pEGFP-C1 (Clonetech, St. German-en-Laye, France).

4.1.1 Tumour development

The development of brain metastases, like tumours in other organs, depends largely on the interplay between tumour cells and the cellular and extracellular components of the tumour microenvironment. Some tumours are more likely to metastasise to the brain than others, in particular lung, breast and melanoma primaries. These results suggest that specific signalling processes take place between tumour cells and the local endothelium, allowing cells to extravasate and proliferate to form metastases (Fidler et al., 2002). This is the basis for the seed and soil hypothesis, first put forward by Paget in 1889. Moreover, not only are there differences in the initiation of metastases between the brain and other organs, but within different regions of the brain itself. Previous studies have shown that certain sites within the brain appear to have a greater chance of metastatic development than others, with a greater propensity of 231-BR cells to metastasise to the parietal cortex and frontal cortex than the basal ganglia or the hypothalamus (Fitzgerald et al., 2008). These results suggest that metastatic cells encounter different environments within different regions of the brain, affecting their development. If this is the case then a non-uniform distribution of 4T1-GFP metastases across the brain is expected, and if the model of VCAM-MPIO detection of brain metastases is robust, a similar distribution of hypointensities should be found.

Furthermore, differences in development arise from the high level of vascularisation in the brain. In order to maintain an adequate supply of oxygen and nutrients, tumours in many other organs require the growth of new blood vessels, a process known as angiogenesis. However, the Mel57 metastatic melanoma lines in the brain have been shown to develop without the use of new vasculature, but are instead able to use the existing vasculature in order to supply the oxygen and nutrients required for their own growth. This feature of tumour growth is known as vascular co-option, a feature first observed in the brain (Leenders et al., 2002). Moreover, Mel57 metastases showed a markedly different

morphology from those that had been transfected with VEGF-A (Küsters et al., 2002), demonstrating that angiogenic and vascular co-optive strategies are two distinct developmental characteristics of brain metastases.

The experiments presented in this chapter use the 4T1-GFP cell line to investigate the normal development of brain metastases and compare developmental characteristics in different brain regions.

4.1.2 Vascular labelling

One of the questions raised in this chapter focuses on the role that different parts of the vasculature play in the development of brain metastases. As discussed in the introductory chapter (Section 1.2), the location of metastatic lesions from a given primary tumour is non-random. Previous studies suggest that arrest, survival and proliferation at a distant site may be controlled by a set of signals between circulating metastatic cells and endothelial cells of the target organ, rather than a purely hit-and-miss mechanical arrest of tumour cells in the vasculature leading to tumour development (Paget, 1889; Sugarbaker, 1979; Hart and Fidler, 1980; Tarin et al., 1984a, 1984b; Schackert and Fidler, 1988; Weiss, 2000; Fidler, 2003). Lorger and Felding-Habermann (2010) have recently described the interactions between circulating metastatic cells and the microstructure of the capillary bed, demonstrating that tumours extravasate in brain capillaries or post-capillary venules, to the exclusion of pre-capillary arterioles. Therefore, we might predict that the arrest of metastatic cells in the vascular bed may be controlled by the type of blood vessel they encounter, whether an afferent arteriole, the capillary bed or an efferent venule. Immunohistochemically it is possible to differentially stain these vessels using α-smooth muscle actin αSMA as an arterial marker (Price et al., 1994; Owens, 1995), and EphrinB4 (EphB4) as a venous marker (Wang et al., 1998; Kudo et al., 2007; Taylor et al., 2007; Kume, 2010).

αSMA is one of six actin isoforms, all of which are involved in cell structure and motility. αSMA is expressed by vascular smooth muscle cells in arteries and arterioles (Gabbiani et al., 1981) and by pericytes in the capillaries (Herman and D'Amore, 1985; Skalli et al., 1989), allowing contractile control over blood flow (Fernández-Klett et al., 2010). The brain vasculature has the highest number of pericytes of any organ in the body (Shepro and Morel, 1993), although different vessel morphology and differential αSMA expression patterns between arteriolar smooth muscle cells and pericytes has made it a reliable marker for arteriolar blood vessels in previous experiments (Lorger and Felding-Habermann, 2010; Sato et al., 2011).

The Ephrins (Eph) are the largest family of receptor tyrosine kinases, whose ligands are the ephrins (eph) (Hirai et al., 1987). Rather than binding soluble factors, Ephrins bind cell surface ligands, allowing an inside-out as well as an outside-in signalling exchange. Ephrin receptor-ligand interactions are involved in the differentiation of vascular identities between arteriolar and venous blood vessels (Wang et al., 1998; Kudo et al., 2007; Taylor et al., 2007; Kume, 2010). The Ephrins and their receptors have also been shown to affect the functional development of new blood vessels and EphB2 and EphB4 are expressed preferentially on arterioles and venules respectively in malignant and metastatic tissues during angiogenesis (Huang et al., 2007; Zhang et al., 2007; Ozgür et al., 2011).

By identifying arterial and venous regions of the cerebral vasculature associated with tumour development my aim was to confirm the observations made by Lorger and Felding-Habermann (2010) that tumour cells preferentially extravasate in the post-capillary venules.

4.1.3 Outstanding questions

The syngeneic 4T1-BALB/c tumour model used in these experiments has been studied before in the brain by Lorger and Felding-Haberman (2010). Their experiments introduced 4T1-GFP cells via injection into the internal carotid artery. This procedure is highly invasive and would initiate an inflammatory response, thus possibly altering the immune status of the animal and the characteristics of tumour cells in circulation. The experiments presented in this chapter aim to replicate the data in Lorger and Felding-Habermann (2010), instead using a less invasive intracardial injection model to administer the cells into the systemic circulation.

The dissemination of metastases to the brain has also been studied in xenograft systems, including the Mel57 human melanoma cell line (Küsters et al., 2002; Leenders et al., 2002, 2004) in relation to their level of vascular co-option, and the MDA-MB-231-BR human breast cancer cell line (Fitzgerald et al., 2008) in relation to glial activation. Fitzgerald et al. (2008) also presented data showing the distribution of metastases in different brain regions with their tumour model. The data presented reported on the frequency at which metastases were found to be present or absent within different brain regions. However, this may be an oversimplification of the real dynamics of metastatic dissemination within the brain. Thus, I aim to present a more detailed analysis using the syngeneic 4T1-BALB/c tumour model.

Thus, the experiments presented in this chapter sought to test the hypotheses:

1 That the automated detection of VCAM-MPIO hypointensities from GE3D MR datasets is a good predictor of tumour location within the brain.

2 That the distribution of 4T1-GFP metastases is not uniform i.e. metastases locate preferentially to certain brain regions, as per Fitzgerald et al. (2008).

3 That the growth patterns of metastases, as determined by their morphology, differ between brain regions.

4 That metastases preferentially develop on venous blood vessels over arteriolar blood vessels, as per Lorger and Felding-Habermann (2010).

4.2 Methods

4.2.1 Animal model

Female BALB/c mice aged 7-10 weeks were intracardially injected with 1×10^5 4T1-GFP cells in 100 µL PBS, and were imaged 10 days later (Figure 4.1, see Section 2.1). The animals were killed after imaging by perfusion/fixation with 0.9% heparinised saline and PLP_{light}, and the brain dissected out for immunohistochemical and immunofluorescent staining.

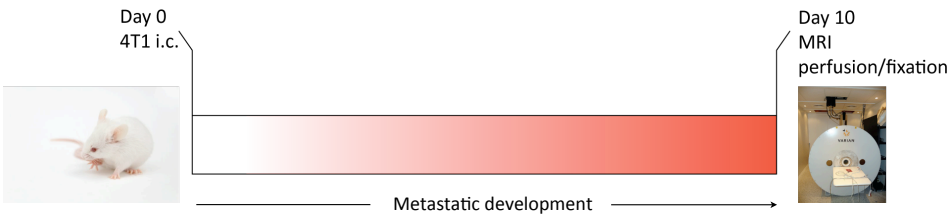


Figure 4.1 – Experimental schedule. Metastatic lesions were allowed to develop for 10 days following intracardiac injection before the animals were imaged and perfused/fixed.

4.2.2 MRI

Animals were injected with VCAM-MPIO (4 mg Fe/kg) (Section 2.3.5) in 100 µL sterile saline 1 h prior to imaging and the tail vein cannulated immediately prior to imaging. Animals were imaged at 7 T under isoflurane anaesthesia in 50:50 O_2:N_2. For detection of VCAM-MPIO, a T_2^*-weighted 3D gradient echo dataset was acquired. T1-weighted pre- and post-Gd datasets

were acquired to identify BBB breakdown, and a T2-weighted dataset to aid colocalisation of metastatic lesions and hypointensities. Total imaging time was approximately 1-1.25 h per animal.

4.2.3 Immunohistochemistry / immunofluorescence

Animals were perfused/fixed in heparinised saline and PLP_{light}. Brains were cryoprotected in 30% sucrose and rapidly frozen in Tissue Tek® before being cut on a cryostat. Sections were either DAB stained immunohistochemically for GFP to locate and characterize metastatic lesions in the brain, or stained immunofluorescently to colocalise VCAM-1, αSMA or EphB4 expression with GFP expression on tumours (Section 2.3.6).

4.2.4 Immunocytochemistry

Immunocytochemistry (Section 2.3.7) was performed on 4T1-GFP cells to visualise expression of EphB4 or αSMA and imaged using an InCell Analyser (Section 2.2.10).

4.2.5 Analysis tools

GE3D datasets acquired from MRI were analysed using ITK-SNAP (Yushkevich et al., 2006) and MATLAB, as described in the previous chapter. Briefly, NIfTI files were constructed from GE3D datasets and masked in ITK-SNAP to extract the brain volume. The NIfTI file and mask were analysed using MATLAB to determine the location of hypointensities in the brain based on statistical differences in voxel intensity between a central voxel and its local distribution. Analysis returned a total volume and number of hypointensities recorded, classified by size, and a new NIfTI file showing the locations of hypointensities that could be overlaid on top of the original brain volume in ITK-SNAP.

Immunohistochemical slides were photographed using an Aperio slide scanner, and the images viewed in Aperio ImageScope (Section 2.3.9). Metastatic lesions were identified by eye on the basis of GFP expression, or by morphology if GFP expression levels were low. Tumour characteristics (volume, range, number of objects, sphericity) were measured by hand.

Positively stained sections using immunofluorescence techniques were photographed using a digital camera mounted on a Leica epifluorescent microscope. VCAM-1, αSMA and EphB4 expression at the tumour site were determined to be present or absent after imaging all sequential sections of the same tumour.

4.2.6 Statistics

The statistics employed in the identification of hypointensities in GE3D datasets are described in the previous chapter. The two other statistical analyses performed in this chapter used Excel for the calculation of 95% confidence intervals (Figure 4.2 & 4.3), and MATLAB for performing 1-way analysis of variance or Kruskal-Wallis non-parametric tests (Section 2.3.10).

4.3 Results

Brain tissue cut from five coronal sections along the AP axis of the brain was analysed for metastases. The most caudal section was cut at *ca.* Bregma –6.72 mm and the most rostral at *ca.* Bregma +2.34 mm. The sections, their locations and the specific brain regions contained within each are listed in Table 4.1.

Section name	Section location	Regions contained
Cerebellar	Bregma – 6.72	Medulla Cerebellum
Collicular	Bregma – 4.84	Posterior cortex Midbrain
Hippocampal	Bregma – 2.18	Parietal cortex Hippocampus Thalamus & hypothalamus
Striatal	Bregma + 0.5	Corpus callosum Cortex Caudate putamen Septum & basal ganglia
Olfactory bulb	Bregma + 2.34	Olfactory bulbs Frontal cortex

Table 4.1 – Brain section names, locations and specific brain regions contained within each.

4.3.1 Correlation between metastatic loci and hypointensities in the brain

The five brain sections sampled were analysed immunohistochemically for the number of tumours and the overall volume of tumours (otherwise referred to as the metastatic burden) they contained, and the total volume of hypointensities as determined by using the automated approach. This analysis tested whether the distribution of metastases and hypointensities across the brain was uniform across all brain sections or whether certain brain sections showed an increase or decrease in the number or volume of metastases compared to a uniform distribution, when weighted for the cross-sectional area of the section. Thus, for the five brain sections analysed, a uniform distribution would expect 20%

of the total tumour number and volume to be found in each brain section. The number or volume of metastases within a given brain section was deemed to be significantly different from expected if the expected value fell outside the 95% confidence interval of the observed value (Figure 4.2). The volume of hypointensities was analysed in the same way, and its distribution was compared to the number and volume of hypointensities in each region in order to determine whether the hypointensity volume could be used as a good predictor of the number or volume of metastases in each of these sections.

The number of metastases was roughly uniform across the five brain sections sampled, with the exception of the olfactory bulb section, which contained a significantly greater number and volume of metastases than the expected value. By contrast, the total metastatic burden was depressed in the cerebellar, collicular and striatal sections. Neither of these distributions appeared to match the highly non-uniform distribution of hypointensities across the five brain regions, which was elevated in the cerebellum and showed a marked decline rostrally along the AP axis of the brain (Figure 4.2). This effect is probably due to a reduction in the MRI signal quality towards the posterior of the brain leading to a larger volume of detected hypointensities (Figure 3.5).

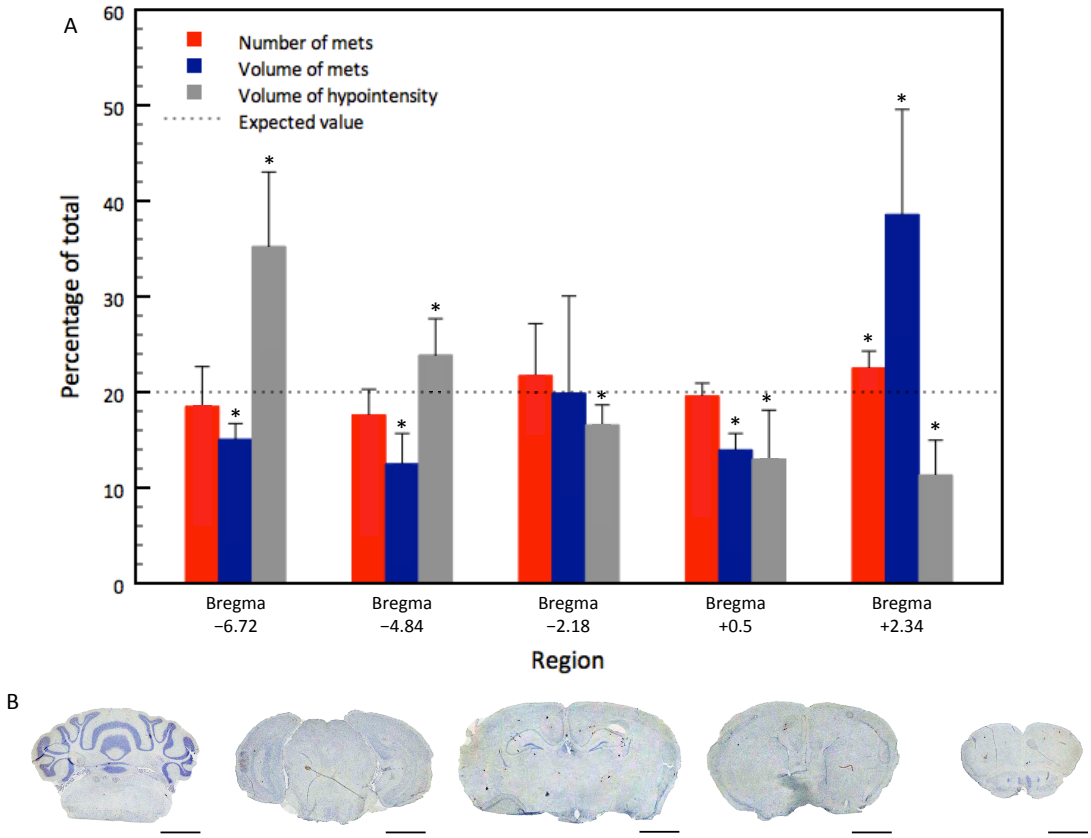


Figure 4.2 – The distribution of metastases and hypointensities across the brain (n=4). (A) The number of metastatic lesions (red bars) is approximately uniform across different brain regions when weighted for the cross-sectional area, with a small, but significant increase in tumour number at Bregma +2.34. The volume distribution (blue bars) is less uniform with significantly less tumour volume at Bregma –6.72, Bregma –4.84 and Bregma +0.5, and significantly more at Bregma +2.34. The distribution of hypointensities is distinctly non-uniform and they are heavily weighted towards the posterior of the brain. Significance was assigned if the expected value of 20% lay outside the 95% confidence interval for each group. (B) Representative images of the five coronal brain slices used, obtained from the Aperio ScanScope CS. Scale bars represent 2 mm.

4.3.2 Relative abundance of tumours across brain regions

The analysis above presented tumour numbers and volumes with respect to overall brain sections, as defined by a specific coronal slice anterior or posterior to Bregma. This analysis is useful to compare the hypointensities within a given overall brain area to the number and volume of tumours contained within that section (Figure 4.2). However, a more precise count of tumours at specific anatomical locations within the brain is needed to draw conclusions about their likelihood to extravasate and proliferate in different vascular beds (Figure 4.3). The numbers of tumours in a given brain structure was counted and weighted for the size of that structure, and the relative abundances were calculated. From this data it appears that the majority of brain regions have a relative tumour abundance that is close to an expected value of 1, with only three regions that showed significant differences in tumour abundance. The posterior cortex showed a significantly greater tumour abundance, compared to the expected value, while the tumour abundance in the midbrain was significantly lower. This reduction in tumour numbers was also observed in the septum and basal ganglia, adjacent structures to the caudate putamen.

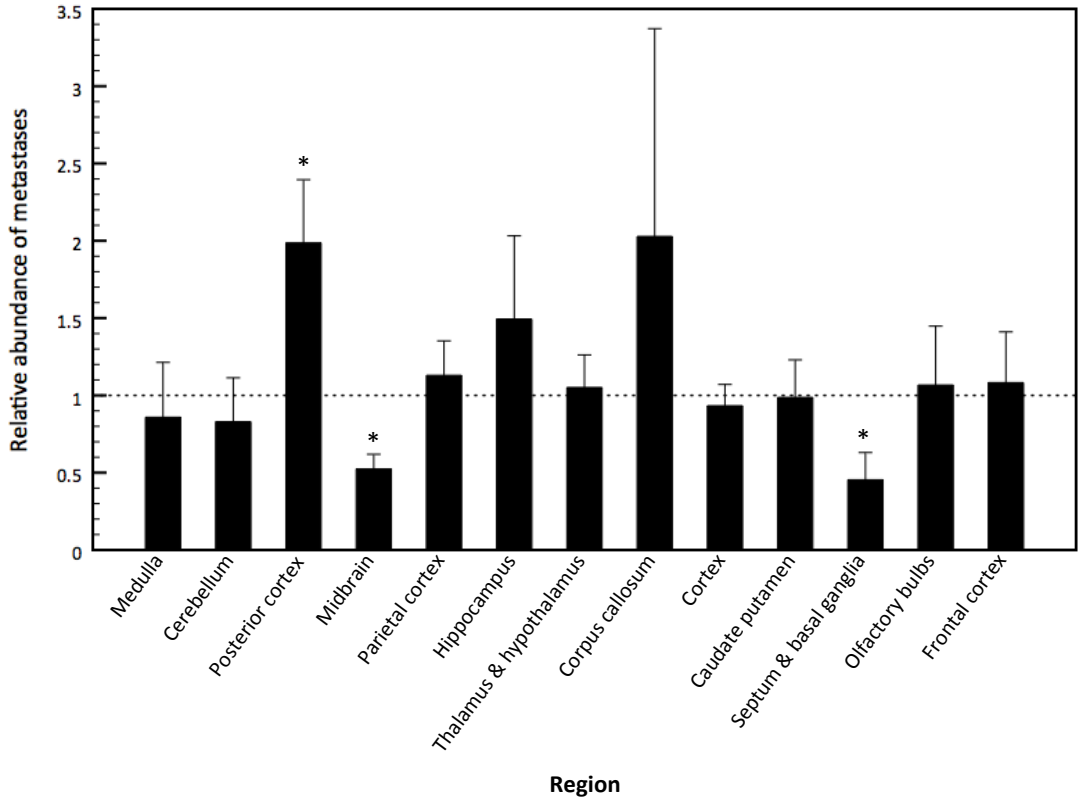


Figure 4.3 – Distribution of metastatic lesions across thirteen brain regions (n=7). The relative abundance of tumours in the posterior cortex was significantly greater than the expected value (dotted line), and significantly lower than the expected value in the midbrain and the septum and basal ganglia. Error bars denote a 95% confidence interval.

The variability in tumour distribution presented in Figure 4.3 may represent differences in the vasculature or tumour-endothelial interactions in different brain regions. When tumour locations were analysed a finer level, more subtle differences were observed. For example, many tumours were found in periventricular locations in the brain. Tumours ventral to the fourth ventricle, in the anterior regions of the brainstem such as the prerubral field were common, as were tumours in close association with lateral ventricle, in the oriens layer and the stratum lucidem of the hippocampus. The same observation was also made in the subventricular zone in the striatum, a region that, like the dentate gyrus, shows a high level of adult neurogenesis (Luzzati et al., 2007).

In contrast, very few tumours were ever found within the choroid. This may in part reflect the proportional volumes of brain vasculature and choroidal vasculature, or a difference in signalling between tumour cells and the surrounding vasculature and/or cells of the immune system.

Tumours found in the corpus callosum, the largest white matter structure in the rodent brain, had a distinct morphology and were normally very elongate, tracking along the length of the structure rather than spreading out into the surrounding grey matter. Similarly, a notable pattern of tumour growth was evident in the cerebellum. The cerebellum comprises an internal region of white matter, surrounded by folia. The folia are made up of three distinct cell layers: the molecular layer, the Purkinje cell layer and the granular layer. Tumours were frequently found to spread across all three layers of the folia, but did not invade the white matter, while others were often found to inhabit solely the central white matter tracts.

4.3.3 Characterisation of tumour morphology

A sample of 1392 metastatic lesions from the five different anatomical sections (Table 4.1) in seven tumour-injected animals were identified and their morphologies characterised. Tumour volumes, sphericities, ranges and the average number of objects per section were calculated. Plotting these parameters against each other (Figures 4.4 and 4.5) revealed that a large proportion of tumours show similar properties to each other: small size and range with only one or two objects per section and a sphericity of 0.7-0.8. These findings suggest that these tumours have not spread along large regions of the adjacent vascular bed. However, a small number of metastatic lesions were much greater in size, and show an

increase in their range and/or the number of objects per section, indicating marked growth along the perivascular space (Figure 4.4).

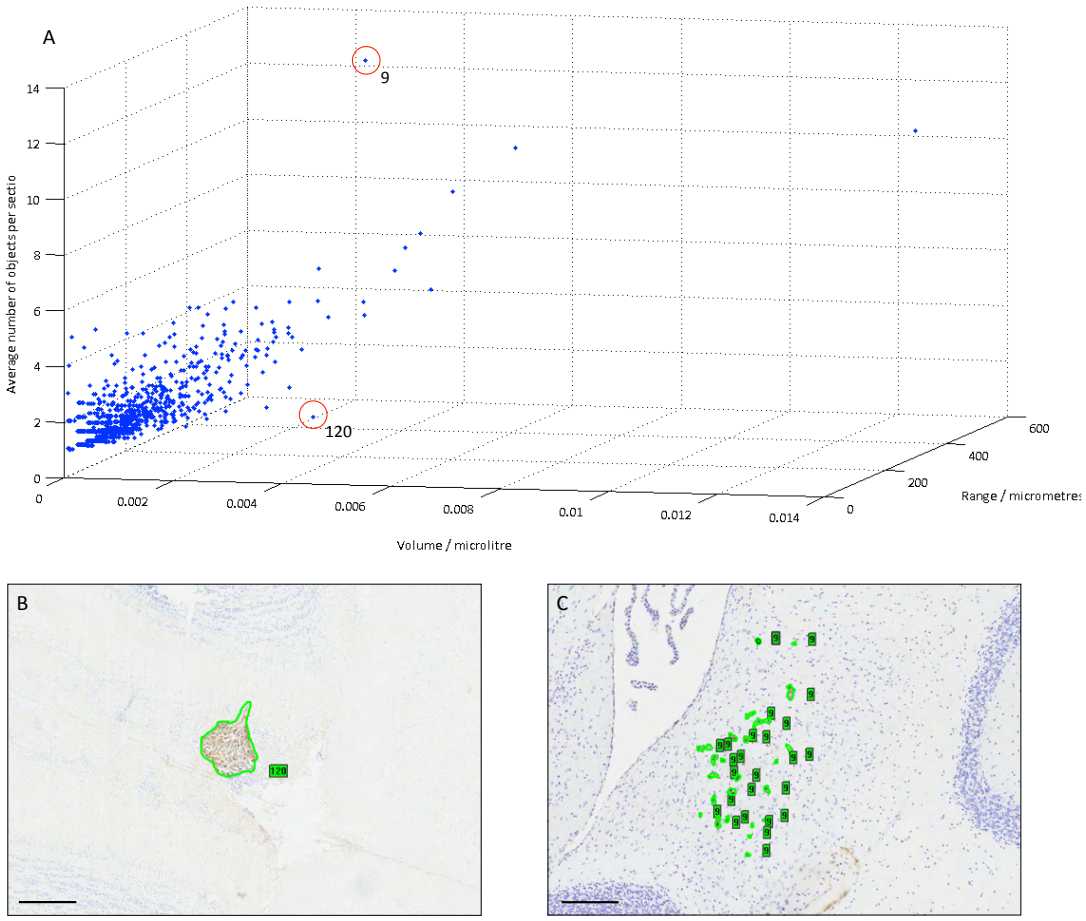


Figure 4.4 – Perivascular growth in brain metastases. (A) Graph showing the range of tumour volumes (x-axis), the range or number of sequential brain sections over which a metastasis was observed (z-axis) and the average number of discrete objects belonging to a single metastasis within each section (y-axis) across 1392 metastatic lesions. The majority of metastases are relatively small with a small range and only one or two objects per section. As metastatic lesions become larger the general trend is towards a greater range and a greater average number of objects per section, suggesting that as the tumour grows it continues to track along the vasculature rather than growing directly into the brain parenchyma. (B) One metastatic lesion, situated in the olfactory bulbs (circled and labelled 120 in A) has reached a large size without increasing its average number of objects per section, suggesting that

this tumour may have spread directly into the brain parenchyma. (C) Another metastatic lesion of a similar volume to (B), located in the cerebellum (circled and labelled 9 in A) appears to have spread down the length of many blood vessels from its site of original arrest and development. Although it may appear that all the objects identified are distinct micro-metastases, sequential sections through this lesion reveal that they all join up and can therefore be classified as a single metastatic lesion. Scale bars represent 200 μm.

The sphericity was calculated by comparing the perimeter of a given metastatic lesion with the circumference of a circle of the same area. The ratio of the two gives a value of the circularity of a tumour, which, averaged over several sections, gives a proxy value for the sphericity of the tumour. Highly non-spherical, elongate tumours have a low sphericity value between 0.4 and 0.6; highly spherical tumours have a value close to 1.0. Elongate structures are further evidence of possible vascular co-option as the tumour spreads along the vascular bed rather than proliferating within a given locus (Figure 4.5). The majority of tumours had a sphericity of 0.7-0.8 (mean = 0.7566, median = 0.7590) and only a smaller number of tumours appeared particularly elongate or spherical (min = 0.3989, max = 0.9370), which suggests that the majority of tumours develop both *in situ* and spread along nearby vasculature. Two metastases of similar overall volume, but varying sphericities (Figure 4.5B & C) suggest that these tumours, both at equal stages of development, have proliferated in a different manner to one another. Thus, the morphological characteristics of a tumour, its sphericity, range and the number of objects can be used to describe the development of a tumour. These features of tumour growth are later explored in response to a systemic inflammatory response (Chapter 5).

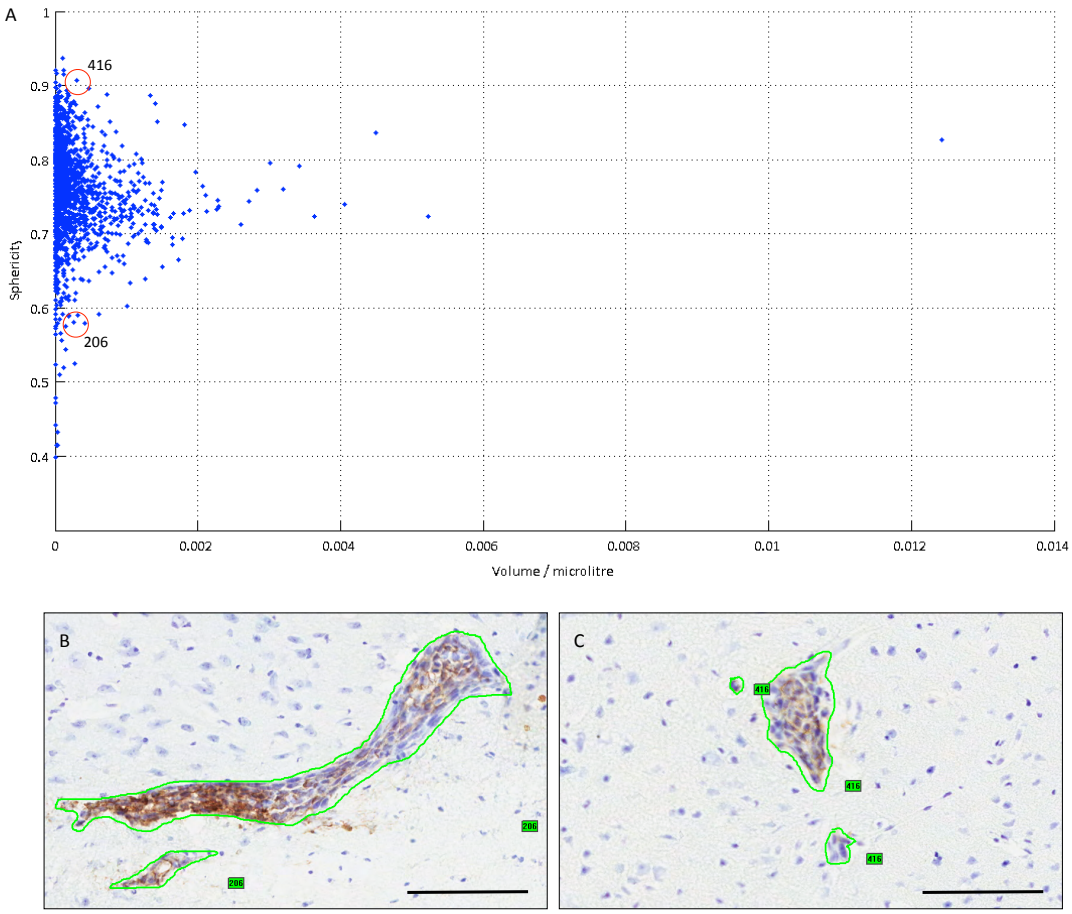


Figure 4.5 – Sphericity of tumours. (A) Graph showing tumour sphericities (y-axis) plotted against their volumes (x-axis) across 1392 metastatic lesions. The majority of tumours have a sphericity value of 0.7-0.8, with a tail at either end of more spherical (high) and more elongate (low) tumours. (B) Two tumours with a similar volume to each other (B, 4.19×10^{-4} µL, circled 206 in A; C, 2.96×10^{-4} µL, circled 416 in A), suggesting a similar stage of development, have markedly different sphericities to one another (B, 0.5797; C, 0.9066), suggesting differences in tumour proliferation between the two. Scale bars represent 100 µm.

4.3.4 Comparison of morphology between brain regions

The data presented in Figures 4.4 and 4.5 demonstrate the tumours can show a wide range of morphologies, varying in volume, range, number of objects and sphericity. Given the differences in tumour number at different sites within the brain (Figure 4.3), we may also expect changes in tumour development to occur at different sites within the brain, possibly dependent on local vasculature and signalling dynamics between tumour cells and endothelial cells. In order to investigate any differences between tumour populations across the five different brain section, all of the metastatic lesions were analysed for each of the four properties described, as presented below. The numerical distribution of tumours has been presented earlier (Figure 4.2).

Volume

At day 10 after tumour cell injection a wide range of metastatic lesion volumes was observed. Volumes ranged from 7.28×10^{-7} μL to 1.24×10^{-2} μL, with the majority of lesions at the smaller end of the volume range (Figure 4.6) (mean = 3.02×10^{-4} μL; median = 1.39×10^{-4} μL). Metastatic lesions were found to be significantly greater in volume in the hippocampal slice compared to the striatal slice ($p = 0.0048$).

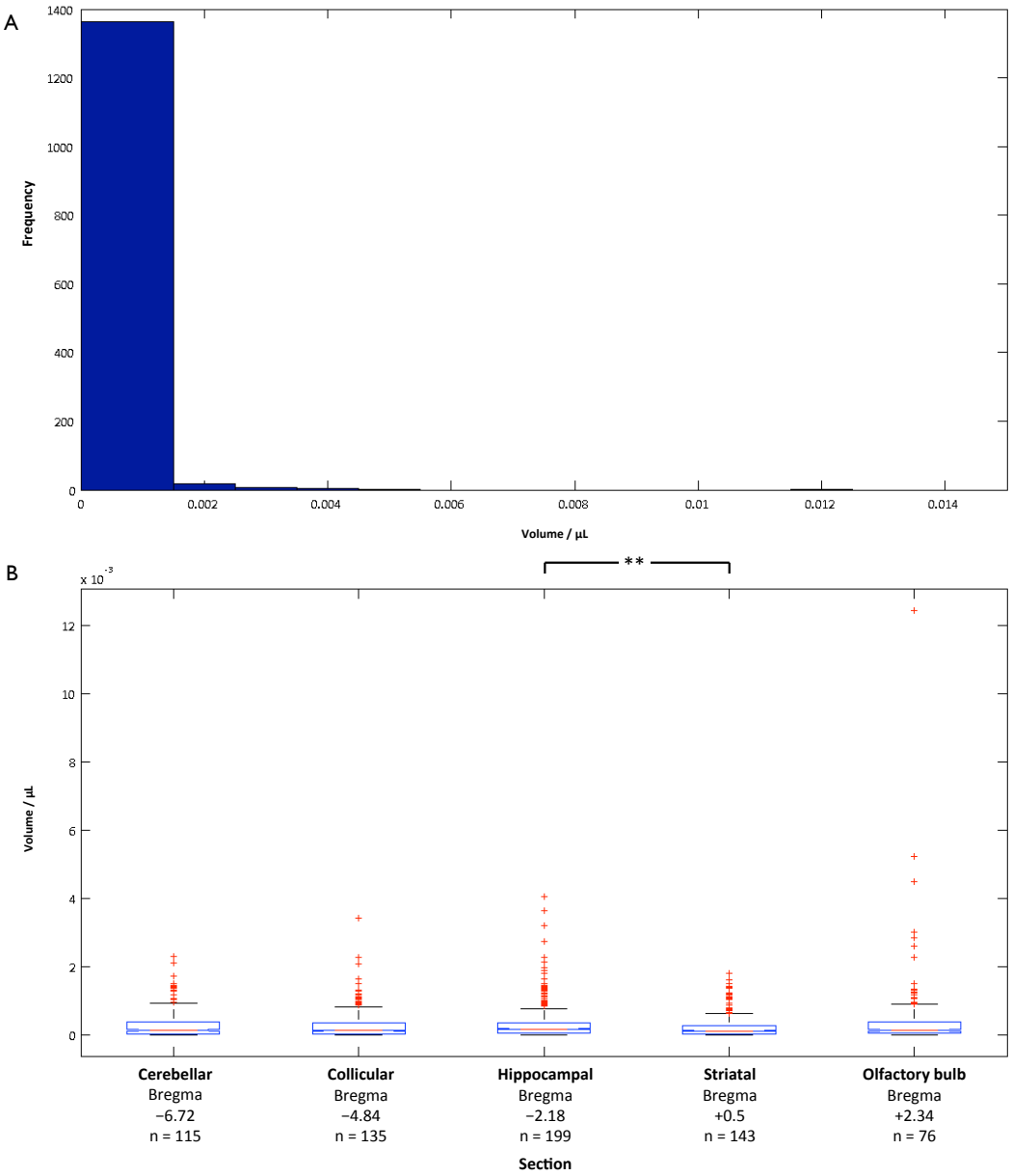


Figure 4.6 – Volume distributions. (A) Histogram showing the volumes of 1392 metastatic lesions across 7 animals. The majority of lesions were small (< 0.002 µL), although a tail of larger metastatic lesions also exists. (B) Boxplots showing the distributions of metastatic lesion volumes across the five brain regions studied. A Kruskal-Wallis test revealed that volumes of metastatic lesions were significantly greater in the hippocampal slice compared to the striatal slice (p = 0.0048). Brain regions defined as per Figure 4.2B.

Range

Tumour range also varied widely, with some tumours visible in only one tissue section (range < 40 μm), while others spread across twenty tissue sections (range ≥ 580 μm). In a similar fashion to tumour volume, most of the lesions were observed at the smaller end of the range (Figure 4.7) (mean = 102.4 μm; median = 70 μm). The cerebellar, hippocampal and olfactory bulb slices contained tumours with greater ranges than those observed in the striatal slice ($p < 0.01$).

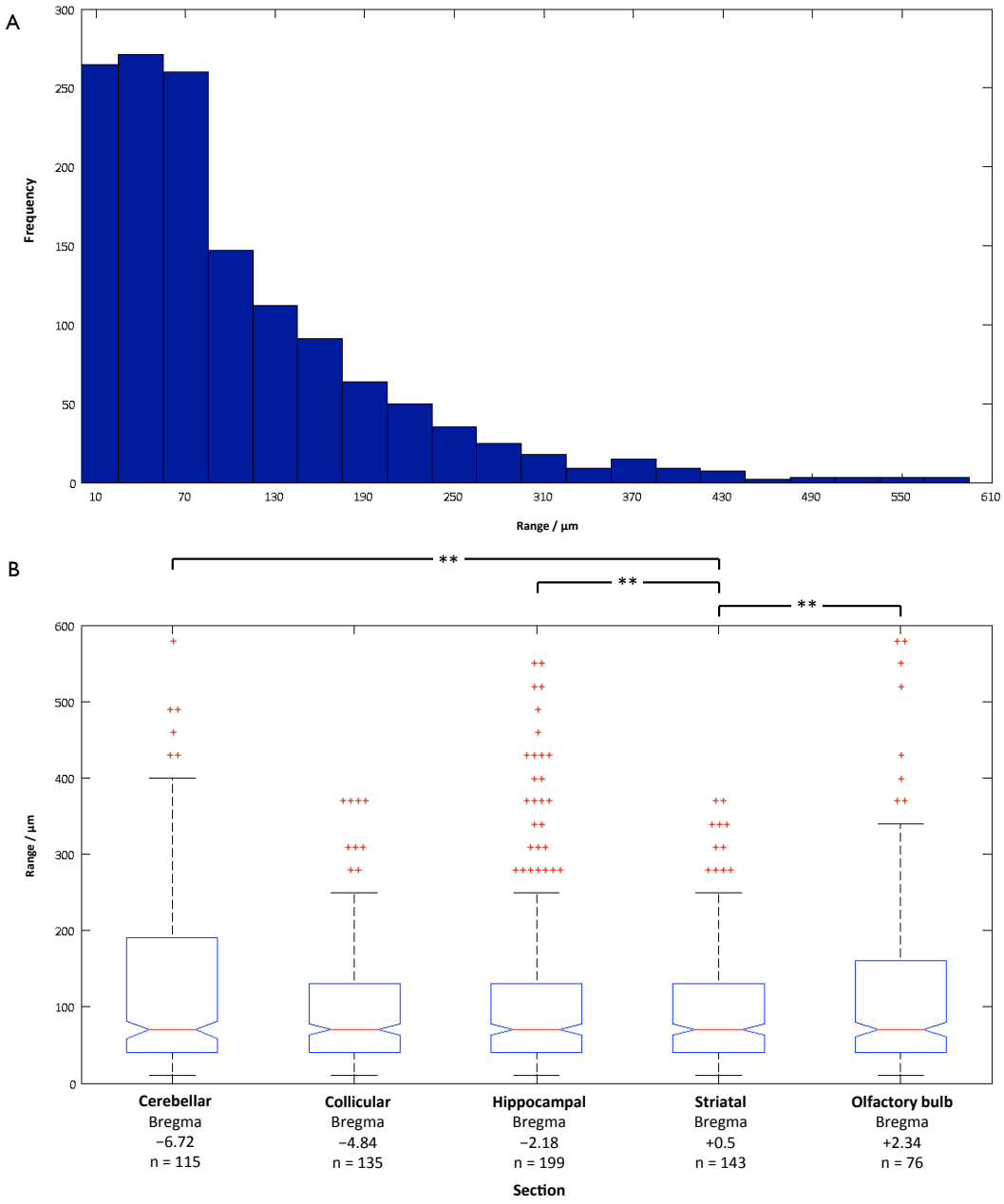


Figure 4.7 – Range distributions. (A) Histogram showing the ranges of 1392 metastatic lesions across 7 animals. Although smaller ranges are more common than larger ones (matching the previous data for volumes), there is a broader distribution of ranges than volumes. The tail is artificially shortened at 580 µm (the greatest tumour range possible given the sampling technique), so any metastatic lesion with a range of greater than 580 µm has been cut off at this value. (B) Boxplots showing the distributions of metastatic lesion ranges across the five brain regions studied. A Kruskal-Wallis test revealed that tumour ranges in the cerebellar, hippocampal and olfactory bulb slices were significantly greater than in the striatum ($p < 0.01$).

Number of distinct parts

The number of distinct parts to a metastatic lesion as it tracks through a vascular bed may indicate the level of vascular co-option that has occurred. As shown in Figure 4.4, two tumours of a similar volume may have markedly different morphologies, suggesting a difference in their respective development. Figure 4.8 demonstrates that the majority of tumours have small numbers of objects per section (mean = 1.47; median = 1), but that a minority have much larger numbers (max = 12.32). A significant difference is observed between different brain regions, with a markedly increased number of distinct parts to each tumour in the cerebellum compared to all other brain regions and an increase in the olfactory bulbs compared to the colliculi and the striatum.

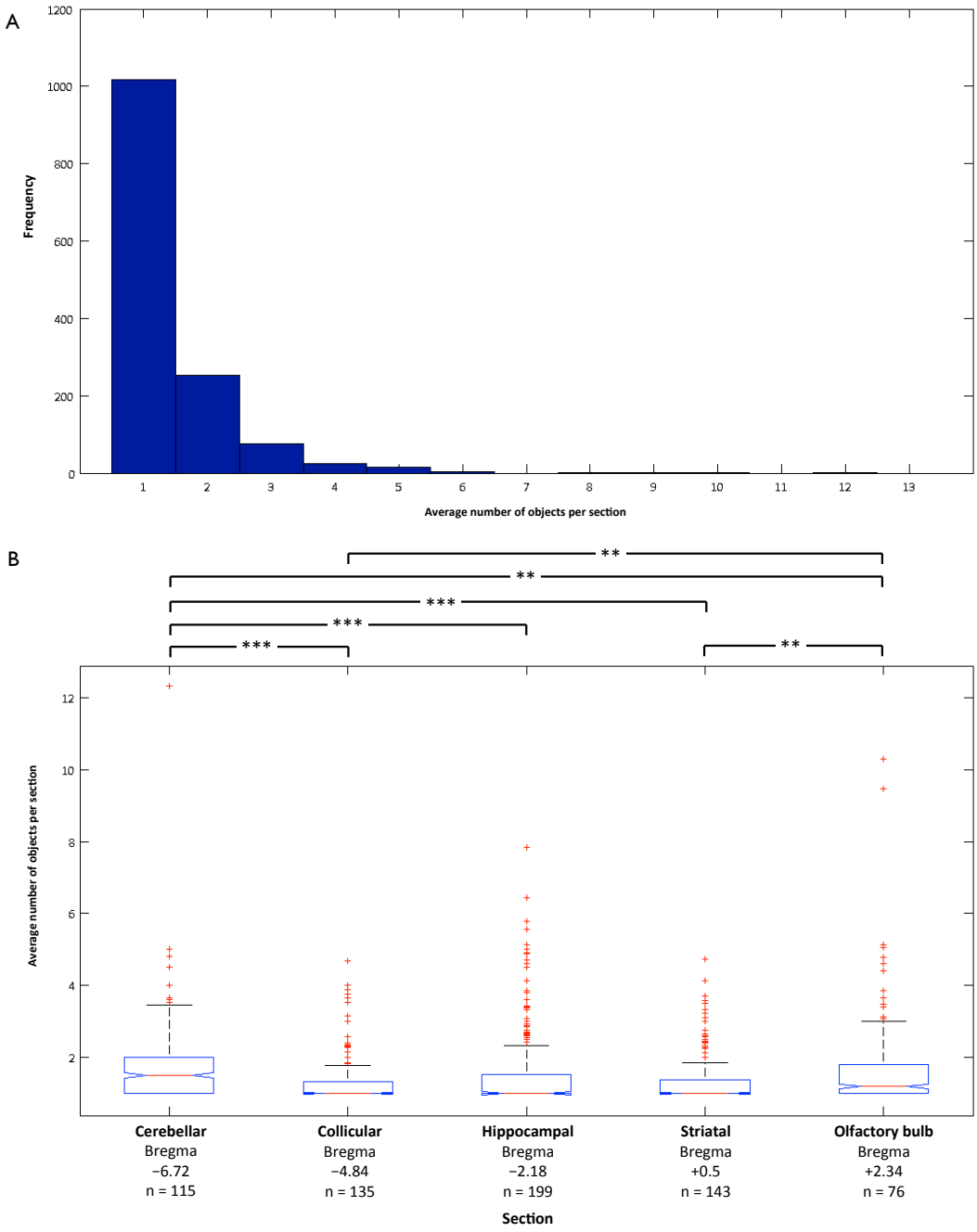


Figure 4.8 – Numbers of objects distributions. (A) Histogram showing the average number of objects per section of 1392 metastatic lesions across 7 animals. There is a clear skew towards metastatic lesions with a small average number of objects per section, although lesions do exist with as many as twelve distinct objects per section. (B) Boxplots showing the distributions of numbers of objects per section across the five brain regions studied. A Kruskal-Wallis test followed by a multiple comparison between groups revealed that the cerebellar slice contained tumours with greater numbers of objects per section than tumours in any other brain region ($p < 0.0001$); numbers of objects for tumours in

the olfactory bulb slice were also elevated, and significantly greater than those in the collicular or the striatal slices ($p < 0.001$).

Sphericity

In a similar fashion to the number of distinct parts, the sphericity of a metastatic lesion may also indicate the level of vascular co-option that has occurred. Figure 4.5 demonstrates that the majority of tumours have a sphericity of 0.7-0.8, which is presented as log-transformed data in Figure 4.9 to allow parametric statistical testing (mean = -0.2833; s.d. = 0.0956). Significant difference were observed between different brain regions, with markedly more elongate tumour development in the cerebellum compared to all other brain regions ($p < 0.0001$), and more spherical tumour development in the striatum compared to the hippocampus and the olfactory bulbs ($p < 0.01$).

Tumour sphericity data may also represent differences in rates of tumour development i.e. tumours of different volumes may exhibit different sphericities. If this is the case then brain sections with significantly different tumour volume distributions to one another may also have different tumour sphericities. In order to validate this hypothesis, all tumour sphericities were divided by their respective volumes and a Kruskal-Wallis test was performed to compare sphericity/volume measurements for all brain sections. This analysis revealed that the striatal section had a higher sphericity/volume than the hippocampal section ($p = 0.003$), but that no other differences were found to be significant (Figure 4.10). These data suggest that although the volume and sphericity of tumours may share information about the development of brain tumours, the striatum nonetheless has an elevated tumour sphericity.

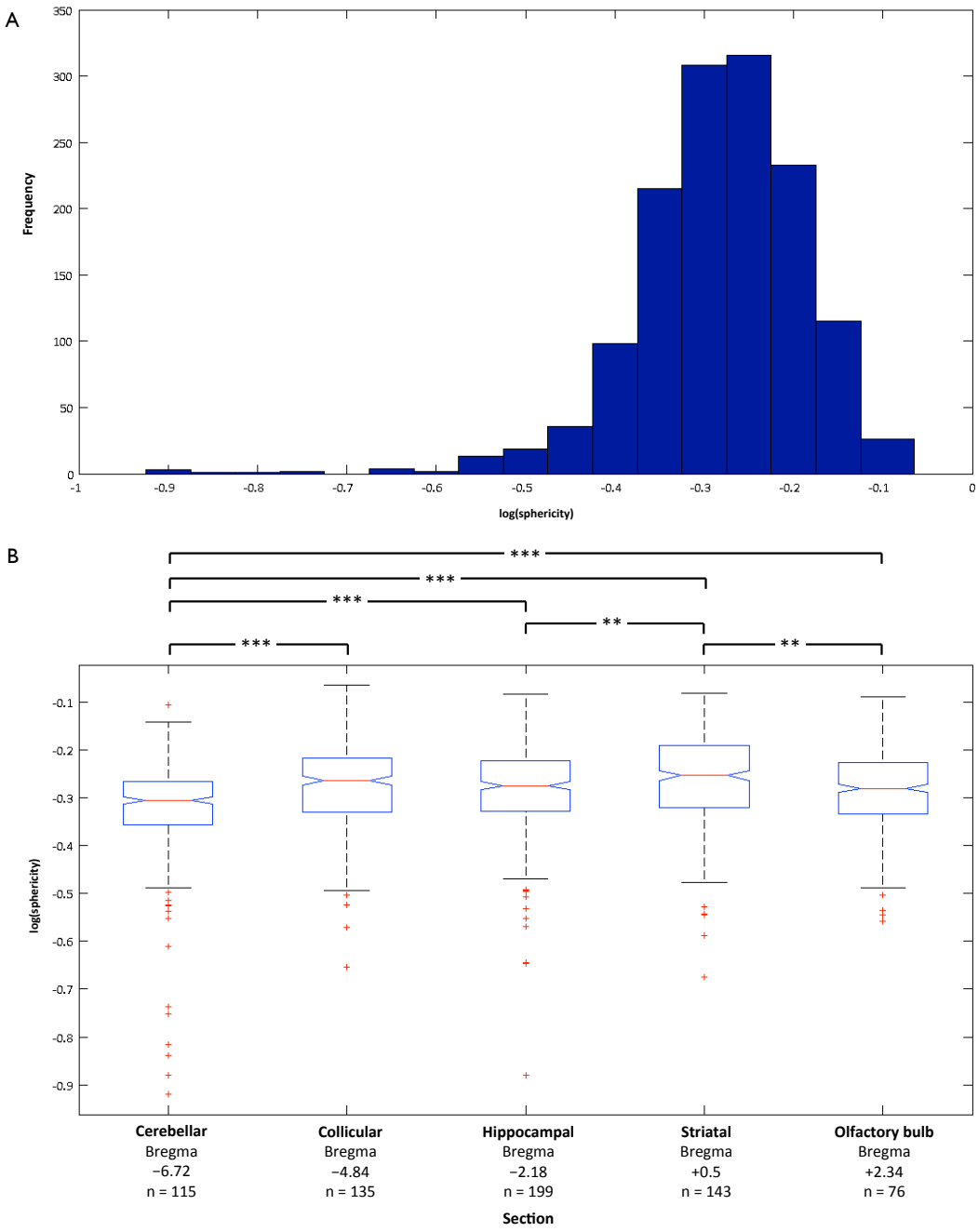


Figure 4.9 – Logarithm of tumour sphericity. (A) Logarithmic transformation of the original data gave a distribution that was approximately normal (mean = -0.2833; median = -0.2757; standard deviation = 0.0951). Highly elongate tumours have the smallest log(sphericity) values; more spherical tumours have the greatest. (B) Analysis of variance demonstrated significant differences in tumour sphericity between brain regions, with the cerebellum showing the greatest degree of elongate tumour development compared to all other brain regions ($p < 0.0001$) and the striatum having significantly more spherical tumours compared to the hippocampus and the olfactory bulbs ($p < 0.01$).

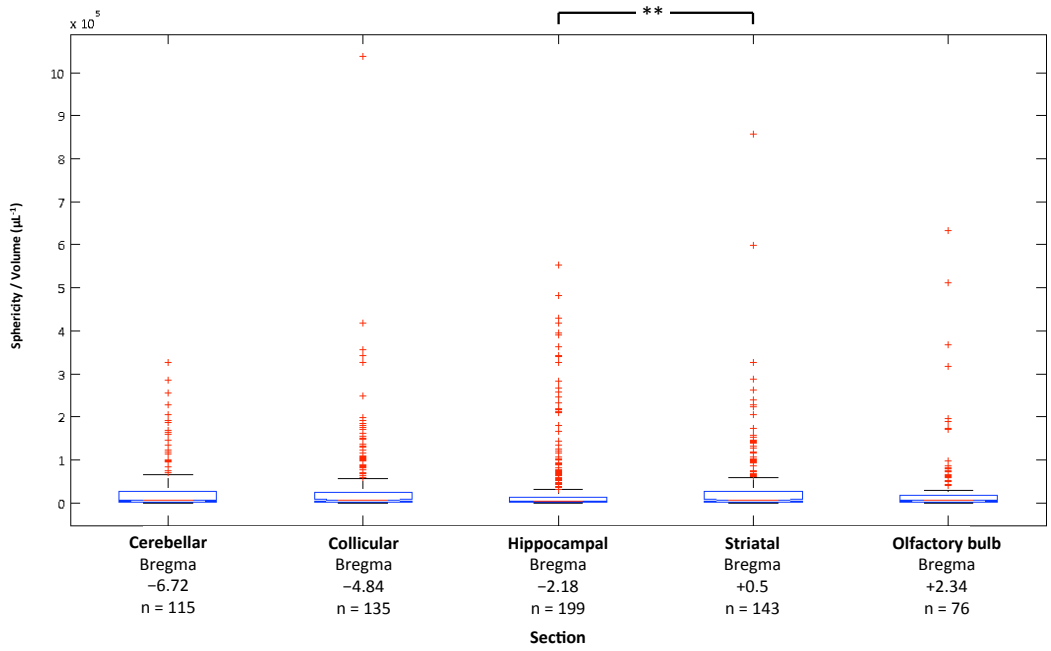


Figure 4.10 – Tumour sphericities weighted for volume. Adjusting the sphericity of each tumour for its volume removes any potential confound with the degree of tumour development. A Kruskal-Wallis test revealed that tumour sphericities were greater in the striatal section compared to the hippocampal section ($p = 0.003$), but no other significant differences were observed.

4.3.5 Development of metastases on arterioles and venules

The two vascular markers used in this study are arterial αSMA and venous EphB4, as already discussed. *In vitro* observations of 4T1-GFP cells revealed that tumour cells express EphB4 in culture, without any prior exposure to mouse serum (Figure 4.11), but not αSMA. Although these results may hamper the positive identification of venous vessels associated with cerebral metastases, the lack of αSMA expression on 4T1-GFP cells should allow confident identification of arteriolar vessels in the brain, and aid identification of the vascular location of cerebral metastases.

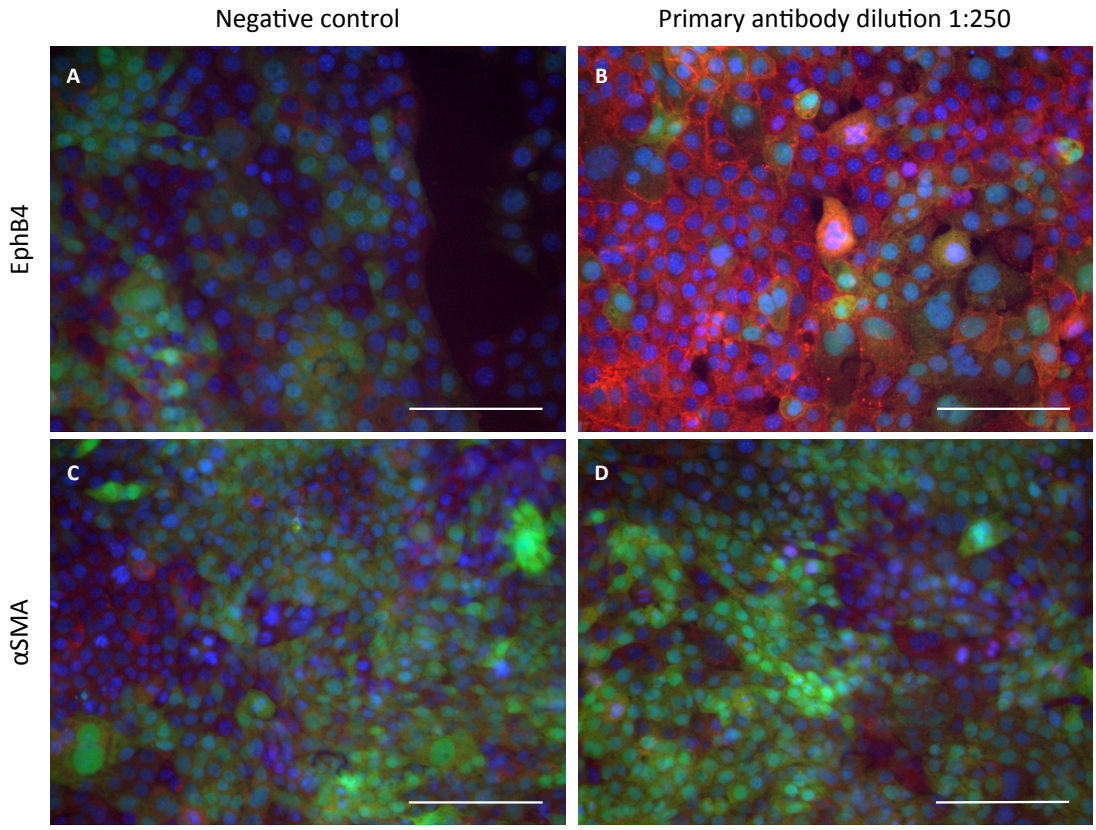


Figure 4.11 – EphB4 and αSMA expression by 4T1-GFP cells *in vitro*. (A) Negative control cells, without addition of primary antibody, show a low level of background fluorescence (red channel), whereas positively stained cells show marked fluorescence, confirming EphB4 expression. (B). (C) Background fluorescence levels are similar in αSMA negative control cells and in positively stained cells (D), suggesting no endogenous expression of αSMA in 4T1-GFP cells. Blue = DAPI; green = GFP. Scale bars represent 50 µm.

The majority of metastatic lesions in the brain appear to colocalise with EphB4-positive blood vessels (Figure 4.12B). The immunofluorescent EphB4 signal appears to occur across the tumour mass as well as on the blood vessels surrounding the tumour, in accord with the results presented in Figure 4.11 showing 4T1 expression of EphB4. In contrast, αSMA was only very rarely found associated with metastatic lesions (Figure 4.12A) and only once tumours had reached a greater volume, and exhibit a greater level of vascular co-option, as determined by the number of objects per section (Figure 4.12E). These data suggest that the

majority of metastases extravasate in the venous end of the capillary bed, as smaller tumours colocalise exclusively with EphB4. As the tumours continue to proliferate and develop, they may continue to spread through the local vasculature, tracking both retrogradely and anterogradely, and eventually encounter an αSMA-positive vessel. Thus, αSMA colocalisation may be a feature of more developed tumours with greater levels of vascular co-option.

VCAM-1 upregulation has also been shown to occur frequently at the tumour site (Figure 3.3, Serres et al., 2012), and has been shown here on EphB4-positive but not αSMA-positive vessels (Figure 4.12C & D) both at the tumour and on vessels proximal to the tumour. However, VCAM-1 expression at a distance from the tumour site is normally associated with αSMA positive vessels only (Figure 4.12A & C, white arrows) rather than EphB4 positive vessels, suggesting that the expression of VCAM-1 as a marker of more widespread tumour-related neuroinflammation is more tightly regulated to arteriolar vessels than local tumour-related neuroinflammation.

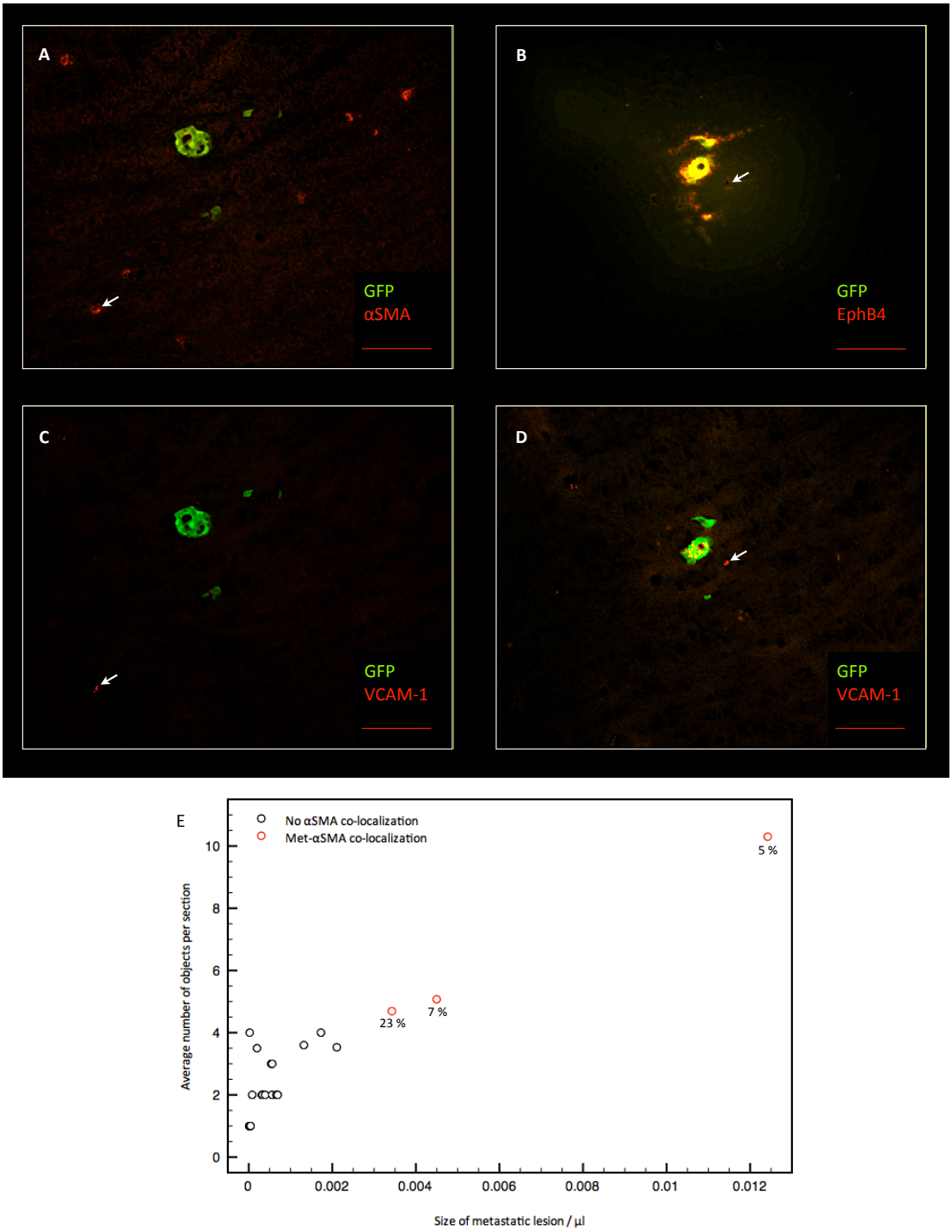


Figure 4.12 – Prevalence of metastases on venous and arteriolar blood vessels. (A) & (B) Tumours (green) were found to colocalise with both αSMA and EphB4 positive blood vessels respectively (red). (A) & (C) An αSMA positive blood vessel distant to the tumour site (white arrow) in (A) colocalises with VCAM-1 expression (red) in (C), although VCAM-1 expression is not visible at the tumour site. (B) & (D) An EphB4 vessel proximal to the tumour site (white arrow) in (A) colocalises with VCAM-1 expression (red) in (D). VCAM-1 expression is visible at the tumour site, and on EphB4-negative

vessels distant to the tumour site. (E) Observations from 23 metastatic lesions from 3 animals demonstrate that only a few tumours are found co-localised with αSMA blood vessels, predominately those of a greater size (x-axis) and those that show an increased level of perivascular growth, as concluded from the average number of objects per section (y-axis). The proportion of sections on which the same tumour was found to colocalise with an αSMA-positive blood vessel is denoted by the percentage values.

4.4 Discussion

In this chapter the normal development of 4T1-GFP brain metastases has been examined in relation to (i) their colocalisation with hypointensities in GE3D MRI datasets, (ii) their distribution across different brain regions, (iii) their growth patterns in different brain sections and (iv) their colocalisation with arteriolar and venous cerebral vasculature.

4.4.1 Spatial distributions of metastases and hypointensities

The spatial correlation of metastases and hypointensities across five regions of the brain (Figure 3.8) revealed the difficulty associated with reliable detection of metastases using VCAM-MPIO-derived hypointensities. A far greater number of hypointensities were detected in the posterior regions, probably due to a reduction in the signal quality towards the back of the brain. SNR decreases further away from the centre of the RF coil, and this is probably the explanation for the reduction in signal quality. This could be improved either by altering the position of the head inside the RF coil, or by segmenting the posterior of the brain separately to the rest and analysing it using different parameters, as was done with the previously used manual approach. One further improvement that could be made to the automated approach would be an adaptive choice of test value. For instance, as the SNR

decreases towards the back of the brain, an additional step in the automated approach could be programmed to identify this change and decrease the value of the mean fraction accordingly.

4.4.2 Development of metastases in the brain

The development and growth of brain tumours has been studied in this chapter in relation to their spatial distribution and their morphology. Fitzgerald et al. (2008) presented data for the dissemination of 231-BR cells in nude mice, and made a quantitative assessment based on the frequency that at least one metastatic lesion has been observed within a given brain region. There are two potential drawbacks to this analysis. Firstly, the cell line used was a xenograft model in nude mice, rather than the syngeneic 4T1-BALB/c model used here. Secondly, there is loss of information about the density of metastases and their relative abundance in each brain region by presenting frequency data in this fashion. Instead, the data presented in this chapter describe not only the likelihood of finding a single metastasis within a given brain region, but the relative abundance of metastases within that region, weighted for the local anatomical volume.

Analysis of tumour volumes reveals features about their growth patterns and development within various brain regions. Although a significant increase was seen in tumour volumes in the hippocampus compared to the striatum, volumes were uniform across the remainder of the brain sections, suggesting that tumour cells in most vascular beds are subject to a similar level of pro- and anti-proliferative signalling as each other. However, differences in tumour morphology were more pronounced between brain sections, suggesting different modes of proliferation between tumours in different locations. In the brain, growth of tumours frequently occurs along the length of the blood vessels, a feature identified in this organ first as vascular co-option, reflecting the ability of tumours to retain access to the brain's blood

supply by using existing blood vessels (Leenders et al., 2002). A number of tumours in these brains exhibit a high level of vascular co-option, as determined by the average number of objects per section, the range and the sphericity for each tumour. Furthermore, the level of vascular co-option differs across anatomical regions of the brain with least in the striatal slice and the most in the cerebellum. This finding may reflect a difference in the shape and density of the vasculature in each of these brain regions, or differences in the signalling exchange between metastatic cells and the local endothelium in each of these locations.

However, statistical difficulties arise when analysing data about tumour morphology. Figure 4.10 revealed changes in significance between brain locations when tumour sphericities were weighted for their respective volumes, suggesting the presence of shared information between the two measures of morphology. Thus, it is possible that these two terms interact. Alternatively, we can imagine a situation in which two identical, cylindrically shaped tumours are either aligned with or perpendicular to the coronal plane in which the brains were cut. A tumour of identical shape and size would therefore have a high range and high sphericity in one scenario and a low range and a low sphericity in the other. In order to account for interaction terms such as these we may wish to perform a multivariate statistical analysis. When all variables are normally distributed, this is a relatively simple task using a MANOVA. However, with the exception of tumour sphericity, the morphological data sampled in these studies was distinctly non-normal, and analysis of variance was conducted using a Kruskal-Wallis test, the non-parametric equivalent of the ANOVA. The development of tools for multivariate non-parametric analysis is a current area of research in statistics (Oja and Randles, 2004; Jurečková and Kalina, 2012), and although methods have been developed for multivariate non-parametric analysis in ecology (Anderson, 2001), these methods require data from different variables to be identically distributed. This is certainly not a feature of

the data sampled in these studies, and as yet no suitable tools exist for the multivariate analysis of these datasets.

One potential confound to accurately assessing the numbers, volumes and morphologies of metastases found within the brain is the possibility that two ore more metastatic cells may have extravasated and proliferated within the same region of vascular bed. When these tumours grow, they become, in effect, a single large metastatic lesion. Thus, a single tumour may not represent a single extravasation event, nor may the growth rate be accurately reflected in its overall size. However, differences in tumour morphology, particularly in varying levels of GFP expression between cell populations, can give some insight into the frequency of these events. It would appear that they happen rarely, as there were only two tumours out of the 1392 studied that seemed to show a 'mixed' morphology, although this process would be undetectable if two tumours of similar GFP expression levels share the same region of vascular bed. One is shown in Figure 4.13.

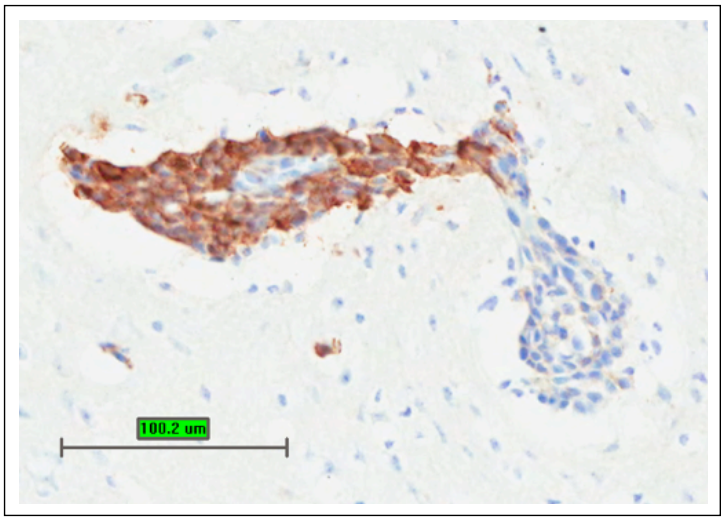


Figure 4.13 – Mixed morphology of cerebral tumours. A single tumour showing variable intensity of GFP DAB staining, suggesting that two individual extravasating cells with high and low GFP expression levels continued to proliferate and merged to become a single metastatic lesion. The extravasation event of the second cell may have been caused in part by the development of the first.

4.4.3 Vascular localisation of brain metastases

The majority of tumours analysed appeared to occur in venous, EphB4-positive blood vessels rather than arterial, αSMA-positive vessels. This was determined both by the presence of EphB4 staining, but also by the absence of αSMA staining by immunofluorescence. Although the Ephrin B2 (EphB2) receptor has been shown to be upregulated in 4T1 murine mammary carcinoma cells (Lou et al., 2008), the same had not been shown for EphB4. However, these experiments have shown that EphB4 is expressed by 4T1-GFP cells *in vitro* and suggest that expression levels remain high *in vivo*. Given the flexible role that Ephrins and their ligands play in the development of the CNS (Xu and Henkemeyer, 2012), development of new blood vessels (Wang et al., 1998; Kudo et al., 2007; Taylor et al., 2007; Kume, 2010) and their elevated expression patterns on many tumour cell lines (Bennett et al., 1994; Berclaz et al., 1996, 2003; Robinson et al., 1996; Tang et al., 1999; Stephenson et al., 2001; Liu et al., 2002; Sinha et al., 2003; Cromer et al., 2004), it may be prudent to suggest that EphB4 expression

in and of itself may not be a reliable indicator of tumour-venule co-localization. However, the absence of αSMA expression in the majority of these tumours suggests that they are not usually located in arterial vessels in the brain, and therefore are located on venous vessels, in the same manner as described in Lorger and Felding-Habermann (2010). Thus, these data demonstrate that, despite the probable systemic inflammation caused by injection of 4T1-GFP cells into the internal carotid artery, tumour extravasation appears to occur preferentially on post-capillary venules in both models.

Current models of tumour extravasation suggest similarities to the mechanisms by which leukocytes extravasate. These tumour data appear to match the current understanding of leukocyte extravasation, which has been shown to occur at the venous end of brain capillaries in preference to the arterial end (Lossinsky and Shivers, 2004; Prendergast and Anderton, 2009). These data add to the current model by demonstrating the distribution of VCAM-1 on blood vessels at and around the tumour site, suggesting that VCAM-1 presentation to circulating leukocytes normally occurs on arteriolar vessels at a distance from the tumour site, but on EphB4 vessels at or proximal to the tumour site.

4.4.4 Future work

The venous marker used throughout this thesis was EphB4, which may have several confounds when used in conjunction with tumour localization in the brain, as described above (see Figure 4.11). Although there appears to be a paucity of venous markers in the literature, the MECA-76 sulphated carbohydrate epitope is a possible target for future work. It is normally expressed on venous blood vessels where there is a high level of leukocyte extravasation, particularly in high endothelial venules (HEVs) associated with lymph nodes (Streeter et al., 1988; Michie et al., 1993; Salmi et al., 1997), although increased expression has been shown on human venules in chronically inflamed synovial tissue in rheumatoid

arthritis, and endothelial colon tissue in Crohn's disease (Middleton et al., 2005). There is no secondary lymphatic tissue in the brain, so we would not expect to observe expression in naïve animals, but expression of this marker at sites of metastasis may give us both a positive identification of a venous blood vessel.

Further markers may provide information about the normal developmental patterns of 4T1-GFP metastases in the brain. Firstly, the data presented in this chapter to describe the co-optive development of metastases along blood vessels are all morphological. A useful validation to this work would be to look for angiogenic markers at the tumour site. Differential staining of angiogenic markers would provide a logical interpretation to the patterns of growth described here. Secondly, a BrdU assay would reveal differences in proliferation rates between metastases in different parts of the brain, and may explain some of the differences found in tumour volume between brain sections.

4.4.5 Concluding remarks

The data presented in this chapter reveal a wide range of tumour morphologies and patterns of tumour growth within the brain, using a single cell line. Tumour growth was dependent on the region of the brain in which the tumour developed, and not all brain regions were equally likely to develop metastases. However, some features of tumour growth appear to be consistent between brain regions, such as the extravasation of metastatic cells in post-capillary venules. These data confirm and improve upon previous work by Fitzgerald et al. (2008) and Lorger and Felding-Habermann (2010), adding weight to the body of evidence about metastasis to the brain. Furthermore, answering these questions is crucial in understanding any changes that occur in tumour development as a result of inflammatory stimuli, as discussed in the following chapter.

Chapter 5

Effects of systemic and local inflammation on the neurovasculature and the development of brain metastases

5.1 Introduction

In the previous chapter data was presented revealing the normal patterns of 4T1-GFP tumour growth in the brain, ten days post-intracardial injection. The experiments presented in this chapter demonstrate the effects of an adenovirus-induced systemic inflammatory challenge and a cytokine-induced local neuroinflammatory challenge on the development of 4T1-GFP brain metastases.

5.1.1 Inflammatory stimulus

One of the characteristics of inflammation at any site in the body is the expression of protein and carbohydrate markers on the luminal surfaces of blood vessels local to the site of injury or infection. These markers allow recruitment of leukocytes to the region of inflammation where they are able to extravasate into the parenchyma. Many similar mechanisms have been proposed for the extravasation of tumour cells, both systemically and in the brain, as discussed in the introductory chapter (Section 1.5). If the interaction between tumour cells and vascular adhesion molecules is a reasonable model to describe the extravasation of tumour cells into the perivascular space in the brain, then it might be hypothesised that

upregulation of these adhesion molecules should lead to increased extravasation and tumour formation. It has previously been shown that a systemic inflammatory response can induce upregulation of multiple adhesion molecules on peripheral blood vessels (Paulus et al., 2011). Systemic exposure to lipopolysaccharide (LPS) (Wu et al., 2012) and λ-carragenan (Huber et al., 2006) has also been shown to cause ICAM-1 upregulation on cerebral blood vessels. However, despite the importance of the VCAM-1 pathway in leukocyte recruitment to the CNS in various neuropathologies (James et al., 2003; Norman et al., 2008; Ou et al., 2008), the effect of systemic inflammation on cerebral upregulation of VCAM-1 expression has not been investigated. Thus, I hypothesised that induction of systemic inflammation would lead to upregulation of adhesion molecules such as VCAM-1 on the cerebral vasculature, the effect of which would be increased cerebral metastasis for tumour cells exposed to such an environment. Furthermore, previous work from our group has shown exacerbation of existing EAE lesions in the rat brain following intraperitoneal LPS injection (Serres et al., 2009), which included recruitment of macrophage and lymphocyte populations. Thus, I also hypothesised that systemic inflammation may cause a similar exacerbation of existing metastatic lesions in the brain, and enhance tumour proliferation via a tumour-promoting inflammatory response.

Investigation of the role of the systemic inflammatory response in the development of brain metastasis requires a strict definition to be placed on the inflammatory response in question. At one end of the spectrum sepsis induced by blood-borne pathogens can lead to multiple organ failure and death, whereas at the other a high dose bolus injection of pro-inflammatory cytokine such as TNF-α gives rise to a transient systemic inflammatory state. In the work described here, a replication-deficient adenovirus was used to induce a prolonged cytokine release into the bloodstream and thus a sustained but moderate inflammatory state.

A bolus intravenous injection of LPS causes a rapid increase in the levels of circulating IL-1β, which peaks after 2 h and is followed by increased levels of circulating IL-1ra, the inhibitor of the pro-inflammatory effects of IL-1α and IL-1β, 3-6 h after LPS injection. This efficiently 'mops up' IL-1β, maintaining inflammatory homeostasis (Granowitz et al., 1991; Arend, 2002). By contrast, using a virus as a vehicle to induce cytokine expression by Kupffer cells in the liver, through incorporation of the viral plasmid, induces a steady up-regulation of the pro-inflammatory cytokine of interest (Kolb et al., 2001). Three different viruses were grown and purified (see Materials and Methods, Section 2.3.2): (i) containing a plasmid encoding the human IL-1β protein (AdIL-1β); (ii) containing a plasmid encoding the mouse TNF-α protein (AdTNF-α); (iii) a control virus that did not encode a specific protein, but that should elicit an inflammatory response as a result of its viral coat protein (Ad70-3) (Bett et al., 1994; Richards et al., 1995; Marr et al., 1997; Kolb et al., 2001; Margetts et al., 2002). The adenoviruses in this study all lacked the E1 and E3 early stage replication proteins, preventing their replication following injection into the mice. Thus, the viruses acted as a vehicle for the induction of the two pro-inflammatory cytokines of interest, but did not contribute to the inflammatory status of the mouse as a result of their own replication.

Next, to determine the effect of local inflammation within the brain on the development of metastases, I injected bolus doses of pro-inflammatory cytokines into the left striatum. The result of this treatment is a transient, unilateral inflammatory response (Blamire et al., 2000; Blond et al., 2002; Sibson et al., 2002; Wilcockson et al., 2002; Ferrari et al., 2004), identifiable by MRI (Sibson et al., 2004). Injection of 4T1 cells into the heart four hours after central cytokine injection allowed determination of the effect of inducing focal central inflammation on the development of metastatic lesions within the brain. The two pro-inflammatory cytokines chosen were murine IL-1β and murine TNF-α. The injection of mIL-

1β injected into the striatum has been shown to cause ipsilateral up-regulation of endothelial VCAM-1 4 hours after injection, but negligible levels of contralateral endothelial VCAM-1 expression (McAteer et al., 2007). Similarly, mTNF-α injection induces unilateral endothelial activation acutely, although to a lesser extent than IL-1β (Sibson et al., 2004). Thus, the contralateral hemisphere acts as an internal control following unilateral injection of IL-1β or TNF-α.

At the same time, injection of mIL-1β or mTNF-α into the rat striatum has been shown to cause differential recruitment of neutrophils or mononuclear cells to the injection site, respectively. Unlike peripheral tissue, where IL-1β and TNF-α induce reciprocal as well as self-expression (Luger and Schwarz, 1990) and recruitment of neutrophils and mononuclear cells is similar, in the brain IL-1β injection promotes further synthesis of IL-β only, whereas TNF-α injection does not cause up-regulation of either itself or IL-1β (Blond et al., 2002). Consequently, it seems, IL-1β injection causes a 10-fold increase in recruitment of neutrophils compared to mononuclear cells, whilst TNF-α injection causes a 20-fold increase in mononuclear cells compared to neutrophils (Schnell et al., 1999).

Central neuroinflammation and its manifestation on cerebral blood vessels may allow pro-arrest or pro-extravasation signalling between tumour cells in the circulation and the vascular endothelium. The differential inflammatory responses in the two hemispheres may, therefore, cause a change in the number of metastatic cells that form tumours in these brain regions. The caudate putamen exhibits a relative abundance of metastases that is close to the expected value (Figure 4.3). Thus, I conducted a pilot study to test the hypothesis that a focal injection of cytokine may cause a 'targeting' of metastatic cells to this region, increasing the relative abundance of tumours here.

5.1.2 Outstanding questions

The use of an adenovirus to induce a specific systemic inflammatory response allows several different avenues to be explored in this work. Unlike a systemic inflammatory response to a broad-range immune inducer such as LPS, the use of an adenovirus enables precise control over the type and magnitude of the inflammatory response, and, therefore, the possible different activation cues to tumour cells in circulation.

Thus, I tested the following six hypotheses in this chapter:

1 That intravenous injection of AdIL-1β, AdTNF-α and Ad70-3 elicit differential upregulation of peripheral cytokines and neurovascular VCAM-1 expression.

2 That the number of metastases seeding in the brain increases in animals pre-treated with adenovirus.

3 That the growth rate of tumours seeded in the brain is greater in animals post-treated with adenovirus.

4 That adenovirus-treatment causes a different pattern of tumour growth, as reflected by tumour morphology.

5 That differences in neuroinflammation as a result of adenovirus injection, in the presence or absence of brain metastases, are detectable by VCAM-MPIO MRI.

6 That local neuroinflammation caused by intrastriatal injection of rmTNF-α or rmIL-1β causes an increase in the number of tumours that develop in the ipsilateral striatum compared to the contralateral striatum.

5.2 Methods

5.2.1 Adenoviruses

Three adenoviruses were used for this work. The first expressed human IL-1β, the second mouse TNF-α, and the third was a null virus that did not express any pro-inflammatory cytokine. Viral stocks were kept refrigerated at -80 °C and were diluted in sterile saline prior to injection. In order to test the efficacy of the virus, medium samples were collected from cultured HEK-293 cells infected with each virus at days 1, 2 and 3, and serum samples were collected from mice infected with each virus at 1, 4, 12, 24 hours, 3, 5, 8, 11 and 14 days post-injection. The concentrations of a range of cytokines were determined using a Quantibody Array (Raybiotech).

5.2.2 Animal models

Systemic inflammatory model

Female BALB/c mice aged 7-10 weeks were intravenously injected with 8×10^6 plaque forming units (pfu) of adenovirus either 1 day pre- or 5 days post-intracardial injection of 1×10^5 4T1-GFP cells in 100 µL PBS (Section 2.1). Animals were imaged 10 days after intracardial injection (Figure 5.1). Animals were killed after imaging by perfusion/fixation with 0.9% heparinised saline and PLP_{light}, and the brain dissected out for immunohistochemical and immunofluorescent staining.

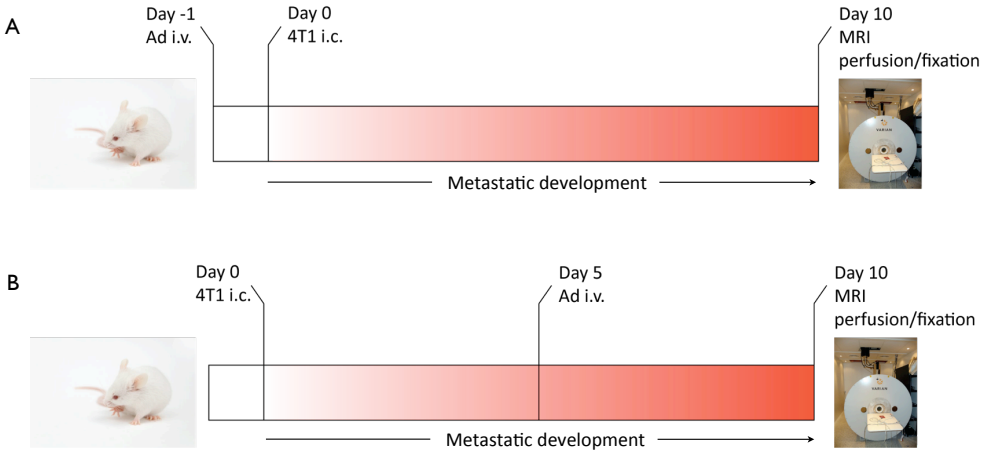


Figure 5.1 –Experimental schedule for systemic inflammation. (A) Mice were intravenously injected with 8 × 10^6 pfu adenovirus 1 day before intracardial tumour injection. (B) Mice were injected intracardially with tumours and 5 days later were intravenously injected with the same titre of adenovirus. In both experimental schedules tumours were allowed to develop for 10 days before the animals were imaged and perfused/fixed.

Localised neuroinflammatory model

Female BALB/c mice aged 7-10 weeks were either intrastriatally injected with saline, mTNF-α or mIL-1β four hours (Figure 5.2) prior to intracardial injection of 10^5 4T1-GFP cells (Section 2.1). Tumours were allowed to develop for ten days before animals were imaged and perfused/fixed with 0.9% saline and PLP_{light}.

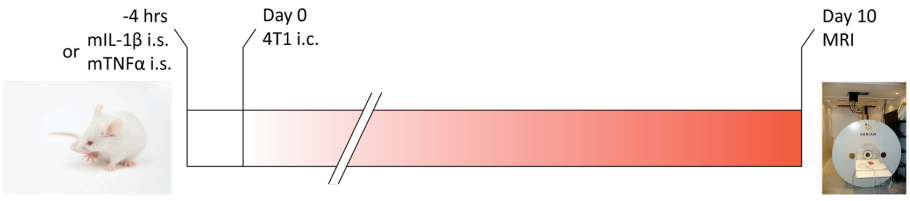


Figure 5.2 – Experimental schedule for localised neuroinflammation. Injection of pro-inflammatory cytokines IL-1β or TNF-α, or sterile saline control, 4 h prior to tumour cell injection. Tumours were allowed to develop for 10 days before the animals were imaged and perfused/fixed.

5.2.3 MRI

Animals were injected with VCAM-MPIO (4 mg Fe/kg) in 100 µL sterile saline 1 h prior to imaging. The tail vein was cannulated immediately prior to imaging. Animals were imaged at 7 T under isoflurane anaesthesia in 50:50 O_2:N_2. GE3D datasets with 2 averages were acquired for all adenovirus- and tumour-burdened animals (40 min scan). GE3D datasets with 1 average were acquired for animals imaged 4 h after central cytokine injection (20 min scan). T1-weighted pre- and post-Gd datasets were acquired to assess BBB breakdown, as well as a T2-weighted dataset to aid colocalisation of metastatic lesions and hypointensities in tumour-burdened animals (Section 2.3.5).

5.2.4 Immunohistochemistry / Immunofluorescence

Brains were cryoprotected in 30% sucrose and rapidly frozen in Tissue Tek before being cut on a cryostat. Sections were either DAB stained immunohistochemically for GFP to locate and characterize metastatic lesions in the brain, or stained immunofluorescently to colocalise VCAM-1 with laminin, αSMA or EphB4 expression on cerebral blood vessels, and GFP expression on tumours. For single fluorophore staining, TSA amplification was used; for double fluorophore staining TSA amplification, followed by A-P amplification (Section 2.3.6).

5.2.5 Analysis tools

Analysis tools developed in MATLAB were used for the analysis of cerebral hypointensities (Chapter 3). Light microscopy images were obtained using an Aperio Slide Scanner; fluorescence microscopy images were obtained using either an epifluorescent microscope or a confocal microscope (Section 2.3.9).

5.2.6 Statistics

Statistics were performed using MATLAB. 1-way and 2-way analysis of variance was performed when the data was suitably distributed; a non-parametric Kruskal-Wallis test was used to test differences between highly skewed datasets. The significance of correlated data was tested using Pearson's correlation coefficient (Section 2.3.10).

5.3 Results

5.3.1 Adenovirus effects on systemic inflammation

To establish efficacy of the viral constructs, HEK-293 cells were cultured with each adenovirus and the medium sampled after 1, 2 and 3 days (Figure 5.3). Subsequently, serum was collected at intervals over 14 days from mice injected with each virus (Figure 5.4) and from mice injected with 4T1-GFP cells alone (Figure 5.5). Expression profiles of ten different cytokines were compared between the groups for both cell media and serum. With the exception of human IL-1β all cytokines studied were murine and comprised the following: TNF-α, Granzyme B, IFN-γ, IL-4, I-Tac, KC, MCP-1, MIG and SDF-1α. The choice of cytokines to study was three-tiered. Firstly, given the expected action of the viruses used in these experiments, it was important to determine whether elevated levels of hIL-1β or mTNF-α could be detected following AdIL-1β and AdTNF-α injection respectively. Secondly, a pilot assay using an R&D systems cytokine panel (see Appendix 3) revealed a number of candidate cytokines that appeared to be differentially upregulated by the three viruses (SDF-1α, I-Tac, IL-4). Thirdly, selected cytokines were chosen to report on relevant features of the immune status of the animals and to reveal whether particular types of cells were activated as a result of viral exposure (Granzyme B, IFN-γ, KC, MCP-1, MIG).

Medium samples from HEK-293 culture

Medium samples showed expression of hIL-1β by AdIL-1β at days 1 and 2 after inoculation of HEK-293 cells with the virus (Figure 5.3). No hIL-1β was observed at day 3, possibly owing to viral-induced cell lysis by this time-point, as observed in HEK-293 cell culture. TNF-α and IL-4 were both detected at day 2 in HEK-293 treated with AdIL-1β. Both the AdTNF-α and Ad70-3 caused increases in MCP-1 in the medium at day 3, with a greater effect from AdTNF-α than Ad70-3. No other cytokines were detected at any time-point.

Serum samples from adenovirus-injected mice

A transient elevation in soluble TNF-α expression was observed in the AdIL-1β- and Ad70-3-injected mice four hours post-injection, but not in AdTNF-α-injected mice (Figure 5.4). Increased expression was no longer detectable at 12 hours post-injection. Expression of I-Tac was observed in AdIL-1β after one hour, and in AdTNF-α and Ad70-3 after 24 hours, with no remaining levels detectable at four hours or 48 hours, respectively. Ad70-3-induced expression of I-Tac coincided with a peak in the expression of MCP-1 at 24 hours, and a later peak in MCP-1 expression was observed five days post-viral injection. Similarly, I-Tac expression in AdTNF-α-injected animals coincided with a peak in MIG expression at 24 hours, with a second peak five days post-viral injection. IFN-γ and SDF-1α expression levels were only observed in Ad70-3 animals, both 14 days post-viral injection. Levels of KC (5 - 27 pg/mL) were detected in serum of animals at all time-points post-viral injection, but similar levels were detected in naïve serum samples. No hIL-1β, Granzyme B or IL-4 was detected in mouse serum samples at any time-point after adenovirus injection.

Serum samples from tumour-injected mice

Low levels of hIL-1β, IFN-γ and I-Tac were observed ten days post-4T1 injection (Figure 5.5). KC levels were observed five and ten days post-4T1 injection at similar levels to that detected in naïve and adenovirus-injected animals (Figure 5.4). No other cytokines were detected either five or ten days post-4T1 injection.

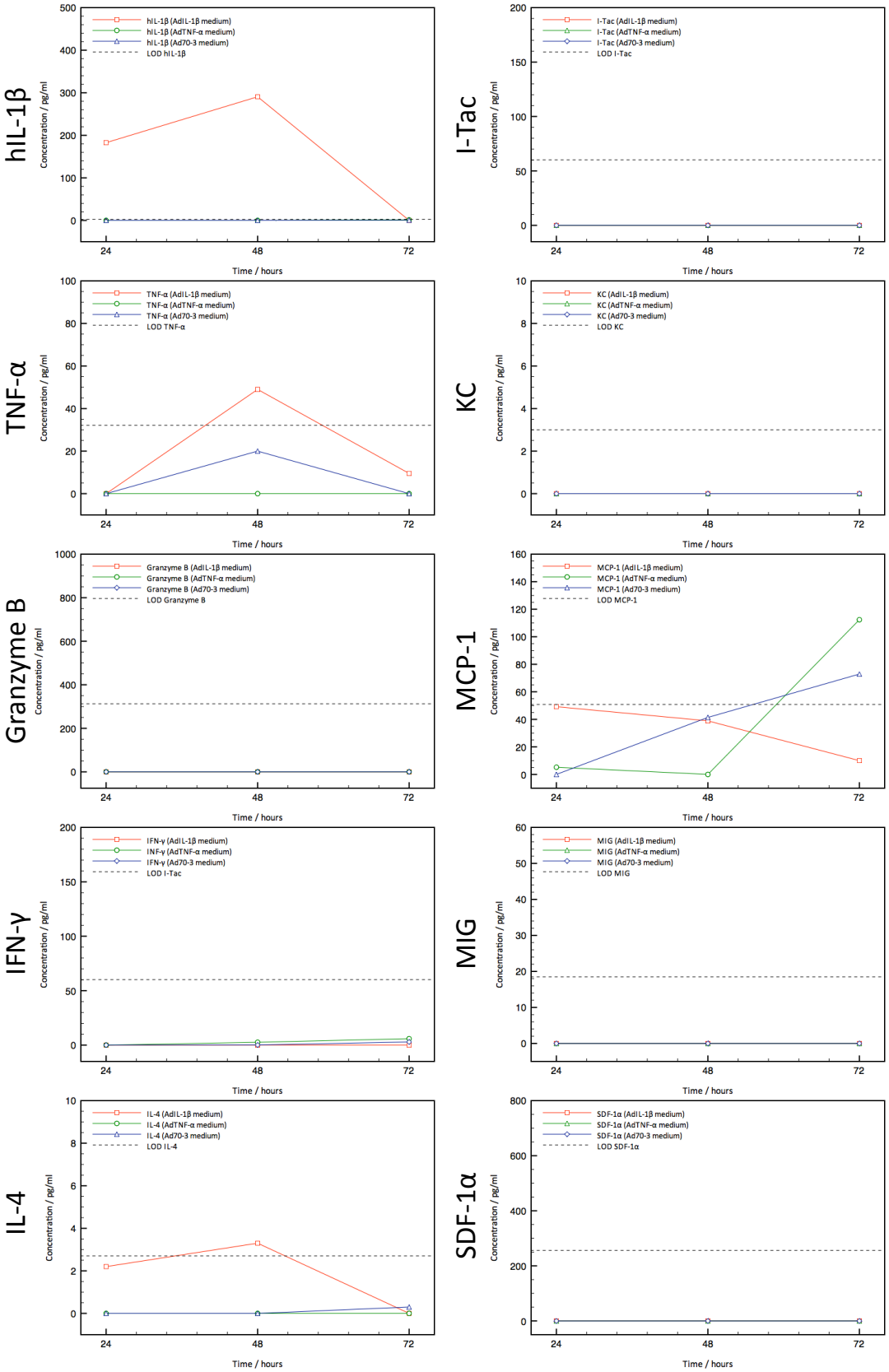


Figure 5.3 – Medium concentrations in picograms per millilitre of ten cytokines at 1, 2 & 3 days following infection of HEK-293 cells with adenoviruses. All data below the LOD is assumed to represent 0 pg/ml.

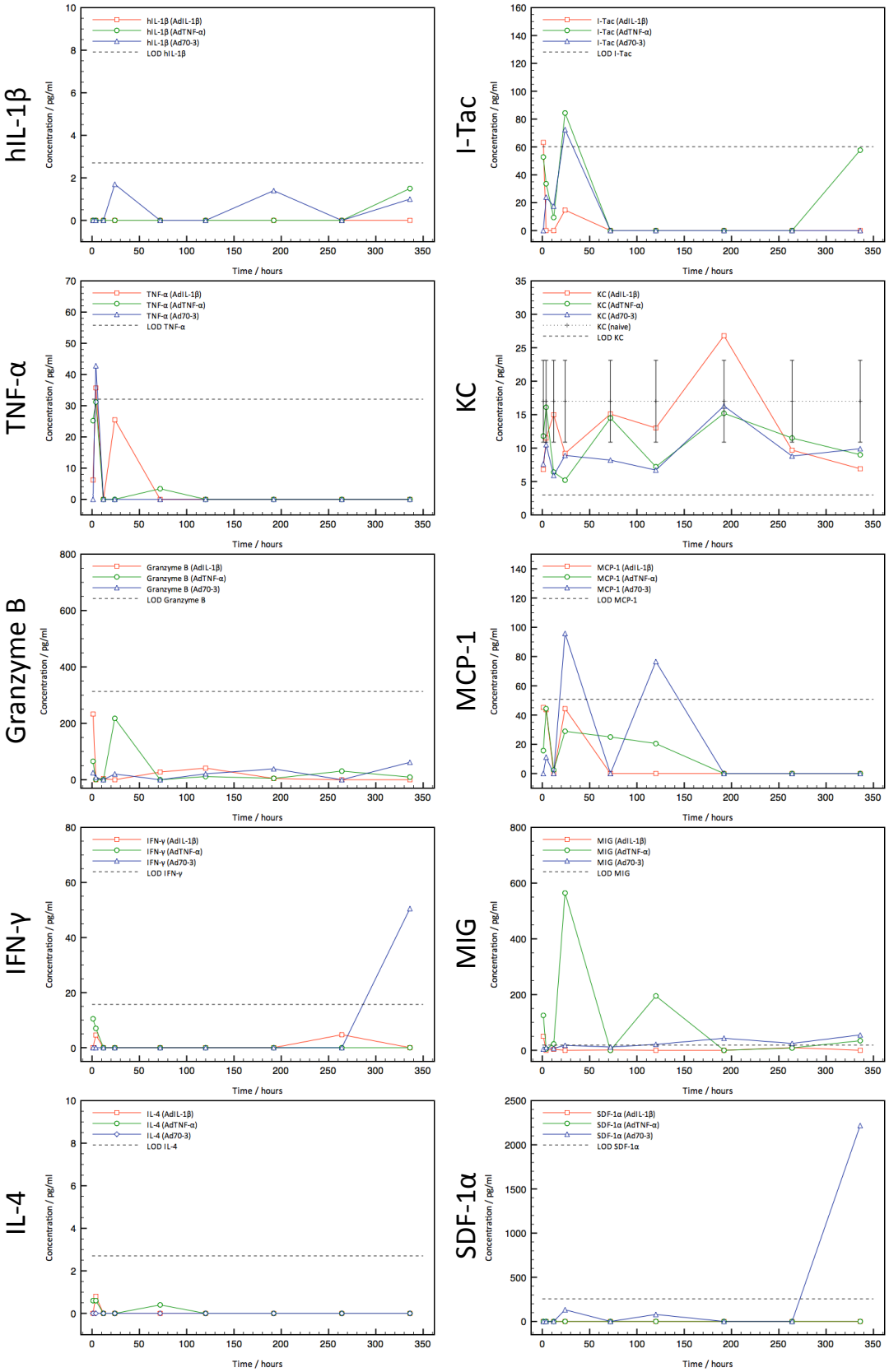


Figure 5.4 – Serum concentrations in picograms per millilitre of ten cytokines at 1, 4, 12, 24 hours, 3, 5, 8, 11 & 14 days following injection of replication-deficient adenoviruses. All data below the LOD is assumed to represent 0 pg/ml.

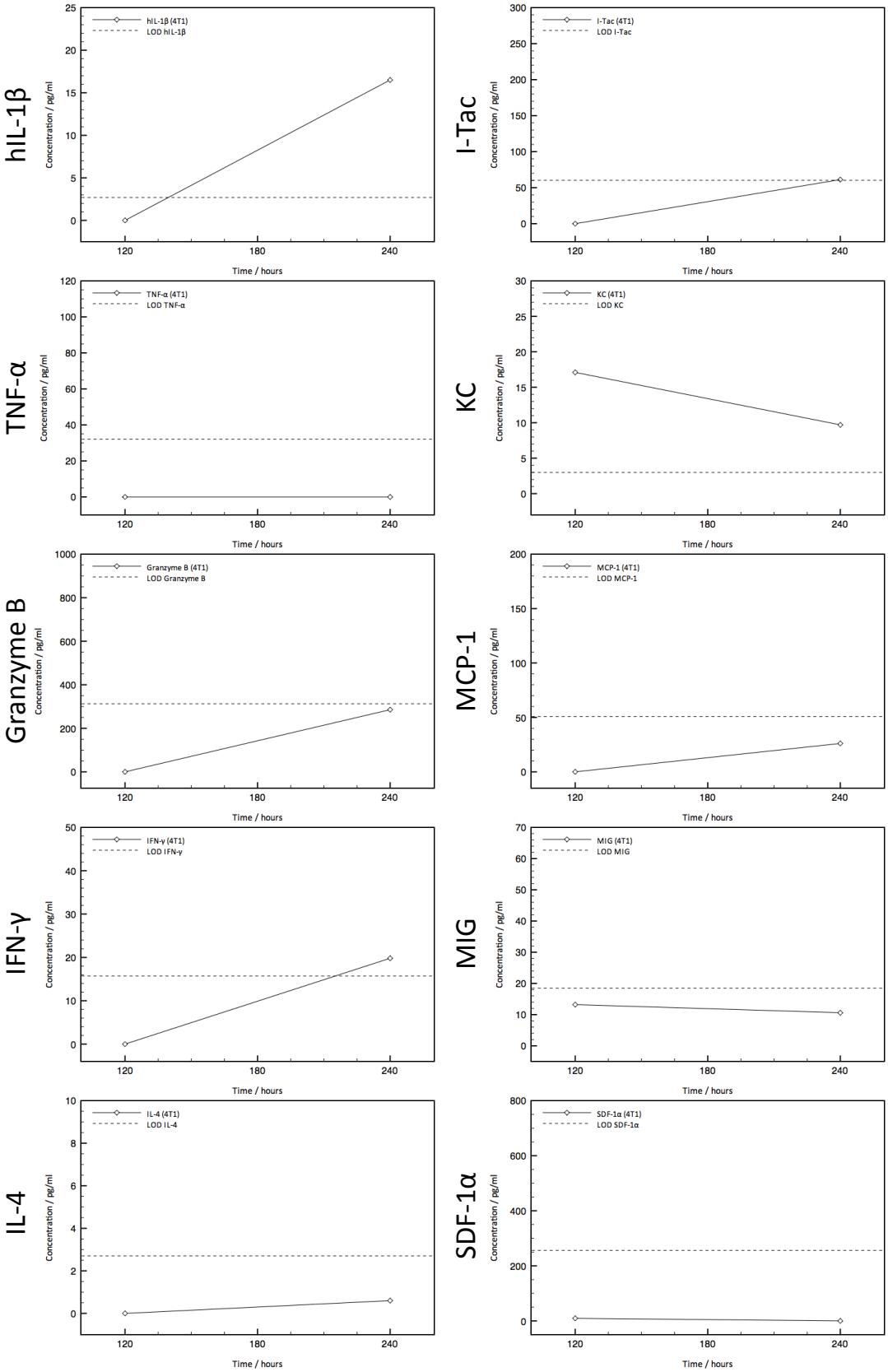


Figure 5.5 – Serum concentrations in picograms per millilitre of ten cytokines 5 & 10 days following intra-cardiac injection with 4T1-GFP tumour cells. All data below the LOD is assumed to represent 0 pg/ml.

5.3.2 Adenovirus effects on cerebral VCAM-1 expression

VCAM-1 is not constitutively expressed by endothelial cells lining cerebral blood vessels (Carlos et al., 1990; Wong and Dorovini-Zis, 1995). However, it has been shown that VCAM-1 expression can be induced in HBMEC culture by treatment with LPS, TNF-α, IL-1β or IFN-γ (Wong and Dorovini-Zis, 1995), or by local administration of Theiler's virus (Mestre et al., 2011), TNF-α or IL-1β *in vivo* (Sibson et al., 2004; McAteer et al., 2007). Immunofluorescent imaging of the cerebral vasculature in naïve animals corresponds with previous observations that there is no constitutive VCAM-1 expression on these vessels. As a result of adenoviral injection, VCAM-1 expression on cerebral blood vessels is induced (Figure 5.6), demonstrating that this model of peripheral systemic inflammation can cause a central inflammatory response. Although VCAM-1 is seen on a small proportion of blood vessels only, with a maximum of about 4% after 5 days in Ad70-3 injected animals (Figure 5.6B), expression is much more common on arterial vessels than venous vessels (Figure 5.6D & F), regardless of the type of virus that has been injected.

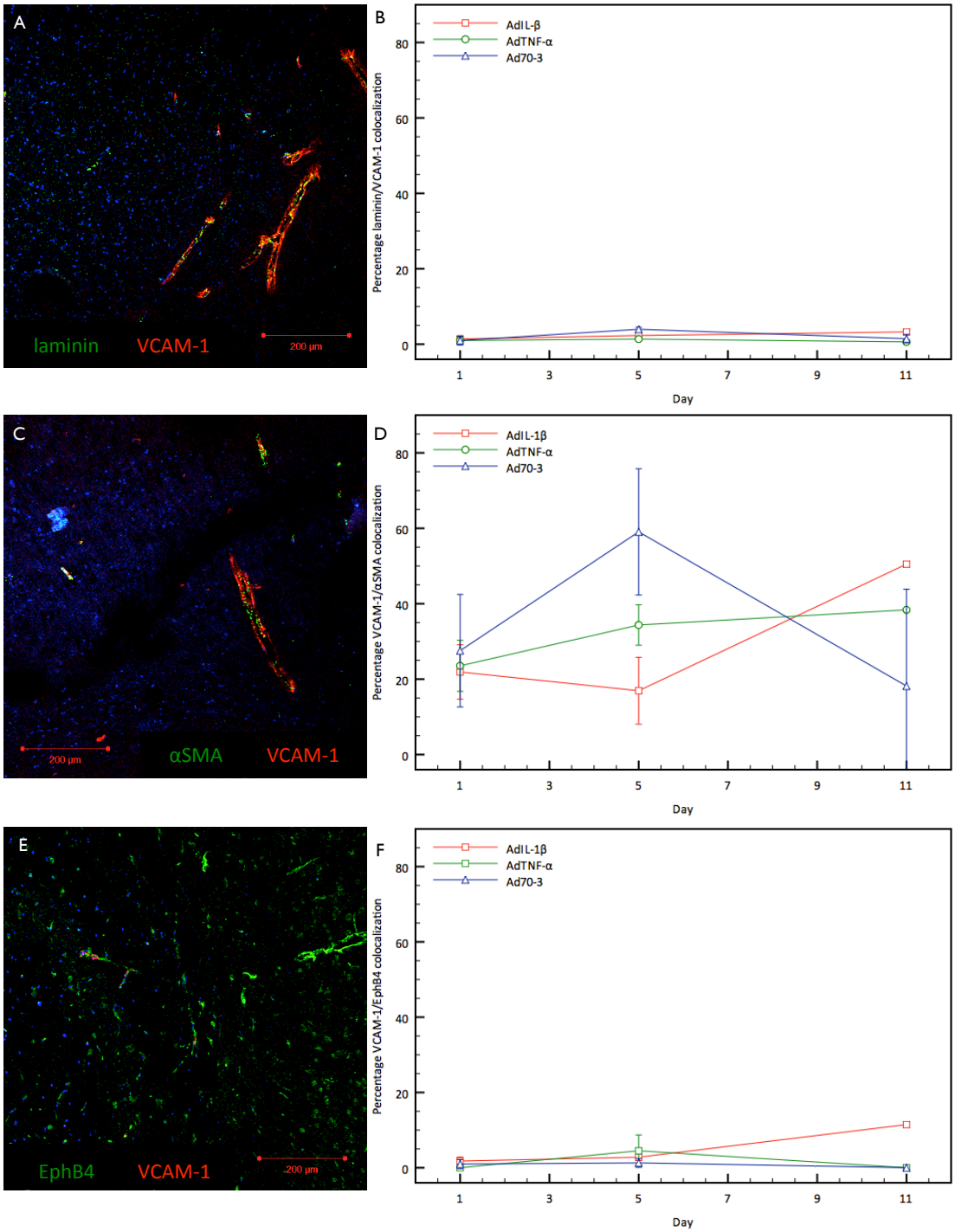


Figure 5.6 – Expression of VCAM-1 on cerebral vasculature as a result of adenoviral exposure. (A) Immunofluorescence image showing the colocalisation of laminin positive cerebral blood vessels (green) and VCAM-1 positive vessels (red). (B) Groups of laminin expressing blood vessels (all blood vessels in the brain) were interrogated to see what proportion were expressing VCAM-1. The proportions are low at around 2% for all viruses at all time points. However, the AdTNF-α virus consistently showed the lowest level of VCAM-1 upregulation; Ad70-3 appears to show higher levels

at day 5, AdIL-1β at day 11. (C) Immunofluorescence image showing the colocalisation of αSMA positive arterial blood vessels (green) and VCAM-1 positive vessels (red). (D) Groups of VCAM-1 expressing blood vessels were interrogated to see what proportion were on αSMA positive arteriolar vessels. In all cases this represented 20 – 60% of all VCAM-1 positive vessels. (E) Immunofluorescence image showing the colocalisation of EphB4 positive venous blood vessels (green) and VCAM-1 positive vessels (red). (F) Groups of VCAM-1 expressing blood vessels were interrogated to see what proportion were on EphB4 positive venous vessels. Many fewer VCAM-1 positive vessels were EphB4 positive, suggesting that the majority of VCAM-1 expression takes place at the arterial end of the vasculature rather than the venous end. Basal levels of VCAM-1 expression in naïve animals were nil. Error bars denote one standard deviation from the mean.

5.3.3 MRI of adenovirus-injected animals

The increased expression of VCAM-1 on brain vasculature described above was also investigated *in vivo* using MRI and VCAM-MPIO, as per the previous chapter.

GE3D data

GE3D data from animals at 5 and 11 days post-adenoviral injection showed no significant differences from naïve animals (Figure 5.7). This is perhaps surprising considering the elevated expression of VCAM-1 on the brain endothelium at these timepoints following adenoviral injection. However, as noted above, this VCAM-1 expression is only evident on a very small percentage of vessels and, thus, is likely to be insufficient to induce a detectable effect on VCAM-MPIO binding. The apparent trend (not significant, $p = 0.0504$) towards a reduction in hypointensities in the AdTNF-α and Ad70-3 pre-treated groups may simply reflect differences in VCAM-MPIO batches or intergroup variability. Increased numbers of animals would further confirm this trend.

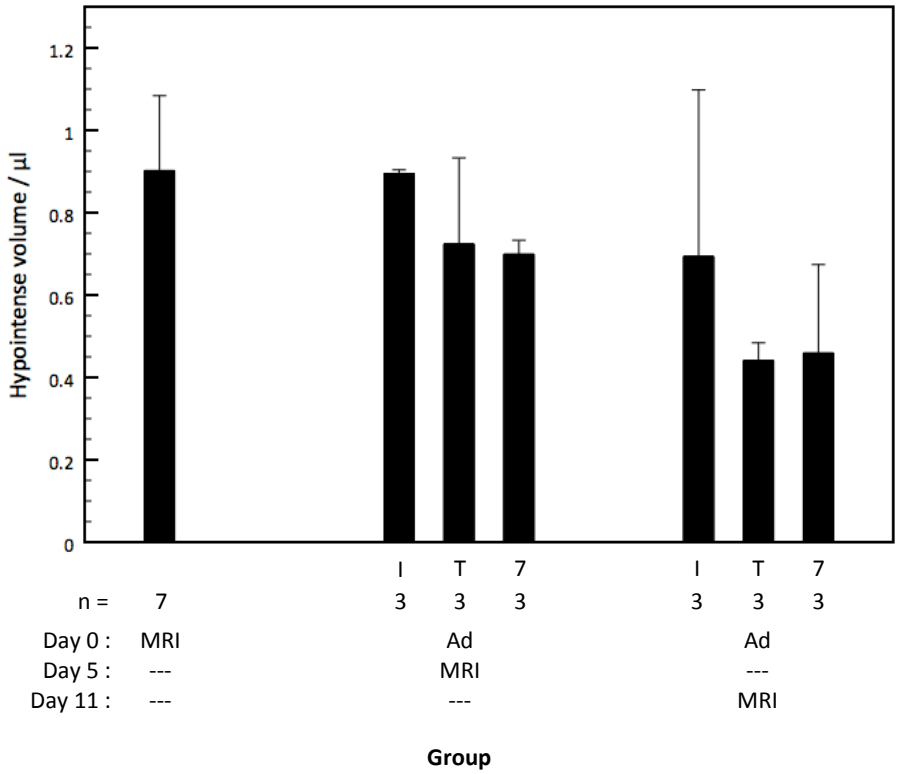


Figure 5.7 – Adenovirus GE3D MRI data. The volume of medium-sized hypointensities comprises 0.90 µL of the entire brain volume in 7 naïve animals studied. This value is in contrast to the naïve values of 0.1-0.2 µL reported in Serres (2012). Slightly lower volumes of hypointensity were detected in all other adenovirus-injected animals at days 5 and 11, although no statistical differences were found between treatment groups ($p = 0.0504$). Error bars denote one standard deviation from the mean. (I = AdIL-1β; T = AdTNF-α; 7 = Ad70-3).

5.3.4 Adenovirus effects on tumour development

Metastases were identified by means of immunohistochemical GFP expression, or, when GFP expression levels in tumour cells were low, by cresyl violet staining. Analysis of tumour numbers revealed that the overall effect of an adenovirus pre- or post-treatment was a significant reduction in the total number of metastases in the brain (Figure 5.8A). When the effect of each virus was analysed separately (Figure 5.8B) the same effect was visible, but no significant differences to untreated animals were observed. Differences between each of the three viruses in the two treatment groups were also suggested by the data, but did not reach significance.

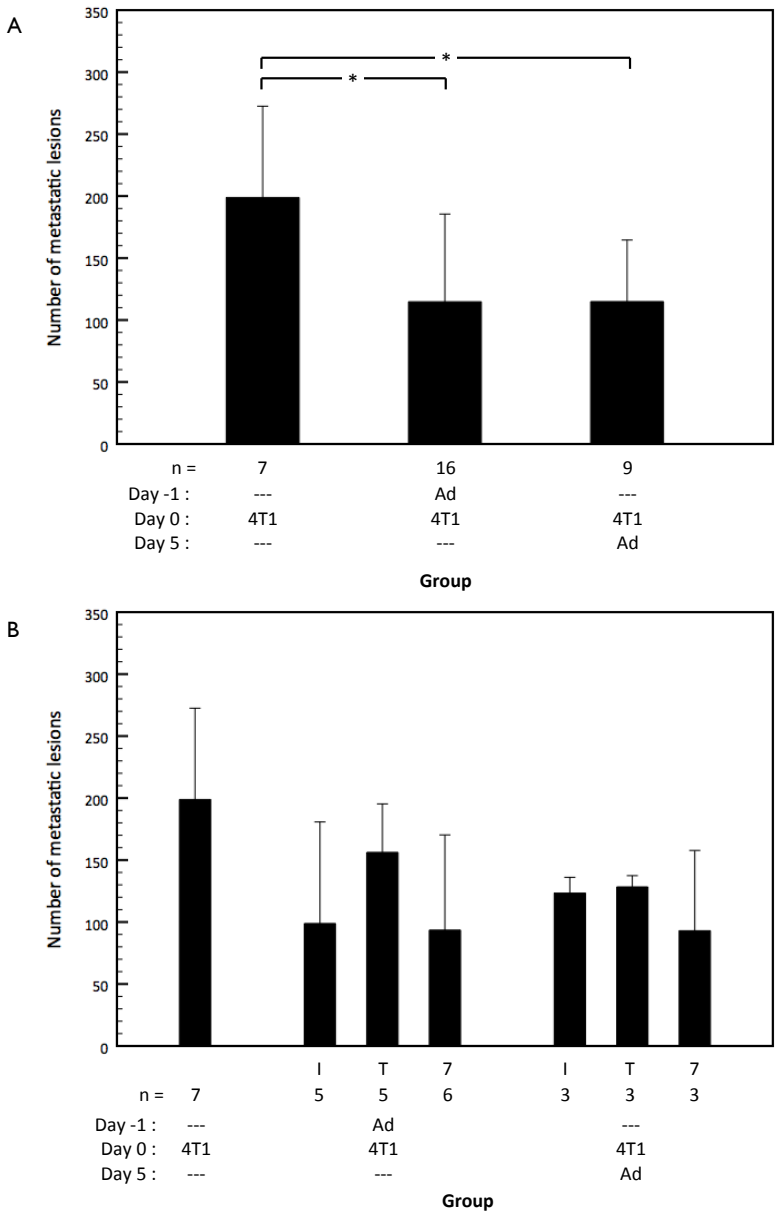


Figure 5.8 – Numbers of metastatic lesions in brains with and without adenovirus treatment. (A) Overall comparison between untreated and adenovirus pre- and post-treatment groups revealed an approximately twofold reduction in the number of cerebral metastases in both groups of adenovirus-treated animals (ANOVA, $p = 0.02$). (B) Individual virus treatments appeared to cause a reduction in the tumour number compared to untreated animals, although this did not reach significance. (I = AdIL-1β; T = AdTNF-α; 7 = Ad70-3).

The volumes of each metastasis were measured and summed to give the total volume of metastases throughout the brain, known as the metastatic burden. In addition to the number of metastases present in the brain, the effect of adenoviral pre- or post-treatment on the metastatic burden was also measured (Figure 5.9). The data suggest a reduction in the metastatic burden as a result of adenoviral treatment, although no significant differences were observed, either looking at overall treatment groups or individual viral treatment groups. Taken alongside the reduction in tumour numbers (Figure 5.8), these data suggest that there may be differences in the rate of growth of individual metastatic lesions between untreated and adenovirus-treated animals.

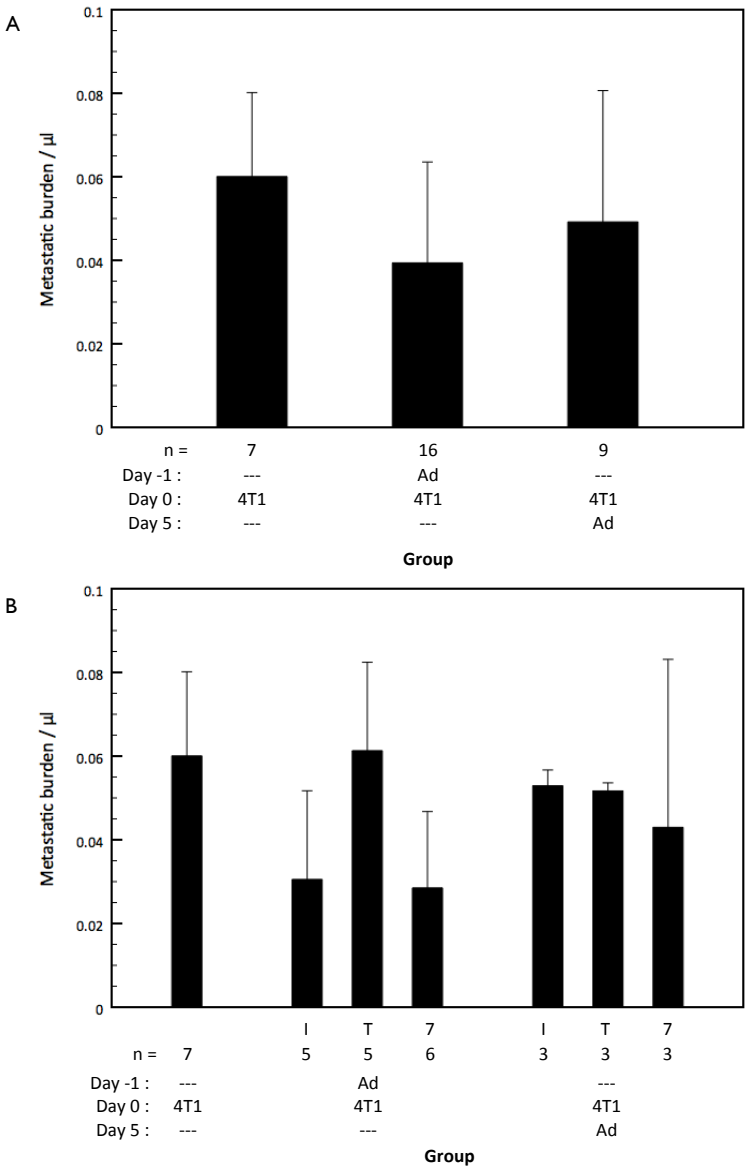


Figure 5.9 – Total metastatic burden in brains with a systemic inflammatory response. (A) A trend towards a decrease in the overall metastatic burden as a result of adenoviral pre- or post-treatment compared to untreated animals was suggested by the data, but no significant differences were observed. (B) Similarly, there appeared to be a general reduction in the metastatic burden across several groups compared to animals that were exposed to 4T1 cells only. The metastatic burden in animals exposed to virus appeared to be smaller in animals pre-treated with AdIL-1β or Ad70-3 than in animals exposed to 4T1 cells only, but no significant differences were found between any groups. (I = AdIL-1β; T = AdTNF-α; 7 = Ad70-3).

In the previous chapter the morphologies of tumours were described (volume, range, number of objects and sphericity) and compared between the five different brain sections sampled (Section 4.3.4; Figures 4.6-4.9). In this chapter tumours were analysed for the same features across all brain sections sampled and their morphologies were compared between treatment groups, (Figures 5.10 - 5.13).

Volume

Tumour areas were measured in sequential 10 µm sections from which volumes were estimated by summing all areas and linear interpolates. Tumour volume distributions were measured for all treatment groups, as shown in Figure 5.10. All treatment groups showed similar distributions of tumour volumes, with a large proportion of small metastases, and a long tail of larger metastases. No significant differences were observed in the distributions of tumour volumes between treatment groups.

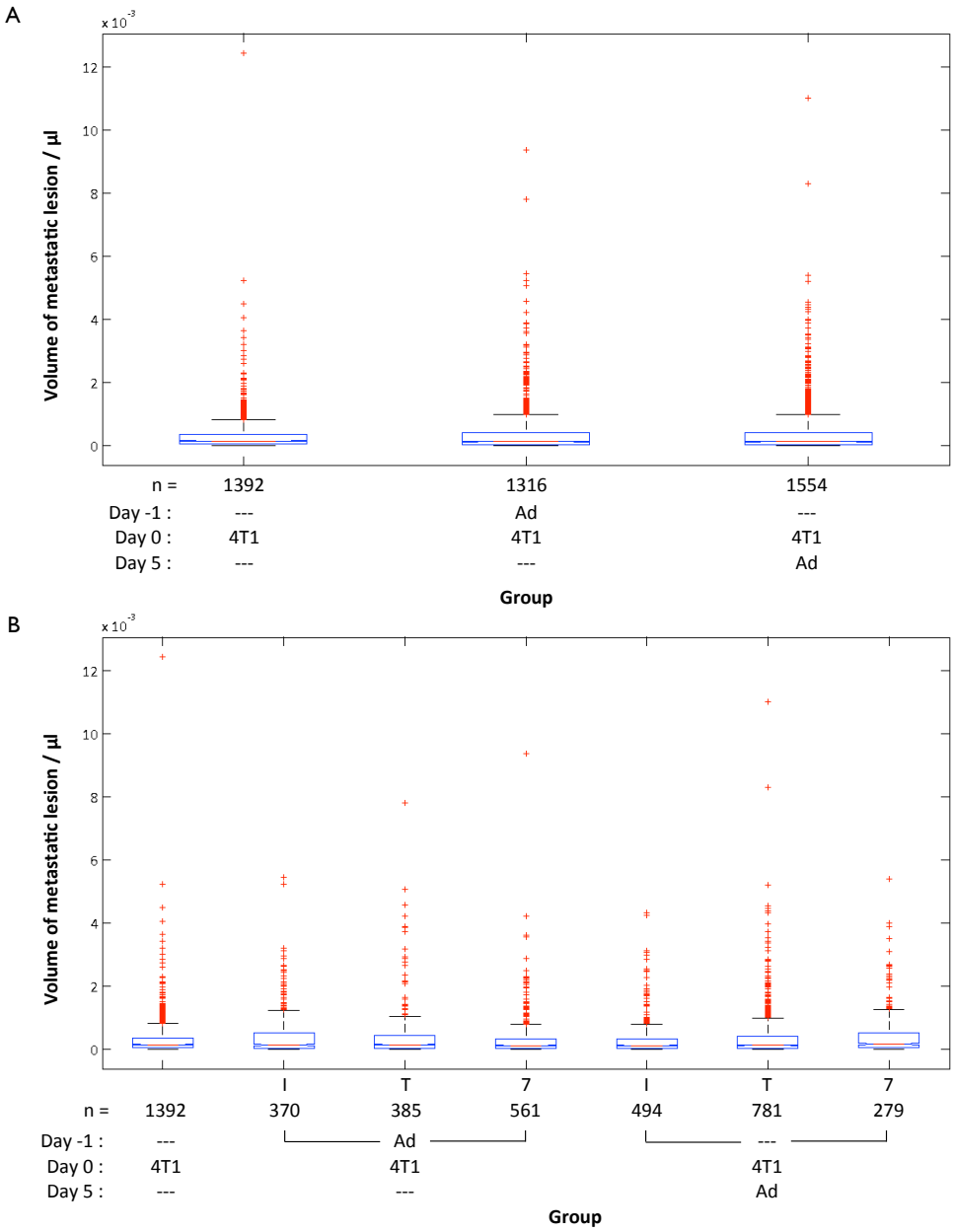


Figure 5.10 – Size distributions of metastases. (A) Boxplots showing the volumes of metastatic lesions comparing untreated, adenovirus pre- and post-treated animals. A Kruskal-Wallis test revealed no significant differences between treatment groups. (B) Boxplots showing the volumes of metastatic lesions comparing all adenoviral groups. No significant differences were observed. (I = AdIL-1β; T = AdTNF-α; 7 = Ad70-3).

Range

Tumour range distributions were measured for all treatment groups, as shown in Figure 5.11. Metastatic lesions in adenovirus pre-treated animals showed a significantly smaller range compared to untreated animals and adenovirus post-treated animals ($p < 0.001$), suggesting that tumours in this treatment group may track less extensively along the local vasculature. Comparing individual adenoviruses identified that post-treatment with Ad70-3 resulted in tumours with greater ranges than those that had been pre-treated with the virus ($p = 0.002$). No other inter-group significant differences were found although a trend towards and increase in tumour range was also evident in mice pre-treated with AdIL-1β.

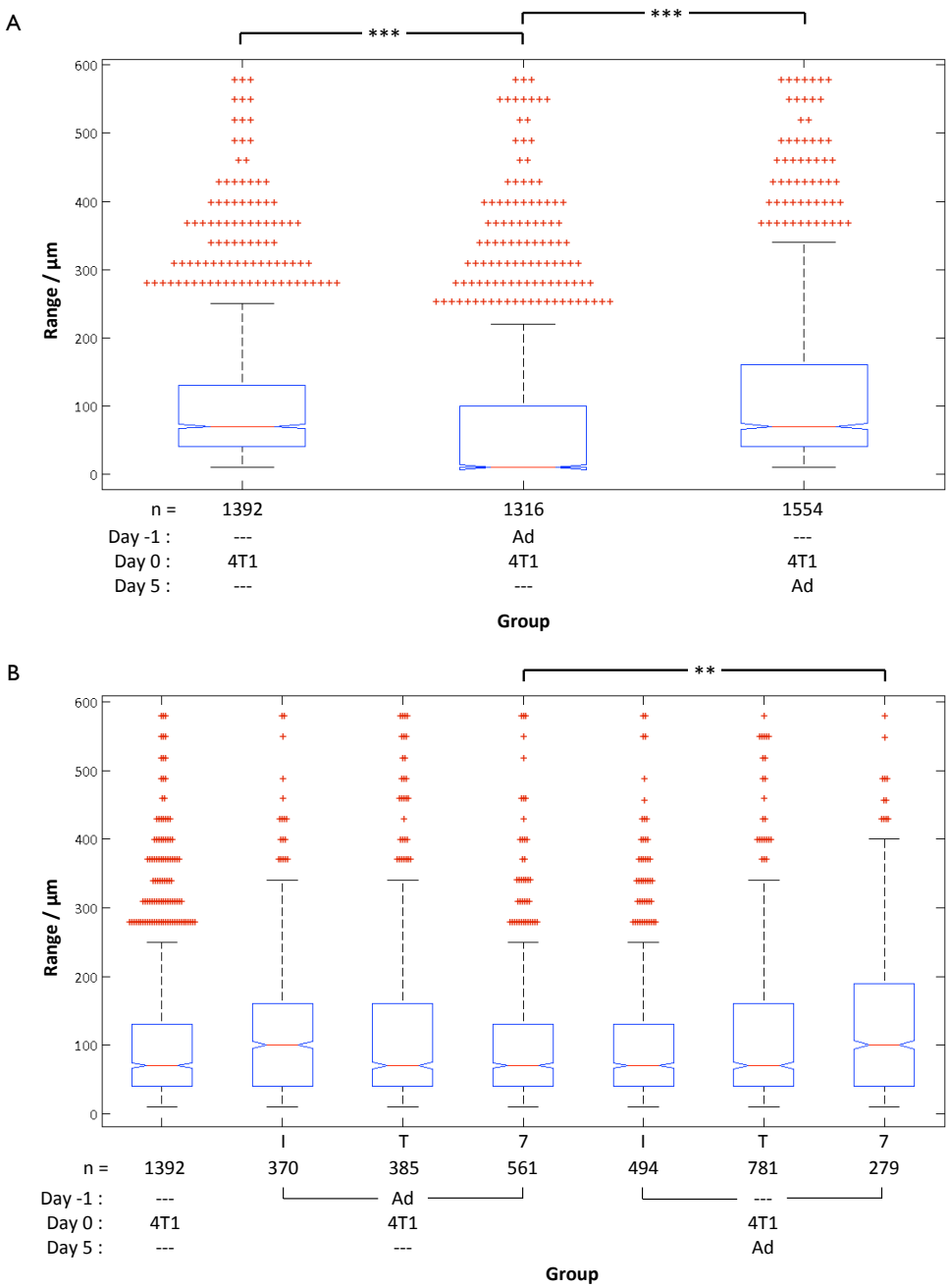


Figure 5.11 – Range distributions of metastases. (A) Boxplots showing the ranges of metastatic lesions comparing untreated, adenovirus pre- and post-treated animals. A Kruskal-Wallis test revealed that tumour ranges were significantly larger in adenovirus pre-treated animals compared to untreated and adenovirus post-treated animals ($p = 0.002$). (B) Boxplots showing the ranges of metastatic lesions comparing all adenoviral groups. Ad70-3 pre-treated animals developed tumours with greater ranges than Ad70-3 post treated animals ($p = 0.002$), although no treatment groups showed significant differences to 4T1-injected animals alone. (I = AdIL-1β; T = AdTNF-α; 7 = Ad70-3).

Number of objects

The average number of objects per section was measured for all treatment groups, as shown in Figure 5.12. The number of objects per metastatic lesion in all three groups was significantly different, suggesting differences in the degree of vascular co-option in each of the three groups ($p < 0.0001$). Adenoviral post-treatment caused the greatest level of vascular co-option and the least was seen in adenoviral pre-treated animals, suggesting not only that the pattern of tumour proliferation is altered by systemic inflammation, but also that the relative timing of systemic inflammation and tumour arrest and extravasation has an effect on the manner in which cerebral metastases develop (Figure 5.12A). Significant effects of individual virus treatments on the average number of objects were also observed ($p < 0.0001$). Pre-treatment with AdIL-1β and AdTNF-α showed an increase vascular co-option, as did post-treatment with AdTNF-α and Ad70-3 (Figure 5.12B), suggesting that effects of each virus resulted in differential tumour development.

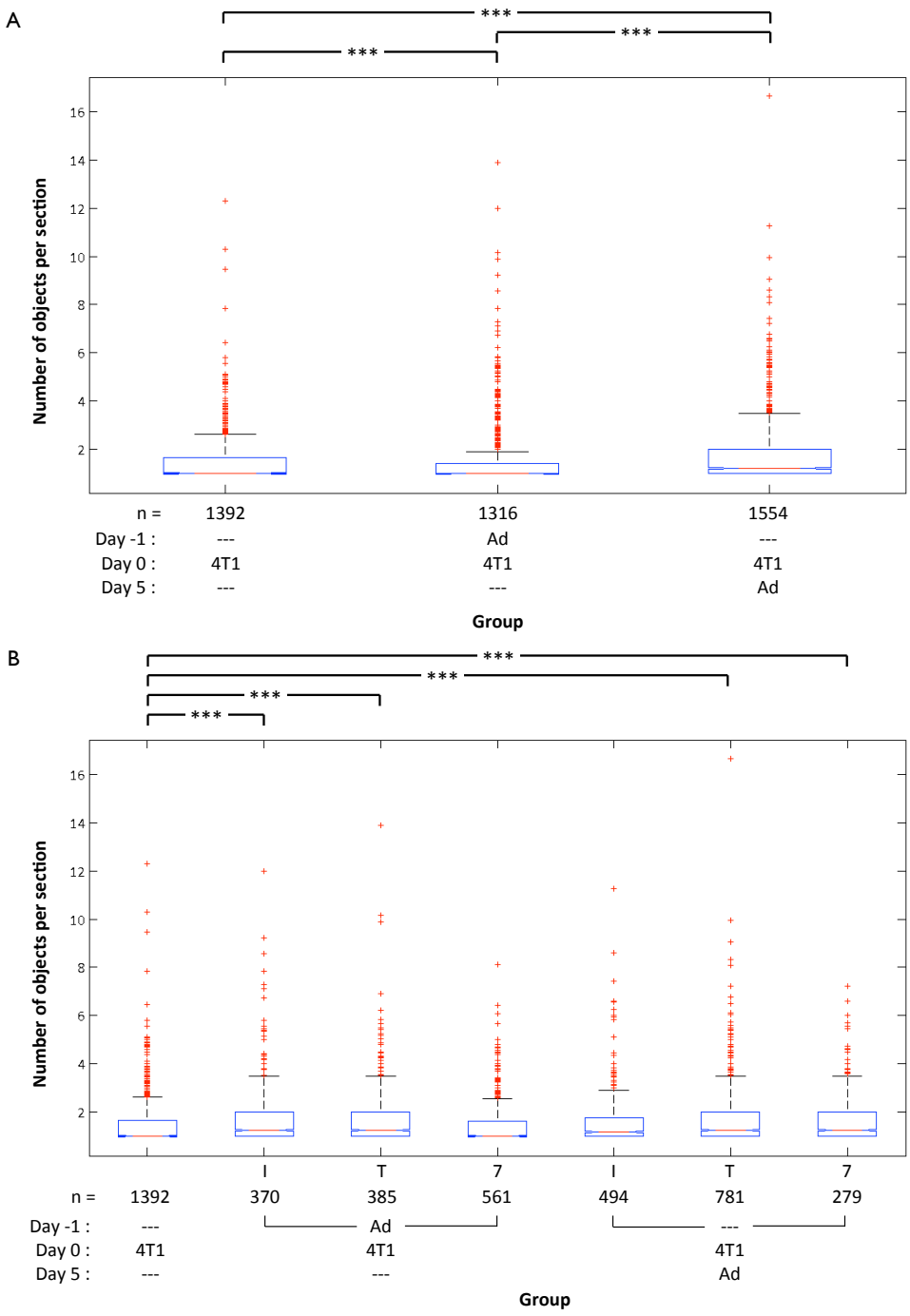


Figure 5.12 – Distributions of average numbers of objects per section. (A) Boxplots showing the numbers of objects per section of metastatic lesions comparing untreated, adenovirus pre- and post-treated animals. A Kruskal-Wallis test revealed that greater numbers of objects were observed as a result of adenovirus post-treatment compared to pre-treatment ($p < 0.0001$); untreated animals also showed a significantly greater numbers of objects compared to pre-treated animals ($p < 0.0001$). (B) Boxplots showing the numbers of objects in tumours comparing all adenoviral groups. A Kruskal-

Wallis test revealed that AdIL-1β and AdTNF-α pre-treated animals exhibited greater numbers of objects compared to untreated animals ($p < 0.0001$). A greater number of objects was found in Ad-TNF-α and Ad70-3 post-treated animals compared to untreated animals ($p < 0.0001$). (I = AdIL-1β; T = AdTNF-α; 7 = Ad70-3).

Sphericity

The average sphericity was measured for all treatment groups, as shown in Figure 5.13. Adenovirus pre-treatment resulted in a significant reduction in tumour sphericity compared to untreated and post-treated animals ($p < 0.0001$), as determined by a 1-way ANOVA (Figure 5.13A). A significant decrease in tumour sphericity was observed as a result of pre-treatment with AdIL-1β and a significant increase was observed as a result of post-treatment with Ad70-3 ($p < 0.0001$). Significant inter- and intra-specific variability was also observed in the adenoviral pre- and post-treatment groups. Tumour sphericities were significantly greater in post-treatment groups compared to pre-treatment groups for both AdIL-1β- and Ad70-3-treated animals ($p < 0.0001$) and greater in animals pre-treated with AdTNF-α compared to AdIL-1β ($p < 0.0001$) (Figure 5.13B).

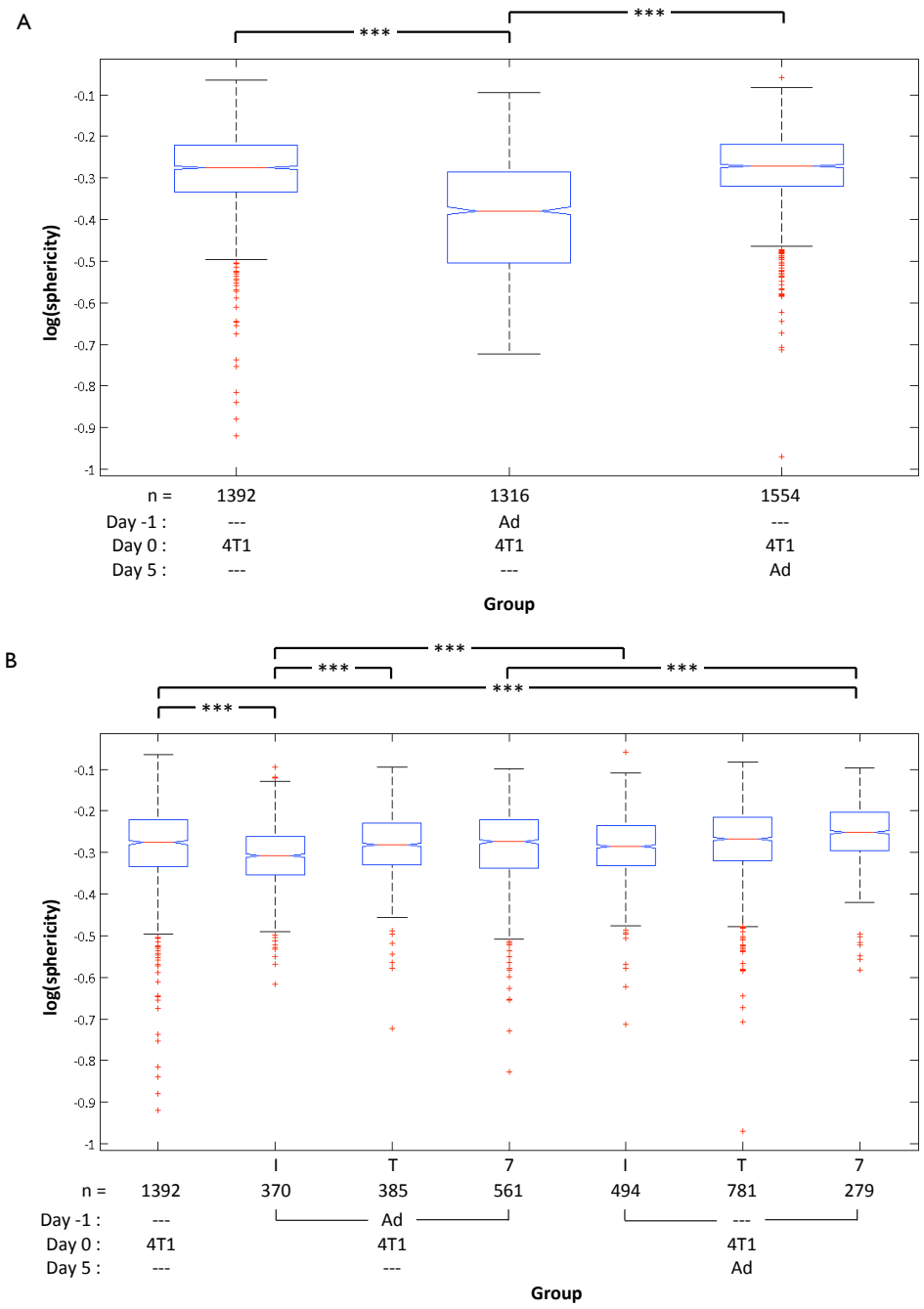


Figure 5.13 – Distributions of tumour sphericity. (A) Boxplots showing the sphericity of tumours comparing untreated, adenovirus pre- and post-treated animals. One-way analysis of variance revealed a significant reduction in tumour sphericity in adenovirus pre-treated animals compared to untreated and adenovirus post-treated animals ($p < 0.0001$). (B) Boxplots showing the sphericity of tumours between all groups. One-way analysis of variance revealed significant intergroup and intragroup differences in tumour sphericity ($p < 0.0001$). (I = AdIL-1β; T = AdTNF-α; 7 = Ad70-3).

5.3.5 MRI of adenovirus and tumour injected animals

GE3D data

GE3D MRI signal was measured in naïve animals, animals with tumours only and animals with a tumour burden and a systemic inflammatory challenge (Figure 5.14). No significant differences were observed between groups, although possible differences may have been masked by the large hypointense volume measured in the naïve animals studied. If the value for the naïve hypointensity were similar to the 0.1 - 0.2 µL, as observed in Serres et al. (2012), then all groups would show a significant increase in VCAM-MPIO binding compared to naïve. Nevertheless, neither pre- nor post-treatment with adenovirus caused any significant change in VCAM-MPIO binding compared to untreated animals when comparing adenovirus pre- or post-treated animals together (Figure 5.14A) or separately (Figure 5.14B).

GE3D MRI signal was also compared between adenovirus-treated, tumour burdened animals and those with adenovirus treatment only (Figure 5.15). The overall effect of an adenoviral pre-treatment compared to adenovirus treatment alone was a significant increase in hypointensity volume when grouping all adenoviruses together ($p = 0.012$) (Figure 5.15A), whereas no such difference was observed between post-treated and adenovirus-treated animals. Each individual virus in both the pre-treatment and post-treatment groups showed a similar trend, although no significant differences were observed (Figure 5.15B).

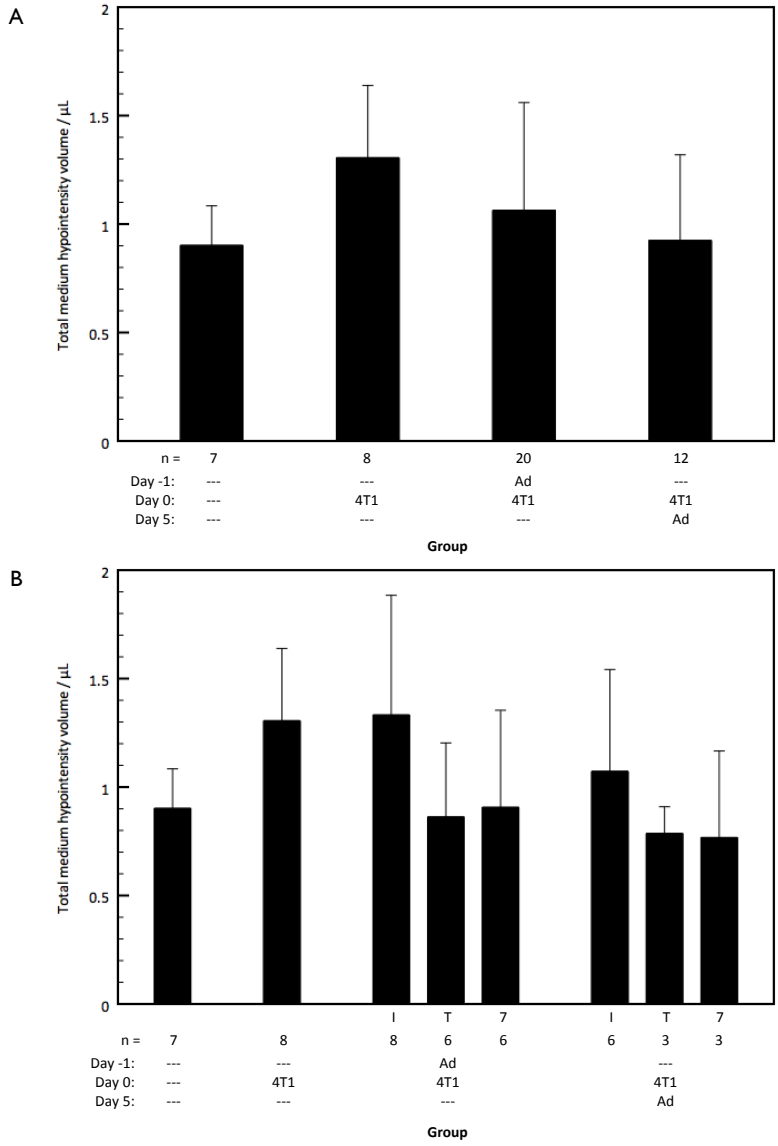


Figure 5.14 – GE3D MRI data. (A) MRI ten days post-Injection of 4T1-GFP tumour cells reveals a small, but insignificant, increase in the volume of hypointensities detected in the cerebral volume, compared to naïve animals, unlike the difference observed in Serres et al. (2012). No significant differences were observed as a result of adenovirus pre- or post-treatment. (B) No significant differences were observed with pre- or post-treatment with any individual adenovirus-treated group. (I = AdIL-1β; T = AdTNF-α; 7 = Ad70-3) Error bars represent one standard deviation from the mean.

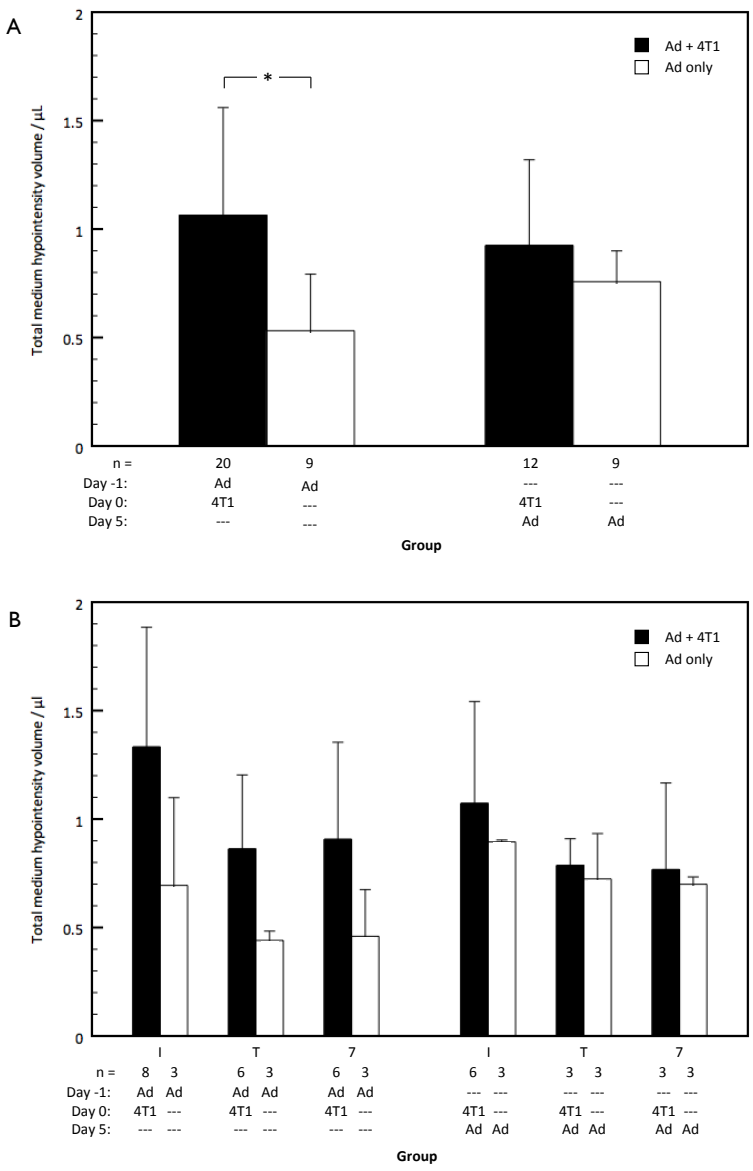


Figure 5.15 – GE3D MRI data. (A) Comparisons between animals with adenovirus alone (white bars) against those with adenovirus and tumour burden (filled bars), either pre- or post-inflammatory challenge. A significant difference in medium hypointensity volume was observed between tumour-burdened animals pre-treated with adenovirus and those treated with adenovirus alone ($p = 0.012$). No significant difference was observed in the post-treatment group. (B) All groups showed a trend towards an increase in hypointense signal as a result of metastatic burden. However, none of these differences reached significance. (I = AdIL-1β; T = AdTNF-α; 7 = Ad70-3) Error bars represent one standard deviation from the mean.

The correlation between the volume of hypointensity in the brain and both the total metastatic burden and the number of tumours was determined ($p = 0.0257$ and 0.0179 respectively) (Figure 5.16), irrespective of the presence or absence of a systemic inflammatory response. The data suggest a correlation in each case, particularly in the case of tumour number, suggesting that VCAM-MPIO-derived signal is a sensitive indicator of tumour load.

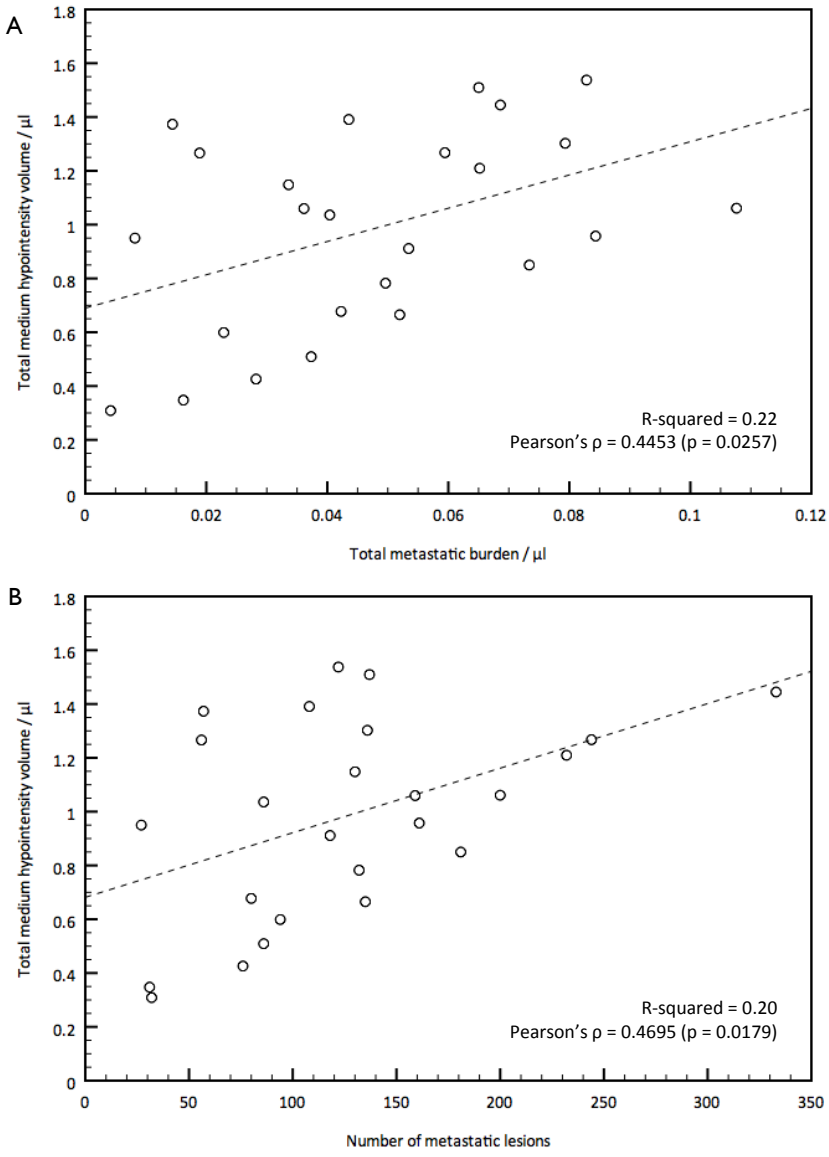


Figure 5.16 – Correlation between metastatic lesions and hypointensities. Significant correlations were observed between (A) the total metastatic burden and the total median hypointensity (R^2 = 0.22; ρ = 0.4453, p = 0.0257) and (B) the number of metastatic lesions and the total median hypointensity volume (R^2 = 0.20; ρ = 0.4695, p = 0.0179).

T1 data

In order to test the sensitivity of VCAM-MPIO detection of cerebral metastases, it was compared to the standard current clinical contrast agent, Gd-DTPA, in order to check whether brain metastases were also associated with gadolinium-induced hyperintensities in

T1-weighted MRI. No focal T1 post-gadolinium hyperintensities were observed at any locations in any of the tumour burdened brains imaged, suggesting that brain metastases had not caused damage to the BBB by this stage in their development. However, the addition of an adenoviral treatment had the potential to confound this observation. Recent, unpublished data from the group has demonstrated that systemic administration of TNF-α or lymphotoxin (TNF-β) can permeabilise the BBB selectively at sites of metastasis (Connell et al., in review). Given the patterns of pro-inflammatory cytokine production by the three adenoviruses used (Figures 5.3-5.5), it is possible that local BBB permeabilisation may have occurred at sites of metastasis as a result of adenoviral post-treatment. Again, no focal T1 post-gadolinium hyperintensities were observed in any virus-treated animals, suggesting that adenovirus treatment does not have this effect.

However, it was also proposed that a further effect of adenovirus treatment could be a low-level global disruption of the BBB. This effect is observed in other viral neuropathological models such as BBB breakdown as a result of peripheral infection with an avirulent (A7) strain of Semliki Forest virus (Erälinna et al., 1996). In order to test this hypothesis, the overall cerebral intensity of pre- and post-gadolinium injected T1-weighted MR images was compared, as shown in Figure 5.17. These data show that there is no apparent permeabilisation of the BBB as a result of viral injection at either 5 or 11 days post-viral injection. Given the transient increase of TNF-α in circulation by AdIL-1β and AdTNF-α four hours post-injection (Figure 5.3), it is possible that a transient increase in the permeability of the BBB occurs at this time in animals post-treated with virus at sites of metastasis. However, our previous data indicate that such permeabilisation is specific to tumour sites, and, thus, would not be expected to occur in the animals pre-treated with virus i.e. without metastatic burden.

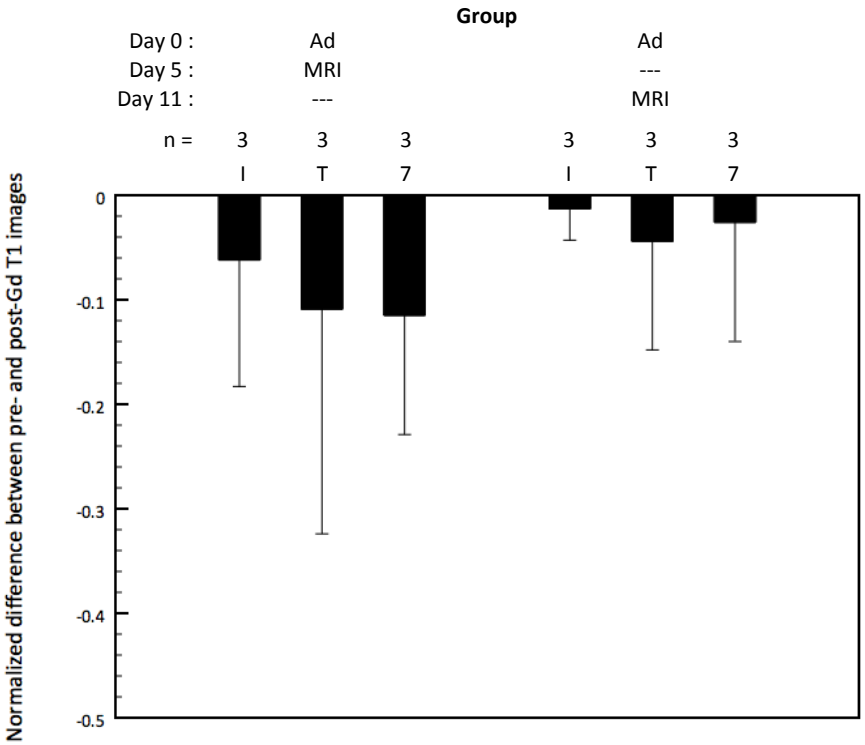


Figure 5.17 – T1-weighted MRI data analysis. Normalized differences between T1-weighted pre- and post-gadolinium contrast images revealed that at neither 5 nor 11 days post-adenovirus injection was a breakdown in the BBB visible in any of the animals. This suggests that the presence of a systemic inflammatory challenge did not cause any increase in the permeability of the BBB at either of these time points. Error bars denote one standard deviation from the mean. (I = AdIL-1β; T = AdTNF-α; 7 = Ad70-3).

The same analysis was performed after treatment with tumour cells and adenovirus. No focal T1 post-gadolinium hyperintensities were observed at any locations in the brain volume, and there was no sign of low-level breakdown of the BBB (Figure 5.18).

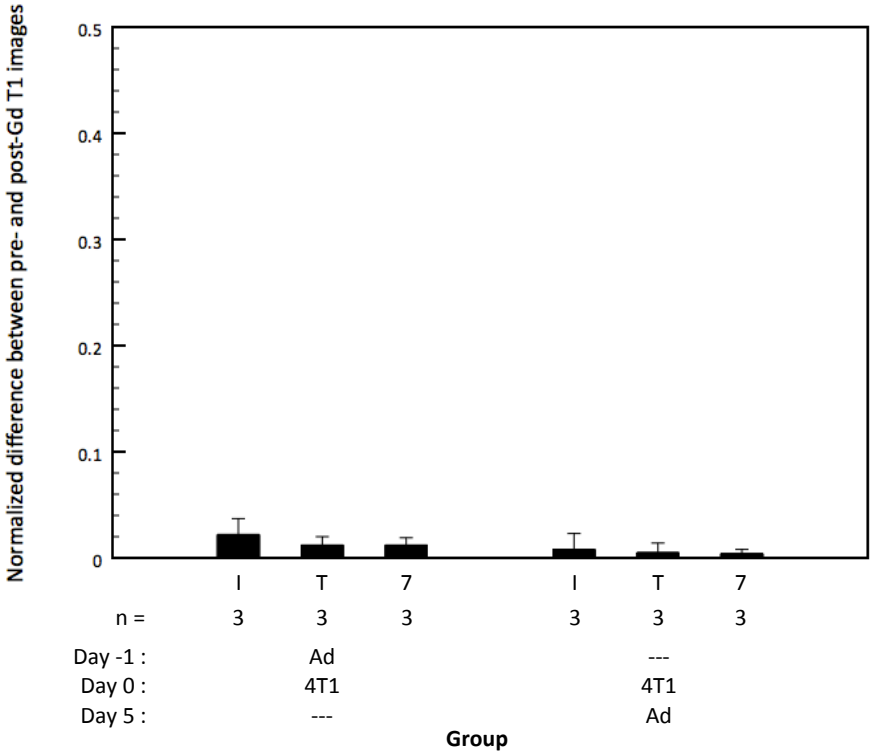


Figure 5.18 – T1-weighted contrast changes after injection of gadolinium in adenovirus-injected, tumour-bearing mice. No focal gadolinium contrast was observed in any of the animals studied. Comparison of the brain voxel intensities before and after gadolinium injection reveals very minor differences between pre- and post-gadolinium-contrasted images, none of which is significant. (I = AdIL-1β; T = AdTNF-α; 7 = Ad70-3). Error bars represent one standard deviation from the mean.

5.3.6 Effects of central inflammation on tumour development

Injection of rmIL-1β and rmTNF-α into the striatum results in localised inflammation and the differential recruitment of neutrophils and mononuclear cells, respectively (Luger and Schwarz, 1990; Anthony et al., 1997; Schnell et al., 1999; Blond et al., 2002; Sibson et al., 2002). Thus, it was hypothesised that intra-striatal injections of rmIL-1β and rmTNF-α followed 4 hours later by intracardial injection of 4T1-GFP cells would cause an increase in tumour numbers in the ipsilateral hemisphere compared to the contralateral hemisphere.

This model should therefore drive an increase in the relative abundance of metastases in the striatum, compared to other brain tissues.

The numbers and proportions of metastatic lesions observed in the control (contralateral) and treated (ipsilateral) striatums of animals injected with tumours alone, and those pre-treated with saline, rmTNF-α or rmIL-1β are shown in Figure 5.19. Very few tumours were detected in the saline-injected animals or the rmTNF-α-injected animals, reducing the power of the statistical analysis in these groups. However, it is clear from the 4T1-GFP cells only that there is no bias for the tumour cells to arrest in either hemisphere. Similarly, the IL-1β-injected animals show no significant difference between the two hemispheres. Only one tumour was detected in three animals treated with TNF-α four hours previously, and this was found in the ipsilateral i.e. injected hemisphere. Tumours were only detected in one of the animals injected with saline four hours previously, with a ratio in favour of the ipsilateral hemisphere. However, the majority of groups exhibited disappointingly few metastases. There may be several biological causes for the scarcity of these tumours, as discussed later.

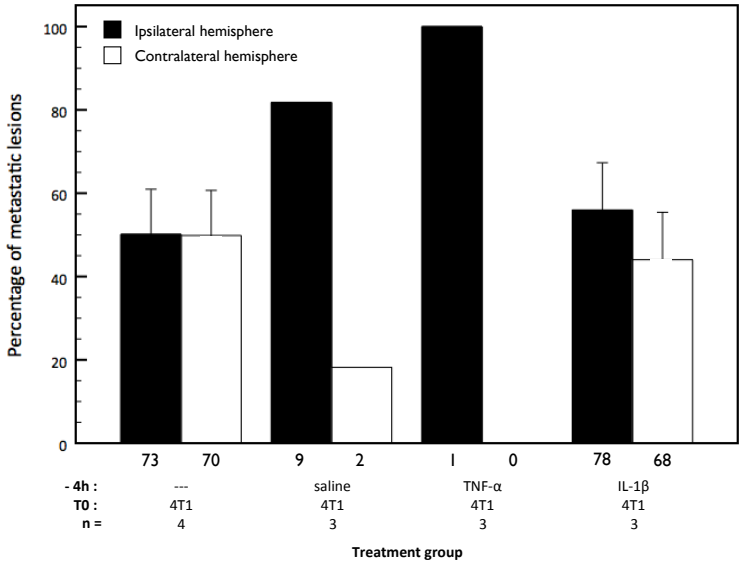


Figure 5.19 – Number of metastatic tumours occurring in the ipsilateral and contralateral striatums expressed as the percentage of total number of striatal tumours. Bars indicate the proportions of metastases in the ipsilateral and contralateral striatums for each treatment group. The numbers at the bottom of each bar show the total number of metastatic lesions found in the ipsilateral or contralateral striatums for each group. Animals injected with 4T1-GFP cells without prior treatment showed equal proportions of tumours in the two hemispheres, suggesting that there is no bias for tumour cells to develop preferentially in either hemisphere. Too few tumours were found in the saline- and rmTNF-α-injected groups to make a reasonable comparison between the proportions of metastases between the two hemispheres. No significant difference between the two hemispheres was observed in IL-1β injected animals. Error bars represent one standard deviation from the mean.

5.3.7 Effects of central inflammation on VCAM-MPIO hypointensities in the brain

In order to confirm activation of the endothelium as expected in animals injected with cytokine, VCAM-MPIO GE3D datasets were acquired four hours post-cytokine injection. These data were used to demonstrate the presence or absence of hypointensity induced by VCAM-MPIO in these animals.

The images show that large areas of hypointensity induced by VCAM-MPIO are only observed in the ipsilateral hemisphere of animals injected with rmIL-1β. In contrast, low levels of hypointensity are observed in the ipsilateral hemispheres of animals injected with saline or rmTNF-α (Figure 5.20). Little or no hypointensity was observed in the contralateral hemisphere in any of the three treatment groups, four hours after injection of saline or cytokine.

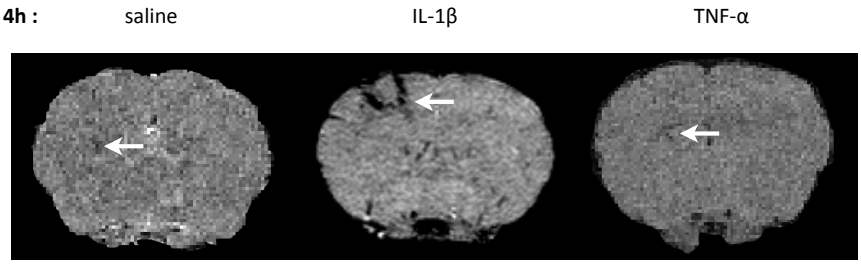


Figure 5.20 – Representative images from gradient echo datasets show VCAM-MPIO binding following cytokine injection. Four hours following injection of saline a small focal hypointensity could be observed in the ipsilateral hemisphere (white arrow). At the same time-point after IL-1β injection a number of clearly hypointense vessels could be seen in the ipsilateral hemisphere, but few or none in the contralateral hemisphere, matching results shown in McAteer et al. (2007). Hypointensities were also visible in animals injected with TNF-α and imaged four hours later.

Animals were injected with tumour cells four hours after injection of cytokine. The tumours were allowed to develop for ten days before the animals were imaged. The striatum was extracted from the GE3D datasets and hypointensities were detected using the automated analysis to give a percentage the striatum volume comprised of medium and large hypointensities (Figure 5.21). A 2-way ANOVA revealed a significant difference in medium hypointensity volumes between treatment groups ($p = 0.0078$), but no significant differences were observed in large hypointensity volumes, nor between ipsilateral and

contralateral hemispheres in any of the treatment groups. For the most part the data in Figure 5.21 suggest a positive correlation between the levels of medium and large hypointense signal, although no differences were found to be significant. These data appear to roughly correspond with the differences in tumour numbers observed in the ipsilateral and contralateral hemispheres of each of these groups of animals (Figure 5.19). With such a small number of tumours recorded in either hemisphere of the saline- and rmTNF-α-injected animals, a low percentage of hypointensities is expected. By contrast, the greater numbers of tumours observed in the rmIL-1β-injected animals and their distribution between the ipsilateral and contralateral hemispheres appears to be reflected in the GE3D data.

The reason for differences between medium and large hypointensities in this scenario may be two-fold. Medium hypointensities, as described in Chapter 3, may represent VCAM-1 expression at specific sites of focal metastatic lesions. Large hypointensities may describe VCAM-1 expression on a larger scale than just the tumour site, possibly the entire length of a single blood vessel or across many vascular networks distant to the site of metastasis. These may create a large-scale inflammatory response covering much of the ipsilateral striatum or the entire hemisphere.

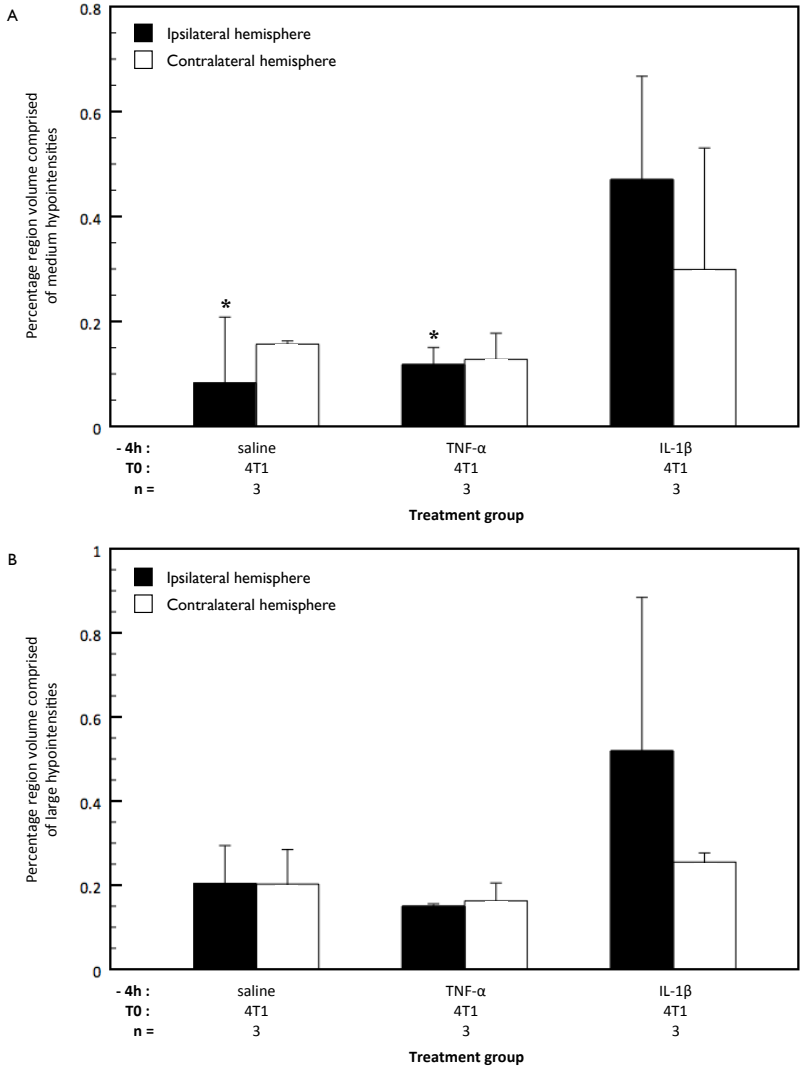


Figure 5.21 – Ipsilateral and contralateral striatum VCAM-MPIO-induced hypointensities ten days after tumour cell injection, expressed as a percentage of the volume of the striatum. (A) Volumes of medium (2 - 19 voxels) hypointensities are low in the saline and rmTNF-α-injected animals and approximately equal in the two hemispheres. The percentage of medium hypointensities is elevated in rmIL-1β-injected animals compared to saline and rmTNF-α-injected animals, as denoted by the asterisks ($p = 0.0078$). Although the data suggest that hypointensities represent a greater percentage of the ipsilateral striatum than the contralateral striatum in rmIL-1β-injected animals, this difference was not found to be significant. (B) Volumes of large (≥ 20 voxels) hypointensities showed a similar pattern between groups and between hemispheres. No differences were found to be significant. Error bars denote one standard deviation from the mean.

5.4 Discussion

The experiments described in this chapter investigated the effects of administering three adenoviruses on (I) systemic inflammation and (ii) their effects on neurovascular inflammation. The numbers, volumes and growth patterns of brain metastases were analysed following both (iii) pre- and (iv) post-treatment with adenoviruses compared to untreated animals, and (v) their effects on VCAM-MPIO-derived hypointensities in the brain. Finally, (vi) the effects of a localised neuroinflammatory response on tumour growth were assessed.

5.4.1 Systemic inflammatory effects of adenoviruses

The inflammatory response induced by the three adenoviruses used was determined from cytokine levels firstly in medium samples post-inoculation of HEK-293 cells with the viruses, and secondarily in serum samples taken post-viral injection (Figures 5.3 & 5.4). Subsequently, the effect of 4T1-GFP cell injection on systemic inflammation was assessed in the same way (Figure 5.5). Serum samples post-adenovirus administration showed no detectable levels of hIL-1β at any timepoint following injection of AdIL-1β. However, the virus appears to function in the way in which we hope, with high levels of hIL-1β detected in medium samples taken from HEK-293 cells infected with the virus at days 1 and 2, suggesting that these cells are synthesising and secreting the cytokine. The levels of hIL-1β detected in serum ten days post 4T1-GFP injection are surprising and may reflect a low level of cross-reactivity with circulating mIL-1β. It is possible that an increase in mIL-1β levels occurred in animals injected with Ad70-3, as there are two transient spikes in MCP-1 expression (induced by IL-1β) at one and five days after viral injection, with similar increases

in expression *in vitro* 3 days after HEK-293 inoculation with AdTNF-α and Ad70-3. No MCP-1 levels were detectable either five or ten days post 4T1-GFP injection.

A transient spike in mTNF-α levels was detected in serum samples four hours after injection of AdIL-1β and Ad70-3, although interestingly not after AdTNF-α injection. Similarly, mTNF-α was only detected one day following infection of HEK-293 cells with AdIL-1β. These data suggest that there may be a degree of cross-talk between the synthesis of IL-1β (either murine or human) and mTNF-α possibly in both Kupffer cells and HEK-293 cells following AdIL-1β injection, and that a proportion of the effect observed in the serum samples is the result of non-specific inoculation with the null adenovirus (Ad70-3). The lack of mTNF-α expression either in the serum samples or *in vitro* is not necessarily of concern; AdTNF-α promotes the membrane-bound form of mTNF-α rather than the soluble form, so we are unlikely to detect elevated levels of soluble mTNF-α. No elevated levels of mTNF-α were observed following injection of 4T1-GFP cells.

There are several patterns of cytokine expression that give some clues to the immunological response to viral inoculation and injection of 4T1-GFP cells. Firstly, there is no detectable expression of granzyme B under any condition at any timepoint. Granzymes function as inducers of apoptosis during targeted cell death by CTLs and NK cells (Russell and Ley, 2002), and although mouse granzyme B shows lower pro-apoptotic activity than its human counterpart (Kaiserman et al., 2006), its lack of expression suggests that there is no elevated activity of CTLs or NK cells in animals injected with 4T1-GFP or any of the adenoviruses used.

Similarly, levels of KC, although clearly detectable above the LOD, do not appear to be any different to those detected in naïve serum samples, either in virus injected animals or in tumour burdened animals. KC acts in the chemotaxis and activation of neutrophils (Haskill et

al., 1990; Sager et al., 1991; Oppenheim et al., 2001), as do MIP-1α, MIP-1β and CXCL5, so these data suggest that there is no elevated activity of neutrophils in response to exposure to virus or to 4T1-GFP cells.

IFN-γ levels were only detected in serum samples in Ad70-3-exposed animals, at 14 days post injection. IFN-γ, mainly produced by T cells and NK cells, exhibits antiviral effects by inhibiting the proliferation of transformed cells. Thus, elevated IFN-γ levels are expected post adenoviral injection. The absence of this cytokine before 14 days is surprising, although this may represent a lack of sensitivity in the assay. Interestingly, SDF-1α (CXCL12) levels are elevated in the same serum samples at the same time. SDF-1α is a potent chemoattractant for mononuclear cells (Bleul et al., 1996), so it is possible that elevated IFN-γ levels are instead the result of release from Th1 cells (Oppenheim et al., 2001). Furthermore, levels of circulating I-Tac are transiently elevated in serum samples from all three viruses, in AdIL-1β serum samples at one hour post-injection, and in AdTNF-α and Ad70-3 serum samples at 24 hours. Expression of I-Tac, which acts as a chemoattractant for activated T cells (Cole et al., 1998), is induced by IFN-γ, suggesting that the levels of IFN-γ may have been elevated but still below the detection threshold, or I-Tac expression in this situation is not regulated by IFN-Y, but rather by IFN-α, IFN-β or TNF-α (Widney et al., 2000). Similarly, MIG, the chemoattractant for activated T cells, is upregulated in serum samples after exposure to each of the three viruses. Low-level transient expression is also detectable one hour after injection of AdIL-1β. A similar effect is seen after injection with AdTNF-α, which is then followed by two much larger peaks in expression one and five days after injection. Ad70-3-injected animals, by contrast, showed limited expression of MIG, detectable at eight and fourteen days after injection. MIG expression is also under the control of IFN-γ (Farber, 1990; Sgadari et al., 1997), suggesting that IFN-γ, although undetected at these timepoints, may nonetheless be playing a role in the immune response to these viruses.

Th1 and Th2 lymphocytic responses are determined by cytokine profiles, with IFN-Y as the primary differentiator in favour of a Th1 response, and IL-4 for a Th2 response (Gilmour and Lavender, 2008). Despite a spike in the IL-4 production by HEK-293 cells two days after inoculation with AdIL-1β, IL-4 was not detected in serum samples post viral injection at any time-point, nor following 4T1-GFP injection. These data, in conjunction with the data relating to IFN-γ discussed in the previous paragraph, suggest that lymphocyte activation as a result of injection of adenovirus is Th1 in nature and not Th2. Given that the 'pathogen' that has been administered is a virus, an IFN-γ-driven Th1 response is the expected immunologic outcome to this challenge.

It may also be possible that injection of a virus promoting human IL-1β causes other immune effects than the simple expression of a cytokine. Polypeptide sequence data (Hughes, 1994) for the two cytokines are shown below:

Human IL-1β `MAEVPELASEMMAYYSGNEDDLFFEADGPKQMK------CSFQDLDL-CP`

Mouse IL-1β `MATVPELNCEMPPF-DSDENDLFFEVDGPQKMK------GCFQTFDLGCP`

Results from the EMBL-EBI pairwise protein sequence alignment tool (http://www.ebi.ac.uk/Tools/psa/) give a sequence identity of 59.1% and a similarity of 70.5% for the mouse and human forms of IL-1β. Given the lack of sequence homology, human IL-1β, rather than being up-regulated in blood serum levels, may instead be loaded onto MHC Class I molecules on the surface of Kupffer cells in the liver and cause a secondary downstream inflammatory response as a result of antigen presentation to circulating T cells. No apparent CTL activity is detected in animals after injection of AdIL-1β at any time-point,

although the design of the experiment may not allow us to spot some of the finer immunologic effects of adenovirus injection.

Although this set of experiments revealed some interesting features of the systemic inflammatory responses to the three different viruses used, a few features of this method prevented adequate diagnosis of the precise responses to each virus. The limits of detection were not low enough to identify many possible patterns of inflammation, and the methods used may have caused degradation of certain cytokines in serum. Instead, measurement of acute phase protein mRNA levels in the liver may give a better idea of the mode of inflammatory response caused by each of the three viruses.

5.4.2 Neuroinflammatory effects of adenoviruses

The neuroinflammatory response caused by adenovirus injection was studied in reference to the VCAM-1 expression on cerebral blood vessels. Although a very low proportion of blood vessels were stained with VCAM-1, the majority of positive staining occurred on arterial vessels rather than venous vessels (Figure 5.6). This suggests that under these conditions circulating leukocytes and tumour cells would first be exposed to VCAM-1 in the arterial end of the capillary bed, despite the observation that the majority of leukocyte extravasation occurs at the venous end (Lossinsky and Shivers, 2004; Prendergast and Anderton, 2009). Whether, as a result of adenovirus-induced neurovascular inflammation, this pattern of VCAM-1 expression translates into arteriolar leukocyte extravasation remains to be determined.

5.4.3 Effects of a systemic inflammatory challenge on tumour development

The effects of viral treatment on the development of brain metastases revealed some significant differences in the numbers, volumes and size distributions of metastases. Contrary to the predicted outcome, tumour numbers showed an approximately twofold drop in animals pre- and post-treated with virus compared to untreated animals. However, once tumour cells have extravasated, the presence of a systemic inflammatory response appears to cause changes in the patterns of tumour proliferation and growth, as evidenced by changes in morphology (Figures 5.10-5.13). Tumours in adenovirus pre-treated groups are larger than their untreated counterparts, and vascular co-option appears to increase across many different adenovirus-treated groups.

The model I propose to explain these data is the result of an elevated innate immune response after treatment with adenovirus (Figure 5.22). Cells injected into a mouse pre-treated with adenovirus are more susceptible to immune policing than cells that have been injected into a naïve mouse. Thus, many tumour cells are killed soon after injection into the pre-treated mouse and are not capable of developing into tumours. In contrast, tumours that are injected into a naïve mouse have five days in which to extravasate and develop into tumours. During these five days they are likely to be within the brain vasculature before they extravasate (Lorger and Felding-Habermann, 2010), and any cells that remain within the vasculature after the onset of systemic inflammation induced by the viruses are exposed to the increased immune policing of peripheral immune cells in the vasculature. These data suggest that tumour cells that are able to cross the BBB into the perivascular space are free from immune surveillance and can escape tumour-killing effects of circulating immune system cells. However, once located in the perivascular space, they are still regulated by the effect of the systemic inflammatory response, possibly via their interactions with activated endothelial cells.

Activation of endothelial cells by adenovirus inoculation leads to upregulated luminal VCAM-1 expression, and may also cause changes in signalling interactions between endothelial cells and metastatic cells located in the vessel lumen or the perivascular space, causing a greater spread along vascular beds than in untreated animals.

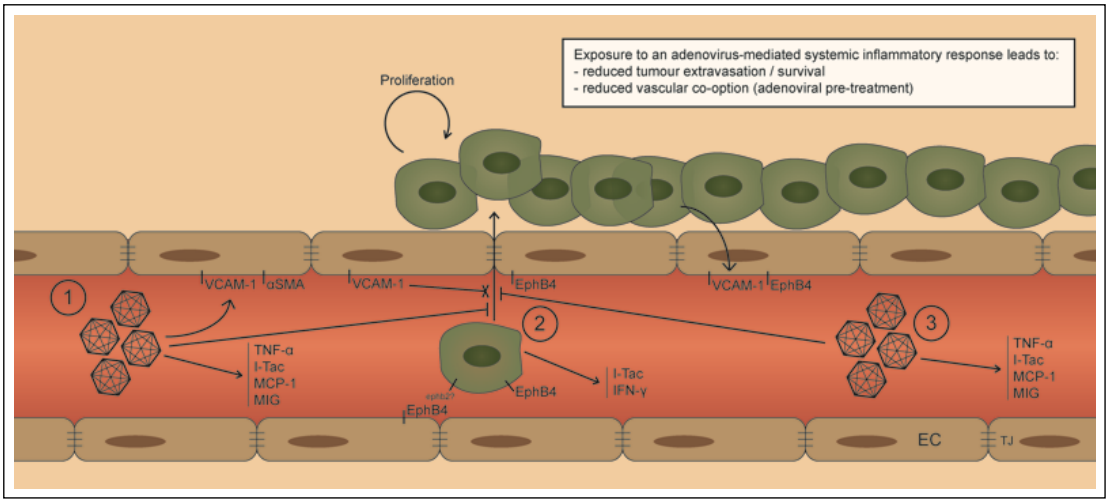


Figure 5.22 – Effects of a systemic inflammatory response on the development of brain metastases.

Step 1 – Pre-treatment with an adenoviral vector causes an increase in pro-inflammatory cytokines (TNF-α, I-Tac, MCP-1 and MIG) during the first 24 h and upregulation of VCAM-1 expression on the luminal surfaces of arterial cerebral blood vessels. Extravasation of tumour cells injected 24 h later is reduced. Vascular co-optive growth of these tumours was reduced, although no effect on tumour proliferation was observed.

Step 2 – 4T1-GFP cells extravasate from the cerebral vasculature preferentially in EphB4 positive post-capillary venules, possibly via EphB4-ephb2 interactions. Tumour cell extravasation appears to be independent of VCAM-1 expression (cross-headed arrow), although this may be because few post-capillary venules are VCAM-1 positive as a result of adenoviral pre-treatment. Tumour development causes upregulation of VCAM-1 expression on the luminal surface of cerebral blood vessels at the tumour site, and preferentially on αSMA-positive blood vessels at a distance from the tumour site. Injection of 4T1-GFP cells also causes an increase in circulating pro-inflammatory cytokines after 10 days (I-Tac and IFN-γ).

Step 3 – Post-treatment with an adenoviral vector causes a reduction in tumour extravasation. Data suggest a mild increase in vascular co-option (increased number of objects per section), but there appears to be little effect on rate the proliferation of tumours that become established in the brain.

5.4.4 MRI analysis of virus and tumour-burdened animals

MRI analysis of the virus- and tumour-bearing animals again revealed interesting, but non-significant changes in the volume of hypointensities detected. One of the major problems encountered during this chapter was the high MRI signal level derived from the naïve animals injected with VCAM-MPIO. This was a hindrance for drawing many conclusions from the data as some of the experimental groups, where neuroinflammation was expected and observed immunohistochemically, were found to have a lower proportion of hypointense volumes in the brain. In particular, naïve animals, when compared to 4T1-injected animals showed only a very mild increase in the quantity of hypointense signal recorded in the brain. This result is at odds with the same comparison made in Serres et al. (2012). There are several possible explanations for this unexpected result. Firstly, hypointense signals may come from a variety of sources, as discussed in Chapter 3, which include deoxygenated blood in cerebral blood vessels, under the possible influence of the level of anaesthesia of the animal. Although the level of anaesthesia was carefully monitored in these animals during MRI, it is possible that mildly elevated levels of deoxygenated blood in circulation in all groups has masked the effect of VCAM-MPIO in circulation. Secondly, the animals imaged in Serres et al. (2012) took place a long time before any of the animals used in this current work, using a different magnet and acquisition software setup, and a different batch of VCAM-MPIO. Clumping of VCAM-MPIO beads is a feature that may have changed over time, with different batches of beads showing different binding dynamics. Although new batches are tested *in vitro* using a flow chamber and 'stickier' batches of beads are evident on MR images, giving a spotty appearance to the brain, inter-study and intra-study differences in

the beads used may give rise to unwanted levels of signal in naïve animals. Increased quality control on all VCAM-MPIO batches has been instigated to ensure that this issue is eliminated. Another possible issue is the use of the automated analysis, and the levels of signal that are detected, particularly in the posterior regions of the brain, which may be masking other effects taking place in other brain regions. If this is the case, segmentation and re-analysis of the posterior regions of each brain may be useful in eliminating this problem, as may modifications in the automated approach that modify the test statistic in different brain regions in response to local contrast levels.

5.4.5 Future work: systemic inflammation

The normal development of 4T1-GFP brain metastases was discussed in the previous chapter, and their usual colocalisation with venous as opposed to arteriolar blood vessels (Figure 4.12). Given the preferential expression of VCAM-1 on arteriolar blood vessels as a result of adenoviral treatment, a future step to this work would be to identify whether a higher proportion metastases have begun to develop on arteriolar blood vessels as a result of adenoviral pre-treatment, further implicating VCAM-1 in the extravasation and development of brain metastases.

It may also be informative to increase the dose of virus administered to the animal with the intention of increasing the severity of the systemic inflammatory response. Although it appears that the level of inflammation caused by the viruses studied is significantly greater than that caused by the development of tumours, an increased systemic inflammatory response could magnify the differences observed between the groups, particularly for the MRI investigations presented. Similarly, injection of a different inflammatory agent, such as LPS may elicit a different response to tumour development. One particular agent of interest is polyinosinic:polycytidylic acid (poly I:C), a simulator of viral infections that induces an

immune response in an IL-1-dependent manner (Fortier et al., 2004). If pre- and post-treatment with poly I:C elicit the same response on tumour development as the adenoviral treatments described in this chapter, we may be able to draw more general conclusions about the role of a virus-mediated inflammatory response on the development of brain metastasis. Agents such as these could be injected several times over the course of tumour development, or injected once at specific points just prior or during tumour development.

It may also be useful to lower the dose of tumour cells administered to the animals. It is possible that the numbers of tumour cells injected is in fact already a limiting factor in the development of cerebral metastases, particularly if these cells are interfering with, or competing with, each other at the metastatic niche. If this is the case then injecting 10-fold fewer cells into the animals may allow us to distinguish between those with a systemic inflammatory response and those without. Furthermore, injection of 4T1-GFP cells into the breast fat pad would be a useful continuation of the current model. The current metastatic model requires injection of 4T1-GFP cells into the left ventricle of the heart, from where tumour cells are able to enter the systemic circulation. The advantages of this model of tumour development are an easily controlled cell titre and time over which metastases develop. However, 4T1 primary tumours cause systemic inflammation in their own right (Bunt et al., 2007), and may present a suitable model for the systemic inflammatory priming prior to the development of brain metastases. Primaries can easily be surgically resected from the breast fat pad (Pulaski and Ostrand-Rosenberg, 2001), thus improving the model compared to the clinical paradigm.

Studying the progression of the tumours, over a variety of different time-points may allow us to draw further conclusions from this work. Do tumour cells cross from the lumen of the blood vessel into the perivascular space faster in the presence of a systemic inflammatory

response? Tumour cells, which normally spend longer in the lumen of cerebral blood vessels than those of other organs in the body (Lorger and Felding-Habermann, 2010), may respond to a systemic inflammatory response by crossing faster in the presence of cellular adhesion molecules such as VCAM-1, or in a vascular environment with greater concentrations of circulating cytokines or chemokines. The work presented has only demonstrated that there are no observable differences in tumour volume after 10 days in adenovirus-treated animals compared to untreated animals, suggesting that rates of proliferation are the same over the ten days studied. Supplementing these results with a BrdU assay would reveal the relative rates of proliferation in each of these treatment groups. Despite the similarities in tumour volume, the pattern of tumour growth over these ten days may be different in each scenario, with a reduced level of vascular co-option, particularly in adenovirus pre-treated animals. Earlier experimental end-points may allow us to observe these changes in tumour development as they occur. Furthermore, taking tumour development out to thirteen days may also allow us to observe a greater difference in VCAM-MPIO-derived MRI signal, as demonstrated in Serres et al., (2012).

A useful complement to this work would be to relate the structures and morphologies of tumours to the local cerebral vascular architecture. No comprehensive atlas of the mouse cerebral vasculature currently exists, although diffusion tensor μMRI of *ex vivo* brain vasculature (Pathak et al., 2011) has produced some detailed, high resolution maps of blood vessels in the brain. Relating tumour locations to the size and types of local blood vessels, in this way, is an obvious next step in answering questions concerning the distribution of metastases in the brain. Data such as this may also explain some of the differences in vascular co-option between different brain regions (Figure 4.6). Regions of the brain where blood vessels run parallel to the coronal slices used for tumour identification may have

greater numbers of objects per section compared to other regions where blood vessels run in a perpendicular manner, possibly confounding the data.

With regards to the cytokine studies, it would be useful to look at mouse IL-1β, which may be upregulated as a response to circulating TNF-α and human IL-1β. Further details may also be learnt by measuring the concentrations of IL-1ra in response to proposed elevated levels of mIL-1β.

The contribution of peripheral immune infiltration into cerebral metastatic lesions may have important implications on their development and survival. As a small pilot study I stained a small amount of brain tissue containing metastases for CD11b, the macrophage and microglial marker, and NK1.1, the NK and NK T cell marker, to see whether there was any colocalisation of these cells with cerebral metastases. The immunofluorescence images are presented in Figure 5.23. It would appear that CD11b+ cells are activated around the metastatic lesion. This may either demonstrate the formation of a glial scar by resident astrocytes, or the presence of infiltrating macrophages from the systemic circulation. In contrast, a population of NK or NK T cells can be seen to have infiltrated the tumour mass from the circulation. Although these data are preliminary, it may bear scrutiny to investigate the roles of a variety of peripheral immune system cells in the development of metastases with and without a systemic inflammatory response.

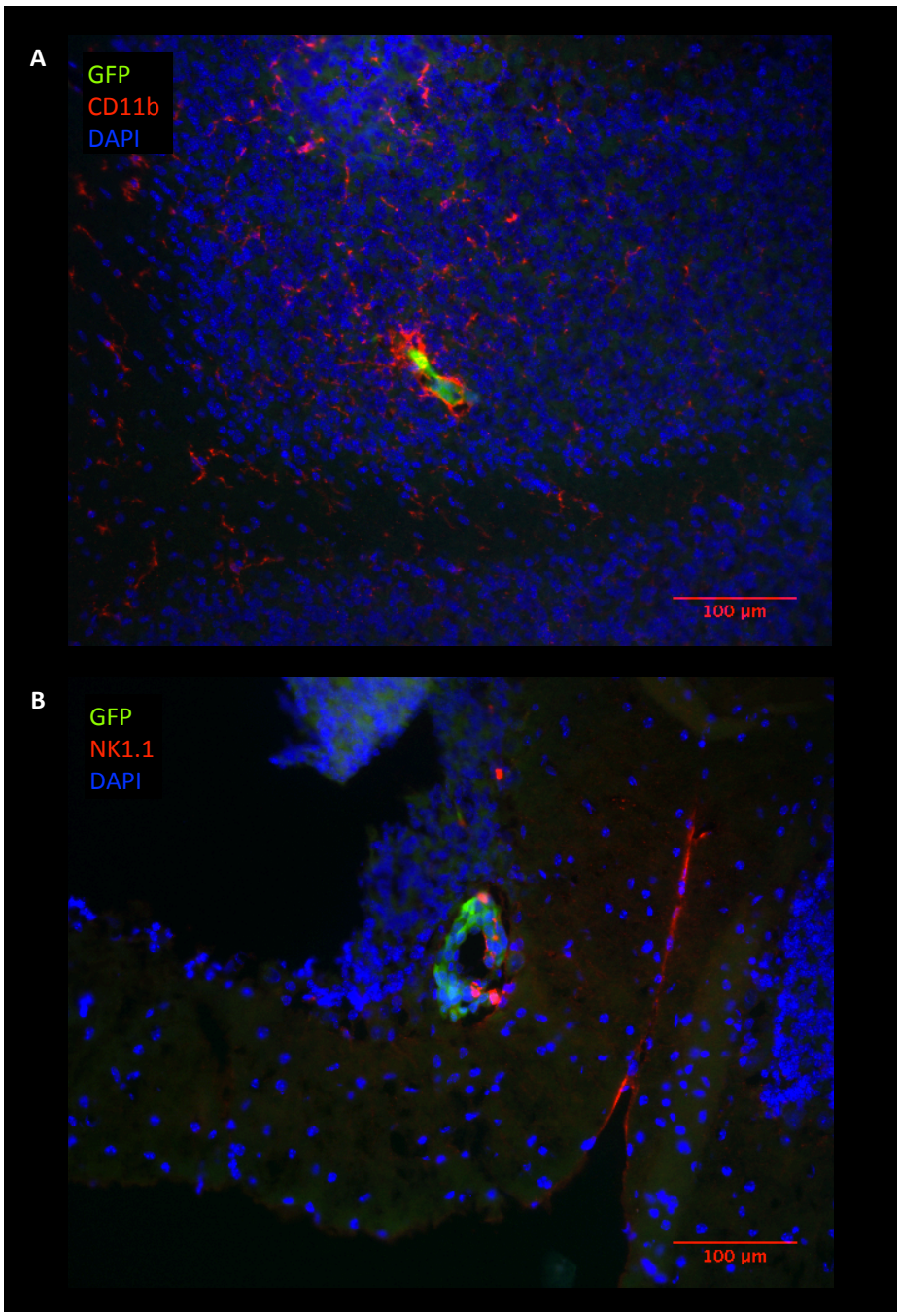


Figure 5.23 – CD11b and NK1.1 colocalisation with brain metastases. (A) The macrophage and microglial marker CD11b is found associated with metastatic lesions in the brain. There appears to be activation of the microglia surrounding the metastatic lesion, with possible formation of a glial scar, or recruitment of peripheral macrophages. (B) NK1.1, a marker for NK and NK T cells, is found associated with metastatic lesions in the brain, suggesting that a degree of peripheral immune infiltration is occurring. Inserts show negative control staining for each marker.

Similarly, there may be roles played by other organs in the sequestration of tumour cells. The reduction in tumour numbers in the brain as a result of adenoviral exposure (Figure 5.8) does not explain the fate of these cells. It is possible that increased immune surveillance causes a greater amount of tumour cell killing by NK cells and CTLs. However, given the lack of elevated granzyme B levels, this does not seem apparent. Instead, there may be greater sequestration of tumour cells in other organs such as the liver and the spleen (Figure 5.24). Although no tumour cells were observed in the liver of an animal pre-treated with AdIL-1β, they were evident in the spleen. These data are entirely preliminary and must be compared to data from untreated animals in order to build further hypotheses. Thus, whether the proportions of cells in other organs increases to match decreased tumour burden in the brain remains to be seen.

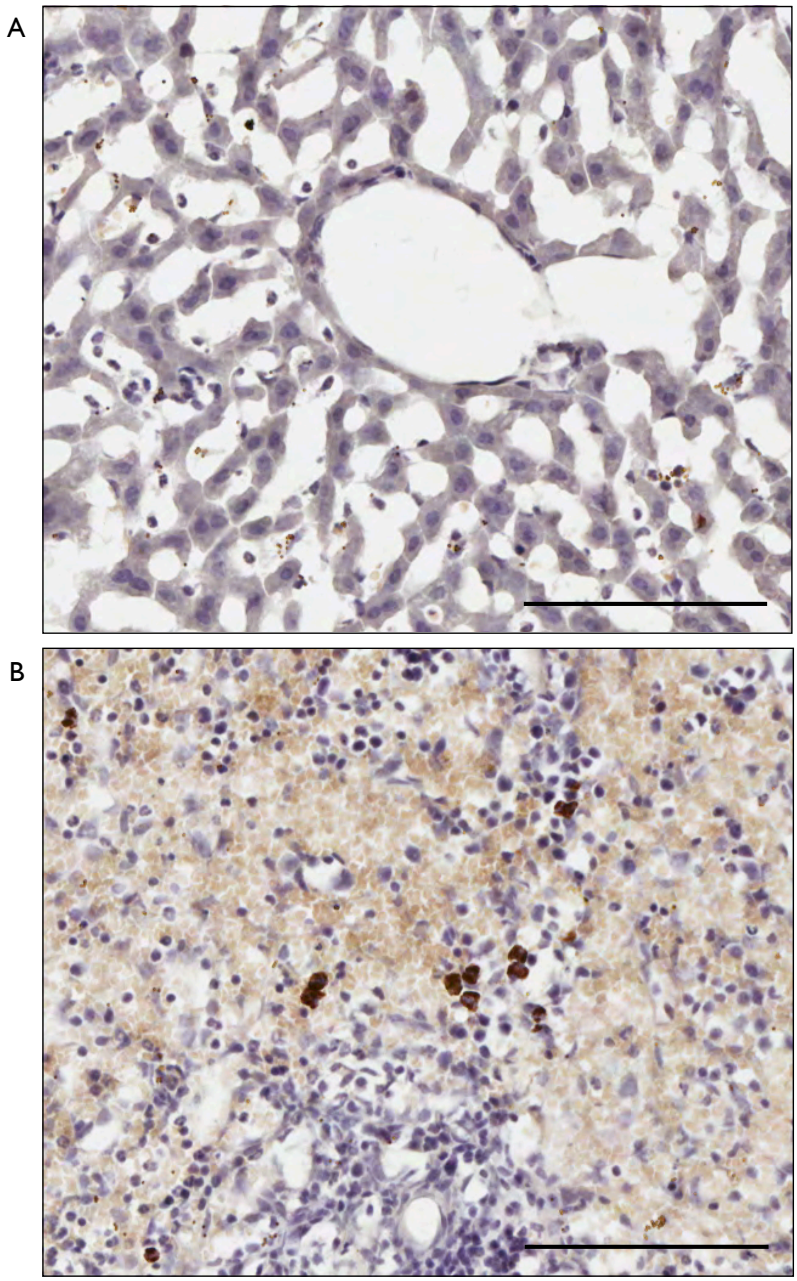


Figure 5.24 – 4T1-GFP cells in the liver and spleen. (A) No tumour cells were observed in the liver 10 days following intracardiac injection in an animal that had been pre-exposed to AdIL-1β, although VCAM-MPIO beads were observed (small, brown circular objects). (B) Tumour cells were observed in the spleen of the same animal, although not apparently forming metastatic lesions. Scale bars represent 100 μm. Sections stained for GFP and counterstained with haematoxylin.

5.4.6 Pilot study on local neuroinflammation

It was proposed that a localized neuroinflammatory response would increase the number of the metastatic lesions in the inflamed brain region. Since localised inflammation causes endothelial activation, it was hypothesised that this would increase the seeding of metastases in the brain. The striatum was chosen because it has a well documented inflammatory response in rats (Blamire et al., 2000; Blond et al., 2002; Wilcockson et al., 2002; Ferrari et al., 2004) and untreated animals have a relative abundance of metastases close to the expected value (Figure 4.3). Therefore, it was suggested that local inflammation might target tumours to develop in this region of the brain.

A major limitation of this pilot study was the low number of metastases found in several of the experimental groups. This reduced number could be the result of several factors. Firstly, low cell viability as a result of minor variations in cell preparation on the days that these injections were performed could have contributed to the low numbers of tumours. The inclusion of control groups (4T1 only) in all cohorts would control for this factor. Secondly, it is possible that the intracerebral surgery itself caused the reduction in tumour numbers, possibly owing to reduced blood oxygenation as a result of prolonged or double anaesthesia. This appears unlikely as neither procedure is particularly lengthy and animals are monitored closely throughout to ensure that their temperature, breathing rate and heart rate are adequately high. Use of a different (milder) anaesthetic regime might shed light on this possible confound. Injecting cells into awake animals whilst scruffed is possible, but is less precise and reproducible than the current methods using ultrasound guidance. Alternatively, surgery itself may induce a protective inflammatory response in the animal following disruption of scalp tissue, skull or dura, which could itself cause a decrease in circulating tumour survival, as per the reduction in tumour numbers as a result of adenovirus injection. This hypothesis could be tested by performing sham surgery on mice without injecting

cytokine or saline. Thirdly, it is possible that injection of 0.5 µL of any substance into the mouse striatum is sufficient to cause a systemic inflammatory response that could limit the survival of tumour cells in circulation, regardless of the pro-inflammatory qualities of the injected substance. This could be tested by measuring the mRNA levels of acute phase proteins in the liver, such as serum amyloid P (SAP) and serum amyloid A (SAA).

Finally, the quality of the intracardiac injections may not be consistent and could, thus, introduce an element of variation. However, animals that are poorly injected, as determined by lack of blooming on the ultrasound or blood back flow in the needle, are routinely discarded and the number of such injections was consistent and low across all groups.

With a very small number of metastatic lesions present in any of these animals, with the exception of the IL-1β injected animals, it may be premature to draw any conclusions thus far. Further work to validate the viability of the cells and the model is needed to satisfy any speculated mechanisms for tumour-promoting or -inhibiting processes that may be occurring. However, one potential difference between the two cytokines studied is the differential recruitment of leukocytes, which may underlie these preliminary indications of differential changes in the survival of tumour cells in the brain. Thus, the original hypothesis that localised inflammation *per se* is a promoter of brain metastasis, may be an oversimplification and the nature of that inflammatory response may be a critical factor.

5.4.7 Concluding remarks

In conclusion, I have successfully developed a model for inducing a systemic inflammatory response via adenoviral injection and have used this to investigate the development of brain metastases in animals pre- and post-treatment with adenovirus. Each of the three different

adenoviruses used elicited a different inflammatory response from one another, with differential upregulation of pro-inflammatory cytokines. However, the effects of initiating a systemic inflammatory response on the development of brain metastases were unexpected. Whereas adenoviral pre-treatment was predicted to cause an increase in the numbers to cerebral tumours, as a result of increased endothelial VCAM-1 expression, the effect was in fact a two-fold reduction in tumour numbers. Similarly, adenoviral post-treatment, which was expected to cause exacerbation of inflammation at sites of pre-existing metastatic lesions, and lead to an increased tumour growth rate, did not have this effect, and also led to a two-fold reduction in tumour numbers. Increased immune surveillance as a result of adenoviral inoculation is presumably the cause for these differences. Morphologically, tumours in adenovirus pre-treated animals differed from those in untreated animals, with greater levels of vascular co-option; a similar but less pronounced difference was observed with adenovirus post-treated animals. These results indicate that a systemic inflammatory response severely modulates tumour growth within the brain, and that the immune response may be responsible for tumour survival and extravasation. Given the increasing development and use of immunotherapies for cancer patients, these findings are relevant to the future treatment of brain metastases.

Discussion

The work covered in this thesis describes the interactions between brain metastases and activation of the local brain endothelium in the context of an induced inflammatory response. The expression of the vascular marker VCAM-1 on the luminal surface of endothelial cells has been identified as a potential marker in the early stages of several neuropathologies (Sasseville et al., 1992; Jovanova-Nesic and Shoenfeld, 2006; Serres et al., 2011; Fréchou et al., 2013). VCAM-1 is not constitutively expressed by brain endothelial cells (Carlos et al., 1990; Wong and Dorovini-Zis, 1995), so its expression at sites of brain metastasis, both in rodent models and in human post-mortem tissue, may allow it to serve as a possible diagnostic marker (Serres et al., 2012). However, VCAM-1 expression on the luminal surface of endothelial cells is also a crucial trigger in the arrest and extravasation of circulating leukocytes, particularly lymphocytes and monocytes (Brankin et al., 1995; dos Santos et al., 1996), at sites of inflammation (Lossinsky and Shivers, 2004). Several authors have hypothesised that metastatic cells in circulation may be able to react to adhesion molecules in a similar fashion, allowing them to extravasate into neighbouring tissues and continue to proliferate (Ruff and Pert, 1984; Calvo et al., 1987; Munzarová and Zemanová, 1992; Munzarová et al., 1992). The primary hypothesis explored here, therefore, was that promotion of VCAM-1 expression on the brain endothelium may cause a greater number of tumour cells to arrest and/or extravasate. VCAM-1 upregulation may be experimentally induced by exposure to a pro-inflammatory stimulus; the data presented in this thesis used

adenoviral vectors to promote systemic inflammation and pro-inflammatory cytokines to promote a localised neuroinflammatory response.

The thesis is split into three main sections, each of which adds a different focus to the work:

1 Histological examination of VCAM-1 expression at sites of brain metastasis and correlation with MRI hypointensities, including a novel analysis method for reliable and reproducible identification of hypointensities in MRI datasets, and filtering techniques for reducing the number of false positive hypointensities (Chapter 3).

2 The normal development of 4T1-GFP brain metastases, describing differences in site-specific metastasis within the brain, and the vascular localisation of brain metastases (Chapter 4).

3 The effects of an adenovirus-induced systemic inflammatory response on peripheral cytokine upregulation, neurovascular VCAM-1 expression and the development of brain metastases, correlated with VCAM-MPIO-derived signal observed in MR datasets. Preliminary results are also presented to determine the effects of a cytokine-induced central inflammatory response on the development of brain metastases (Chapter 5).

The results obtained from each of these three sections are discussed in more detail below.

6.1 VCAM-1 expression at the site of metastasis is associated with MRI hypointensities

The intravascular MRI contrast agent, VCAM-MPIO, has been developed to exploit VCAM-1 upregulation on the brain vasculature during early stages of neuropathology and has been shown to specifically bind to VCAM-1 *in vivo* (McAteer et al., 2007). Mice injected intracardially with 4T1-GFP cells reliably develop brain metastases that often show upregulation of VCAM-1 expression on the local tumour vasculature (Figure 3.3, Chapter 3). It is also possible to detect VCAM-MPIO attached to the vascular endothelium on immunohistochemical sections at the tumour site. VCAM-MPIO contrast is visible as dark hypointense regions on grey scale T2*-weighted brain images. The efficacy of VCAM-MPIO as a contrast agent for identifying the location of brain metastases has to meet two criteria: (i) reliable identification of hypointensities arising from VCAM-MPIO contrast in brain volumes, and (ii) correspondence between the locations of hypointensities and the locations of brain metastases.

6.1.1 Identification of hypointensities

Chapter 3 described the development of a novel technique for the accurate identification of VCAM-MPIO-induced hypointensities. The premise for the technique is simple: a statistical test using global values across the brain determines the identification of a given voxel as hypointense based on the intensity of its neighbouring voxels. This approach has several advantages. Firstly, the test has a small number of parameters (radius, test type, value of the test statistic, margin, size threshold), which allows for efficient optimisation of parameter values. This also makes the approach versatile, as the parameter values can easily be modified for alternative datasets and applied to identify hypointense or hyperintense voxels in a range of other tissues. Secondly, the mathematics is computationally straightforward, so

calculation times are low (2-3 minutes for a brain volume containing 6-8 million voxels at an isotropic resolution of 88 μm^3), and the test can easily be modified to match a user's requirements. An alternative approach to the identification of blood vessels in diffusion tensor imaging is described by Pathak et al. (2011), using a Frangi filter (Frangi et al., 1998; Sato et al., 1998) and an iterative thresholding method (Ridler and Calvard, 1978). The use of a Frangi filter should improve the SNR in the MRI datasets acquired, thus improving the ability to detect hypointensities from background signal. However, it is a computationally intensive process by comparison to the filtering techniques described in this thesis, and requires the calculation of eigenvalues for the Hessian matrix at each voxel to determine the 'tubeness' of the object in question, and potentially removing punctate signal of interest from brain volumes. Furthermore, this approach does not take into account temporal differences in datasets such as transient binding or arrest of MPIO in blood vessels and may therefore maintain unwanted false positive hypointensities.

One drawback of the basic automated approach is its inability to adaptively distinguish large hypointense structures such as sinuses and ventricles (and sulci in the human brain) that are not associated with VCAM-MPIO binding, from smaller, punctate hypointensities that are much more likely to be MPIO-derived signal. To address this issue, a size threshold was applied to the hypointensities *post hoc*, but any fixed size cut-off is prone to error from objects of a similar size to the threshold. An adaptive approach capable of identifying large non-VCAM-MPIO-derived structures such as sinuses and ventricles *ad hoc* would be a useful tool to develop in the automated detection of hypointensities. Furthermore, the differences in contrast from the front to the back of the brain (Figure 3.5C) that prompted the development of an automated approach to identify hypointensities, still present a confound in their detection (Figure 4.2). Further development of the automated approach should include an adaptive value of the test statistic to account for changes in contrast over the

length of the brain, to more accurately identify hypointensities as opposed to noise. This approach could use some of the iterative tools described by Ridler and Calvard (1978) to determine the correct value for the local test statistic based on the local contrast levels.

6.1.2 Co-localisation of tumours and hypointensities

The co-localisation data presented in the first half of Chapter 3 demonstrate that the majority of tumours above approximately 0.001 µL in volume are detected by MRI signal from VCAM-MPIO, and that the correspondence with VCAM-1 expression at the tumour site is high (Figure 3.4). VCAM-MPIO show a paramagnetic effect of *ca.* 50 times their radius (Sibson et al., 2011). For a particle of diameter 1 µm and an isotropic resolution of 88 μm^3 in the GE3D dataset, several MPIO must be bound to VCAM-1 on the vasculature associated with a metastatic lesion in order to cause a hypointense signal, where a 20% drop in signal intensity can be detected as hypointense (Shapiro et al., 2004). This suggests that chance binding of a single MPIO in the vasculature is unlikely to cause a hypointensity on the MR image. The chance binding of several MPIO at one location is less likely, so hypointensities should, in theory, be the result of real binding events to VCAM-1 expressed on cerebral blood vessels. However, the dynamics of MPIO movement in the bloodstream are not yet understood. Periodic clumping and dispersal of MPIO in blood vessels may nonetheless cause hypointensities that are not related to VCAM-1 binding in cerebral blood vessels.

This supposition may go some way to explaining one apparent contradiction: the presence of a number of tumours that were VCAM-1 negative but MRI positive, that is, tumours that were co-localised with hypointensities in the MR image, but when stained by immunofluorescence did not express detectable levels of VCAM-1 (Figure 3.4). Two possible explanations are discussed in Section 3.4.1. Firstly, VCAM-1 expression may have been present at the tumour site, but was not observed, either as a result of low signal

enhancement during staining, or staining of brain sections that did not traverse a tumour-associated blood vessel. Secondly, transient clumping of MPIO at the tumour site, independently of VCAM-1 expression, possibly as a result of reduced internal diameter of local blood vessels (Pathak et al., 2011), may cause hypointensities on MR images. Given the latter possibility, one extension to the work would be to randomly assign hypointensities from a donor brain with known tumour locations onto a naïve recipient brain, in the same manner as presented in Figure 3.16. Many randomly-assigned hypointensities will not colocalise with tumour locations in the donor brain; others would do so by chance. By repeating this process multiple times, these data would give us a rate at which tumours and associated hypointensities will colocalise at random. If random assignment of hypointensities results in a similar degree of tumour colocalisation as the VCAM-1 negative, MRI positive tumours discussed, this observation would provide an explanation for this apparent contradiction.

Another approach to reduce the likelihood of detecting non-tumour specific hypointensities was the development of filters to smooth the data and remove potential non-specific signal (Figures 3.18 and 3.19). The first, a temporal mean filter, required two brain volumes to be acquired in series, and the mean of the equivalent voxels in the two datasets was calculated. The second, a spatial median filter, calculated the median of the neighbouring 2D voxels in a single dataset. Mean filtering proved to be more promising approach to removing non-specific hypointensities in the dataset and at no cost to the overall imaging acquisition time.

6.2 Tumour development in different anatomical brain regions

The total metastatic burden, the number of metastases and the morphology of individual metastases were analysed in five broad brain regions (Figure 4.2). These data suggest that

the development of 4T1-GFP metastases differs between brain regions, a feature that was also observed in the MDA-MB-231-Brain (231-BR) metastasizing breast cancer cell line by Fitzgerald et al. (2008). Although the data of Fitzgerald et al. was collected in a different manner to the experiments presented in this thesis, there is concordance between their observations and those described here. 231-BR metastasis to the parietal cortex, the frontal cortex and hippocampus was extremely common; lower levels were detected in the caudoputamen. Many of these patterns were shared by 4T1-GFP brain metastasis, suggesting a commonality of brain vascular signalling to circulating metastatic cells, or possibly flow characteristics, resulting in differential survival or extravasation in various brain regions. A level of metastasis close to the expected value in the mouse striatum after 4T1-GFP injection was one motivation for attempting to target metastasis to this location by focal injection of mIL-1β or mTNF-α (Chapter 5).

Morphological differences between metastases in different brain regions may also tell us something about the different vascular environments that tumour cells encounter. Increases in individual tumour volumes in specific brain regions suggest a more pro-proliferative environment for circulating metastatic cells. Furthermore, proxy measurements for vascular co-option (range, number of objects and sphericity), suggest that tumour cells track along local vasculature more readily in certain parts of the brain compared to others. Vascular co-option is a feature of tumour growth that was first identified in the brain (Leenders et al., 2002), and allows a developing tumour to obtain an oxygen supply from pre-existing blood vessels rather than having to turn on an 'angiogenic switch', and develop new vessels. Histological examination of tumours showed some with long finger-like protrusions along a single or branching blood vessel while others had multiple discrete parts that appear to have developed on multiple branches of the same vascular bed. In both cases this was considered a sign of increase vascular co-option. Other tumours, generally smaller, showed limited

growth within one vascular location and had a much more globular appearance (Figure 4.4). However, the manner in which tumours are presented histologically may be related to the direction in which blood vessels develop in different brain regions. Correlating the data acquired with a high-resolution vascular brain map, such as the one presented in Pathak et al. (2011) may allow greater interrogation of the development of these tumours. Proliferating tumours that are not tracking along local vasculature must presumably be expanding within a confined region of the perivascular space, or into the brain parenchyma. Without more precise staining to identify breakdown of laminin basement membranes and withdrawal of astrocyte endfeet, parenchymal colonisation cannot be formally demonstrated. As yet, the signalling and developmental cues that are responsible for this shift in phenotype are yet to be elucidated, although the similarities between the syngeneic 4T1-GFP and non-syngeneic 231-BR models (Fitzgerald et al., 2008; Lorger and Felding-Habermann, 2010) suggest that similar signalling processes may govern extravasation and proliferation for a variety of brain-metastasizing cells.

6.3 Adenovirus-mediated inflammation

The systemic inflammation model used for the experiments presented in Chapter 5 was induced through intravenous injection of three strains of replication-deficient adenovirus. Two 'active' viruses were used to induce expression of either hIL-1β or membrane-bound mTNF-α, respectively, whilst an otherwise identical null adenovirus was used as a control that did not contain a plasmid coding for expression of an inflammatory cytokine. The choice of inflammatory cytokines promoted by these viruses was informed by the observation that TNF-α and IL-1β in the periphery upregulate each other's activity, whereas in the brain the two pathways operate independently of one another (Blond et al., 2002). Human and mouse IL-1β have been shown to cross-react (Libert et al., 1990; Vandenabeele et al., 1990), and

exogenous exposure to IL-1β has been demonstrated to cause increased endogenous expression of IL-1β *in vitro* (Tsuzaki et al., 2003). Consequently, it is likely that hIL-1β expression will lead to additional synthesis of mIL-1β systemically. Furthermore, synthesis of hIL-1β may in itself cause an inflammatory response mediated by MHC Class I presentation of foreign antigen to circulating T cells. Analysis of medium samples from cultured HEK-293 cells inoculated with virus showed inflammatory activity as a result of all three viruses, as did serum samples obtained up to 14 days after *in vivo* viral injection. As such, the three adenoviruses used in these experiments were useful vehicles for initiating a systemic inflammatory response. Cytokine responses were different as a result of inoculation with each of the three viruses (Figures 5.3 - 5.5), as were VCAM-1 expression responses on cerebral vasculature (Figure 5.6). The advantages of initiating a systemic inflammatory response in this manner are the ability to maintain elevated levels of inflammation over several days, as opposed to the effects of a bolus injection of cytokine (Granowitz et al., 1991), the ability to easily alter the level of viral inoculum used, and the ease of administration.

Despite the advantages of using these adenoviruses to promote systemic inflammation, it would also be useful to investigate the effect of poly I:C injection on systemic inflammation, upregulation of VCAM-1 expression on cerebral vasculature and the development of brain metastases. Any similar patterns of tumour development and growth as a result would suggest a commonality between the inflammatory responses to poly I:C and each of the three viruses used, and any downstream effects on signalling between tumour cells, brain endothelial cells and systemic immune cells.

6.4 VCAM-1 expression as a possible effector and consequence of brain metastasis

VCAM-1 expression on cerebral endothelial cells is common at the tumour site ten days after injection of tumour cells (Figure 3.3; Serres et al., 2012). 4T1 cells can remain in the brain vasculature for up to five days, and have been shown to be fully extravasated seven days post-injection (Lorger and Felding-Habermann, 2010), after which time they develop within the perivascular space. Expression of VCAM-1 on EphB4-positive vessels must occur some time after tumour arrest, although at what stage during tumour development this takes place is uncertain. VCAM-1 acts as a mediator of leukocyte arrest in the brain vasculature, as in other organs (Lossinsky and Shivers, 2004; Greenwood et al., 2011), and may, therefore, promote influx of circulating immune cells to the tumour site. Inflammation is a common feature of tumour biology, and the pro-tumorigenic properties of inflammatory cytokines and chemokines in the tumour microenvironment are now starting to be understood. Thus, VCAM-1 expression on endothelial cells may either be mediated in response to local damage caused by the extravasation and development of tumour cells within the perivascular space, or during direct interaction between tumour cells and the endothelium. Further studies, aimed at blocking the effects of specific adhesion molecules at different points during metastatic progression, may help to elucidate this question.

Initiation of a systemic inflammatory response by injection of an adenovirus caused VCAM-1 upregulation on the brain vasculature (Figure 5.6), with preferential expression of VCAM-1 on arterial rather than venous vessels. VCAM-1 expression detected at a distance from the tumour site in untreated animals, appeared to occur preferentially on αSMA-positive vessels, rather than EphB4-positive vessels, consistent with VCAM-1 expression patterns caused by the injection of the three adenoviruses. These data suggest that the patterns of VCAM-1 expression as a result of systemic viral infection metastasis development are under

similar control. Under normal developmental circumstances, 4T1-GFP cells were found preferentially on EphB4 positive blood vessels and not on αSMA positive blood vessels, suggesting that tumour cells extravasate preferentially at the venous end of the vascular bed as opposed to the arteriolar end. One question arising from the data collected in these experiments is the degree to which tumours may have extravasated in arteriolar blood vessels as a result of adenoviral pre-treatment. If VCAM-1 were to aid the arrest and/or extravasation of tumour cells in the brain vasculature, then we might expect to find more metastases on αSMA-positive vessels in the case where animals had been pre-treated with adenovirus. Thus, although the number of tumours that developed was reduced, it is possible that the surviving metastases were targeted towards αSMA positive blood vessels as a result.

The above observations about the normal development of 4T1-GFP brain metastases suggest that the tumours studied here probably arrest and extravasate preferentially on EphB4-positive vessels. This finding agrees with data from Lorger and Felding-Habermann (2010), who identified tumour extravasation in the capillaries and the post-capillary venules, to the exclusion of the pre-capillary arterioles. Post-capillary venules have fewer P-face tight junctions than pre-capillary arterioles (Nagy et al., 1984; Ge et al., 2005), possibly aiding leukocyte arrest and extravasation, which also occurs more frequently on post-capillary venules than pre-capillary arterioles (Lossinsky and Shivers, 2004; Prendergast and Anderton, 2009). These features of brain capillary beds, thus, support the observation that tumour arrest and extravasation occurs more frequently on these vessels.

However, current models of leukocyte extravasation in the brain suggest that the majority takes place at the venous end of the vascular bed (Lossinsky and Shivers, 2004). Despite a lack of colocalisation between VCAM-1 expression after adenovirus injection and tumour

development, it is still possible that VCAM-1 still plays a role in the priming of metastatic cells, causing them to arrest within nearby vasculature, possibly at the venous end of the same vascular bed. However, the effect of adenovirus injection is not only the upregulation of VCAM-1 on cerebral blood vessels, but a whole range of other inflammatory responses. It would seem, therefore, that were tumour arrest to be promoted by virally-induced VCAM-1 expression, that other immune responses may be responsible for decreased extravasation and tumour development, possibly via immune-mediated tumour cell death.

Further work is needed to determine the importance of VCAM-1 in the initiation and development of brain metastases. This thesis has concentrated on the increased expression of VCAM-1 via injection of viruses or a cerebral injection of cytokine. A variety of experiments should also be run evaluate the effects of VCAM-1 signal down-regulation. Although the VCAM-$1^{-/-}$ knockout phenotype is lethal, conditional VCAM-1 mutant mice have been bred on a C57BL/6 background (Koni et al., 2001; Leuker et al., 2001). All of the experiments, thus far, have concentrated on the syngeneic 4T1–BALB/c model, so experiments looking at the knockout of VCAM-1 expression would have to be developed with a new tumour model such as a B16 melanoma cell line in a C57Bl/6 mouse. An alternative strategy could be to block VCAM-1 / VLA-4 binding either by prior injection of a VCAM-1 agonist or by co-culture of 4T1-GFP cells with an antibody that binds and blocks VLA-4. A straightforward comparison of tumour numbers and sizes at day 10 would elucidate whether blocking this signalling pathway is adequate to reduce the number of metastatic lesions in the brain. If this blocked the initiation of metastasis entirely it would demonstrate the necessity of VCAM-1 in the formation of brain metastasis. This work is currently in progress within the lab and indicates an active functional role for VLA-4/VCAM-1 in tumour seeding to the brain (Soto et al., in review).

The importance of Ephrins and their ligands, the ephrins, in relation to cancer biology has already been described (Section 4.4.3). Recent work has demonstrated the importance of EphA2-epha4 signalling in transendothelial migration of leukocytes across HUVECs (Trinidad et al., 2010), so it is possible that expression of EphB4 on 4T1-GFP cells can act via a similar signalling pathway with ephrins expressed on endothelial cells or circulating immune cells. In a similar manner to the VCAM-1/VLA-4 blocking experiment described above, blocking of EphB4 binding sites with a non-competitive antagonist *in vitro* prior to tumour cell injection may alter the metastatic potential of these cells.

6.5 Effects of inflammation on tumour morphology

In addition to promoting VCAM-1 expression on cerebral vasculature and reducing the number of tumours that develop in the brain, a systemic inflammatory response caused changes in the morphology of the tumours within the brain. Patterns of tumour development were altered in inflamed environments, with greater levels of vascular co-option visible in many tumours. Angiogenesis has been advanced as a mechanism by which tumour cells are able to maintain access to an adequate blood supply without the need for an angiogenic switch (Leenders et al., 2002). The signalling mechanisms by which a co-optive pattern of growth occurs are not known, but it appears that tumour spread can occur along arterial vessels in the largest tumours (Figure 4.12). This finding suggests that tumour proliferation and migration are direction-independent and that tumours are able to track both retrogradely and anterogradely. It is possible this behaviour is related to activated endothelial cells signalling to metastatic cells on their abluminal surfaces, or that infiltrating leukocytes play a part in this behaviour.

6.6 Effects of localised neuroinflammation on tumour development

Injection of pro-inflammatory cytokines into the rodent brain has previously been shown to invoke a set of transient inflammatory responses (Blamire et al., 2000; Blond et al., 2002; Sibson et al., 2002, 2004; Wilcockson et al., 2002; Ferrari et al., 2004; Docagne et al., 2005; McAteer et al., 2007). Localised neuroinflammation following injection of mIL-1β or mTNF-α is demonstrated by VCAM-1 upregulation on cerebral blood vessels, and was hypothesised to have a tumour promoting effect, in a similar manner to the endothelial activation caused by a systemic inflammatory response. However, in the pilot study reported here the differences in tumour uptake by the contralateral and ipsilateral hemispheres were too low in most treatment groups to draw any firm conclusions about the development of tumours. If a tumour-promoting effect were observed, this would fit with the model of VCAM-1 upregulation on cerebral blood vessels promoting the extravasation of metastatic cells in circulation; tumour-repression would suggest an immune-regulated neuroprotective effect of cytokine injection. Increased n numbers would allow further elucidation of this point.

6.7 Wider implications of the work

In summary, in this thesis I have demonstrated:

1 The use of novel filtering and analysis methods for the detection of VCAM-MPIO-induced hypointensities in MRI brain volumes and their correlation with VCAM-1 expression at the tumour site.

2 The regional and morphological development of 4T1-GFP cerebral metastases and their preferential colocalisation with venous blood vessels.

3 The effects on cytokine profiles, neurovascular VCAM-1 expression and tumour development of a systemic inflammatory response induced by adenovirus treatment pre- or post-tumour cell injection, and preliminary data with respect to the effects on tumour development of a localised neuroinflammatory response.

In its broader scope, the experiments described in this thesis relate to the development of primary tumours in humans and subsequent metastasis to the brain. Paget (1889) first described the specificity of metastasis to distant organs from a given primary tumour, and the current work has sought to both explain some of the mechanisms by which tumours are able to metastasize to the brain, describe some of the features of their development there and help develop tools for improving diagnosis of the condition. Despite the differences in anatomy and physiology between mice and humans, many immune functions are conserved between the two species. Given the protective role that a systemic inflammatory response appears to play in preventing tumour extravasation, the maintenance of a pro-inflammatory environment in man may be beneficial in preventing or reducing brain metastasis. These results have implications for the treatment and post-surgical management of patients with malignant primary tumours. For those patients that do develop cerebral metastases, prognosis is often poor, in part as a result of late detection of tumours. Earlier detection could offer a reduction in mortality. One further barrier to overcome is that of the BBB and its effect on blocking many therapeutic molecules from leaving the circulation. Immunotherapy has become more and more relevant in recent years as an adjunct to, or replacement for, more traditional chemotherapy and radiotherapy in other organs. Although the experiments described in this thesis have not focused on the BBB specifically, the means by which tumour cells and immune system cells are able to leave the vasculature and enter

the brain may be of importance in developing immunotherapies towards brain metastasis in the future.

References

Web Resources:

Cancer Research UK, Cancer Incidence by Age, accessed 29-07-13, <http://www.cancerresearchuk.org/cancer-info/cancerstats/incidence/age/>

EMBL-EBI, Pairwise Protein Sequence Alignment Tool, accessed 01-10-12, <http://www.ebi.ac.uk/Tools/psa/>

ITK-SNAP, accessed 11-27-12, <http://www.itksnap.org>

MATLAB Central File Exchange, Tools for NIfTI and ANALYZE image, last accessed 07-03-13, <https://www.mathworks.co.uk/matlabcentral/fileexchange/8797-tools-for-nifti-and-analyze-image>

MATLAB Central File Exchange, Protein Array Tool, accessed 01-10-10, <http://www.mathworks.co.uk/matlabcentral/fileexchange/35128-protein-array-tool >

Virapur, Plaque Assay, accessed 01-07-11, <http://www.virapur.com/protocols/Virus%20Plaque%20Assay%20Protocol.pdf>

Virapur, $TCID_{50}$ assay, accessed 01-07-11, <http://www.virapur.com/protocols/TCID50%20Protocol.pdf>

Yale University, $TCID_{50}$ infectivity calculator, accessed 01-07-11, <www.med.yale.edu/micropath/pdf/Infectivity%20calculator.xls>

Books and Journals:

Afonso P V, Ozden S, Cumont M-C, Seilhean D, Cartier L, Rezaie P, Mason S, Lambert S, Huerre M, Gessain A, Couraud P-O, Pique C, Ceccaldi P-E, Romero IA (2008) Alteration of blood-brain barrier integrity by retroviral infection. PLoS Pathogens 4:e1000205.

Aichel O (1911) Über Zellverschmelzung mit qualitativ abnormer Chromosomenverteilung als Ursache der Geschwulstbildung. Leipzig: W. Engelmann.

Albright CD, Salganik RI, Van Dyke T (2004) Dietary depletion of vitamin E and vitamin A inhibits mammary tumor growth and metastasis in transgenic mice. The Journal of Nutrition 134:1139–1144.

Andersen T, Boissy P, Sondergaard T, Kupisiewicz K, Plesner T, Rasmussen T, Haaber J, Kølvraa S, Delaissé JM (2007) Osteoclast nuclei of myeloma patients show chromosome translocations specific for the myeloma cell clone: a new type of cancer-host partnership? The Journal of Pathology 211:10–17.

Anderson CMH, Thwaites DT (2010) Hijacking solute carriers for proton-coupled drug transport. Physiology (Bethesda, Md) 25:364–377.

Anderson MJ (2001) A new method for non-parametric multivariate analysis of variance. Austral Ecology 26:32–46.

Anthony DC, Bolton SJ, Fearn S, Perry VH (1997) Age-related effects of interleukin-1 beta on polymorphonuclear neutrophil-dependent increases in blood-brain barrier permeability in rats. Brain 120:435–444.

Anthony DC, Sibson NR, McAteer MA, Davis B, Choudhury RP (2011) Detection of brain pathology by magnetic resonance imaging of iron oxide micro-particles. Methods in molecular biology (Clifton, NJ) 686:213–227.

Arend WP (2002) The balance between IL-1 and IL-1Ra in disease. Cytokine & Growth Factor Reviews 13:323–340.

Aslakson CJ, Miller FR (1992) Selective events in the metastatic process defined by analysis of the sequential dissemination of subpopulations of a mouse mammary tumor. Cancer Research 52:1399–1405.

Baba T, Iwasaki S, Maruoka T, Suzuki A, Tomaru U, Ikeda H, Yoshiki T, Kasahara M, Ishizu A (2008) Rat CD4+CD8+ macrophages kill tumor cells through an NKG2D- and granzyme/perforin-dependent mechanism. The Journal of Immunology 180:2999–3006.

Babior BM (2000) Phagocytes and oxidative stress. The American Journal of Medicine 109:33–44.

Bagnara JT (1985) Biological, molecular, and clinical aspects of pigmentation : proceedings of the XIIth International Pigment Cell Conference, Giessen, Federal Republic of Germany. In, pp xxxiv, 774 p., 3 p. of plates. Tokyo, Japan: University of Tokyo Press.

Balathasan L, Beech JS, Muschel RJ (2013) Ultrasonography-Guided Intracardiac Injection: An Improvement for Quantitative Brain Colonization Assays. The American Journal of Pathology 183:26–34.

Ballinger Jr. WE, Schimpff RD (1979) An experimental model for cerebral metastasis: preliminary light and ultrastructural studies. Journal of Neuropathology & Experimental Neurology 38:19–34.

Barajas RF, Cha S (2012) Imaging diagnosis of brain metastasis. Progress in Neurological Surgery 25:55–73.

Barbu E, Molnàr E, Tsibouklis J, Górecki DC (2009) The potential for nanoparticle-based drug delivery to the brain: overcoming the blood-brain barrier. Expert Opinion on Drug Delivery 6:553–565.

Beaumont M, Lemasson B, Farion R, Segebarth C, Rémy C, Barbier EL (2009) Characterization of tumor angiogenesis in rat brain using iron-based vessel size index MRI in combination with gadolinium-based dynamic contrast-enhanced MRI. Journal of Cerebral Blood Flow and Metabolism 29:1714–1726.

Beckmann N, Gérard C, Abramowski D, Cannet C, Staufenbiel M (2011) Noninvasive magnetic resonance imaging detection of cerebral amyloid angiopathy-related microvascular alterations using superparamagnetic iron oxide particles in APP transgenic mouse models of Alzheimer's disease: application to passive Abeta immunotherap. The Journal of Neuroscience 31:1023–1031.

Bennett BD, Wang Z, Kuang WJ, Wang A, Groopman JE, Goeddel D V, Scadden DT (1994) Cloning and characterization of HTK, a novel transmembrane tyrosine kinase of the EPH subfamily. The Journal of Biological Chemistry 269:14211–14218.

Berclaz G, Andres AC, Albrecht D, Dreher E, Ziemiecki A, Gusterson BA, Crompton MR (1996) Expression of the receptor protein tyrosine kinase myk-1/htk in normal and malignant mammary epithelium. Biochemical and Biophysical Research Communications 226:869–875.

Berclaz G, Karamitopoulou E, Mazzucchelli L, Rohrbach V, Dreher E, Ziemiecki A, Andres A-C (2003) Activation of the receptor protein tyrosine kinase EphB4 in endometrial hyperplasia and endometrial carcinoma. Annals of oncology : official journal of the European Society for Medical Oncology / ESMO 14:220–226.

Bett AJ, Haddara W, Prevec L, Graham FL (1994) An efficient and flexible system for construction of adenovirus vectors with insertions or deletions in early regions 1 and 3. Proceedings of the National Academy of Sciences of the United States of America 91:8802–8806.

Bierie B, Moses HL (2006) Tumour microenvironment: TGFbeta: the molecular Jekyll and Hyde of cancer. Nature Reviews Cancer 6:506–520.

Bindea G, Mlecnik B, Fridman W-H, Pagès F, Galon J (2010) Natural immunity to cancer in humans. Current Opinion in Immunology 22:215–222.

Blamire AM, Anthony DC, Rajagopalan B, Sibson NR, Perry VH, Styles P (2000) Interleukin-1beta - induced changes in blood-brain barrier permeability, apparent diffusion coefficient, and cerebral blood volume in the rat brain: a magnetic resonance study. The Journal of Neuroscience 20:8153–8159.

Bleul CC, Fuhlbrigge RC, Casasnovas JM, Aiuti A, Springer TA (1996) A highly efficacious lymphocyte chemoattractant, stromal cell-derived factor 1 (SDF-1). The Journal of Experimental Medicine 184:1101–1109.

Bloch F, Rabi I (1945) Atoms in Variable Magnetic Fields. Reviews of Modern Physics 17:237–244.

Blond D, Campbell SJ, Butchart AG, Perry VH, Anthony DC (2002) Differential induction of interleukin-1beta and tumour necrosis factor-alpha may account for specific patterns of leukocyte recruitment in the brain. Brain Research 958:89–99.

Bolton SJ, Anthony DC, Perry VH (1998) Loss of the tight junction proteins occludin and zonula occludens-1 from cerebral vascular endothelium during neutrophil-induced blood-brain barrier breakdown in vivo. Neuroscience 86:1245–1257.

Boyer JC, Thomas DC, Maher VM, McCormick JJ, Kunkel TA (1993) Fidelity of DNA Replication by Extracts of Normal and Malignantly Transformed Human Cells. Cancer Research 53:3270–3275.

Brankin B, Hart MN, Cosby SL, Fabry Z, Allen I V (1995) Adhesion molecule expression and lymphocyte adhesion to cerebral endothelium: effects of measles virus and herpes simplex 1 virus. Journal of Neuroimmunology 56:1–8.

Brightman MW, Reese TS (1969) Junctions between intimately apposed cell membranes in the vertebrate brain. The Journal of Cell Biology 40:648–677.

Briley-Saebo KC, Johansson LO, Hustvedt SO, Haldorsen AG, Bjørnerud A, Fayad ZA, Ahlstrom HK (2006) Clearance of iron oxide particles in rat liver: effect of hydrated particle size and coating material on liver metabolism. Investigative Radiology 41:560–571.

Brodt P, Fallavollita L, Bresalier R, Meterissian S, Norton C, Wolitzky B (1997) Liver endothelial E-selectin mediates carcinoma cell adhesion and promotes liver metastasis. International Journal of Cancer 71:612–621.

Bunt SK, Yang L, Sinha P, Clements VK, Leips J, Ostrand-Rosenberg S (2007) Reduced inflammation in the tumor microenvironment delays the accumulation of myeloid-derived suppressor cells and limits tumor progression. Cancer Research 67:10019–10026.

Burke B, Lewis CE (2002) The macrophage, 2nd ed. Oxford: Oxford University Press.

Burnet M (1957) Cancer; a biological approach. I. The processes of control. British Medical Journal 1:779–786.

Burrell JS, Walker-Samuel S, Baker LCJ, Boult JKR, Jamin Y, Ryan AJ, Waterton JC, Halliday J, Robinson SP (2012) Evaluation of novel combined carbogen USPIO (CUSPIO) imaging biomarkers in assessing the antiangiogenic effects of cediranib (AZD2171) in rat C6 gliomas. International Journal of Cancer 131:1854–1862.

Burrell JS, Walker-Samuel S, Baker LCJ, Boult JKR, Ryan AJ, Waterton JC, Halliday J, Robinson SP (2011) Investigating temporal fluctuations in tumor vasculature with combined carbogen and ultrasmall superparamagnetic iron oxide particle (CUSPIO) imaging. Magnetic Resonance in Medicine 66:227–234.

Calvo F, Martin P, Jabrane N, De Cremoux P, Magdelenat H (1987) Human breast cancer cells share antigens with the myeloid monocyte lineage. British Journal of Cancer 56:15–24.

Campbell SJ, Wilcockson DC, Butchart AG, Perry VH, Anthony DC (2002) Altered chemokine expression in the spinal cord and brain contributes to differential interleukin-1beta-induced neutrophil recruitment. Journal of Neurochemistry 83:432–441.

Cannella B, Raine CS (1995) The adhesion molecule and cytokine profile of multiple sclerosis lesions. Annals of Neurology 37:424–435.

Carbonell WS, Ansorge O, Sibson N, Muschel R (2009) The vascular basement membrane as “soil” in brain metastasis. PLoS One 4:e5857.

Carlos TM, Schwartz BR, Kovach NL, Yee E, Rosa M, Osborn L, Chi-Rosso G, Newman B, Lobb R, Rosso M (1990) Vascular cell adhesion molecule-1 mediates lymphocyte adherence to cytokine-activated cultured human endothelial cells. Blood 76:965–970.

Carr H, Purcell E (1954) Effects of Diffusion on Free Precession in Nuclear Magnetic Resonance Experiments. Physical Review 94:630–638.

Carrithers MD, Visintin I, Viret C, Janeway CS (2002) Role of genetic background in P selectin-dependent immune surveillance of the central nervous system. Journal of Neuroimmunology 129:51–57.

Chabrerie A, Ozlen F, Nakajima S, Leventon ME, Atsumi H, Grimson E, Jolesz F, Kikinis R, Black PM (1998) Three-dimensional image reconstruction for low-grade glioma surgery. Neurosurgical Focus 4:e7.

Chabrerie A, Ozlen F, Nakajima S, Leventon ME, Atsumi H, Grimson E, Keeve E, Helmers S, Riviello J, Holmes G, Duffy F, Jolesz F, Kikinis R, Black PM (1997) Three-dimensional reconstruction and surgical navigation in pediatric epilepsy surgery. Pediatric Neurosurgery 27:304–310.

Chakraborty AK, De Freitas Sousa J, Espreafico EM, Pawelek JM (2001) Human monocyte x mouse melanoma fusion hybrids express human gene. Gene 275:103–106.

Chakraborty AK, Kolesnikova N, Sousa J de F, Espreafico EM, Peronni KC, Pawelek J (2003) Expression of c-Met proto-oncogene in metastatic macrophage x melanoma fusion hybrids: implication of its possible role in MSH-induced motility. Oncology Research 14:163–174.

Chambers AF, Groom AC, MacDonald IC (2002) Dissemination and growth of cancer cells in metastatic sites. Nature Reviews Cancer 2:563–572.

Chaumeil MM, Gini B, Yang H, Iwanami A, Sukumar S, Ozawa T, Pieper RO, Mischel PS, James CD, Berger MS, Ronen SM (2012) Longitudinal evaluation of MPIO-labeled stem cell biodistribution in glioblastoma using high resolution and contrast-enhanced MR imaging at 14.1 tesla. Neuro-Oncology 14:1050–1061.

Chen HH, Le Visage C, Qiu B, Du X, Ouwerkerk R, Leong KW, Yang X (2005) MR imaging of biodegradable polymeric microparticles: a potential method of monitoring local drug delivery. Magnetic Resonance in Medicine 53:614–620.

Cheng W, Ping Y, Zhang Y, Chuang K-H, Liu Y (2013) Magnetic resonance imaging (MRI) contrast agents for tumor diagnosis. Journal of Healthcare Engineering 4:23–45.

Chien L-Y, Hsiao J-K, Hsu S-C, Yao M, Lu C-W, Liu H-M, Chen Y-C, Yang C-S, Huang D-M (2011) In vivo magnetic resonance imaging of cell tropism, trafficking mechanism, and therapeutic impact of human mesenchymal stem cells in a murine glioma model. Biomaterials 32:3275–3284.

Coffelt SB, Lewis CE, Naldini L, Brown JM, Ferrara N, De Palma M (2010) Elusive identities and overlapping phenotypes of proangiogenic myeloid cells in tumors. The American Journal of Pathology 176:1564–1576.

Cole KE, Strick CA, Paradis TJ, Ogborne KT, Loetscher M, Gladue RP, Lin W, Boyd JG, Moser B, Wood DE, Sahagan BG, Neote K (1998) Interferon-inducible T cell alpha chemoattractant (I-TAC): a novel non-ELR CXC chemokine with potent activity on activated T cells through selective high affinity binding to CXCR3. The Journal of Experimental Medicine 187:2009–2021.

Collado M, Serrano M (2010) Senescence in tumours: evidence from mice and humans. Nature Reviews Cancer 10:51–57.

Cormack BP, Valdivia RH, Falkow S (1996) FACS-optimized mutants of the green fluorescent protein (GFP). Gene 173:33–38.

Cossetti C, Smith JA, Iraci N, Leonardi T, Alfaro-Cervello C, Pluchino S (2012) Extracellular membrane vesicles and immune regulation in the brain. Frontiers in Physiology 3:117.

Couch Y, Alvarez-Erviti L, Sibson N, Wood M, Anthony D (2011) The acute inflammatory response to intranigral alpha-synuclein differs significantly from intranigral lipopolysaccharide and is exacerbated by peripheral inflammation. Journal of Neuroinflammation 8:166.

Cromer A, Carles A, Millon R, Ganguli G, Chalmel F, Lemaire F, Young J, Dembélé D, Thibault C, Muller D, Poch O, Abecassis J, Wasylyk B (2004) Identification of genes associated with tumorigenesis and metastatic potential of hypopharyngeal cancer by microarray analysis. Oncogene 23:2484–2498.

Cucullo L, Hossain M, Tierney W, Janigro D (2013) A new dynamic in vitro modular capillaries-venules modular system: cerebrovascular physiology in a box. BMC Neuroscience 14:18.

Cunningham C, Wilcockson D, Campion S, Lunnon K, Perry V (2005) Central and systemic endotoxin challenges exacerbate the local inflammatory response and increase neuronal death during chronic neurodegeneration. The Journal of Neuroscience 25:9275–9359.

Daniels BP, Cruz-Orengo L, Pasieka TJ, Couraud P-O, Romero IA, Weksler B, Cooper JA, Doering TL, Klein RS (2013) Immortalized human cerebral microvascular endothelial cells maintain the properties of primary cells in an in vitro model of immune migration across the blood brain barrier. Journal of Neuroscience Methods 212:173–179.

Das SK, Hashimoto T, Shimizu K, Yoshida T, Sakai T, Sowa Y, Komoto A, Kanazawa K (2005) Fucoxanthin induces cell cycle arrest at G0/G1 phase in human colon carcinoma cells through up-regulation of p21WAF1/Cip1. Biochimica et Biophysica Acta 1726:328–335.

De Palma M, Murdoch C, Venneri MA, Naldini L, Lewis CE (2007) Tie2-expressing monocytes: regulation of tumor angiogenesis and therapeutic implications. Trends in Immunology 28:519–524.

Deloire MSA, Touil T, Brochet B, Dousset V, Caillé J-M, Petry KG (2004) Macrophage brain infiltration in experimental autoimmune encephalomyelitis is not completely compromised by suppressed T-cell invasion: in vivo magnetic resonance imaging illustration in effective anti-VLA-4 antibody treatment. Multiple Sclerosis 10:540–548.

DeNardo DG, Andreu P, Coussens LM (2010) Interactions between lymphocytes and myeloid cells regulate pro- versus anti-tumor immunity. Cancer Metastasis Reviews 29:309–316.

DeNardo DG, Barreto JB, Andreu P, Vasquez L, Tawfik D, Kolhatkar N, Coussens LM (2009) CD4(+) T cells regulate pulmonary metastasis of mammary carcinomas by enhancing protumor properties of macrophages. Cancer Cell 16:91–102.

Dexter DL, Kowalski HM, Blazar BA, Fligiel Z, Vogel R, Heppner GH (1978) Heterogeneity of tumor cells from a single mouse mammary tumor. Cancer Research 38:3174–3181.

Dick AP, Harik SI (1986) Distribution of the glucose transporter in the mammalian brain. Journal of Neurochemistry 46:1406–1411.

Disibio G, French SW (2008) Metastatic patterns of cancers: results from a large autopsy study. Archives of Pathology & Laboratory Medicine 132:931–939.

Docagne F, Campbell SJ, Bristow AF, Poole S, Vigues S, Guaza C, Perry VH, Anthony DC (2005) Differential regulation of type I and type II interleukin-1 receptors in focal brain inflammation. The European Journal of Neuroscience 21:1205–1214.

Dos Santos WL, Rahman J, Klein N, Male DK (1996) Control of lymphocyte adhesion to brain and aortic endothelium: ICAM-1, VCAM-1 and negative charge. Journal of Neuroimmunology 66:125–134.

Dousset V, Ballarino L, Delalande C, Coussemacq M, Canioni P, Petry KG, Caillé JM (1999a) Comparison of ultrasmall particles of iron oxide (USPIO)-enhanced T2-weighted, conventional

T2-weighted, and gadolinium-enhanced T1-weighted MR images in rats with experimental autoimmune encephalomyelitis. American Journal of Neuroradiology 20:223–227.

Dousset V, Gomez C, Petry KG, Delalande C, Caille JM (1999b) Dose and scanning delay using USPIO for central nervous system macrophage imaging. Magma (New York, NY) 8:185–189.

Duelli D, Lazebnik Y (2003) Cell fusion: a hidden enemy? Cancer Cell 3:445–448.

Duffy BA, Choy M, Riegler J, Wells JA, Anthony DC, Scott RC, Lythgoe MF (2012) Imaging seizure-induced inflammation using an antibody targeted iron oxide contrast agent. NeuroImage 60:1149–1155.

Duffy KR, Pardridge WM (1987) Blood-brain barrier transcytosis of insulin in developing rabbits. Brain Research 420:32–38.

Duffy KR, Pardridge WM, Rosenfeld RG (1988) Human blood-brain barrier insulin-like growth factor receptor. Metabolism: Clinical and Experimental 37:136–140.

Dvorak H (1986) Tumors: wounds that do not heal. Similarities between tumor stroma generation and wound healing. The New England Journal of Medicine 315:1650–1659.

Egeblad M, Nakasone ES, Werb Z (2010) Tumors as organs: complex tissues that interface with the entire organism. Developmental Cell 18:884–901.

Elices MJ, Osborn L, Takada Y, Crouse C, Luhowskyj S, Hemler ME, Lobb RR (1990) VCAM-1 on activated endothelium interacts with the leukocyte integrin VLA-4 at a site distinct from the VLA-4/fibronectin binding site. Cell 60:577–584.

Erälinna JP, Soilu-Hänninen M, Röyttä M, Hukkanen V, Salmi AA, Salonen R (1996) Blood-brain barrier breakdown and increased intercellular adhesion molecule (ICAM-1/CD54) expression after Semliki Forest (A7) virus infection facilitates the development of experimental allergic encephalomyelitis. Journal of Neuroimmunology 66:103–114.

Farber JM (1990) A macrophage mRNA selectively induced by gamma-interferon encodes a member of the platelet factor 4 family of cytokines. Proceedings of the National Academy of Sciences of the United States of America 87:5238–5242.

Ferjancic S, Gil-Bernabé AM, Hill SA, Allen PD, Richardson P, Sparey T, Savory E, McGuffog J, Muschel RJ (2013) VCAM-1 and VAP-1 recruit myeloid cells that promote pulmonary metastasis in mice. Blood in press.

Ferlay J, Shin H-R, Bray F, Forman D, Mathers C, Parkin DM (2010) Estimates of worldwide burden of cancer in 2008: GLOBOCAN 2008. International Journal of Cancer 127:2893–2917.

Fernández-Klett F, Offenhauser N, Dirnagl U, Priller J, Lindauer U (2010) Pericytes in capillaries are contractile in vivo, but arterioles mediate functional hyperemia in the mouse brain. Proceedings of the National Academy of Sciences of the United States of America 107:22290–22295.

Ferrari CC, Depino AM, Prada F, Muraro N, Campbell S, Podhajcer O, Perry VH, Anthony DC, Pitossi FJ (2004) Reversible demyelination, blood-brain barrier breakdown, and pronounced neutrophil recruitment induced by chronic IL-1 expression in the brain. The American Journal of Pathology 165:1827–1837.

Ferrone C, Dranoff G (2010) Dual roles for immunity in gastrointestinal cancers. Journal of Clinical Oncology 28:4045–4051.

Fidler I, Yano S, Zhang R-D, Fujimaki T, Bucana C (2002) The seed and soil hypothesis: vascularisation and brain metastases. The Lancet Oncology 3:53–60.

Fidler IJ (2002) The organ microenvironment and cancer metastasis. Differentiation 70:498–505.

Fidler IJ (2003) The pathogenesis of cancer metastasis: the “seed and soil” hypothesis revisited. Nature Reviews Cancer 3:453–458.

Fishman JB, Rubin JB, Handrahan J V, Connor JR, Fine RE (1987) Receptor-mediated transcytosis of transferrin across the blood-brain barrier. Journal of Neuroscience Research 18:299–304.

Fitzgerald DP, Palmieri D, Hua E, Hargrave E, Herring JM, Qian Y, Vega-Valle E, Weil RJ, Stark AM, Vortmeyer AO, Steeg PS (2008) Reactive glia are recruited by highly proliferative brain metastases of breast cancer and promote tumor cell colonization. Clinical & Experimental Metastasis 25:799–810.

Floris S, Blezer ELA, Schreibelt G, Döpp E, Van der Pol SMA, Schadee-Eestermans IL, Nicolay K, Dijkstra CD, De Vries HE (2004) Blood-brain barrier permeability and monocyte infiltration in experimental allergic encephalomyelitis: a quantitative MRI study. Brain 127:616–627.

Fokas E, Steinbach JP, Rödel C (2013) Biology of brain metastases and novel targeted therapies: Time to translate the research. Biochimica et Biophysica Acta 1835:61–75.

Fortier M-E, Kent S, Ashdown H, Poole S, Boksa P, Luheshi GN (2004) The viral mimic, polyinosinic:polycytidylic acid, induces fever in rats via an interleukin-1-dependent mechanism. American Journal of Physiology - Regulatory, Integrative and Comparative Physiology 287:R759–66.

Frangi A, Niessen W, Vincken K, Viergever M (1998) Multiscale vessel enhancement filtering. In: 1st International Conference on Medical Image Computing and Computer-Assisted Intervention (MICCAI 98), pp 130–137. Cambridge, MA.

Fréchou M, Beray-Berthat V, Raynaud J-S, Mériaux S, Gombert F, Lancelot E, Plotkine M, Marchand-Leroux C, Ballet S, Robert P, Louin G, Margaill I (2013) Detection of vascular cell adhesion molecule-1 expression with USPIO-enhanced molecular MRI in a mouse model of cerebral ischemia. Contrast Media & Molecular Imaging 8:157–164.

Frisch SM, Schaller M, Cieply B (2013) Mechanisms that link the oncogenic epithelial-mesenchymal transition to suppression of anoikis. Journal of Cell Science 126:21–29.

Gabbiani G, Schmid E, Winter S, Chaponnier C, De Ckhastonay C, Vandekerckhove J, Weber K, Franke WW (1981) Vascular smooth muscle cells differ from other smooth muscle cells: predominance of vimentin filaments and a specific alpha-type actin. Proceedings of the National Academy of Sciences of the United States of America 78:298–302.

Gambarota G, Leenders W, Maass C, Wesseling P, Van der Kogel B, Van Tellingen O, Heerschap A (2008) Characterisation of tumour vasculature in mouse brain by USPIO contrast-enhanced MRI. British Journal of Cancer 98:1784–1789.

Garroway AN, Grannell PK, Mansfield P (1974) Image formation in NMR by a selective irradiative process. Journal of Physics C: Solid State Physics 7:L457.

Gavrilovic IT, Posner JB (2005) Brain metastases: epidemiology and pathophysiology. Journal of Neuro-Oncology 75:5–14.

Ge S, Song L, Pachter J (2005) Where is the blood-brain barrier ... really? Journal of Neuroscience Research 79:421–428.

Gilmour J, Lavender P (2008) Control of IL-4 expression in T helper 1 and 2 cells. Immunology 124:437–444.

Golby AJ, Kindlmann G, Norton I, Yarmarkovich A, Pieper S, Kikinis R (2011) Interactive diffusion tensor tractography visualization for neurosurgical planning. Neurosurgery 68:496–505.

Gomes FG, Nedel F, Alves AM, Nör JE, Tarquinio SBC (2013) Tumor angiogenesis and lymphangiogenesis: tumor/endothelial crosstalk and cellular/microenvironmental signaling mechanisms. Life Sciences 92:101–107.

Gottesman MM (1990) Introduction: Do proteases play a role in cancer? Seminars in Cancer Biology 1:97–98.

Graham FL, Smiley J, Russell WC, Nairn R (1977) Characteristics of a human cell line transformed by DNA from human adenovirus type 5. The Journal of General Virology 36:59–74.

Granowitz E V, Santos AA, Poutsiaka DD, Cannon JG, Wilmore DW, Wolff SM, Dinarello CA (1991) Production of interleukin-1-receptor antagonist during experimental endotoxaemia. Lancet 338:1423–1424.

Green C, Liu T, Montel V, Hsiao G, Lester R, Subramaniam S, Gonias S, Klemke R (2009) Chemoattractant signaling between tumor cells and macrophages regulates cancer cell migration, metastasis and neovascularization. PloS One 4:e6713.

Greenwood J, Heasman SJ, Alvarez JI, Prat A, Lyck R, Engelhardt B (2011) Review: leucocyte-endothelial cell crosstalk at the blood-brain barrier: a prerequisite for successful immune cell entry to the brain. Neuropathology and Applied Neurobiology 37:24–39.

Griffin GK, Newton G, Tarrio ML, Bu D-X, Maganto-Garcia E, Azcutia V, Alcaide P, Grabie N, Luscinskas FW, Croce KJ, Lichtman AH (2012) IL-17 and TNF-α Sustain Neutrophil Recruitment during Inflammation through Synergistic Effects on Endothelial Activation. Journal of Immunology 188:6287–6299.

Grivennikov S, Greten F, Karin M (2010) Immunity, inflammation, and cancer. Cell 140:883–982.

Grossman RI, Gomori JM, Goldberg HI, Hackney DB, Atlas SW, Kemp SS, Zimmerman RA, Bilaniuk LT (1988) MR imaging of hemorrhagic conditions of the head and neck. Radiographics 8:441–454.

Gupta GP, Massagué J (2006) Cancer metastasis: building a framework. Cell 127:679–695.

Haddad O, Chotard-Ghodsnia R, Verdier C, Duperray A (2010) Tumor cell/endothelial cell tight contact upregulates endothelial adhesion molecule expression mediated by NFkappaB: differential role of the shear stress. Experimental Cell Research 316:615–641.

Hahn E (1950) Spin Echoes. Physical Review 80:580–594.

Hamilton A, Sibson NR (2013) Role of the systemic immune system in brain metastasis. Molecular and Cellular Neuroscience 53:42–51.

Hamoudeh M, Fessi H (2006) Preparation, characterization and surface study of poly-epsilon caprolactone magnetic microparticles. Journal of Colloid and Interface Science 300:584–590.

Hanahan D, Weinberg RA (2011) Hallmarks of cancer: the next generation. Cell 144:646–674.

Harlan JM, Liu DY (1992) Adhesion : its role in inflammatory disease. New York: W.H. Freeman.

Hart IR, Fidler IJ (1980) Role of organ selectivity in the determination of metastatic patterns of B16 melanoma. Cancer Research 40:2281–2287.

Haskill S, Peace A, Morris J, Sporn SA, Anisowicz A, Lee SW, Smith T, Martin G, Ralph P, Sager R (1990) Identification of three related human GRO genes encoding cytokine functions. Proceedings of the National Academy of Sciences of the United States of America 87:7732–7736.

Hemmingsson A, Carlsten J, Ericsson A, Klaveness J, Sperber GO, Thuomas KA (1987) Relaxation enhancement of the dog liver and spleen by biodegradable superparamagnetic particles in proton magnetic resonance imaging. Acta Radiologica 28:703–705.

Herman IM, D'Amore PA (1985) Microvascular pericytes contain muscle and nonmuscle actins. The Journal of Cell Biology 101:43–52.

Hickey WF, Kimura H (1988) Perivascular microglial cells of the CNS are bone marrow-derived and present antigen in vivo. Science 239:290–292.

Hinton C V, Avraham S, Avraham HK (2008) Role of the CXCR4/CXCL12 signaling axis in breast cancer metastasis to the brain. Clinical & Experimental Metastasis 27:97–105.

Hirai H, Maru Y, Hagiwara K, Nishida J, Takaku F (1987) A novel putative tyrosine kinase receptor encoded by the eph gene. Science 238:1717–1720.

Hochstenbag MM, Twijnstra A, Wilmink JT, Wouters EF, Ten Velde GP (2000) Asymptomatic brain metastases (BM) in small cell lung cancer (SCLC): MR-imaging is useful at initial diagnosis. Journal of neuro-Oncology 48:243–248.

Hoyte LC, Brooks KJ, Nagel S, Akhtar A, Chen R, Mardiguian S, McAteer MA, Anthony DC, Choudhury RP, Buchan AM, Sibson NR (2010) Molecular magnetic resonance imaging of acute vascular cell adhesion molecule-1 expression in a mouse model of cerebral ischemia. Journal of Cerebral Blood Flow and Metabolism 30:1178–1187.

Huang Q, Deng J, Xie Z, Wang F, Chen S, Lei B, Liao P, Huang N, Wang Z, Wang Z, Cheng Y (2012) Effective gene transfer into central nervous system following ultrasound-microbubbles-induced opening of the blood-brain barrier. Ultrasound in Medicine & Biology 38:1234–1243.

Huang X, Yamada Y, Kidoya H, Naito H, Nagahama Y, Kong L, Katoh S-Y, Li W, Ueno M, Takakura N (2007) EphB4 overexpression in B16 melanoma cells affects arterial-venous patterning in tumor angiogenesis. Cancer Research 67:9800–9808.

Huber JD, Campos CR, Mark KS, Davis TP (2006) Alterations in blood-brain barrier ICAM-1 expression and brain microglial activation after lambda-carrageenan-induced inflammatory pain. American Journal of Physiology - Heart and Circulatory Physiology 290:H732–40.

Hughes AL (1994) Evolution of the interleukin-1 gene family in mammals. Journal of Molecular Evolution 39:6–12.

Husseini GA, Pitt WG (2009) Ultrasonic-activated micellar drug delivery for cancer treatment. Journal of Pharmaceutical Sciences 98:795–811.

Huysentruyt L, Mukherjee P, Banerjee D, Shelton L, Seyfried T (2008) Metastatic cancer cells with macrophage properties: evidence from a new murine tumor model. International Journal of Cancer 123:73–157.

Ikeda M, Bhattacharjee AK, Kondoh T, Nagashima T, Tamaki N (2002) Synergistic effect of cold mannitol and Na(+)/Ca(2+) exchange blocker on blood-brain barrier opening. Biochemical and Biophysical Research Communications 291:669–674.

Ikushima H, Miyazono K (2010) TGFbeta signalling: a complex web in cancer progression. Nature Reviews Cancer 10:415–424.

Itzhaki RF, Wozniak MA, Appelt DM, Balin BJ (2004) Infiltration of the brain by pathogens causes Alzheimer's disease. Neurobiology of Aging 25:619–627.

James WG, Bullard DC, Hickey MJ (2003) Critical Role of the {alpha}4 Integrin/VCAM-1 Pathway in Cerebral Leukocyte Trafficking in Lupus-Prone MRL/faslpr Mice. Journal Of Immunology 170:520–527.

Jefferson A, Wijesurendra RS, McAteer MA, Choudhury RP (2012) Development and application of endothelium-targeted microparticles for molecular magnetic resonance imaging. Nanomedicine and Nanobiotechnology 4:247–256.

Jia J, Zhang W, Liu J-Y, Chen G, Liu H, Zhong H-Y, Liu B, Cai Y, Zhang J-L, Zhao Y-F (2012) Epithelial mesenchymal transition is required for acquisition of anoikis resistance and metastatic potential in adenoid cystic carcinoma. PloS One 7:e51549.

Johansson M, Denardo DG, Coussens LM (2008) Polarized immune responses differentially regulate cancer development. Immunological Reviews 222:145–154.

Jovanova-Nesic K, Shoenfeld Y (2006) MMP-2, VCAM-1 and NCAM-1 expression in the brain of rats with experimental autoimmune encephalomyelitis as a trigger mechanism for synaptic plasticity and pathology. Journal of Neuroimmunology 181:112–121.

Jurečková J, Kalina J (2012) Nonparametric multivariate rank tests and their unbiasedness. Bernoulli 18:229–251.

Kaiserman D, Bird CH, Sun J, Matthews A, Ung K, Whisstock JC, Thompson PE, Trapani JA, Bird PI (2006) The major human and mouse granzymes are structurally and functionally divergent. The Journal of Cell Biology 175:619–630.

Kamerkar S, Davis PH (2012) Toxoplasma on the brain: understanding host-pathogen interactions in chronic CNS infection. Journal of Parasitology Research 2012:589295.

Kawaguchi T, Endo M, Yokoya S, Nakamura K (1982) Difference in proliferation-kinetics between tumor cells arrested in the brain and liver. Experientia 38:1236–1237.

Kerfoot SM, Kubes P (2002) Overlapping roles of P-selectin and alpha 4 integrin to recruit leukocytes to the central nervous system in experimental autoimmune encephalomyelitis. Journal of Immunology 169:1000–1006.

Kety SS, Skenkin HA, Schmidt CF (1948) The effects of increased intracranial pressure on cerebral circulatory functions in man. Journal of Clinical Investigation 27:493–499.

Khatib A, Kontogiannea M, Fallavollita L, Jamison B, Meterissian S, Brodt P (1999) Rapid induction of cytokine and E-selectin expression in the liver in response to metastatic tumor cells. Cancer Research 59:1356–1417.

Kienast Y, Von Baumgarten L, Fuhrmann M, Klinkert W, Goldbrunner R, Herms J, Winkler F (2010) Real-time imaging reveals the single steps of brain metastasis formation. Nature Medicine 16:116–138.

Kikinis R, Gleason PL, Moriarty TM, Moore MR, Alexander E, Stieg PE, Matsumae M, Lorensen WE, Cline HE, Black PM, Jolesz FA (1996) Computer-assisted interactive three-dimensional planning for neurosurgical procedures. Neurosurgery 38:640–9; discussion 649–51.

Kim E, Zhang J, Hong K, Benoit NE, Pathak AP (2011) Vascular phenotyping of brain tumors using magnetic resonance microscopy (μMRI). Journal of Cerebral Blood Flow and Metabolism 31:1623–1636.

Kivisäkk P, Trebst C, Liu Z, Tucky BH, Sørensen TL, Rudick RA, Mack M, Ransohoff RM (2002) T-cells in the cerebrospinal fluid express a similar repertoire of inflammatory chemokine receptors in the absence or presence of CNS inflammation: implications for CNS trafficking. Clinical and Experimental Immunology 129:510–518.

Kleinschnitz C, Schütz A, Nölte I, Horn T, Frank M, Solymosi L, Stoll G, Bendszus M (2005) In vivo detection of developing vessel occlusion in photothrombotic ischemic brain lesions in the rat by iron particle enhanced MRI. Journal of Cerebral Blood Flow and Metabolism 25:1548–1555.

Knudson AG (1971) Mutation and cancer: statistical study of retinoblastoma. Proceedings of the National Academy of Sciences of the United States of America 68:820–823.

Koch S, Claesson-Welsh L (2012) Signal transduction by vascular endothelial growth factor receptors. Cold Spring Harbor Perspectives in Medicine 2:a006502.

Kohchi C, Inagawa H, Nishizawa T, Soma G-I (2009) ROS and innate immunity. Anticancer Research 29:817–838.

Kolb M, Margetts PJ, Anthony DC, Pitossi F, Gauldie J (2001) Transient expression of IL-1beta induces acute lung injury and chronic repair leading to pulmonary fibrosis. The Journal of Clinical Investigation 107:1529–1536.

Koni PA, Joshi SK, Temann UA, Olson D, Burkly L, Flavell RA (2001) Conditional vascular cell adhesion molecule 1 deletion in mice: impaired lymphocyte migration to bone marrow. The Journal of Experimental Medicine 193:741–754.

Krüger S, Mottaghy FM, Buck AK, Maschke S, Kley H, Frechen D, Wibmer T, Reske SN, Pauls S (2011) Brain metastasis in lung cancer. Comparison of cerebral MRI and 18F-FDG-PET/CT for diagnosis in the initial staging. Nuclear Medicine 50:101–106.

Kudo FA, Muto A, Maloney SP, Pimiento JM, Bergaya S, Fitzgerald TN, Westvik TS, Frattini JC, Breuer CK, Cha CH, Nishibe T, Tellides G, Sessa WC, Dardik A (2007) Venous identity is lost but arterial identity is not gained during vein graft adaptation. Arteriosclerosis, Thrombosis, and Vascular Biology 27:1562–1571.

Kume T (2010) Specification of arterial, venous, and lymphatic endothelial cells during embryonic development. Histology and Histopathology 25:637–646.

Kundel HL (2006) History of research in medical image perception. Journal of the American College of Radiology 3:402–408.

Küsters B, Leenders WPJ, Wesseling P, Smits D, Verrijp K, Ruiter DJ, Peters JPW, Van Der Kogel AJ, De Waal RMW (2002) Vascular endothelial growth factor-A(165) induces progression of melanoma brain metastases without induction of sprouting angiogenesis. Cancer Research 62:341–345.

Lagerwaard FJ, Levendag PC, Nowak PJ, Eijkenboom WM, Hanssens PE, Schmitz PI (1999) Identification of prognostic factors in patients with brain metastases: a review of 1292 patients. International Journal of Radiation Oncology, Biology, Physics 43:795–803.

Landis MS, Boyden T, Pegg S (2012) Nasal-to-CNS drug delivery: where are we now and where are we heading? An industrial perspective. Therapeutic Delivery 3:195–208.

Läubli H, Borsig L (2010) Selectins as mediators of lung metastasis. Cancer Microenvironment 3:97–202.

Lauterbur PC (1973) Image Formation by Induced Local Interactions - Examples Employing Nuclear Magnetic Resonance. Nature 242:190–191.

Lazova R, LaBerge G, Duvall E, Spoelstra N, Sznol M, Cooper D, Spritz R, Pawelek J (2011) 21st International Pigment Cell Conference (IPCC), Bordeaux, France, September 20-24, 2011 Abstracts. Pigment Cell Melanoma Research 24:792.

Lee B-C, Lee T-H, Avraham S, Avraham H (2004) Involvement of the chemokine receptor CXCR4 and its ligand stromal cell-derived factor 1alpha in breast cancer cell migration through human brain microvascular endothelial cells. Molecular Cancer Research 2:327–365.

Lee T-H, Avraham H, Jiang S, Avraham S (2003) Vascular endothelial growth factor modulates the transendothelial migration of MDA-MB-231 breast cancer cells through regulation of brain microvascular endothelial cell permeability. The Journal of Biological Chemistry 278:5277–5361.

Leenders W, Küsters B, Pikkemaat J, Wesseling P, Ruiter D, Heerschap A, Barentsz J, De Waal RMW (2003) Vascular endothelial growth factor-A determines detectability of experimental melanoma brain metastasis in GD-DTPA-enhanced MRI. International Journal of Cancer 105:437–443.

Leenders WPJ, Küsters B, De Waal RMW (2002) Vessel co-option: how tumors obtain blood supply in the absence of sprouting angiogenesis. Endothelium 9:83–87.

Leenders WPJ, Küsters B, Verrijp K, Maass C, Wesseling P, Heerschap A, Ruiter D, Ryan A, De Waal R (2004) Antiangiogenic therapy of cerebral melanoma metastases results in sustained tumor progression via vessel co-option. Clinical Cancer Research 10:6222–6230.

Leuker CE, Labow M, Müller W, Wagner N (2001) Neonatally induced inactivation of the vascular cell adhesion molecule 1 gene impairs B cell localization and T cell-dependent humoral immune response. The Journal of Experimental Medicine 193:755–768.

Ley K, Laudanna C, Cybulsky MI, Nourshargh S (2007) Getting to the site of inflammation: the leukocyte adhesion cascade updated. Nature Reviews Immunology 7:678–689.

Libert C, Brouckaert P, Shaw A, Fiers W (1990) Induction of interleukin 6 by human and murine recombinant interleukin 1 in mice. European Journal of Immunology 20:691–694.

Lin M, Chen J-H, Nie K, Chang D, Nalcioglu O, Su M-Y (2009) Algorithm-based method for detection of blood vessels in breast MRI for development of computer-aided diagnosis. Journal of Magnetic Resonance Imaging 30:817–824.

Lippmann ES, Al-Ahmad A, Palecek SP, Shusta E V (2013) Modeling the blood-brain barrier using stem cell sources. Fluids and Barriers of the CNS 10:2.

Liu S, Agalliu D, Yu C, Fisher M (2012) The role of pericytes in blood-brain barrier function and stroke. Current Pharmaceutical Design 18:3653–3662.

Liu W, Ahmad SA, Jung YD, Reinmuth N, Fan F, Bucana CD, Ellis LM (2002) Coexpression of ephrin-Bs and their receptors in colon carcinoma. Cancer 94:934–939.

Loeb LA (2001) A mutator phenotype in cancer. Cancer Research 61:3230–3239.

Long D (1979) Capillary ultrastructure in human metastatic brain tumors. Journal of Neurosurgery 51:53–61.

Lorger M, Felding-Habermann B (2010) Capturing changes in the brain microenvironment during initial steps of breast cancer brain metastasis. American Journal of Pathology 176:2958–2971.

Lorger M, Lee H, Forsyth JS, Felding-Habermann B (2011) Comparison of in vitro and in vivo approaches to studying brain colonization by breast cancer cells. Journal of Neuro-Oncology 104:689–696.

Löscher W, Potschka H (2005) Blood-brain barrier active efflux transporters: ATP-binding cassette gene family. NeuroRx 2:86–98.

Lossinsky A, Shivers R (2004) Structural pathways for macromolecular and cellular transport across the blood-brain barrier during inflammatory conditions. Review. Histology and Histopathology 19:535–599.

Lou Y, Preobrazhenska O, auf dem Keller U, Sutcliffe M, Barclay L, McDonald PC, Roskelley C, Overall CM, Dedhar S (2008) Epithelial-mesenchymal transition (EMT) is not sufficient for spontaneous murine breast cancer metastasis. Developmental Dynamics 237:2755–2768.

Louis N, Evelegh C, Graham FL (1997) Cloning and sequencing of the cellular-viral junctions from the human adenovirus type 5 transformed 293 cell line. Virology 233:423–429.

Lu F, Selak M, O'Connor J, Croul S, Lorenzana C, Butunoi C, Kalman B (2000) Oxidative damage to mitochondrial DNA and activity of mitochondrial enzymes in chronic active lesions of multiple sclerosis. Journal of the Neurological Sciences 177:95–103.

Lu P, Weaver VM, Werb Z (2012) The extracellular matrix: a dynamic niche in cancer progression. The Journal of Cell Biology 196:395–406.

Ludwig R, Boehme B, Podda M, Henschler R, Jager E, Tandi C, Boehncke W-H, Zollner T, Kaufmann R, Gille J (2004) Endothelial P-selectin as a target of heparin action in experimental melanoma lung metastasis. Cancer Research 64:2743–2793.

Luger TA, Schwarz T (1990) Evidence for an epidermal cytokine network. The Journal of Investigative Dermatology 95:100S–104S.

Luzzati F, De Marchis S, Fasolo A, Peretto P (2007) Adult neurogenesis and local neuronal progenitors in the striatum. Neurodegenerative Diseases 4:322–327.

Luzzi KJ, MacDonald IC, Schmidt EE, Kerkvliet N, Morris VL, Chambers AF, Groom AC (1998) Multistep nature of metastatic inefficiency: dormancy of solitary cells after successful extravasation and limited survival of early micrometastases. The American Journal of Pathology 153:865–873.

Mamani JB, Pavon LF, Miyaki LAM, Sibov TT, Rossan F, Silveira PH, Cárdenas WHZ, Amaro Junior E, Gamarra LF (2012) Intracellular labeling and quantification process by magnetic resonance imaging using iron oxide magnetic nanoparticles in rat C6 glioma cell line. Einstein (São Paulo) 10:216–221.

Margetts PJ, Kolb M, Yu L, Hoff CM, Holmes CJ, Anthony DC, Gauldie J (2002) Inflammatory cytokines, angiogenesis, and fibrosis in the rat peritoneum. The American Journal of Pathology 160:2285–2294.

Marr RA, Addison CL, Snider D, Muller WJ, Gauldie J, Graham FL (1997) Tumour immunotherapy using an adenoviral vector expressing a membrane-bound mutant of murine TNF alpha. Gene Therapy 4:1181–1188.

Maru Y (2007) Which came first, tumor cells or macrophages? Cell Adhesion & Migration 1:107–116.

Massagué J (2008) TGFbeta in Cancer. Cell 134:215–230.

Matyszak M, Perry V (1995) Demyelination in the central nervous system following a delayed-type hypersensitivity response to bacillus Calmette-Guérin. Neuroscience 64:967–1044.

McAteer MA, Choudhury RP (2009) Chapter 4 - Applications of nanotechnology in molecular imaging of the brain. Progress in Brain Research 180:72–96.

McAteer MA, Sibson NR, Von Zur Muhlen C, Schneider JE, Lowe AS, Warrick N, Channon KM, Anthony DC, Choudhury RP (2007) In vivo magnetic resonance imaging of acute brain inflammation using microparticles of iron oxide. Nature Medicine 13:1253–1258.

McColl B, Rothwell N, Allan S (2007) Systemic inflammatory stimulus potentiates the acute phase and CXC chemokine responses to experimental stroke and exacerbates brain damage via interleukin-1- and neutrophil-dependent mechanisms. The Journal of neuroscience : the official journal of the Society for Neuroscience 27:4403–4415.

Mestre L, Iñigo PM, Mecha M, Correa FG, Hernangómez-Herrero M, Loría F, Docagne F, Borrell J, Guaza C (2011) Anandamide inhibits Theiler's virus induced VCAM-1 in brain endothelial cells and reduces leukocyte transmigration in a model of blood brain barrier by activation of CB(1) receptors. Journal of Neuroinflammation 8:102.

Michie SA, Streeter PR, Bolt PA, Butcher EC, Picker LJ (1993) The human peripheral lymph node vascular addressin. An inducible endothelial antigen involved in lymphocyte homing. The American Journal of Pathology 143:1688–1698.

Middleton J, Americh L, Gayon R, Julien D, Mansat M, Mansat P, Anract P, Cantagrel A, Cattan P, Reimund J-M, Aguilar L, Amalric F, Girard J-P (2005) A comparative study of endothelial cell markers expressed in chronically inflamed human tissues: MECA-79, Duffy antigen receptor for

chemokines, von Willebrand factor, CD31, CD34, CD105 and CD146. The Journal of Pathology 206:260–268.

Mital P, Hinton BT, Dufour JM (2011) The blood-testis and blood-epididymis barriers are more than just their tight junctions. Biology of Reproduction 84:851–858.

Modo M, Bulte JWM (2011) From molecules to man: the dawn of a vitreous man. Methods in Molecular Biology (Clifton, NJ) 711:3–14.

Munzarová M, Kovarík J (1987) Is cancer a macrophage-mediated autoaggressive disease? Lancet 1:952–956.

Munzarová M, Lauerova L, Capkova J (1992) Are advanced malignant melanoma cells hybrids between melanocytes and macrophages? Melanoma Research 2:127–136.

Munzarová M, Zemanová D (1992) Transformation of blood monocytes to multinucleated giant cells in vitro: are there any differences between malignant and nonmalignant states? Physiological Research / Academia Scientiarum Bohemoslovaca 41:221–227.

Murdoch C, Muthana M, Coffelt SB, Lewis CE (2008) The role of myeloid cells in the promotion of tumour angiogenesis. Nature Reviews Cancer 8:618–631.

Nagy Z, Peters H, Hüttner I (1984) Fracture faces of cell junctions in cerebral endothelium during normal and hyperosmotic conditions. Laboratory Investigation 50:313–322.

Nakajima S, Atsumi H, Bhalerao AH, Jolesz FA, Kikinis R, Yoshimine T, Moriarty TM, Stieg PE (1997) Computer-assisted surgical planning for cerebrovascular neurosurgery. Neurosurgery 41:403–9; discussion 409–10.

Nelson BH (2008) The impact of T-cell immunity on ovarian cancer outcomes. Immunological Reviews 222:101–116.

Nicolson GL (1988a) Cancer metastasis: tumor cell and host organ properties important in metastasis to specific secondary sites. Biochimica et Biophysica Acta 948:175–224.

Nicolson GL (1988b) Organ specificity of tumor metastasis: role of preferential adhesion, invasion and growth of malignant cells at specific secondary sites. Cancer Metastasis Reviews 7:143–188.

Niu X, Wang H, Fu ZF (2011) Role of chemokines in rabies pathogenesis and protection. Advances in Virus Research 79:73–89.

Norman MU, James WG, Hickey MJ (2008) Differential roles of ICAM-1 and VCAM-1 in leukocyte-endothelial cell interactions in skin and brain of MRL/faslpr mice. Journal of Leukocyte Biology 84:68–76.

Nussbaum ES, Djalilian HR, Cho KH, Hall WA (1996) Brain metastases. Histology, multiplicity, surgery, and survival. Cancer 78:1781–1788.

Oja H, Randles RH (2004) Multivariate Nonparametric Tests. Statistical Science 19:598–605.

Oppenheim JJ, Feldmann M, Durum SK (2001) Cytokine Reference: Ligands. Academic Press.

Osanai M, Chiba H, Kojima T, Fujibe M, Kuwahara K, Kimura H, Satoh M, Sawada N (2002) Hepatocyte nuclear factor (HNF)-4alpha induces expression of endothelial Fas ligand (FasL) to prevent

cancer cell transmigration: a novel defense mechanism of endothelium against cancer metastasis. Japanese Journal of Cancer Research 93:532–573.

Ou R, Zhang M, Huang L, Flavell RA, Koni PA, Moskophidis D (2008) Regulation of immune response and inflammatory reactions against viral infection by VCAM-1. Journal of Virology 82:2952–2965.

Owens GK (1995) Regulation of differentiation of vascular smooth muscle cells. Physiological Reviews 75:487–517.

Ozgür E, Heidenreich A, Dagtekin O, Engelmann U, Bloch W (2011) Distribution of EphB4 and EphrinB2 in normal and malignant urogenital tissue. Urologic Oncology 29:78–84.

Pagès F, Galon J, Dieu-Nosjean M-C, Tartour E, Sautès-Fridman C, Fridman W-H (2010) Immune infiltration in human tumors: a prognostic factor that should not be ignored. Oncogene 29:1093–1102.

Paget S (1889) The distribution of secondary growths in cancer of the breast. 1889. Lancet 133:571–573.

Paku S, Dome B, Toth R, Timar J (2000) Organ-specificity of the extravasation process: an ultrastructural study. Clinical & Experimental Metastasis 18:481–492.

Pardridge WM (1998) CNS drug design based on principles of blood-brain barrier transport. Journal of Neurochemistry 70:1781–1792.

Pardridge WM (2005) The blood-brain barrier: bottleneck in brain drug development. NeuroRx 2:3–14.

Pardridge WM, Triguero D, Buciak J (1989) Transport of histone through the blood-brain barrier. The Journal of Pharmacology and Experimental Therapeutics 251:821–826.

Pardridge WM, Triguero D, Buciak J, Yang J (1990) Evaluation of cationized rat albumin as a potential blood-brain barrier drug transport vector. The Journal of Pharmacology and Experimental Therapeutics 255:893–899.

Pathak AP, Kim E, Zhang J, Jones M V (2011) Three-dimensional imaging of the mouse neurovasculature with magnetic resonance microscopy. PloS One 6:e22643.

Pathirana W, Abhayawardhana P, Kariyawasam H, Ratnasooriya WD (2009) Transcranial route of brain targeted delivery of methadone in oil. Indian Journal of Pharmaceutical Sciences 71:264–269.

Paulus P, Jennewein C, Zacharowski K (2011) Biomarkers of endothelial dysfunction: can they help us deciphering systemic inflammation and sepsis? Biomarkers 16 Suppl 1:S11–21.

Pawelek J, Chakraborty A (2008) Fusion of tumour cells with bone marrow-derived cells: a unifying explanation for metastasis. Nature Reviews Cancer 8:377–463.

Percy DB, Ribot EJ, Chen Y, McFadden C, Simedrea C, Steeg PS, Chambers AF, Foster PJ (2011) In vivo characterization of changing blood-tumor barrier permeability in a mouse model of breast cancer metastasis: a complementary magnetic resonance imaging approach. Investigative Radiology 46:718–725.

Piccio L, Rossi B, Scarpini E, Laudanna C, Giagulli C, Issekutz AC, Vestweber D, Butcher EC, Constantin G (2002) Molecular mechanisms involved in lymphocyte recruitment in inflamed brain microvessels: critical roles for P-selectin glycoprotein ligand-1 and heterotrimeric G(i)-linked receptors. Journal of Immunology 168:1940–1949.

Piraino PS, Yednock TA, Freedman SB, Messersmith EK, Pleiss MA, Vandevert C, Thorsett ED, Karlik SJ (2002) Prolonged reversal of chronic experimental allergic encephalomyelitis using a small molecule inhibitor of alpha4 integrin. Journal of Neuroimmunology 131:147–159.

Poduslo JF, Curran GL (1996a) Increased permeability of superoxide dismutase at the blood-nerve and blood-brain barriers with retained enzymatic activity after covalent modification with the naturally occurring polyamine, putrescine. Journal of Neurochemistry 67:734–741.

Poduslo JF, Curran GL (1996b) Polyamine modification increases the permeability of proteins at the blood-nerve and blood-brain barriers. Journal of Neurochemistry 66:1599–1609.

Polman CH, O'Connor PW, Havrdova E, Hutchinson M, Kappos L, Miller DH, Phillips JT, Lublin FD, Giovannoni G, Wajgt A, Toal M, Lynn F, Panzara MA, Sandrock AW (2006) A randomized, placebo-controlled trial of natalizumab for relapsing multiple sclerosis. The New England Journal of Medicine 354:899–910.

Pott Godoy M, Tarelli R, Ferrari C, Sarchi M, Pitossi F (2008) Central and systemic IL-1 exacerbates neurodegeneration and motor symptoms in a model of Parkinson's disease. Brain 131:1880–1974.

Prendergast C, Anderton S (2009) Immune cell entry to central nervous system--current understanding and prospective therapeutic targets. Endocrine, Metabolic & Immune Disorders - Drug Targets 9:315–342.

Price RJ, Owens GK, Skalak TC (1994) Immunohistochemical identification of arteriolar development using markers of smooth muscle differentiation. Evidence that capillary arterialization proceeds from terminal arterioles. Circulation Research 75:520–527.

Pu J, Gu S, Liu S, Zhu S, Wilson D, Siegfried JM, Gur D (2012) CT based computerized identification and analysis of human airways: a review. Medical Physics 39:2603–2616.

Pulaski BA, Ostrand-Rosenberg S (2001) Mouse 4T1 breast tumor model. Current protocols in Immunology Chapter 20:Unit 20.2.

Purcell E, Torrey H, Pound R (1946) Resonance Absorption by Nuclear Magnetic Moments in a Solid. Physical Review 69:37–38.

Pytliak M, Vargová V, Mechírová V (2012) Matrix metalloproteinases and their role in oncogenesis: a review. Onkologie 35:49–102.

Rabi I, Zacharias J, Millman S, Kusch P (1938) A New Method of Measuring Nuclear Magnetic Moment. Physical Review 53:318–318.

Rajadhyaksha M, Boyden T, Liras J, El-Kattan A, Brodfuehrer J (2011) Current advances in delivery of biotherapeutics across the blood-brain barrier. Current Drug Discovery Technologies 8:87–101.

Ransohoff RM, Engelhardt B (2012) The anatomical and cellular basis of immune surveillance in the central nervous system. Nature Reviews Immunology 12:623–635.

Ransohoff RM, Kivisäkk P, Kidd G (2003) Three or more routes for leukocyte migration into the central nervous system. Nature Reviews Immunology 3:569–581.

Rausch M, Baumann D, Neubacher U, Rudin M (2002) In-vivo visualization of phagocytotic cells in rat brains after transient ischemia by USPIO. NMR in Biomedicine 15:278–283.

Rausch M, Hiestand P, Baumann D, Cannet C, Rudin M (2003) MRI-based monitoring of inflammation and tissue damage in acute and chronic relapsing EAE. Magnetic Resonance in Medicine 50:309–314.

Rausch M, Sauter A, Fröhlich J, Neubacher U, Radü EW, Rudin M (2001) Dynamic patterns of USPIO enhancement can be observed in macrophages after ischemic brain damage. Magnetic Resonance in Medicine 46:1018–1022.

Raz A, Lotan R (1987) Endogenous galactoside-binding lectins: a new class of functional tumor cell surface molecules related to metastasis. Cancer Metastasis Reviews 6:433–452.

Reading CL, Hutchins JT (1985) Carbohydrate structure in tumor immunity. Cancer Metastasis Reviews 4:221–260.

Reese TS, Karnovsky MJ (1967) Fine structural localization of a blood-brain barrier to exogenous peroxidase. The Journal of Cell Biology 34:207–217.

Reichel A, Begley DJ, Abbott NJ (2003) An overview of in vitro techniques for blood-brain barrier studies. Methods in Molecular Medicine 89:307–324.

Richards CD, Braciak T, Xing Z, Graham F, Gauldie J (1995) Adenovirus vectors for cytokine gene expression. Annals of the New York Academy of Sciences 762:282–92; discussion 292–3.

Ridler TW, Calvard S (1978) Picture thresholding using an iterative selection method. IEEE transactions on Systems, Man and Cybernetics 8:630–632.

Robinson D, He F, Pretlow T, Kung HJ (1996) A tyrosine kinase profile of prostate carcinoma. Proceedings of the National Academy of Sciences of the United States of America 93:5958–5962.

Rochman Y, Spolski R, Leonard WJ (2009) New insights into the regulation of T cells by gamma(c) family cytokines. Nature Reviews Immunology 9:480–490.

Rosen JE, Chan L, Shieh D-B, Gu FX (2012) Iron oxide nanoparticles for targeted cancer imaging and diagnostics. Nanomedicine: Nanotechnology, Biology, and Medicine 8:275–290.

Rosner K, Ross C, Karlsmark T, Skovgaard GL (2001) Role of LFA-1/ICAM-1, CLA/E-selectin and VLA-4/VCAM-1 pathways in recruiting leukocytes to the various regions of the chronic leg ulcer. Acta Dermato-Venereologica 81:334–339.

Ruff M, Pert C (1984) Small cell carcinoma of the lung: macrophage-specific antigens suggest hemopoietic stem cell origin. Science 225:1034–1040.

Russell JH, Ley TJ (2002) Lymphocyte-mediated cytotoxicity. Annual Review of Immunology 20:323–370.

Sager R, Haskill S, Anisowicz A, Trask D, Pike MC (1991) GRO: a novel chemotactic cytokine. Advances in Experimental Medicine and Biology 305:73–77.

Salganik RI, Albright CD, Rodgers J, Kim J, Zeisel SH, Sivashinskiy MS, Van Dyke TA (2000) Dietary antioxidant depletion: enhancement of tumor apoptosis and inhibition of brain tumor growth in transgenic mice. Carcinogenesis 21:909–914.

Salmi M, Rajala P, Jalkanen S (1997) Homing of mucosal leukocytes to joints. Distinct endothelial ligands in synovium mediate leukocyte-subtype specific adhesion. The Journal of Clinical Investigation 99:2165–2172.

Sasieni PD, Shelton J, Ormiston-Smith N, Thomson CS, Silcocks PB (2011) What is the lifetime risk of developing cancer?: the effect of adjusting for multiple primaries. British Journal of Cancer 105:460–465.

Sasseville VG, Newman WA, Lackner AA, Smith MO, Lausen NC, Beall D, Ringler DJ (1992) Elevated vascular cell adhesion molecule-1 in AIDS encephalitis induced by simian immunodeficiency virus. The American Journal of Pathology 141:1021–1030.

Sato S, Sato Y, Hatakeyama K, Marutsuka K, Yamashita A, Takeshima H, Asada Y (2011) Quantitative analysis of vessels with smooth muscle layer in astrocytic tumors: correlation with histological grade and prognostic significance. Histology and Histopathology 26:497–504.

Sato Y, Nakajima S, Shiraga N, Atsumi H, Yoshida S, Koller T, Gerig G, Kikinis R (1998) Three-dimensional multi-scale line filter for segmentation and visualization of curvilinear structures in medical images. Medical Image Analysis 2:143–168.

Schackert G, Fidler IJ (1988) Site-specific metastasis of mouse melanomas and a fibrosarcoma in the brain or meninges of syngeneic animals. Cancer Research 48:3478–3484.

Schackert G, Simmons R, Buzbee T, Hume D, Fidler I (1988) Macrophage infiltration into experimental brain metastases: occurrence through an intact blood-brain barrier. Journal of the National Cancer Institute 80:1027–1061.

Schnell L, Fearn S, Schwab ME, Perry VH, Anthony DC (1999) Cytokine-induced acute inflammation in the brain and spinal cord. Journal of Neuropathology and Experimental Neurology 58:245–254.

Schroeter M, Saleh A, Wiedermann D, Hoehn M, Jander S (2004) Histochemical detection of ultrasmall superparamagnetic iron oxide (USPIO) contrast medium uptake in experimental brain ischemia. Magnetic Resonance in Medicine 52:403–406.

Scully EP, Baden LR, Katz JT (2008) Fungal brain infections. Current Opinion in Neurology 21:347–352.

Seki N, Brooks AD, Carter CR, Back TC, Parsoneault EM, Smyth MJ, Wiltrout RH, Sayers TJ (2002) Tumor-specific CTL kill murine renal cancer cells using both perforin and Fas ligand-mediated lysis in vitro, but cause tumor regression in vivo in the absence of perforin. The Journal of Immunology 168:3484–3492.

Serres S, Anthony DC, Jiang Y, Broom KA, Campbell SJ, Tyler DJ, Van Kasteren SI, Davis BG, Sibson NR (2009) Systemic inflammatory response reactivates immune-mediated lesions in rat brain. The Journal of Neuroscience 29:4820–4828.

Serres S, Mardiguian S, Campbell SJ, McAteer MA, Akhtar A, Krapitchev A, Choudhury RP, Anthony DC, Sibson NR (2011) VCAM-1-targeted magnetic resonance imaging reveals subclinical disease in a mouse model of multiple sclerosis. FASEB Journal 25:4415–4422.

Serres S, Soto MS, Hamilton A, McAteer MA, Carbonell WS, Robson MD, Ansorge O, Khrapitchev A, Bristow C, Balathasan L, Weissensteiner T, Anthony DC, Choudhury RP, Muschel RJ, Sibson NR

(2012) Molecular MRI enables early and sensitive detection of brain metastases. Proceedings of the National Academy of Sciences of the United States of America 109:6674–6679.

Sgadari C, Farber JM, Angiolillo AL, Liao F, Teruya-Feldstein J, Burd PR, Yao L, Gupta G, Kanegane C, Tosato G (1997) Mig, the monokine induced by interferon-gamma, promotes tumor necrosis in vivo. Blood 89:2635–2643.

Shapiro EM, Sharer K, Skrtic S, Koretsky AP (2006) In vivo detection of single cells by MRI. Magnetic Resonance in Medicine 55:242–249.

Shapiro EM, Skrtic S, Sharer K, Hill JM, Dunbar CE, Koretsky AP (2004) MRI detection of single particles for cellular imaging. Proceedings of the National Academy of Sciences of the United States of America 101:10901–10906.

Shepro D, Morel NM (1993) Pericyte physiology. FASEB Journal 7:1031–1038.

Sibson NR, Anthony DC, Van Kasteren S, Dickens A, Perez-Balderas F, McAteer MA, Choudhury RP, Davis BG (2011) Molecular MRI approaches to the detection of CNS inflammation. In: Methods in Molecular Biology (Clifton, N.J.), pp 379–396.

Sibson NR, Blamire AM, Bernades-Silva M, Laurent S, Boutry S, Muller RN, Styles P, Anthony DC (2004) MRI detection of early endothelial activation in brain inflammation. Magnetic Resonance in Medicine 51:248–252.

Sibson NR, Blamire AM, Perry VH, Gauldie J, Styles P, Anthony DC (2002) TNF-alpha reduces cerebral blood volume and disrupts tissue homeostasis via an endothelin- and TNFR2-dependent pathway. Brain 125:2446–2459.

Sinha UK, Kundra A, Scalia P, Smith DL, Parsa B, Masood R, Gill PS (2003) Expression of EphB4 in head and neck squamous cell carcinoma. Ear, Nose, & Throat Journal 82:866, 869–870, 887.

Skalli O, Pelte MF, Peclet MC, Gabbiani G, Gugliotta P, Bussolati G, Ravazzola M, Orci L (1989) Alpha-smooth muscle actin, a differentiation marker of smooth muscle cells, is present in microfilamentous bundles of pericytes. The Journal of Histochemistry and Cytochemistry 37:315–321.

Stehelin D, Varmus HE, Bishop JM, Vogt PK (1976) DNA related to the transforming gene(s) of avian sarcoma viruses is present in normal avian DNA. Nature 260:170–173.

Stephenson SA, Slomka S, Douglas EL, Hewett PJ, Hardingham JE (2001) Receptor protein tyrosine kinase EphB4 is up-regulated in colon cancer. BMC molecular biology 2:15.

Streeter PR, Rouse BT, Butcher EC (1988) Immunohistologic and functional characterization of a vascular addressin involved in lymphocyte homing into peripheral lymph nodes. The Journal of Cell Biology 107:1853–1862.

Streilein JW (2003) Ocular immune privilege: the eye takes a dim but practical view of immunity and inflammation. Journal of Leukocyte Biology 74:179–185.

Sugarbaker E V (1979) Cancer metastasis: a product of tumor-host interactions. Current Problems in Cancer 3:1–59.

Suojun Z, Feng W, Dongsheng G, Ting L (2012) Targeting Raf/MEK/ERK pathway in pituitary adenomas. European Journal of Cancer 48:389–395.

Suzuki K, Yamamoto M, Hasegawa Y, Ando M, Shima K, Sako C, Ito G, Shimokata K (2004) Magnetic resonance imaging and computed tomography in the diagnoses of brain metastases of lung cancer. Lung Cancer 46:357–360.

Svenningsson A, Hansson GK, Andersen O, Andersson R, Patarroyo M, Stemme S (1993) Adhesion molecule expression on cerebrospinal fluid T lymphocytes: evidence for common recruitment mechanisms in multiple sclerosis, aseptic meningitis, and normal controls. Annals of Neurology 34:155–161.

Tang XX, Brodeur GM, Campling BG, Ikegaki N (1999) Coexpression of transcripts encoding EPHB receptor protein tyrosine kinases and their ephrin-B ligands in human small cell lung carcinoma. Clinical Cancer Research 5:455–460.

Tarin D, Price JE, Kettlewell MG, Souter RG, Vass AC, Crossley B (1984a) Mechanisms of human tumor metastasis studied in patients with peritoneovenous shunts. Cancer Research 44:3584–3592.

Tarin D, Price JE, Kettlewell MG, Souter RG, Vass AC, Crossley B (1984b) Clinicopathological observations on metastasis in man studied in patients treated with peritoneovenous shunts. British Medical Journal (Clinical Research ed) 288:749–751.

Taylor AC, Murfee WL, Peirce SM (2007) EphB4 expression along adult rat microvascular networks: EphB4 is more than a venous specific marker. Microcirculation 14:253–267.

Thomsen LB, Lichota J, Eskehave TN, Linemann T, Mortensen JH, Du Jardin KG, Moos T (2012) Brain delivery systems via mechanism independent of receptor-mediated endocytosis and adsorptive-mediated endocytosis. Current Pharmaceutical Biotechnology 13:2349–2354.

Thorek DLJ, Tsourkas A (2008) Size, charge and concentration dependent uptake of iron oxide particles by non-phagocytic cells. Biomaterials 29:3583–3590.

Trinidad EM, Zapata AG, Alonso-Colmenar LM (2010) Eph-ephrin bidirectional signaling comes into the context of lymphocyte transendothelial migration. Cell Adhesion & Migration 4:363–367.

Tsao MN, Khuntia D, Mehta MP (2012a) Brain metastases: what's new with an old problem? Current Opinion in Supportive and Palliative Care 6:85–90.

Tsao MN, Lloyd N, Wong RK, Chow E, Rakovitch E, Laperriere N, Xu W, Sahgal A (2012b) Whole brain radiotherapy for the treatment of newly diagnosed multiple brain metastases. Cochrane Database of Systematic Reviews (Online) 4:CD003869.

Tsuzaki M, Guyton G, Garrett W, Archambault JM, Herzog W, Almekinders L, Bynum D, Yang X, Banes AJ (2003) IL-1 beta induces COX2, MMP-1, -3 and -13, ADAMTS-4, IL-1 beta and IL-6 in human tendon cells. Journal of Orthopaedic Research 21:256–264.

Turner GA (1982) Surface properties of the metastatic cell. Invasion & Metastasis 2:197–216.

Vandenabeele P, Guisez Y, Declercq W, Bauw G, Vandekerckhove J, Fiers W (1990) Response of murine cell lines to an IL-1/IL-2-induced factor in a rat/mouse T hybridoma (PC60): differential induction of cytokines by human IL-1 alpha and IL-1 beta and partial amino acid sequence of rat GM-CSF. Lymphokine Research 9:381–389.

Vidal-Vanaclocha F, Fantuzzi G, Mendoza L, Fuentes A, Anasagasti M, Martv≠n J, Carrascal T, Walsh P, Reznikov L, Kim S, Novick D, Rubinstein M, Dinarello C (2000) IL-18 regulates IL-1beta-dependent hepatic melanoma metastasis via vascular cell adhesion molecule-1. Proceedings of the National Academy of Sciences of the United States of America 97:734–743.

Vignery A (2005) Macrophage fusion: are somatic and cancer cells possible partners? Trends in Cell Biology 15:188–193.

Vladimirova O, Lu FM, Shawver L, Kalman B (1999) The activation of protein kinase C induces higher production of reactive oxygen species by mononuclear cells in patients with multiple sclerosis than in controls. Inflammation Research 48:412–416.

Von Zur Muhlen C, Sibson NR, Peter K, Campbell SJ, Wilainam P, Grau GE, Bode C, Choudhury RP, Anthony DC (2008) A contrast agent recognizing activated platelets reveals murine cerebral malaria pathology undetectable by conventional MRI. The Journal of Clinical Investigation 118:1198–1207.

Wadghiri YZ, Sigurdsson EM, Sadowski M, Elliott JI, Li Y, Scholtzova H, Tang CY, Aguinaldo G, Pappolla M, Duff K, Wisniewski T, Turnbull DH (2003) Detection of Alzheimer's amyloid in transgenic mice using magnetic resonance microimaging. Magnetic Resonance in Medicine 50:293–302.

Wang HU, Chen ZF, Anderson DJ (1998) Molecular distinction and angiogenic interaction between embryonic arteries and veins revealed by ephrin-B2 and its receptor Eph-B4. Cell 93:741–753.

Wang M, Etu J, Joshi S (2007) Enhanced disruption of the blood brain barrier by intracarotid mannitol injection during transient cerebral hypoperfusion in rabbits. Journal of Neurosurgical Anesthesiology 19:249–256.

Warburg O (1956) On the origin of cancer cells. Science 123:309–314.

Weil RJ, Palmieri DC, Bronder JL, Stark AM, Steeg PS (2005) Breast cancer metastasis to the central nervous system. The American Journal of Pathology 167:913–920.

Weiss L (2000) Metastasis of cancer: a conceptual history from antiquity to the 1990s. Cancer Metastasis Reviews 19:193–383.

Wekerle H, Fierz W (1985) T cell approach to demyelinating diseases. Springer Seminars in Immunopathology 8:97–110.

Wengenack TM, Curran GL, Poduslo JF (2000) Targeting alzheimer amyloid plaques in vivo. Nature Biotechnology 18:868–872.

Westbrook C, Roth CK, Talbot J (2005) MRI in Practice. John Wiley & Sons.

Widney DP, Xia YR, Lusis AJ, Smith JB (2000) The murine chemokine CXCL11 (IFN-inducible T cell alpha chemoattractant) is an IFN-gamma- and lipopolysaccharide-inducible glucocorticoid-attenuated response gene expressed in lung and other tissues during endotoxemia. Journal of Immunology 164:6322–6331.

Wilcockson DC, Campbell SJ, Anthony DC, Perry VH (2002) The systemic and local acute phase response following acute brain injury. Journal of Cerebral Blood Flow and Metabolism 22:318–326.

Wirtz D, Konstantopoulos K, Searson P (2011) The physics of cancer: the role of physical interactions and mechanical forces in metastasis. Nature Reviews Cancer 11:512–534.

Wong D, Dorovini-Zis K (1995) Expression of vascular cell adhesion molecule-1 (VCAM-1) by human brain microvessel endothelial cells in primary culture. Microvascular Research 49:325–339.

Wong SY, Hynes RO (2006) Lymphatic or hematogenous dissemination: how does a metastatic tumor cell decide? Cell Cycle 5:812–817.

Wu CL, Zukerberg LR, Ngwu C, Harlow E, Lees JA (1995) In vivo association of E2F and DP family proteins. Molecular and Cellular Biology 15:2536–2546.

Wu KLH, Chan SHH, Chan JYH (2012) Neuroinflammation and oxidative stress in rostral ventrolateral medulla contribute to neurogenic hypertension induced by systemic inflammation. Journal of Neuroinflammation 9:212.

Xu N-J, Henkemeyer M (2012) Ephrin reverse signaling in axon guidance and synaptogenesis. Seminars in Cell & Developmental Biology 23:58–64.

Yednock TA, Cannon C, Fritz LC, Sanchez-Madrid F, Steinman L, Karin N (1992) Prevention of experimental autoimmune encephalomyelitis by antibodies against alpha 4 beta 1 integrin. Nature 356:63–66.

Yushkevich PA, Piven J, Hazlett HC, Smith RG, Ho S, Gee JC, Gerig G (2006) User-guided 3D active contour segmentation of anatomical structures: significantly improved efficiency and reliability. NeuroImage 31:1116–1128.

Zamani Boroujeni F, Rahmat RWOK, Mustapha N, Affendey LS, Maskon O (2012) Coronary artery center-line extraction using second order local features. Computational and Mathematical Methods in Medicine 2012:940981.

Zhang S, Jiang T, Liang M (2007) Expression of Eph B4 and Ephrin B2 in cervical cancer tissues and angiogenesis. International Journal of Gynaecology and Obstetrics 96:46–47.

Zhu D, White RD, Hardy PA, Weerapreeyakul N, Sutthanut K, Jay M (2006) Biocompatible nanotemplate-engineered nanoparticles containing gadolinium: stability and relaxivity of a potential MRI contrast agent. Journal of Nanoscience and Nanotechnology 6:996–1003.

Zimmer C, Weissleder R, Poss K, Bogdanova A, Wright SC, Enochs WS (1995) MR imaging of phagocytosis in experimental gliomas. Radiology 197:533–538.

Zudaire E, Gambardella L, Kurcz C, Vermeren S (2011) A computational tool for quantitative analysis of vascular networks. PloS One 6:e27385.

Appendix 1

Health and Behavioural Scoring Guidelines for 4T1 brain metastasis model.
Animals will be inspected and weighed on a daily basis as a minimum after tumour induction, and behavioural assessment and health scoring used.

In all cases refer to naïve animals for "normal" reading.

Note: The frequency of monitoring should be tailored to the particular stage of the experiment and the frequency of monitoring must be increased at critical periods or where an animal's condition might rapidly deteriorate. e.g. If neurological symptoms become evident, monitoring and scoring frequency will be increased (e.g. 2-4 times/day depending on symptoms and likelihood of deterioration).

APPEARANCE	
Normal	0
General lack of grooming	1
Ocular, and nasal discharges	2
Piloerection, hunched up	3
FOOD AND WATER INTAKE	
Normal	0
Body weight decreased by <10%	1
Body weight decreased by 10-15%	2
Body weight decreased by 15-20%	3
NATURAL BEHAVIOUR	
Normal	0
Decreased	1
Loss of startle response	2
Vocalization, restlessness or very reduced activity	3
PROVOKED BEHAVIOUR	
Normal	0
Decreased activity	1
Loss of extensor reflex	2
Loss of righting reflex	3
Reacts violently or very weak response	4
SCORE ADJUSTMENT	
If you have scored a 3 or 4 more than once, score an extra point for each.	2-4
TOTAL	0-17

Judgement:
0-4 normal
5-7 monitor more frequently
8-11 seek opinion from day-to-day care person and/or named veterinary surgeon
12-17 terminate.

Example of additional conditions:

Terminate if significant haemorrhage is evident after intracardiac injection.
Terminate if self-mutilation is evident.
Terminate if lesions are ulcerated and wet.
Terminate if unresponsive to activity or provocation (pre-comatose or comatose).
Terminate if breathing is laboured or persistently rapid.
Terminate if marked skin tenting is evident indicating severe dehydration.
Terminate if weight loss is > 20% relative to weight at time of tumour implant.
Terminate if signs of large tumour burden are observed, as indicated by enlarged lymph nodes and/or distended abdomen.

The expected score for this procedure is 0-2 from day 1-10, and may increase to 5-7 between days 10 and 13.

Appendix 2

MATLAB scripts for automated hypointensity analysis

1 – LoadBrainVolumes
2 – CreateMeanSdBrainVolumes
3 – CreateBrainHypoMask_regionprops
4 – pda_SphericalRegion
5 – pda_SphericalMask

---

1 – LoadBrainVolumes

```
function [Volume,Mask] = LoadBrainVolumes(VolumeName, MaskName)

% Loads the Brain volume and mask volume in NIFTI format

if nargin < 2
    % Select Brain Volume
    if exist('BrainVolumeFilePath.mat') == 2
    load BrainVolumeFilePath;
    if BrainVolumeFilePath ~= 0
        [VolumeFileName,BrainVolumeFilePath] =
uigetfile('*.nii','Select Brain Volume',BrainVolumeFilePath);
    else
        [VolumeFileName,BrainVolumeFilePath] = uigetfile('*.nii');
    end
    else
        [VolumeFileName,BrainVolumeFilePath] = uigetfile('*.nii');
    end

    save 'BrainVolumeFilePath' BrainVolumeFilePath;


    % Select Brain Mask
    if exist('BrainMaskFilePath.mat') == 2
    load BrainMaskFilePath;
    if BrainMaskFilePath ~= 0
        [MaskFileName,BrainMaskFilePath] = uigetfile('*.nii','Select
Brain Mask',BrainMaskFilePath);
    else
        [MaskFileName,BrainMaskFilePath] = uigetfile('*.nii');
    end
    else
        [MaskFileName,BrainMaskFilePath] = uigetfile('*.nii');
    end

    save 'BrainMaskFilePath' BrainMaskFilePath;
```

```
    VolumeName = fullfile(BrainVolumeFilePath,VolumeFileName);
    MaskName = fullfile(BrainMaskFilePath,MaskFileName);
end


% Load the selected volumes;
nii = load_nii(VolumeName);
save_nii(nii,'ReferenceVolume.nii');
Volume = double(nii.img);

nii = load_nii(MaskName);
Mask = nii.img;

% Fill any internal holes in Mask
FullMask = Mask;
h = waitbar(0,'Filling in holes...');
for slice = 1:size(Mask,3)
    %display(slice);
    image = Mask(:,:,slice);
    image = imfill(image,'holes');
    FullMask(:,:,slice) = image;
    waitbar(slice/size(Mask,3));
end
close(h);


% Normalise Volume
Volume = Volume - min(Volume(:));
Volume = Volume ./ max(Volume(:));

% Save Volume and FullMask in current directory
save 'Volume' Volume;
save 'FullMask' FullMask;
```

---

2 – CreateMeanSdBrainVolumes

```
function CreateMeanSdBrainVolumes(R,Margin)
tic;
% Calculates local Mean and Sd within Brain Mask

% Load data from previous step
load Volume;
load FullMask;

FullMask_no_erode = FullMask;

% If specified, erode brain mask by margin.
if nargin > 1
    h = pda_SphericalMask(round(Margin/2));
    FullMask = imerode(FullMask,h);
end

% Create empty arrays
MeanVolume = zeros(size(Volume));
SdVolume = zeros(size(Volume));
```

```
% Find index points within mask
BrainIndex = find(FullMask==1);

% Create a sphere of points within a radius R
[X,Y,Z] = pda_SphericalRegion(R);

VX = size(Volume,2);
VY = size(Volume,1);
VZ = size(Volume,3);

% For each point within brain mask:
display('Calculating local Mean and Sd ...');
for i = 1:length(BrainIndex)
    p = BrainIndex(i);
    %display(p);
    [yp,xp,zp] = ind2sub(size(Volume),p); % convert index point into
xzy coordinates
    XR = X + xp;                          % Center spherical region
on this point
    YR = Y + yp;
    ZR = Z + zp;

    % Exclude any points actually outside of image volume
    where = find(XR > 0 & XR < VX & YR > 0 & YR < VY & ZR > 0 & ZR <
VZ);
    XR = XR(where);
    YR = YR(where);
    ZR = ZR(where);

    index = sub2ind(size(Volume),YR,XR,ZR); % Convert xyz back into
an array index
    index = index(index ~= p);              % Exclude center voxel
from calculation

    % Create index of remaining points within brain mask
    MaskVal = FullMask(index);
    Valid = find(MaskVal == 1);

    Values = Volume(index(Valid)); % Extract data values
corresponding to remaining points

    MeanVolume(p) = mean(Values);
    SdVolume(p) = std(Values);
    %workbar(i/length(BrainIndex),'Calculating Local Mean and Sd
...');
end
save 'MeanVolume' MeanVolume;
save 'SdVolume' SdVolume;
save 'FullMask' FullMask;
save 'FullMask_no_erode' FullMask_no_erode;
time = toc;
display(time);
display('...finished');
```

---

3 – CreateBrainHypoMask_regionprops

```
function [Volume_new,Number_new] =
CreateBrainHypoMask_regionprops(Type,Val,Size,Margin)
```

```
% Select regions of brain where value is set number of Sd below local
mean

% Load reference nii to get nii structure right
nii = load_nii('ReferenceVolume.nii');

% Load Values
load Volume;
load FullMask;
load FullMask_no_erode;
load MeanVolume;
load SdVolume;

% If specified, erode brain mask by margin.
if nargin > 2
    if Margin > 0
        h = pda_SphericalMask(round(Margin/2));
        FullMask = imerode(FullMask,h);
    end
end

BrainIndex = find(FullMask==1);
BrainIndex_no_erode = find(FullMask_no_erode==1);
a = size(BrainIndex_no_erode);

disp(sprintf('Brain volume: %i voxels',a(1)))

BrainValues = Volume(BrainIndex);
MeanValues = MeanVolume(BrainIndex);
SdValues = SdVolume(BrainIndex);

switch lower(Type)
    case 'sdnum'
        Thresh = MeanValues - (SdValues * Val);
    case 'meanfrac'
        Thresh = MeanValues .* Val;
    otherwise
        display('ERROR: Unknown option');
        HypoVolume = 'null';
        return;
end

HypoMask = zeros(size(Volume));

HypoMask_mod = zeros(size(Volume));
HypoMask_mod_large = zeros(size(Volume));
HypoMask_combine = zeros(size(Volume));

where = find(BrainValues < Thresh);

HypoMask_combine(BrainIndex_no_erode) = 1;
HypoMask(BrainIndex(where)) = 2;

HypoMask_combine(BrainIndex(where)) = 2;


HypoMask_label = bwlabeln(HypoMask,18);
STATS = regionprops(HypoMask_label, 'PixelIdxList', 'Area',
'Centroid');
hypo_number = size(STATS, 1);
```

```
largest_hypo = max([STATS(:).Area]);
smallest_hypo = min([STATS(:).Area]);
mean_hypo = mean([STATS(:).Area]);
std_hypo = std([STATS(:).Area]);

hypo_descriptor = zeros(largest_hypo,hypo_number);

max_BV = max(BrainValues);
min_BV = min(BrainValues);
mean_BV = mean(BrainValues);
std_BV = std(BrainValues);
U = numel(unique(BrainValues));

volume_small = 0;
number_small = 0;
volume_medium = 0;
number_medium = 0;
volume_large = 0;
number_large = 0;

for i=1:hypo_number

    this_hypo_pixels = STATS(i).PixelIdxList;
    hypo_area = STATS(i).Area;

    if hypo_area == 1

        volume_small = volume_small + 1;
        number_small = number_small + 1;

    end

    if hypo_area > 1 && hypo_area < Size

        volume_medium = volume_medium + hypo_area;
        number_medium = number_medium + 1;

        HypoMask_mod(this_hypo_pixels) = 3;
        HypoMask_combine(this_hypo_pixels) = 3;

        for j=1:length(this_hypo_pixels)

            hypo_descriptor(j,i) = Volume(this_hypo_pixels(j));

        end

    elseif hypo_area >= Size

        volume_large = volume_large + hypo_area;
        number_large = number_large + 1;

        HypoMask_mod_large(this_hypo_pixels) = 4;
        HypoMask_combine(this_hypo_pixels) = 4;

    else

        HypoMask_mod(this_hypo_pixels) = 0;

    end
```

```
end

total_volume = volume_small + volume_medium + volume_large;
total_number = number_small + number_medium + number_large;

disp(sprintf('Total volume of small hypos (size = 1): %i
voxels',volume_small))
disp(sprintf('Total number of small hypos (size = 1):
%i',number_small))
disp(sprintf('Total volume of medium hypos (1 < size < %i): %i
voxels',Size,volume_medium))
disp(sprintf('Total number of medium hypos (1 < size < %i): %i',Size,
number_medium))
disp(sprintf('Total volume of large hypos (size >= %i): %i
voxels',Size,volume_large))
disp(sprintf('Total number of large hypos (size >= %i):
%i',Size,number_large))
disp(sprintf('Total volume of hypos (all sizes): %i
voxels',total_volume))
disp(sprintf('Total number of hypos (all sizes): %i',total_number))

index = zeros(1,hypo_number);
hypo_descriptor_max = zeros(1,hypo_number);
hypo_descriptor_min = zeros(1,hypo_number);
hypo_descriptor_mean = zeros(1,hypo_number);
hypo_descriptor_std = zeros(1,hypo_number);

for i=1:hypo_number

    index(i) = i;
    hypo_descriptor_max(i) = max(hypo_descriptor(:,i));
    hypo_descriptor_min(i) = min(hypo_descriptor(:,i));
    hypo_descriptor_mean(i) = mean(hypo_descriptor(:,i));
    hypo_descriptor_std(i) = std(hypo_descriptor(:,i));

end

HypoMask_mod_label = bwconncomp(HypoMask_mod,18);
STATS_mod = regionprops(HypoMask_mod_label);
stats_mod(:,1) = cat(1, STATS_mod.Area);
a = stats_mod(:,1);
% dfittool(a)

largest_hypo_mod = max([STATS_mod(:).Area]);
smallest_hypo_mod = min([STATS_mod(:).Area]);
mean_hypo_mod = mean([STATS_mod(:).Area]);
std_hypo_mod = std([STATS_mod(:).Area]);

Volume_new = sum(stats_mod(:,1));
Number_new = size(STATS_mod, 1);

nii.img = HypoMask_mod;
save_nii(nii,'HypoSegmentation_filter.nii');

nii.img = HypoMask_mod_large;
save_nii(nii,'HypoSegmentation_large.nii');

nii.img = HypoMask_combine;
save_nii(nii,'HypoSegmentation_combine.nii');

% Find the total volume of Hypo-intense objects
```

```
HypoVolume = length(BrainIndex(where));

% Find the total number of Hypo-intense objects
LabelVolume = bwlabeln(HypoMask);
HypoNumber = max(LabelVolume(:));


% Save Hypo mask in nifti format
nii.img = HypoMask;
save_nii(nii,'HypoSegmentation.nii');
```

---

4 – pda_SphericalRegion

```
function [X,Y,Z] = pda_SphericalRegion(R)


% Create Bounding Box
Length = (R * 2) + 1;

Vol = zeros(Length, Length, Length);

[y,x,z] = ind2sub(size(Vol),1:length(Vol(:)));

x = x - R;
y = y - R;
z = z - R;

Dist = sqrt(x.^2 + y.^2 + z.^2);

where = find(Dist < R);

X = x(where);
Y = y(where);
Z = z(where);
```

---

5 – pda_SphericalMask

```
function [Vol] = pda_SphericalMask(R)


% Create Bounding Box
Length = (R * 2) + 1;

Vol = zeros(Length, Length, Length);

[y,x,z] = ind2sub(size(Vol),1:length(Vol(:)));

x = x - R;
y = y - R;
z = z - R;

Dist = sqrt(x.^2 + y.^2 + z.^2);
```

```
where = find(Dist < R);

X = x(where);
Y = y(where);
Z = z(where);

X = X + R + 1;
Y = Y + R + 1;
Z = Z + R + 1;

index = sub2ind(size(Vol),Y,X,Z);
Vol(index) = 1;
```

MATLAB scripts for GE3D filtering

1 – MedianFilter

```
function [Median_Volume] = MedianFilter(VolumeName1, VolumeName2,
MaskName)

% Loads the Brain volume and mask volume in NIFTI format

if nargin < 3
    % Select Brain Volume
    if exist('BrainVolumeFilePath1.mat') == 2
    load BrainVolumeFilePath1;
    if BrainVolumeFilePath1 ~= 0
        [VolumeFileName1,BrainVolumeFilePath1] =
uigetfile('*.nii','Select Brain Volume 1',BrainVolumeFilePath1);
    else
        [VolumeFileName1,BrainVolumeFilePath1] = uigetfile('*.nii');
    end
    else
        [VolumeFileName1,BrainVolumeFilePath1] = uigetfile('*.nii');
    end

    save 'BrainVolumeFilePath1' BrainVolumeFilePath1;


    % Select Brain Volume
    if exist('BrainVolumeFilePath2.mat') == 2
    load BrainVolumeFilePath2;
    if BrainVolumeFilePath2 ~= 0
        [VolumeFileName2,BrainVolumeFilePath2] =
uigetfile('*.nii','Select Brain Volume 2',BrainVolumeFilePath2);
    else
        [VolumeFileName2,BrainVolumeFilePath2] = uigetfile('*.nii');
    end
    else
        [VolumeFileName2,BrainVolumeFilePath2] = uigetfile('*.nii');
    end

    save 'BrainVolumeFilePath2' BrainVolumeFilePath2;
```

```
    % Select Brain Mask
    if exist('BrainMaskFilePath.mat') == 2
    load BrainMaskFilePath;
    if BrainMaskFilePath ~= 0
        [MaskFileName,BrainMaskFilePath] = uigetfile('*.nii','Select
Brain Mask',BrainMaskFilePath);
    else
        [MaskFileName,BrainMaskFilePath] = uigetfile('*.nii');
    end
    else
        [MaskFileName,BrainMaskFilePath] = uigetfile('*.nii');
    end

    save 'BrainMaskFilePath' BrainMaskFilePath;


    % Select output folder
    output = uigetdir;


    VolumeName1 = fullfile(BrainVolumeFilePath1,VolumeFileName1);
    VolumeName2 = fullfile(BrainVolumeFilePath2,VolumeFileName2);
    MaskName = fullfile(BrainMaskFilePath,MaskFileName);
end


% Load the selected volumes;
nii = load_nii(VolumeName1);
Volume1 = double(nii.img);

nii = load_nii(VolumeName2);
Volume2 = double(nii.img);

nii_mask = load_nii(MaskName);
Mask = nii_mask.img;


% Fill any internal holes in Mask
FullMask = Mask;

for slice = 1:size(Mask,3)
    image = Mask(:,:,slice);
    image = imfill(image,'holes');
    FullMask(:,:,slice) = image;
end

BrainIndex = find(FullMask==1);

% MeanVolume = zeros(size(Volume1));
Vol1_med2 = zeros(size(Volume1));
Vol2_med2 = zeros(size(Volume1));
MedianVolume1 = zeros(size(Volume1));
MedianVolume2 = zeros(size(Volume1));
Median2MeanVolume = zeros(size(Volume1));
Median3MeanVolume = zeros(size(Volume1));
MeanMedian2Volume = zeros(size(Volume1));
MeanMedianVolume = zeros(size(Volume1));


%% Straight mean filter
```

```
disp(sprintf('\rMean Filter...\r'))
tic
MeanVolume = wfusmat(Volume1,Volume2,'mean');
nii.img = MeanVolume;
save_nii(nii,sprintf('%s//MeanVolume.nii',output));
toc


%% Straight 1px 2D median filter on 1st brain volume
disp(sprintf('\r2D Median Filter (Brain 1)...\r'))
tic
for i=1:length(Volume1)
    Vol1_med2(:,:,i) = medfilt2(Volume1(:,:,i));
end
nii.img = Vol1_med2;
save_nii(nii,sprintf('%s//Median2Volume1.nii',output));
toc


%% Straight 1px 2D median filter on 1st brain volume
disp(sprintf('\r2D Median Filter (Brain 2)...\r'))
tic
for i=1:length(Volume2)
    Vol2_med2(:,:,i) = medfilt2(Volume2(:,:,i));
end
nii.img = Vol2_med2;
save_nii(nii,sprintf('%s//Median2Volume2.nii',output));
toc


%% Straight 1px 3D median filter on 1st brain volume
disp(sprintf('\r3D Median Filter (Brain 1)...\r'))
tic
for i=1:length(BrainIndex(:))

    j = BrainIndex(i);
    [y,x,z] = ind2sub(size(Volume1),j);

    median_store = [Volume1(y,x,z), ...
% Central voxel
                    Volume1(y-1,x-1,z), Volume1(y-1,x,z), Volume1(y-
1,x+1,z), ...          % Voxels in same z plane
                    Volume1(y,x-1,z), Volume1(y,x+1,z), ...
                    Volume1(y+1,x-1,z), Volume1(y+1,x,z),
Volume1(y+1,x+1,z), ...
                    Volume1(y-1,x-1,z-1), Volume1(y-1,x,z-1),
Volume1(y-1,x+1,z-1), ...    % Voxels in z-1 plane
                    Volume1(y,x-1,z-1), Volume1(y,x,z-1),
Volume1(y,x+1,z-1), ...
                    Volume1(y+1,x-1,z-1), Volume1(y+1,x,z-1),
Volume1(y+1,x+1,z-1), ...
                    Volume1(y-1,x-1,z+1), Volume1(y-1,x,z+1),
Volume1(y-1,x+1,z+1), ...    % Voxels in z+1 plane
                    Volume1(y,x-1,z+1), Volume1(y,x,z+1),
Volume1(y,x+1,z+1), ...
                    Volume1(y+1,x-1,z+1), Volume1(y+1,x,z+1),
Volume1(y+1,x+1,z+1)];

    MedianVolume1(j) = median(median_store);
%     median_volume1 = median(median_store1);
%     MedianVolume(j) = median_volume1;
```

```
end

nii.img = MedianVolume1;
save_nii(nii,sprintf('%s//Median3Volume1.nii',output));
toc


%% Straight 1px 3D median filter on 1st brain volume
disp(sprintf('\r3D Median Filter (Brain 2)...\r'))
tic
for i=1:length(BrainIndex(:))

    j = BrainIndex(i);
    [y,x,z] = ind2sub(size(Volume2),j);

    median_store = [Volume2(y,x,z), ...
% Central voxel
                    Volume2(y-1,x-1,z), Volume2(y-1,x,z), Volume2(y-
1,x+1,z), ...          % Voxels in same z plane
                    Volume2(y,x-1,z), Volume2(y,x+1,z), ...
                    Volume2(y+1,x-1,z), Volume2(y+1,x,z),
Volume2(y+1,x+1,z), ...
                    Volume2(y-1,x-1,z-1), Volume2(y-1,x,z-1),
Volume2(y-1,x+1,z-1), ...    % Voxels in z-1 plane
                    Volume2(y,x-1,z-1), Volume2(y,x,z-1),
Volume2(y,x+1,z-1), ...
                    Volume2(y+1,x-1,z-1), Volume2(y+1,x,z-1),
Volume2(y+1,x+1,z-1), ...
                    Volume2(y-1,x-1,z+1), Volume2(y-1,x,z+1),
Volume2(y-1,x+1,z+1), ...    % Voxels in z+1 plane
                    Volume2(y,x-1,z+1), Volume2(y,x,z+1),
Volume2(y,x+1,z+1), ...
                    Volume2(y+1,x-1,z+1), Volume2(y+1,x,z+1),
Volume2(y+1,x+1,z+1)];

    MedianVolume2(j) = median(median_store);
%     median_volume1 = median(median_store1);
%     MedianVolume(j) = median_volume1;

end

nii.img = MedianVolume2;
save_nii(nii,sprintf('%s//Median3Volume2.nii',output));
toc


%% 1px 2D median filters, mean filtered
disp(sprintf('2D Median Mean Filter...\r'))
tic
Median2MeanVolume = wfusmat(Vol1_med2,Vol2_med2,'mean');
nii.img = Median2MeanVolume;
save_nii(nii,sprintf('%s//Median2MeanVolume.nii',output));
toc

%% 1px 3D median filters, mean filtered
disp(sprintf('3D Median Mean Filter...\r'))
tic
Median3MeanVolume = wfusmat(MedianVolume1,MedianVolume2,'mean');
nii.img = Median3MeanVolume;
save_nii(nii,sprintf('%s//Median3MeanVolume.nii',output));
toc
```

```
%% Mean filter, then 1px 2D median filter
disp(sprintf('Mean 2D Median Filter...\r'))
tic
for i=1:length(MeanVolume)
    MeanMedian2Volume(:,:,i) = medfilt2(MeanVolume(:,:,i));
end
nii.img = MeanMedian2Volume;
save_nii(nii,sprintf('%s//MeanMedian2Volume.nii',output));
toc


%% Mean filter, then 1px 3D median filter
disp(sprintf('Mean 3D Median Filter...\r'))
tic
for i=1:length(BrainIndex(:))

    j = BrainIndex(i);

    [y,x,z] = ind2sub(size(Volume1),j);

    % Mean filter already complete, so move on to median filter using
    % MeanVolume
    median_store = [MeanVolume(y,x,z), ...
% Central voxel
                    MeanVolume(y-1,x-1,z), MeanVolume(y-1,x,z),
MeanVolume(y-1,x+1,z), ...          % Voxels in same z plane
                    MeanVolume(y,x-1,z), MeanVolume(y,x+1,z), ...
                    MeanVolume(y+1,x-1,z), MeanVolume(y+1,x,z),
MeanVolume(y+1,x+1,z), ...
                    MeanVolume(y-1,x-1,z-1), MeanVolume(y-1,x,z-1),
MeanVolume(y-1,x+1,z-1), ...    % Voxels in z-1 plane
                    MeanVolume(y,x-1,z-1), MeanVolume(y,x,z-1),
MeanVolume(y,x+1,z-1), ...
                    MeanVolume(y+1,x-1,z-1), MeanVolume(y+1,x,z-1),
MeanVolume(y+1,x+1,z-1), ...
                    MeanVolume(y-1,x-1,z+1), MeanVolume(y-1,x,z+1),
MeanVolume(y-1,x+1,z+1), ...    % Voxels in z+1 plane
                    MeanVolume(y,x-1,z+1), MeanVolume(y,x,z+1),
MeanVolume(y,x+1,z+1), ...
                    MeanVolume(y+1,x-1,z+1), MeanVolume(y+1,x,z+1),
MeanVolume(y+1,x+1,z+1)];

    MeanMedianVolume(j) = median(median_store);

end

nii.img = MeanMedianVolume;
save_nii(nii,sprintf('%s//MeanMedian3Volume.nii',output));
toc

disp('Analysis complete')
```

MATLAB script for metastasis analysis

1 – analyse_met_list_unique_mod_circ_new

```
%% Script to analyze brain met lists

% Start with a spreadsheet with columns:
% 'number','area','length','met','section'

function [descriptors] =
analyze_met_list_unique_mod_circ_new(varname)

list_sorted = sortrows(varname, [4 5]);
save 'list_sorted' list_sorted;
entries = length(list_sorted(:,1));

the_number_that_shall_not_be_spoken = find(list_sorted(:,5)>20);
if any(the_number_that_shall_not_be_spoken) == 1

    errordlg('There is an error in the 5th column: one of the values
is greater than 20');
    return

end

% Calculate the number of mets in the list
met_num_list = unique(list_sorted(:,4));
met_num = numel(met_num_list);
disp(sprintf('Number of mets: %i',met_num));

met_num_min = min(list_sorted(:,4));
met_num_max = max(list_sorted(:,4));

% Set up empty variables
descriptors = zeros(met_num,6);
% descriptors(:,1) = met_num_min:met_num_max;
descriptors(:,1) = 1:met_num;
descriptors(:,6) = met_num_list(:);
volume_blob = zeros(entries,1);
volume_met_section = [];
% volume_section = zeros(met_num,4);

% Working with each_section rather than volume_section
% each_section = zeros(entries,4);

volume_blobs = 0;
else_end = 0;
gap = [];

for i=1:entries

    % Calculate the volume of individual met blobs
%     met_id = list_sorted(i,4);
%     met_section = list_sorted(i,5);
    volume_blob(i) = list_sorted(i,3)*10;
```

```
end

list_sorted(:,6) = volume_blob;

for m=1:met_num

%     descriptors
    % Calculate the range
    met_number = met_num_list(m);

    list_index = find(list_sorted(:,4) == met_number);
    z_min = min(list_sorted(list_index,5));
    z_max = max(list_sorted(list_index,5));
    z_diff = z_max - z_min;
    range = 10 + 30*z_diff;
    descriptors(m,3) = range;
%     descriptors(m,6) = met_num_min -1 +m;

    % Calculate the average area:length ratio
    al_ratio = [];
    lengths = list_sorted(list_index,2);
    areas = list_sorted(list_index,3);
    l_div_a = zeros(length(lengths),1);
    spheres_store = zeros(length(lengths),2);
    circumference = zeros(length(lengths),1);

    for n=1:length(lengths)
        circumference(n,1) = 2*pi*sqrt(areas(n)/pi);
        spheres_store(n,1) = circumference(n);
        spheres_store(n,2) = lengths(n);
        l_div_a(n,1) = circumference(n)/lengths(n);
    end

%     l_div_a = lengths/areas;
    al_ratio = mean(l_div_a(:));
    new_al_ratio = sum(spheres_store(:,1))/sum(spheres_store(:,2));
    descriptors(m,5) = al_ratio;
    descriptors(m,6) = new_al_ratio;
end

count = 1;
% volume_section = zeros(list_index,4);

for m=1:met_num

met_number = met_num_list(m);

    list_index = find(list_sorted(:,4) == met_number);
    list_index_min = min(list_index);
    list_index_max = max(list_index);
    list_index_size = list_index_max - list_index_min;
    each_section = zeros(length(list_index),3);

    for met_entries = list_index_min:list_index_max
        volume_this = volume_blob(met_entries);

        if met_entries == list_index_max

            if volume_blobs > 0
                each_section(met_entries-list_index_min+1,1) =
```

```
volume_blobs;
            else
                each_section(met_entries-list_index_min+1,1) =
volume_this;
            end
            each_section(met_entries-list_index_min+1,3) = count;
            volume_blobs = 0;
            count = 1;

        elseif list_sorted(met_entries,4) ==
list_sorted(met_entries+1,4) & list_sorted(met_entries,5) ==
list_sorted(met_entries+1,5)
            if volume_blobs == 0
                volume_blobs = volume_this +
volume_blob(met_entries+1);
            elseif volume_blobs ~= 0
                volume_blobs = volume_blobs +
volume_blob(met_entries+1);
            end
            count = count + 1;

        else

            if volume_blobs > 0
                each_section(met_entries-list_index_min+1,1) =
volume_blobs;
            else
                each_section(met_entries-list_index_min+1,1) =
volume_this;
            end
            each_section(met_entries-list_index_min+1,3) = count;
            volume_blobs = 0;
            count = 1;

        end

%         each_section

    end

    average_count = each_section(:,3);
    idx_zero = find(average_count == 0);
    average_count(idx_zero) = NaN;
    average_count = nanmean(average_count(:));
    descriptors(m,4) = average_count;

    % Build a collapsed version of each_section for the next bit
    each_section_clean_index = find(each_section(:,1) ~= 0);
    each_section_clean = zeros(length(each_section_clean_index),3);
    each_section_clean(:,2) = each_section(each_section_clean_index);
    sections = list_sorted(list_index_min:list_index_max,5);
    each_section_clean(:,1) = sections(each_section_clean_index);

    for met_entries = 1:length(each_section_clean(:,1))-1

        gap = each_section_clean(met_entries+1,1) -
each_section_clean(met_entries,1);

        if gap == 0

        else
```

```
            if gap > 3
                disp(sprintf('Error at %ith line',i))
                errordlg('The gap is greater than 3. Check the
original file and re-analyse if necessary.')
                xlswrite('list_sorted.xls',list_sorted);
            end

            missing = 3*gap - 1;
            interpolations = zeros(missing,1);

            for j=1:missing

            ratio_p = (3*gap)-j;
            ratio_q = (3*gap)-ratio_p;

            % Need to look for the next non-zero element, not just
the
            % next element

            missing_value =
((ratio_p*each_section_clean(met_entries,2)) +
(ratio_q*each_section_clean(met_entries+1,2)))/(3*gap);

            interpolations(j) = missing_value;

            end

        total_missing = sum(interpolations);
        each_section_clean(met_entries,3) = total_missing;

        end

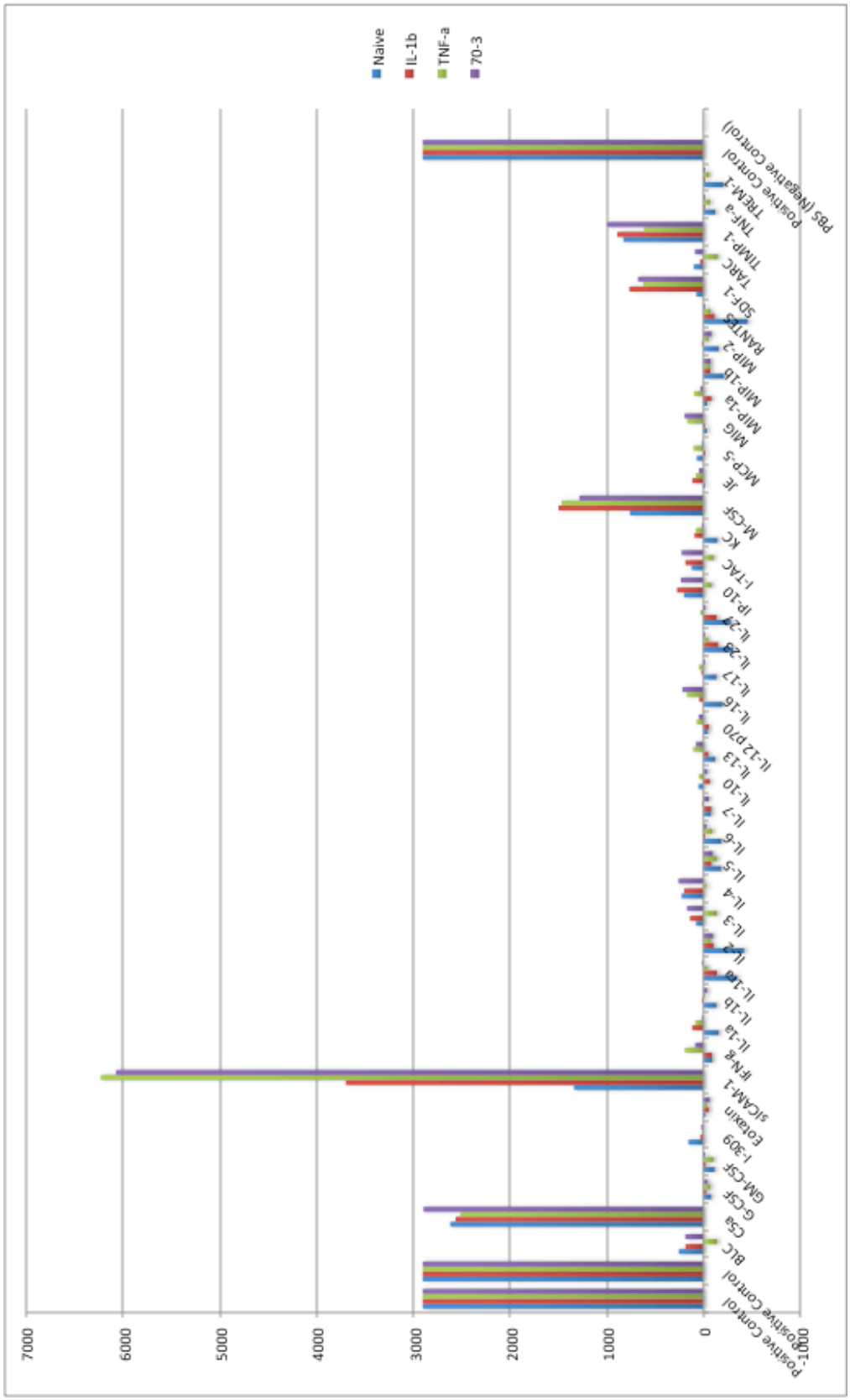

    end


    total_met_volume = sum(each_section_clean(:,2)) +
sum(each_section_clean(:,3));
    descriptors(m,2) = total_met_volume;
%     each_section_clean

end

xlswrite('met_descriptors.xls',descriptors);
```

Appendix 3


Naive
IL-1b
TNF-a
70-3
PBS (Negative Control)
Positive Control
TREM-1
TNF-a
TIMP-1
TARC
SDF-1
RANTES
MIP-2
MIP-1b
MIP-1a
MIG
MCP-5
JE
M-CSF
KC
I-TAC
IP-10
IL-27
IL-23
IL-17
IL-16
IL-12 P70
IL-13
IL-10
IL-7
IL-6
IL-5
IL-4
IL-3
IL-2
IL-1ra
IL-1b
IL-1a
IFN-g
sICAM-1
Eotaxin
I-309
GM-CSF
G-CSF
CSa
BLC
Positive Control
7000
6000
5000
4000
3000
2000
1000
0
-1000